



Durham E-Theses

Simulation studies of the imaging atmospheric cherenkov technique using the Durham mark 6 and H.E.S.S. stand-alone telescopes

Nolan, Sam Joffre

How to cite:

Nolan, Sam Joffre (2002) *Simulation studies of the imaging atmospheric cherenkov technique using the Durham mark 6 and H.E.S.S. stand-alone telescopes*, Durham theses, Durham University. Available at Durham E-Theses Online: <http://etheses.dur.ac.uk/4193/>

Use policy

The full-text may be used and/or reproduced, and given to third parties in any format or medium, without prior permission or charge, for personal research or study, educational, or not-for-profit purposes provided that:

- a full bibliographic reference is made to the original source
- a [link](#) is made to the metadata record in Durham E-Theses
- the full-text is not changed in any way

The full-text must not be sold in any format or medium without the formal permission of the copyright holders.

Please consult the [full Durham E-Theses policy](#) for further details.

The copyright of this thesis rests with the author.
No quotation from it should be published without
his prior written consent and information derived
from it should be acknowledged.

**Simulation Studies of the Imaging Atmospheric Cherenkov
Technique using the Durham Mark 6 and H.E.S.S.
Stand-Alone Telescopes**

Sam Joffre Nolan, MSci

A thesis submitted to the University of Durham in accordance with the
regulations for admittance to the degree of Doctor of Philosophy

September 2002
Department of Physics
University of Durham
South Road
Durham
United Kingdom

Thesis

2002/

NOL

Simulation Studies of the Imaging Atmospheric Cherenkov Technique using the Durham Mark 6 and H.E.S.S. Stand-Alone Telescopes.

By Sam Nolan, MSci

Ph. D. Thesis, University of Durham, 2002

Abstract

The subject of this thesis is the simulation study of the development of extensive air showers produced by very high energy gamma-ray and hadronic cosmic rays with respect to the Cherenkov light they produce, and its imaging in ground based telescopes. Chapters 1-4 are introductory: Chapter 1 covers the mechanisms responsible for the production of very high energy gamma-rays, whereas, chapter 2 focusses on the development of extensive air showers and Cherenkov light production. Chapter 3 covers the instrumentation used to measure the Cherenkov light using the imaging atmospheric Cherenkov technique. Chapter 4 covers known and possible sources of very high energy gamma-rays. Chapters 5, 6 and 7 cover research performed by the author: Chapter 5 discusses some of the differences between three popular extensive air shower simulations codes, namely ALTAI, CORSIKA and MOCCA. Chapter 6 details the simulation of the response of two ground based imaging atmospheric Cherenkov telescope (the Durham Mark 6 and stand-alone H.E.S.S. telescopes), and in particular details the derivation of the flux of the x-ray selected BL-LAC PKS 2155-304 with the Durham Mark 6 telescope. This represents the refinement of a published measurement given an improved telescope simulation. The significance of the signal seen is 6.8σ , and the integral flux derived above 1.5 TeV (assuming a differential spectral slope of -2.6) is $(2.5 \pm 0.7_{stat} \pm \frac{0.5}{1.6}_{syst}) \times 10^{-7}$ photons $\text{m}^{-2} \text{s}^{-1}$. Chapter 7 discusses the importance of the atmosphere, and the results of shower simulations under different atmospheric assumptions are presented, which indicate the importance of atmospheric calibration for the new generation of Cherenkov telescopes. The results of this chapter suggest that to first order large changes in the low level aerosol concentration have a much more significant effect on the trigger rate of a stand-alone H.E.S.S. telescope, than on the Hillas parameter distributions seen. Chapter 8 brings together the work done in this thesis, and highlights a final set of fluxes for the active galactic nuclei sources seen with the Durham Mark 6 telescope, many of which will form future sources to be measured with the H.E.S.S. system. The current status of the stand-alone H.E.S.S. system is also covered in chapter 8. The thesis concludes with a further brief discussion of the future prospects for imaging atmospheric Cherenkov astronomy.

Preface

The work described in this thesis is associated with the Durham University Mark 6 imaging atmospheric Cherenkov previously sited in Narrabri, NSW, Australia and the first stand-alone H.E.S.S. imaging atmospheric Cherenkov telescope, sited near the Gamsberg Mountain in Namibia. The author has been involved in the data analysis and simulations of the Durham Mark 6 telescope, and is an active member of the H.E.S.S. Monte Carlo group.

All of the material presented in this thesis is the author's own work, none of which has been submitted previously for admittance to a degree in this or any other University, except where due reference is made. The copyright of this thesis rests with the author.

Acknowledgements

There are many people who I am indebted too for their assistance in my studies over the last three years. Firstly, I would like to express my deep gratitude towards my supervisor, Dr. John Osborne for many useful discussions and ideas, and for his willingness to answer my (sometimes) inane questions. I would also like to thank my colleagues at the observatory for their help, assistance and friendship over the last three years, in particular I would like to thank Drs. Paula Chadwick and Steve Rayner, and also my fellow students Michael Daniel, Joy Mckenny and Klaus-Michael Aye. All have shown me great tolerance and have contributed to many useful conversations on the subjects of this thesis. Outside the gamma-ray group, but within Durham, I wish to extend thanks to Dr. Peter Draper for his support in complex computing matters. Also, outside Durham, but within the H.E.S.S. collaboration, I would like to thank Drs. Alexander Konopelko and Konrad Bernlöhner for their constant assistance with integrating the results from ALTAI and CORSIKA respectively into the software for first the Mark 6 telescope and currently the stand-alone H.E.S.S. telescope. Their friendly enthusiasm for the field has encouraged me from the beginning of my studies. Dr Eric Shettle from the Naval Laboratories in Washington is also thanked for providing several papers on his aerosol light attenuation models for the atmosphere, which would be difficult to obtain without his permission.

This thesis has been made possible by the provision of the facilities of the Physics Department at the University of Durham, for which I thank Prof. Michael Pennington, and my research studentship which was funded by the Particle Physics and Astronomy Research Council.

To my parents, without whose constant love and support, I could not have taken even the first step on this journey

*“Every time it rains,
it rains pennies from heaven ...”*

- J. Burke

Contents

1	Very High Energy Particle Production	1
1.1	Introduction	1
1.2	The Gamma-Ray Spectrum and Observational Techniques	2
1.3	The Production of Cosmic Rays	3
1.3.1	Dynamo Mechanism	4
1.3.2	Second Order Fermi Mechanism	4
1.3.3	First Order Fermi Mechanism	7
1.4	Very High Energy Photon Production	12
1.4.1	Gamma-Ray Production via Meson Decay	12
1.4.2	Gamma-Ray Production by Particle Acceleration Mechanisms	13
1.4.3	Summary	16
1.5	Attenuation of the VHE Gamma-Ray Signal	16
1.5.1	Single Photon Pair Production	17
1.5.2	Photon-Photon Pair Production	17
1.6	Summary	19
2	Extensive Air Showers and Cherenkov Light Production	21
2.1	Introduction	21
2.2	Gamma-Ray Initiated EAS	22
2.3	Hadron Initiated EAS	25
2.4	Cherenkov Radiation	26
2.5	Cherenkov Radiation in the Atmosphere	29
2.6	Differences in Cherenkov Emission from Nucleon and Photon Initiated EAS	32
2.6.1	The Gamma-Ray Initiated EAS Cherenkov Light Pool	33
2.6.2	The Cosmic Ray Initiated EAS Cherenkov Light Pool	34
2.6.3	Time Profiles of Gamma-Ray and Cosmic Ray EAS Cherenkov Light Pulses	35

2.7	Summary	36
3	Imaging Atmospheric Cherenkov Astronomy	38
3.1	Introduction	38
3.1.1	History	38
3.2	Physical Specifications of an imaging atmospheric Cherenkov telescope (IACT)	40
3.2.1	Effective Sensitive Area (ESA)	40
3.2.2	Field of View (FOV)	41
3.2.3	Threshold Energy (E_T)	42
3.3	The Imaging Atmospheric Cherenkov Technique	42
3.3.1	The Moments Technique	44
3.3.2	The Hillas Parameters	45
3.3.3	Hillas Parameters in Action	46
3.4	Imaging Atmospheric Cherenkov telescopes	51
3.4.1	The Durham Mark 6 Telescope	51
3.4.2	H.E.S.S.	55
3.4.3	Stereoscopy	57
3.5	Future Prospects for Ground Based Gamma-Ray Astronomy	58
4	TeV Astrophysics	60
4.1	Introduction	60
4.2	Physics Motivation	60
4.3	Astrophysical Sources	62
4.3.1	Plerions	62
4.3.2	Isolated Pulsars	64
4.3.3	Supernova Remnants	66
4.3.4	Accreting Binary Systems	68
4.3.5	Active Galactic Nuclei (AGN)	71
4.3.6	Gamma-Ray Bursts	76
4.3.7	Cosmological Uses	77
4.4	Current Status	78
5	Simulations of Extensive Air Showers	80
5.1	Introduction	80

5.2	A History of EAS Simulation	81
5.3	Monte Carlo EAS Simulation Codes	82
5.3.1	Gamma-Ray Initiated EAS	83
5.3.2	Hadron Initiated EAS	88
5.3.3	Cherenkov Light Deposition	94
5.4	Simulation Comparisons	97
5.4.1	Mono-energetic Simulations	97
5.4.2	Conclusion of Spatial Cherenkov Deposition Study	99
5.5	Higher Order Differences	100
5.5.1	Gamma-Rays	100
5.5.2	Cosmic Rays	101
5.5.3	Results	102
5.6	Conclusion	102
6	Simulations of Imaging Atmospheric Cherenkov Telescope Response	108
6.1	Introduction	108
6.2	Simulations of the Telescope System	108
6.2.1	Photon Attenuation	108
6.2.2	Triggering	109
6.3	Simulations in Practice	114
6.3.1	Shower Simulation	114
6.3.2	Refined Telescope Simulation	116
6.3.3	Result	118
6.3.4	Flux Derivation in Principle	121
6.4	Flux Derivation for PKS 2155-304	127
6.4.1	Observations	127
6.4.2	Finding the Spectral Index	129
6.4.3	Calculation of Flux	130
6.4.4	Sources of Error	131
6.4.5	Conclusion	133
6.5	Spectral Simulations for H.E.S.S. Stand Alone Telescope	134
6.5.1	Results	134
6.6	Conclusion	135

7	Atmospheric Effects on the Cherenkov Light Deposition	136
7.1	Introduction	136
7.2	Atmospheric Profile	137
7.2.1	Profile Calibration	140
7.3	Attenuation of Cherenkov Light	141
7.4	Mapping the Aerosol Structure	144
7.4.1	Horizontal Extinction Length Monitor	145
7.4.2	Optical Depth Monitor	146
7.4.3	Sky Clarity using a mid Infra-Red Radiometer	147
7.4.4	Stellar Photometry Measure	148
7.5	Further Simulation Studies of Atmospheric Effects	148
7.5.1	Ground at Different Levels	150
7.5.2	Aerosols at Different Levels	152
7.5.3	Different Aerosol Structures	154
7.5.4	Changes in Tropospheric Model	155
7.5.5	Current Standard Model	156
7.5.6	Atmospheric Profile Effects	157
7.5.7	Conclusion	160
7.6	Hillas Parameter Changes	161
7.6.1	Discussion	164
7.6.2	Conclusion of Study	167
7.7	Other Effects - Geomagnetism	168
7.8	Chapter Conclusion	170
8	Conclusion: A New Era in Cherenkov Astronomy	173
8.1	Introduction	173
8.2	AGN in the Durham Mark 6 Observing Program	174
8.2.1	Conclusion	176
8.3	Status of H.E.S.S.	177
8.3.1	Single Photoelectron Pulse Profiles and Simulation Comparisons	177
8.3.2	Status of Atmospheric Measurements at the H.E.S.S. Site	180
8.4	The Future of Cherenkov Astronomy	183
8.4.1	Analysis and Simulation Refinement	183
8.4.2	New Instrumentation	184

CONTENTS	xi
8.4.3 New Physics	185
8.5 Final Conclusions	186
Appendix A: MODTRAN Atmospheric Models	189
Appendix B: MODTRAN Aerosol Models	196
8.5.1 Composition	196
8.5.2 Light Attenuation Calculation	198
Appendix C: Camera Images	199
Appendix D: Differences In Hillas Parameter Distributions due to Atmosphere	212

Chapter 1

Very High Energy Particle Production

1.1 Introduction

Around the turn of the century, an interesting phenomenon was discovered by Rutherford and Cooke [179]. Once charged, the leaf of a gold-leaf electroscope was seen to droop within a short time, as if the charge were leaking from the leaf. This effect was seen to be less pronounced, if instead of being placed on the bench, the electroscope was placed within a thick metal box. This experiment is still used in classrooms to this day, to easily link the students with the strange world of sub-atomic particle interactions. The story of the deduction of the origin of the radiation which causes this leaf to droop is ongoing, as to this day no definite and unambiguous evidence has been found for the source of this energy, however within this thesis some of the current techniques and technologies employed in the search will be discussed.

The hypothesis in 1903 was that the radiation causing the leaf to droop was terrestrial in origin and came from radioactive decay of materials within the Earth's crust. However, some 7 years later in 1910, the historic balloon flights of Victor Hess proved that instead of decreasing with altitude, above a certain level (~ 1.5 km), the amount of ionising radiation actually increased with altitude [80], [69]. After these experiments, the radiation was inferred to be extra-terrestrial in origin, and was subsequently termed cosmic radiation. Since this time, studies into the energy and composition of cosmic radiation and suggestions for the possible progenitors of this radiation have formed an active part of astrophysics. It now turns out that the energy density of cosmic rays within the galaxy is approximately the same as that of the starlight photons, the turbulent gas motions in

the interstellar medium, and of galactic magnetic fields [124], [191].

Since the majority of cosmic radiation is charged and of low mass (90% being protons) its trajectories are affected by the galactic magnetic field ($\sim 10^{-6}$ G, [170]). Over interstellar distances, the trajectories are altered so much, that only the highest energy charged cosmic rays may have their paths easily traced back to their origin. Therefore, what is seen at Earth is mostly an isotropic flux of cosmic radiation.

Neutral components of the cosmic radiation include neutrons, neutrinos and gamma-rays. However, compared to the time taken to traverse interstellar distances the lifetime of the neutron is quite short, and thus neutrons cannot realistically be used to trace the origin of cosmic radiation. For example, a neutron from a distance of ~ 7 kpc, would require an energy of ~ 1 EeV to survive the journey to Earth without decaying. Neutrinos, on the other hand, have a very small interaction cross-section, and thus interactions between neutrinos and detecting hardware would be quite rare. Therefore (except in the case of a recent nearby supernova) the origin of most cosmic radiation has been difficult to ascertain so far using neutrino detectors. Gamma radiation interacts readily and being neutral, is unaffected by the intervening magnetic fields and thus points back to its origin. Also, being forced to travel in a straight line between source and observer the gamma-rays can give timing information about the processes occurring within the source. Therefore, gamma-ray astronomy is a useful tool in locating and studying sources of cosmic radiation.

1.2 The Gamma-Ray Spectrum and Observational Techniques

There has been some confusion as to the energy at which the gamma-ray spectrum starts; however, a consensus of the rest mass energy of the electron (0.511 MeV) has been reached. From here the spectrum covers 9 decades of energy, and is constrained only by the maximum energy photon ever observed. Obviously over such a wide range of energy, different observational techniques are required to observe in different energy ranges. To simplify matters a nomenclature of the energies involved in the gamma-ray spectrum has been created: low energy (0.5 to 5 MeV), medium energy (5 to 30 MeV), high energy (0.03 to 30 GeV), very high energy (0.01 to 50 TeV) and ultra high energy (0.05 to 0.1 PeV).

From low to high energy, gamma-rays are absorbed very high in the atmosphere and their energy dispersed in small electromagnetic cascades. Thus to observe at these energies satellite technology is used. At very high energies (> 30 GeV) the gamma-

Energy Range	Classification	Technique
0.5 – 5 MeV	Low Energy (LE)	Scintillation Detector (Satellite)
5 – 30 MeV	Medium Energy (ME)	Compton Telescope (Satellite)
0.03 – 30 GeV	High Energy (HE)	Spark Chamber (Satellite)
0.01 – 50 TeV	Very High Energy (VHE)	Atmospheric Cherenkov Detector (Ground Based)
0.05 – 0.1 PeV	Ultra High Energy (UHE)	Scintillation Detector Array (Ground Based)

Table 1.1: Table indicating the technique used for observing different parts of the gamma-ray spectrum.

rays cascades persist deeper and thus have sufficient energy to generate an appreciable amount of Cherenkov radiation (discussed at length in Chapter 2). The atmosphere is partially transparent to Cherenkov radiation; therefore ground-based telescopes can image this. By studying the images the Cherenkov radiation produces within the telescope, the energy and direction of the primary may be reconstructed. At ultra high energies, large proportions of the electromagnetic cascade reach ground level. Arrays of ground-based scintillation counters can be used to reconstruct the energy and direction of the primary ultra high energy gamma-ray. All this discussion is summarised in table 1.1.

The main topics of this thesis revolve around very high energy (VHE) gamma-rays, and utilise what is referred to as the ground-based atmospheric imaging Cherenkov technique.

1.3 The Production of Cosmic Rays

The acceleration of cosmic rays is of fundamental interest to physicists, and as will be seen as this thesis develops, the sites of production of charged cosmic rays are believed to be the same as the sites of production of VHE gamma radiation. Therefore, it seems to be appropriate to discuss in turn: the acceleration mechanisms for charged particles, the production of gamma radiation from populations of charged particles, and the attenuation of gamma radiation between source and observer. In doing this the history of the radiation from its creation in extreme astrophysical environments to its eventual interactions with the atmosphere of the Earth is traced out. To this end in chapter 2 the interactions of VHE gamma-rays and cosmic rays with the atmosphere are discussed, and in chapter 3 the eventual imaging by ground-based Cherenkov telescopes is covered. Firstly however,

a few of the popular models for charged particle acceleration are introduced.

1.3.1 Dynamo Mechanism

It is a well know fact that conductors moving (at velocity \mathbf{v}) in a magnetic field (\mathbf{B}) generate an electric field, given by $\underline{\mathbf{E}} = \underline{\mathbf{v}} \times \underline{\mathbf{B}}$. In the case of a magnetic field moving through a dense conductive plasma (for instance around a spinning neutron star), it has been postulated that if irregularities exist within the charge density of the plasma, then extreme potential differences will be generated between areas of high and low charge density. These potential differences will accelerate charged particles, and hence (by the mechanisms illustrated later in this chapter) produce VHE gamma-rays.

1.3.2 Second Order Fermi Mechanism

The second order mechanism is a descendant of Fermi's first order mechanism that he detailed in 1949 [57], and on which the focus shall be placed in a moment. The second order mechanism is a statistical mechanism for gaining a net increase in the energy of a population through collisions with magnetic mirrors. These mirrors are caused by irregularities in the galactic magnetic field that reflect charged particles with which they interact, such as the shock waves produced by stellar winds or supernova explosions. Fermi asked what the net increase in energy would be if the particles remained within the acceleration region for a time τ . Only a simple one dimensional case is presented here. We take it that there as many mirrors (or clouds) moving towards a particle as well as away from it. Consider figure 1.1 with a cosmic ray particle of energy E and momentum p in the observer's frame. Here we assume that $M \gg m$, so that the cloud's velocity is unchanged in the collision. The centre of momentum frame is therefore that of the cloud moving at velocity V with respect to the observer. The energy of the particle in this frame is thus:

$$E' = \gamma_V(E + Vp) \quad (1.1)$$

where

$$\gamma_V = \left(1 - \frac{V^2}{c^2}\right)^{-1/2} \quad (1.2)$$

and the relativistic three-momentum is

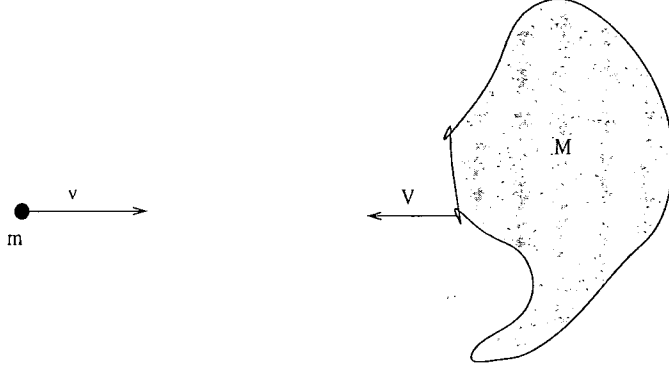


Figure 1.1: Illustration of the collision between a particle of mass m and velocity v and a cloud of mass M and velocity V . Taken from [124]

$$\mathbf{p}' = \gamma_V \left(\mathbf{p} + \frac{\mathbf{V}E}{c^2} \right) \quad (1.3)$$

where the bold-face font indicates a vector. In the collision, the particle's energy is conserved and the direction of its momentum vector is reversed. Therefore transforming back to the observer's frame, we find its energy to be:

$$E'' = \gamma_V (E' + Vp') = \gamma_V^2 E \left(1 + \frac{2Vv}{c^2} + \left(\frac{V}{c} \right)^2 \right) \quad (1.4)$$

i.e. expanding to second order in V/c :

$$\Delta E = 2E \frac{V}{c} \left(\frac{V}{c} + \frac{v}{c} \right) \quad (1.5)$$

If instead the collision had been a 'following' collision, energy would have been lost, i.e.:

$$\Delta E = -2E \frac{V}{c} \left(\frac{v}{c} - \frac{V}{c} \right) \quad (1.6)$$

However, from figure 1.2 we can see that the probability of each type of encounter is proportional to the relative velocity of particle and cloud. Therefore the probability of a 'head-on' collision is $\frac{1}{2}((V + v)/v)$ and a 'following' collision is $\frac{1}{2}((v - V)/v)$. Therefore, the net mean energy gain per collision is:

$$\Delta E = \frac{1}{2} \left(\frac{v+V}{v} \right) 2E \frac{V}{c} \left(\frac{V}{c} + \frac{v}{c} \right) - \frac{1}{2} \left(\frac{v-V}{v} \right) 2E \frac{V}{c} \left(\frac{v}{c} - \frac{V}{c} \right) \quad (1.7)$$

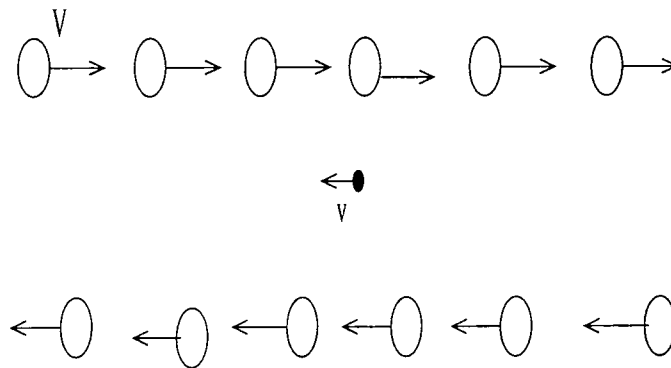


Figure 1.2: Illustration of the collision between a particle and a large number of clouds moving in the opposite direction in one dimension. Taken from [124].

or

$$\frac{\Delta E}{E} = 4 \left(\frac{V}{c} \right)^2 \quad (1.8)$$

Therefore, the rate of gain of energy is:

$$\frac{dE}{dt} = 4K \left(\frac{V}{c} \right)^2 E = \alpha E \quad (1.9)$$

where K is the number of collisions per second. Assuming that the particle stays in the accelerating region for a characteristic time τ , we may then solve the diffusion equation for particle acceleration, namely:

$$\frac{dN}{dt} = D\nabla^2 N + \frac{\partial}{\partial E} [b(E)N(E)] - \frac{N}{\tau} + Q(E) \quad (1.10)$$

If we consider the steady-state solution, such that $dN/dt = 0$, and ignore diffusion and sources then $D\nabla^2 N = Q(E) = 0$. The energy loss term $b(E) = -dE/dt$ which in this case is $-\alpha E$. Therefore the diffusion equation reduces to:

$$-\frac{\partial}{\partial E} [\alpha E N(E)] - \frac{N(E)}{\tau} = 0 \quad (1.11)$$

Therefore:

$$\frac{dN(E)}{dE} = - \left(1 + \frac{1}{\alpha\tau} \right) \frac{N(E)}{E} \quad (1.12)$$

and thus

$$N(E) = \text{constant} \times E^{-(1+\alpha^{-1}\tau^{-1})} \quad (1.13)$$

This explanation is based on that found in [124]. Although this mechanism may produce a power law spectrum similar to that seen at Earth, the relatively slow velocities of the magnetic mirrors in actuality make the rate of collisions with cosmic rays too small to account for the spectrum of cosmic rays seen at Earth. However, this mechanism may still be important in areas such as young supernovae remnants and accretion disks, where there are vast amounts of turbulent plasma and highly energetic charged particles.

1.3.3 First Order Fermi Mechanism

We may recast and simplify the problem somewhat, if we let β be the average increase in energy of the cosmic-ray particle per collision, and P be the probability that the particle stays within the accelerating region after a collision. Then given initial energy E_o and number N_o , after k collisions one would find that there are $N = N_o P^k$ particles with energies $E = E_o \beta^k$. Eliminating k , we derive the following relation:

$$\frac{N}{N_o} = \left(\frac{E}{E_o} \right)^{\ln P / \ln \beta} \quad (1.14)$$

In fact this N is $N(\geq E)$, since this is the number that reach energy E , and some of these may go on to reach higher energies. Thus:

$$dN(E) = \text{constant} \times E^{-1+\ln P / \ln \beta} dE \quad (1.15)$$

Again we have derived a power law, whose slope is dependent on the values of P and β . To calculate P and β we now consider a version of the Fermi mechanism where, only head-on collisions occur, generally involving shock waves propagating through plasma with velocity greater than the Alfvén velocity in the plasma. Examples of the possible sites of this mechanism include supernovae expanding into space and the jets of active galactic nuclei. In this version of Fermi's theory the fractional energy increases are first order in V/c .

Figure 1.3 illustrates as annotated the following discussion. Here a supersonic shock of velocity U interacts with interstellar gas. The density, pressure and temperature behind

the shock are ρ_2 , P_2 and T_2 respectively, and the same parameters for the interstellar gas ahead of the shock are given by ρ_1 , P_1 and T_1 . This is illustrated in figure 1.3-a. It is convenient to transform into the frame of reference where the shock front is at rest, and the upstream gas flows into the shock front at velocity $v_1 = U$, and leaves the shock with downstream velocity v_2 , as indicated in figure 1.3-b. Given the continuity equation,

$$\rho_1 v_1 = \rho_2 v_2 \quad (1.16)$$

the simplifying feature of these strong shocks is that the density enhancement on crossing the shock is given by:

$$\frac{\rho_2}{\rho_1} = \frac{\gamma + 1}{\gamma - 1} \quad (1.17)$$

where the subscripts 1 and 2 refer to the gas in front of the shock and behind the shock respectively, and γ is the ratio of the specific heats. For a fully ionised or monoatomic gas $\gamma = \frac{5}{3}$ and hence $\frac{\rho_2}{\rho_1} = 4$, and hence $v_2 = v_1/4 = U/4$. Now consider what happens to the charged cosmic ray particles in the vicinity of the shock. In front of the shock scattering ensures the particle distribution is isotropic in the frame of reference in which the gas is at rest.

Let us first consider the fate of the upstream particles. The shock advances through the medium at velocity U , but the gas behind the shock travels at velocity $3/4 U$ relative to the upstream gas (see figure 1.3-c). When a high energy particle crosses the shock front, it obtains a small energy increase of the order $\Delta E/E \sim U/c$. The particles are then scattered by the turbulence behind the shock front so that their velocity distributions become isotropic with respect to that flow. Considering the opposite case, i.e. the fate of particles diffusing from behind the shock to the upstream region in front of the shock (see figure 1.3-d), the velocity distribution of the particles behind the shock is isotropic. When they cross the shock front they encounter gas moving towards the shock front, again with the same velocity $3/4 U$. In other words the particles undergo exactly the same process of receiving a small energy increase ΔE on crossing the shock from downstream to upstream as they did in travelling from upstream to downstream.

If we now perform a quantitative calculation based on these arguments we may arrive at values for β and P . Firstly we evaluate the average increase in energy of a particle on crossing from the upstream to the downstream side of the shock. The gas on the

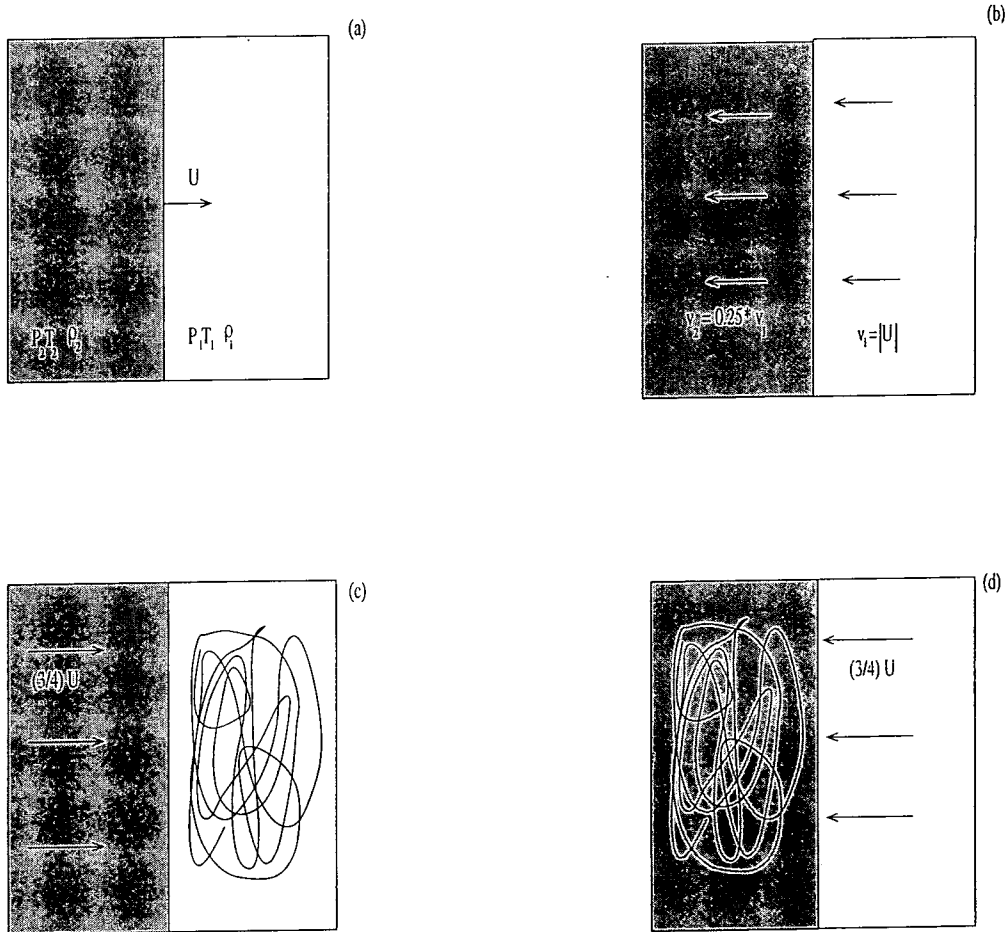


Figure 1.3: Illustration of the first order Fermi mechanism. (a) A strong shock wave propagating at a super sonic velocity U , through stationary interstellar gas with density ρ_1 , pressure P_1 and temperature T_1 . The density, temperature and pressure behind the shock are ρ_2 , P_2 and T_2 respectively. (b) The flow of the interstellar gas in the vicinity of the shock front in the reference frame in which the shock front is at rest. In this frame of reference the ratio of the upstream to the downstream velocity is $v_1/v_2 = (\gamma + 1)/(\gamma - 1)$. Where for a fully ionised plasma $\gamma = \frac{5}{3}$, and hence $v_1/v_2 = 4$. (c) The flow of gas as observed in the reference frame in which the upstream gas is stationary and the velocity distribution of the high energy particles is isotropic. (d) The flow of gas as observed in the reference frame in which the downstream gas is stationary and the velocity distribution of the high energy particles is isotropic. Taken from [124].

downstream side of the shock approaches the particle at a velocity of $V=3/4 U$, and by performing a Lorentz transformation, the particle's energy when it passes into the downstream region is given by:

$$E' = \gamma_V(E + p_x V) \quad (1.18)$$

where we take the x-coordinate to be perpendicular to the shock. We assume that the shock is non-relativistic, such that $V \ll c$ and $\gamma_V = 1$, where γ_V is given by:

$$\gamma_V = \left(1 - \frac{V^2}{c^2}\right)^{-1/2} \quad (1.19)$$

It is also assumed that the particles are relativistic, so that $E = pc$ and $p_x = (E/c) \cos(\theta)$. Therefore:

$$\Delta E = pV \cos(\theta) \quad (1.20)$$

$$\frac{\Delta E}{E} = \frac{V}{c} \cos(\theta) \quad (1.21)$$

The number of particles within the angle θ to $\theta + d\theta$ is proportional to $\sin \theta d\theta$, but the rate at which they approach the shock front is proportional to the x component of their velocities, $c \cos \theta$. Therefore the probability of the particles crossing the shock is proportional to $\sin \theta \cos \theta d\theta$. Normalising so that the integral of the probability distribution over all the particles approaching the shock is equal to unity, that is, those with θ in the range from 0 to $\pi/2$, we find the probability distribution $p(\theta)$ is given by:

$$p(\theta) = 2 \sin \theta \cos \theta d\theta \quad (1.22)$$

Therefore the average gain in energy on crossing the shock is:

$$\left\langle \frac{\Delta E}{E} \right\rangle = \frac{V}{c} \int_0^{\pi/2} 2 \cos^2 \theta \sin \theta d\theta = \frac{2}{3} \frac{V}{c} \quad (1.23)$$

The particle's velocity vector is randomised without any energy loss by scattering in the downstream region and it then recrosses the shock, as illustrated in figure 1.3-d. As it recrosses it gains another identical increase in energy, so that on one round trip across the shock and back again, the fractional increase in energy is, on average:

$$\left\langle \frac{\Delta E}{E} \right\rangle = \frac{4V}{3c} \quad (1.24)$$

Therefore

$$\beta = \frac{E}{E_0} = 1 + \frac{4V}{3c} \quad (1.25)$$

in one round trip.

According to classical kinetic theory, the number of particles crossing the shock per unit time is $\frac{1}{4}Nc$ where N is the number density of the particles. This is the average number of particles crossing the shock in either direction, since as noted above, the particles scarcely notice the shock. Downstream the particles are swept away from the shock, because the particles are isotropic in that frame. Referring to figure 1.3-b, it can be seen that the particles are removed from this region at a rate of $NV = \frac{1}{4}NU$. Thus the fraction of particles lost per unit time is $\frac{1}{4}NU / \frac{1}{4}Nc = U/c$. Since we have assumed that the shock is non-relativistic, it can be seen that only a very small fraction of the particles is lost per cycle. Thus $P = 1 - (U/c)$. Therefore:

$$\ln P = \ln \left(1 - \frac{U}{c} \right) = -\frac{U}{c} \quad (1.26)$$

$$\ln \beta = \ln \left(1 + \frac{4V}{3c} \right) = \frac{4V}{3c} = \frac{U}{c} \quad (1.27)$$

$$\frac{\ln P}{\ln \beta} = -1 \quad (1.28)$$

and therefore:

$$N(E)dE \propto E^{-2}dE \quad (1.29)$$

This argument has been based around that given in [124]. It should be noted however that this is the spectral slope for the simplest case of a plane shock front, and leads to an overestimation of gamma-ray production. More recent work, reviewed elsewhere [112], discusses more realistic models of shock propagation, which highlights the fact that the cosmic ray spectrum may be significantly softer than -2.

However, even the most modern models, are still based around first order Fermi, making it the most plausible candidate for acceleration of charged particles. To continue this discussion, the production of photons by energetic charged particles is now covered.

1.4 Very High Energy Photon Production

Many astronomical sources have been suggested as the producers of VHE gamma-rays (and by inference other cosmic rays). These include, within our own galaxy: supernova remnants, pulsars, X-ray binaries, the galactic plane and the galactic centre, and outside our galaxy: primordial black holes, active galactic nuclei and neutralino annihilation. So far the current generation of VHE Cherenkov telescopes have seen instances of emission from some of these sources, the details of which will be given in chapter 4. However, in most cases, the basic mechanisms behind VHE gamma-ray production are the same, generally involving the emission of gamma-rays via the acceleration of charged particles and subsequent particle interactions. As the rate of energy loss by these particles is inversely proportional to their mass (or a power of the mass), it is hypothesised that electrons and positrons (hitherto also referred to as “electrons” for simplicity) form the most relevant part of these charged particles. It should be noted though that some models exist which have populations of protons as the progenitors of the VHE gamma-ray signal ([5]), and the basic general mechanism (via neutral pion decay) is given below.

1.4.1 Gamma-Ray Production via Meson Decay

Neutral pions (π_0) can be produced either by nucleon-antinucleon annihilation or the inelastic collision of cosmic ray hadrons with interstellar matter. The neutral pion has a mass of $m = 135 \text{ MeV}/c^2$, and a very short lifetime of 8×10^{-17} seconds. The pion may decay into two gamma-rays, each having energy ($E_0 = m/2$) in the meson rest frame.

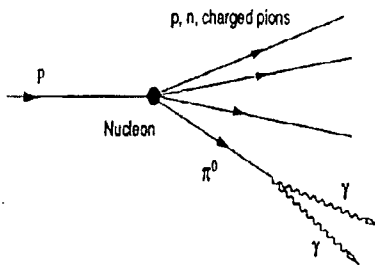


Figure 1.4: Gamma Production via π_0 decay

The basic particle interactions thought to be at work in the emission of VHE gamma radiation derived from the populations of highly energetic electrons produced by the acceleration mechanisms previously outlined are now detailed.

1.4.2 Gamma-Ray Production by Particle Acceleration Mechanisms

Synchrotron Emission

Synchrotron radiation is emitted by relativistic charged particles gyrating in external magnetic fields. Electrons trace out a helix along the magnetic field lines, resulting in oscillations of the electromagnetic field that are emitted as photons. The photons are polarised depending on the angle at which they are viewed, for looking down a field line, one sees the radiation as circularly polarised and beamed in the direction of the instantaneous circular particle motion.

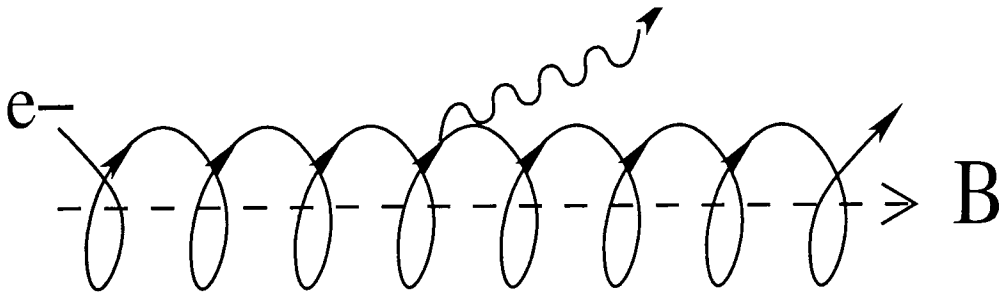


Figure 1.5: The production of synchrotron radiation

The Lorentz factor of a particle moving at speed βc , is:

$$\gamma = \frac{1}{\sqrt{1 - \beta^2}} \quad (1.30)$$

For synchrotron emission the photons are emitted within a cone with half angle, $\sim 1/\gamma$. If one assumes a power law distribution of electron energy (with index s), then this produces a power law synchrotron emission spectrum (see figure 1.6). The slope of the optically thin part of the synchrotron spectrum, with index α , is linked to s via a simple expression derived in [175], and given below:

$$\alpha = \frac{1 - s}{2} \quad (1.31)$$

A turnover in the spectrum occurs at low frequencies, where some of the synchrotron emission is self-absorbed. At high frequencies, the highest energy electrons emit photons. These electrons radiate large fractions of their energy, therefore causing the spectrum to depart from the power law regime as the electrons suffer severe energy losses.

The typical energy of radiation produced is given by:

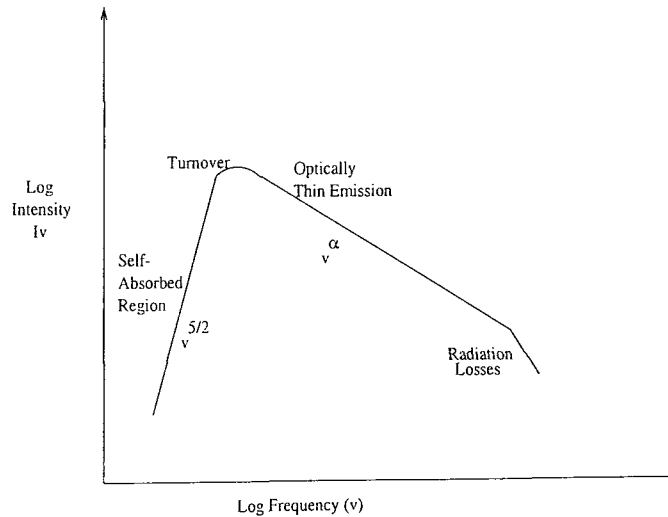


Figure 1.6: Schematic of synchrotron spectrum. Taken from [175].

$$E_\gamma = 20B(E_e)^2 \quad (1.32)$$

Where E_γ is the energy of the produced photon, and is measured in GeV, E_e is the energy of the electron and is measured in EeV, and B is the magnetic field measured in μG .

Thus, the energy of the photon is generally several decades lower than that of the electron, and is therefore often not of interest to atmospheric Cherenkov astronomers, though the presence of synchrotron radiation in a source indicates the presence of relativistic electrons, which are vital in most modern theories of VHE gamma-ray production [160].

Bremsstrahlung (Braking Radiation)

When an accelerated charged particle is within the external Coulomb field of an atomic nucleus or electron, it may experience a change in direction and suffer an energy loss, which is emitted as a photon. The energy of the photon is proportional to the deflection, and the maximum energy obtainable is approximately equal to the kinetic energy of the initial particle, hence the term 'braking radiation' describes this process exactly. The rate of energy loss by bremsstrahlung is inversely proportional to the square of the mass of the particle, and is therefore approximately 10^6 times greater for electrons than for protons.

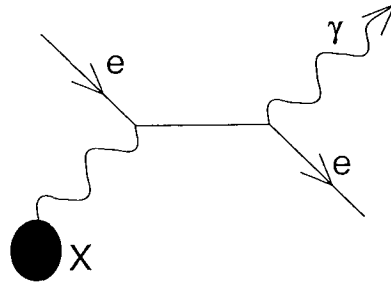


Figure 1.7: The production of bremsstrahlung radiation

Curvature Radiation

Curvature radiation was first proposed as a mechanism for gamma-ray emission from pulsars [189]. In the region of pulsars there are believed to exist very strong, curved magnetic fields ($B \sim 10^{12} \text{G}$). Even the highest energy charged particles will follow these field lines very closely, as a deviation would be damped out by synchrotron emission. The synchrotron emission depends then on the curvature of the field lines, the strength of the field and the kinetic energy of the charged particles involved. The energy of the emitted photons is expected to be γ^3 times the angular frequency of the electrons ($\beta c/r$). Magnetic fields greater than 10^{12}G are required to produce VHE gamma-rays by this method.

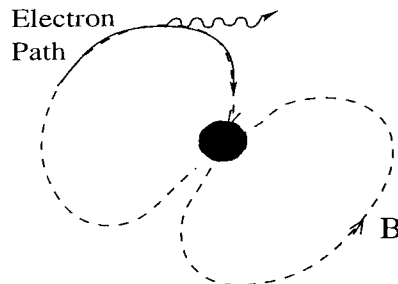


Figure 1.8: Gamma-ray production via synchrotron emission with intense curved magnetic fields.

Inverse Compton Effect

When a relativistic electron encounters a low energy photon in a radiation field, it will suffer a loss in energy to the low energy photon, thus boosting the photon to higher energy. Given that the electron has initial energy of γmc^2 then, in the frame of the electron, the low energy photon (of energy E), has a much higher energy of $E' = \gamma(E + cp_1)$, where p_1

is the longitudinal component of the photon's momentum the photon's momentum (i.e. that parallel to the electrons momentum in the lab frame). To simplify the problem, if we take a head-on collision, then $E' = 2\gamma E$, and if the photon is scattered directly backwards in the electron's rest frame, then the energy of the photon is boosted to $E'' = 2\gamma^2 E$. If $E' < 1\text{MeV}$, the cross-section for interaction is large enough to make the inverse Compton effect an efficient method for the acceleration of photons into the VHE regime.

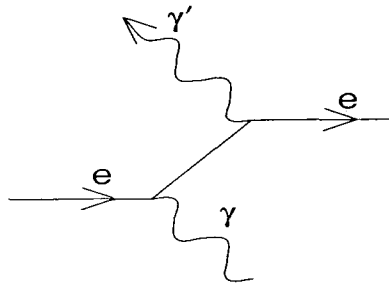


Figure 1.9: The inverse Compton effect

1.4.3 Summary

In summary of the points discussed above, a current popular theory for VHE gamma-ray production serves as an example of how these ideas inter-relate. The synchrotron-self-Compton theory suggests that highly energetic electrons produce X-ray photons by synchrotron emission, and then these photons are up scattered to VHE energies by inverse Compton interactions either with their progenitor electrons or other charged particles. This (and other mechanisms) are discussed elsewhere [160]. To continue following the produced radiation along its path, the mechanisms that may attenuate the VHE signal from an astrophysical source are now introduced.

1.5 Attenuation of the VHE Gamma-Ray Signal

During their propagation through galactic and extra-galactic space it is plausible that TeV gamma-rays may interact with other matter and energy, and in doing so may lose energy, to the point where they are no longer visible by VHE Cherenkov telescopes at Earth. However, for photons with energy $> 100\text{ keV}$, the collision cross-section for interactions with atomic Hydrogen is negligible. The pair production mean free path of a typical photon is 25 g cm^{-2} in the intergalactic medium, whereas a typical intergalactic column density is $10^{-5}\text{ g cm}^{-2}\text{ Mpc}^{-1}$. This leaves the two most important particle interactions that can

lead to attenuation, namely interactions with magnetic fields and other photons, both actually involving the same process of electron-positron pair production.

1.5.1 Single Photon Pair Production

In the presence of a strong magnetic field, a single VHE photon (of angular frequency ω) may interact with a virtual photon and produce an electron-positron pair.

$$\gamma + \gamma \rightarrow e^- + e^+ \quad (1.33)$$

This process was first described by Klepikov in 1954 [110], and is discussed in more detail by Erber [55] and Ogelman et al. [152]. The threshold for the process is given by $2m_e c^2 / \sin\theta$, for a photon whose momentum makes an angle of θ with the magnetic field. Even for energies well in excess of the threshold, very high magnetic fields ($B > 10^9$ G) were required for a non-negligible rate of pair production. In the limit of high photon energies the rate of pair production depends on the parameter $\chi = (\hbar\omega/2m_e c^2)(B \sin\theta/B_{cr})$. Where $B_{cr} = m_e^2 c^3 / e\hbar = 4.414 \times 10^{13}$ G, is the critical field strength, in which the gyroenergy $\hbar\omega_c$ of an electron (or positron) is equal to its rest mass. Since changes in the electron's energy perpendicular to the field are quantised in units of $\Delta E \approx \hbar\omega_c$, B_{cr} sets a scale on which to gauge the importance of quantum effects in magnetic fields. This is discussed in greater detail in [49]. Magnetic fields of this magnitude are thought to exist only around neutron stars, making this an unimportant attenuation process over galactic distances. It does, however, place constraints on the sites of production of gamma-rays of neutron stars.

1.5.2 Photon-Photon Pair Production

Cosmic gamma-rays may interact with the interstellar and intergalactic photon flux and be absorbed, again via a simple pair production process. Obviously the combined energy of the two photons involved must exceed the threshold energy ($2m_e c^2$) in the centre of mass of the system. This leads to the following expression where a signal photon of energy E_γ interacts with a background photon of energy E_{bg} , where the two momentum vectors of the photons are separated by an angle θ :

$$E_{bg} E_\gamma = \frac{2(m_e c^2)^2}{(1 - \cos\theta)} \quad (1.34)$$

In a head-on collision, where $\theta = \pi$, one requires $E_{bg}E_\gamma > 0.26 \text{ (MeV)}^2$ for pair production. If we now consider background photons of different energies it can be seen, from figure 1.10, that the mean free path of a VHE photon for interaction with starlight is very large, and therefore this may only become important over large intergalactic distances.

Interactions with the extragalactic infra-red light become important over intergalactic distance scales, and in particular when studying active galactic nuclei (AGN) at VHE energies. In a recent paper [98] a model is proposed for VHE absorption by infra-red light. The model gives predictions based on observed spectral data for the unabsorbed spectra of the sources, fitting to EGRET data simultaneously. This model has been utilised in studies of the AGN Markarian 501, and it shall be discussed further in chapter 4. Above 10 TeV, the gamma-rays will become susceptible to pair production with the cosmic microwave background photons [71], [102]. At higher energies ($> 50\text{TeV}$), this process will dominate. In summary, figure 1.10 shows the energy dependence of the gamma-ray interaction length over various photon backgrounds, and table 2 shows the location and energy requirements on the background and incident gamma-ray for attenuation due to pair production to occur.

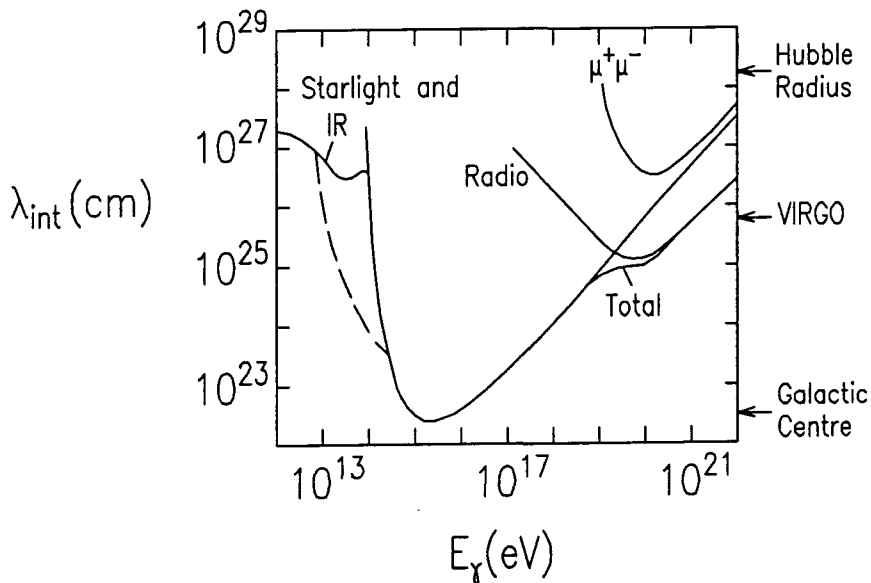


Figure 1.10: γ attenuation length as a function of energy [199]. The dotted curve indicates possible effects due to the infra-red background.

All in all this form of VHE attenuation is more important for gamma-rays near a neutron star and when studying AGN, interactions with the infra-red background and (at

Background	Example Location	E_b (eV)	E_γ (eV)
Cosmic Microwave Background	Extragalactic Space	6×10^{-4}	4×10^{14}
Starlight	Interstellar Space	2	10^{11}
Infra-Red Background Starlight	Extragalactic Space	0.24	10^{12}
X Ray	Neutron Star	10^3	3×10^8

Table 1.2: Examples of astrophysical locations of photon fields, of energy E_b , where pair production can occur and attenuate gamma-rays of energy E_γ . This is taken from [124].

higher energies) the cosmic microwave background will become important.

1.6 Summary

In this first chapter the discovery of charged cosmic radiation has been highlighted, and an argument that gamma-ray astrophysics may be a tool for identifying the sources of galactic charged cosmic radiation has been presented. A discussion of the gamma-ray energy spectrum over many decades of energy, and the observational techniques required in the different energy decades has been given. By starting with simple charged particle acceleration and gamma-ray production mechanisms, hints at how charged cosmic ray and gamma-ray production are linked have been made. Then by tracking the produced gamma-rays, possible attenuation mechanisms that they may undergo with different real (and virtual) photon backgrounds have been covered. Therefore, a study of the flux of astrophysical gamma radiation from creation to the point just before its first interaction with the atmosphere of Earth has been made, and is summarised in figure 1.11.

The next chapter deals with the interactions VHE gamma-rays and charged cosmic rays undergo with the Earth's atmosphere, including the production of extensive air showers and the associated Cherenkov radiation.

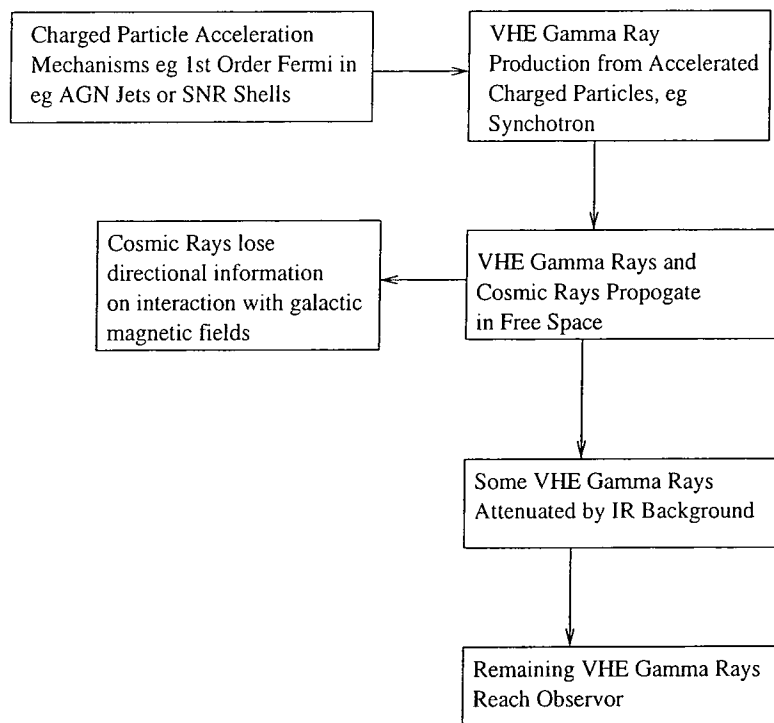


Figure 1.11: A summary of the order of the process undergone in the production of VHE gamma-rays and cosmic rays discussed in this chapter

Chapter 2

Extensive Air Showers and Cherenkov Light Production

2.1 Introduction

In this chapter a detailed discussion of what happens when a VHE gamma-ray or cosmic ray enters the Earth's atmosphere is presented. In doing this the formation of extensive air showers (EAS) and the associated secondary Cherenkov radiation produced is covered, and the differences in the Cherenkov light pool produced by gamma-ray and cosmic ray initiated EAS is hinted at as a source for their identification.

In the first chapter a discussion of the different techniques for observation at different energy intervals in the gamma-ray spectrum was presented. By first readdressing this, an indication of the highly useful nature of the formation of EAS and the secondary Cherenkov radiation will be presented. The Compton Gamma-Ray Observatory (CGRO) was launched in 1991, and in its nine year lifetime was one of the most powerful space based high-energy observatories. It consisted of four instruments: OSSE (Orientation Scintillation Spectroscopy Experiment (0.5-10 MeV)) [103], BATSE (Burst and Transient Source Experiment (30 keV-1.9 MeV and 15 keV to 110 MeV)) [59], COMPTEL (Compton Telescope (0.8-30 MeV)) [51] and EGRET (Energetic Gamma-Ray Experiment (30 MeV - 30 GeV)) [108]. The EGRET detector is of most relevance to this thesis. It was the largest spark chamber to ever operate on a satellite with an effective area of approximately 1000 cm², and in its lifetime it detected 271 distinct sources of gamma-rays between 30 MeV and 20 GeV (i.e. medium energy to high energy) [76]. The suggestion is that these sources should also be detectable in the VHE window. However, even the currently planned GLAST (Gamma-Ray Large Area Space Telescope) satellite, due for launch in 2005 [68]

has an effective area of only 0.8 m^2 , which as will be seen is very much smaller than the current generation of ground-based imaging Cherenkov telescopes. Above GLAST's energy range the size (and hence cost) of the experiment needed to collect the low fluxes of highly penetrating gamma-rays becomes prohibitive. However, above $\sim 10 \text{ GeV}$ gamma-rays interact with the Earth's atmosphere to produce EAS of electrons and positrons. These showers produce secondary Cherenkov radiation that can be detected at ground level by large detectors. Since this radiation may be detected at large lateral distances from the intersection point of the original particle's path and the ground, the detectors have a large effective area (of the order of up to 10^5 m^2). Unfortunately, there are problems to deal with using this technique. Most notably, high energy cosmic rays also initiate EAS which produce Cherenkov radiation, and these showers outnumber the gamma-ray initiated showers by of order 1000 times at VHE energies (for a source similar to the Crab Nebula at a zenith angle of 0°). However, as discussed later, differences in the spatial and temporal Cherenkov light distributions for gamma-ray and hadron initiated EAS allow the gamma-ray signal to be found even with this strong source of background noise. In the following sections, the formation of the two types of EAS is covered in detail.

2.2 Gamma-Ray Initiated EAS

A gamma-ray hitting the upper atmosphere has a finite chance of undergoing pair production whilst in the Coulomb field of an atmospheric atom X , i.e.:

$$\gamma + X \rightarrow X + e^- + e^+ \quad (2.1)$$

The probability of this interaction is much greater than that of a direct gamma-ray nucleus interaction. For electrons (and positrons) with kinetic energies above 84 MeV the dominant energy loss mechanism is bremsstrahlung (an electron is deflected by an atmospheric atom's nucleus and loses energy which is released, in this case, as a high energy gamma-ray), i.e.:

$$e^- + X \rightarrow X + e^- + \gamma \quad (2.2)$$

The gamma-ray thus produced is then available to create more electron-positron pairs, so a shower that is purely electromagnetic in origin (consisting of gamma-rays, electrons

and positrons) can grow rapidly in size as it develops. The maximum number of particles in the shower is reached when the average electron energy drops to 84 MeV, after which point ionisation takes over from bremsstrahlung as the dominant energy loss mechanism (as described by the Bethe- Bloch equation in [209] among others). The energy losses incurred via ionisation are much greater than those via bremsstrahlung, so the electrons in the cascade quickly lose energy and the number of gamma-rays produced via bremsstrahlung is rapidly reduced. The cross-section for pair production also falls off fast with energy, and eventually photoelectric absorption and Compton scattering are the dominant energy loss mechanisms for gamma-rays, and the shower stops growing.

To indicate the longitudinal development of the shower, a simple model proposed by Allan et al. is invoked [7]. This model assumes that the radiation length for bremsstrahlung (the mean length over which a particle loses $1/e$ of its energy, which is 37 g cm^{-2} for high energy electrons undergoing bremsstrahlung in air) is the same as the interaction length for pair production, X_0 . Allan then proposes that for this model we assume that after traversing $X \text{ g cm}^{-2}$ there is a 50% probability of pair production and a 50% probability of bremsstrahlung, such that:

$$\exp - (X/X_0) = \frac{1}{2} \quad (2.3)$$

If we assume energy conservation for the shower as a whole, then we can infer that after each cascade length, the average energy of the particles has halved. So if the initial gamma-ray energy was E_0 , after n interactions the average particle energy is:

$$\langle E \rangle = \frac{E_0}{2^n} \quad (2.4)$$

In this simple model, the number of particles doubles after each cascade length, however in reality (as mentioned before) at 84 MeV and below, ionisation and the reduction of the cross-section for pair production cause the shower to die out. We thus set a critical energy E_c of roughly 80 MeV. Using this model one can ascertain the depth of shower maximum (i.e. where the shower contains the most particles), by using:

$$X_{\max} \sim X_0 \ln \left(\frac{E_0}{E_c} \right) \quad (2.5)$$

For gamma-rays of a few hundred GeV, X_{\max} is 300 g cm^{-2} . Assuming an exponential decrease in atmospheric density with increasing altitude, with a scale height of 7 km and a

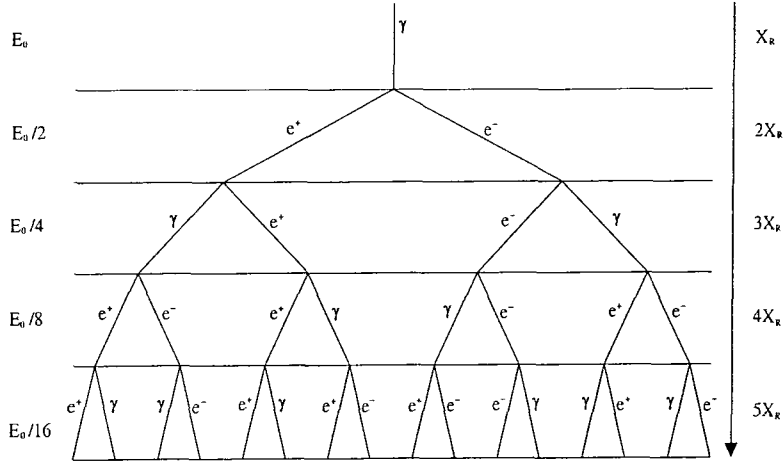


Figure 2.1: Production of gamma-ray initiated EAS, due to model by Allan [7]

maximum depth of 1000 g cm^{-2} , one can infer an altitude of 8.4 km for shower maximum. However, this does not take into account the ionisation occurring above 84MeV and thus in reality the shower maximum is a bit higher, typically for these energies around 9 km.

At first thought one would assume that the opening angles for bremsstrahlung and pair production affect the lateral development of the shower; however, the lateral development is dominated by the Coulomb scattering of the electrons. For many scatterings the mean angle of deflection of an electron travelling δx radiation lengths is:

$$\langle \delta\theta^2 \rangle = \left(\frac{21 \text{ MeV}}{E} \right)^2 \delta x \quad (2.6)$$

This leads to a Gaussian distribution of scattering angles with width $= \sqrt{\langle \delta\theta^2 \rangle}$. For instance, for an 80 MeV electron travelling through 1 radiation length (37 g cm^{-2}) of atmosphere the mean angle of deflection is $\sim \pm 12^\circ$. The lateral displacement of low energy (80 MeV) particles in a shower is given by the Molière length, r_l ;

$$r_l \approx \frac{21}{80} X_0 \approx 9.3 \text{ g cm}^{-2} \quad (2.7)$$

Which is approximately 80 m at sea level, although at higher energies (E) this is smaller by a factor of $80 \text{ MeV}/E$. Multiple Coulomb scattering and its treatment within EAS simulation codes will be readdressed in detail in chapter 5.

2.3 Hadron Initiated EAS

In contrast to gamma-ray initiated EAS, cosmic ray initiated showers are much more complex, and contain many more different particle interactions. If one looks at the composition of cosmic rays incident upon the Earth (see figure 2.2), one finds that 90% of the flux is composed of protons, with most of the rest being alpha particles (Helium nuclei), (it should be understood that this composition is only well measured for energies below 100 TeV.) Therefore proton initiated showers are introduced first, and then a brief discussion concerning the more complicated scenario of heavier cosmic ray initiated showers follows, towards the end of this section.

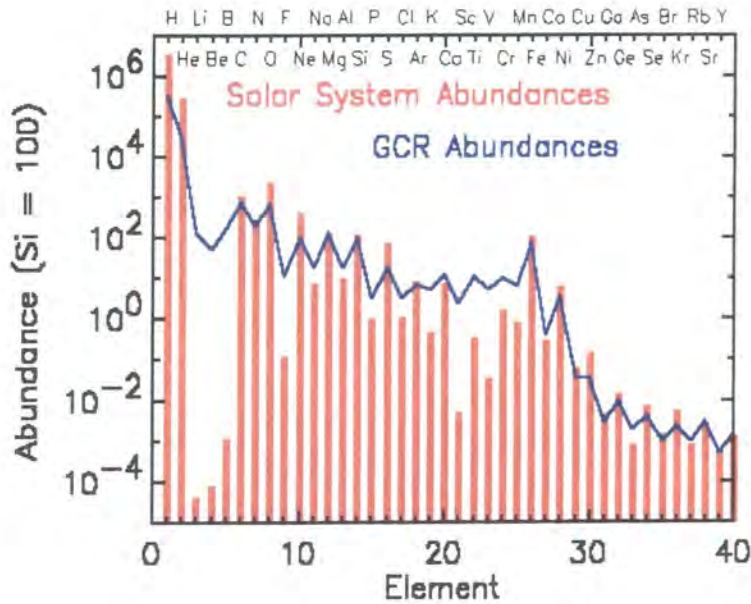


Figure 2.2: Illustration of cosmic ray composition taken from [145]. Plotted line shows results from galactic cosmic rays and bar chart shows results due to solar cosmic rays, abundances normalised such that Si=100.

The air shower process starts with pionisation, where the cosmic ray proton interacts with an atmospheric nucleus, producing kaons, pions and nuclear fragments, and loses approximately half its energy. Typically for a 100 GeV proton this occurs after it has passed through approximately 86 g cm^{-2} of the atmosphere. The kaons, pions and nuclear fragments may go on to interact with other atmospheric nuclei and produce further hadrons. This continues until the average energy per particle drops below approximately 1GeV, which is the energy needed for multiple pion production.

The neutral pions (π_0) produced have a short lifetime ($8 \times 10^{-17}\text{s}$) and decay into two

gamma-rays, which initiate EAS in the manner outlined in section 2.2. The charged pions have a much longer lifetime (1.2×10^{-8} s), and either interact first with atmospheric nuclei and produce fragmentation as in the case of the primary cosmic ray, or decay directly into very penetrating muons. These in turn have an even longer lifetime (2.2×10^{-6} s), this results in further lateral development of the shower. Muons are produced high up in the atmosphere by pions with transverse momenta (~ 0.5 GeV), thus resulting in a large lateral spread of muons. Muons with energies greater than 3GeV may penetrate to ground level, as they suffer little from ionisation losses, however at lower energies muons may decay into electrons (which may in turn produce Cherenkov radiation), by:

$$\mu^+ \rightarrow e^+ + \bar{\nu}_e + \nu_\mu \quad (2.8)$$

$$\mu^- \rightarrow e^- + \bar{\nu}_e + \nu_\mu \quad (2.9)$$

As we move from protons to more massive cosmic rays the interaction length for pionisation decreases with increasing mass number, via the relationship:

$$\lambda_N \propto \frac{1}{\sqrt{N^{1/3}}} \quad (2.10)$$

Where λ_N is the interaction length (in g cm^{-2}) and N is the number of Nucleons composing the cosmic ray. An overall schematic diagram of the development of cosmic ray initiated EAS is shown in figure 2.3.

As can be seen from the more complex particle interactions, and the different lifetimes of the products of these interactions, the lateral extent of cosmic ray initiated showers is much greater than that of electromagnetic EAS. In addition, cosmic ray showers can be thought of as consisting of (among other things) many simpler electromagnetic showers, thus any lateral distribution of particles at ground level will have several peaks corresponding to the products of the different sub-showers, differing from the simpler case of gamma-ray EAS. The presence of relativistic charged particles travelling through the atmosphere generates Cherenkov radiation, which is now discussed in more detail.

2.4 Cherenkov Radiation

Scientists first observed Cherenkov radiation as a bluish glow from transparent materials near radioactive sources in the late 1800's. In 1890, Heaviside gave a detailed (and very accurate) classical description of the effect. However, experiments into the nature

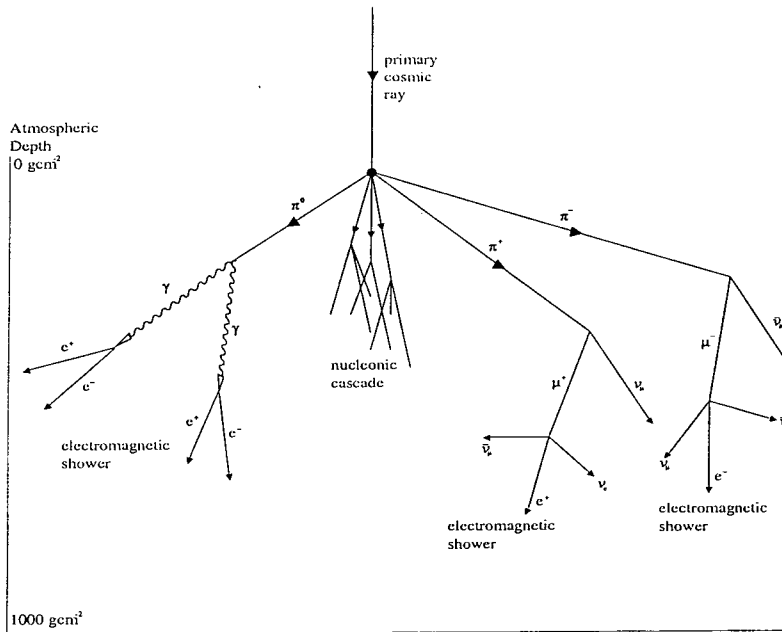


Figure 2.3: Illustration of possible development of nucleon initiated EAS, taken from [124]

of the radiation had to wait until the work of Mallet in 1926 and Cherenkov in 1937 [42], and a full quantum mechanical description was given by Frank and Tamm in 1937 [62]. The following qualitative description of the effect is taken from Jelley [100]. If a charged particle passes through a dielectric medium (with refractive index n), it induces a polarisation in the atoms surrounding it. If the charged particle's velocity is less than the phase velocity of light in that medium ($v < c/n$), then the polarised atoms are azimuthally and axial symmetric about the charged particle, and so no resultant field is seen at a distant point. If, however, the charged particle's velocity is greater than the phase velocity of light in the medium ($v > c/n$), then the axial symmetry of the atoms is lost, and a dipole is induced in the atoms behind the charged particle with no dipole in front of the charged particle. This leads to a net EM pulse for every elemental length of the charged particle's track, in an analogous way to supersonic aircraft producing sonic booms, when they exceed the speed of sound in air. This is illustrated in figure 2.4.

A Huygens reconstruction of the interaction of the individual elemental wavefronts, allows the calculation of the angle of emission (θ) with respect to the track of the charged particle as seen in figure 2.5.

If the relativistic charged particle travels from A to B (as seen in figure 2.5) with velocity $v = (\beta c)$ in time t and emits light along the way. Then in the same time t , light emitted at point A, may travel to point C at a velocity of c/n . Individual wavelets from

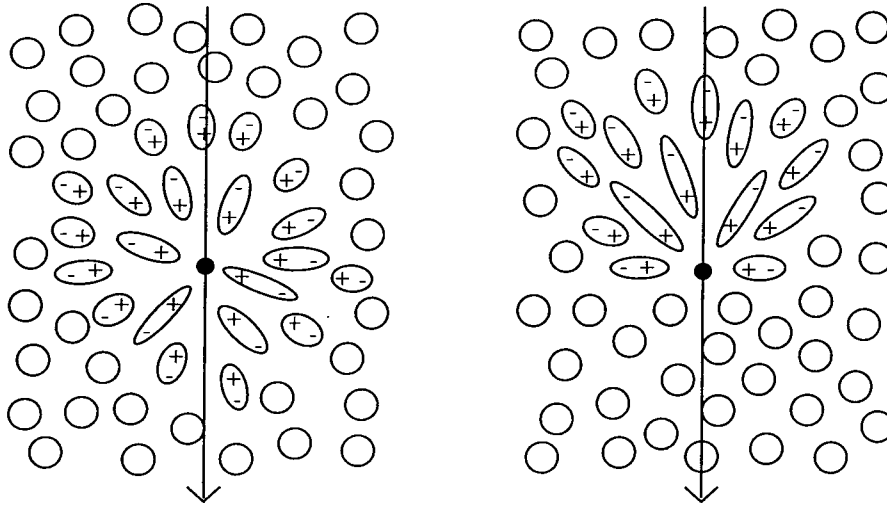


Figure 2.4: Illustration of effects of charged particles moving through media, in the first the particle moves slower than the phase velocity of light in the medium, however in the second it moves faster than the phase velocity

separate points combine to give a plane wavefront such that:

$$\cos\theta = \frac{AC}{AB} = \frac{1}{\beta n} \quad (2.11)$$

However, the polarised atoms still possess an azimuthal symmetry. This forces radiation from each elemental length of the particle track to be emitted over the surface of a cone, with semi-vertical angle θ and apex at A.

For Cherenkov emission, $v > c/n$, therefore we can set:

$$\beta_{\min} = \frac{1}{n} \quad (2.12)$$

Thus if $v = \beta_{\min}c$, $\theta = 0$, and:

$$\theta_{\max} = \arccos\left(\frac{1}{n}\right) \quad (2.13)$$

Most media are dispersive so $n = n(\lambda)$ and therefore $\beta_{\min} = \beta_{\min}(\lambda)$. If $n(\lambda) < 1$, then there is no solution and no photons are emitted. Also there are several absorption effects, some of which will be detailed later, which limit the wavelength of Cherenkov photons to the near UV and optical wavebands.

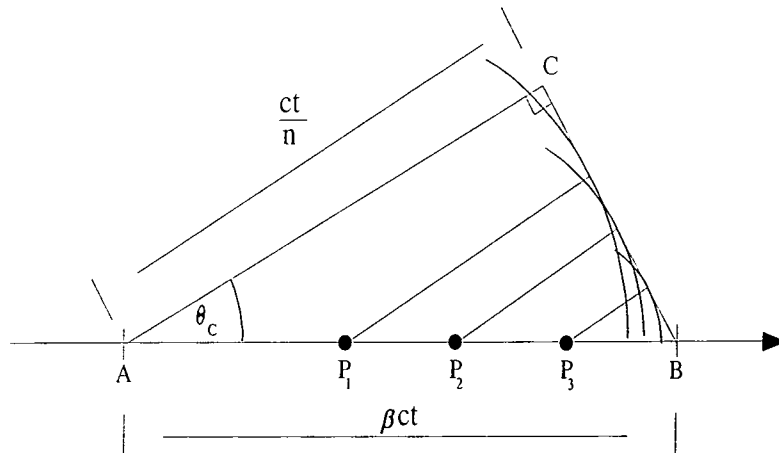


Figure 2.5: Illustration of how Cherenkov wavefronts interfere constructively via Huygens reconstruction.

2.5 Cherenkov Radiation in the Atmosphere

Blackett first suggested Cherenkov radiation from EAS in 1948, but it was not seen experimentally until 7 years later by Galbraith and Jelley [101]. The Cherenkov radiation seen at ground level is a product of the entire shower history, and provides information not only about the primary particle and its energy and direction, but also the effects of atmosphere on energy dissipation. The refractive index of air at standard temperature and pressure (STP) is $n = 1.000293$. This is only slightly different from the refractive index of vacuum, and therefore indicates that the charged particles producing the light must be extremely energetic in order to produce Cherenkov radiation, and the maximum Cherenkov angle (θ_{\max}) will be quite small.

However the refractive index of the atmosphere is not constant with altitude. If we make a small differences approximation and assume that the refractive index n is $n = 1 + \eta$, where $\eta \propto p$, where p is pressure, and to a good approximation given by $p \propto e^{-\frac{h}{h_0}}$, it is found that:

$$\eta(h) = \eta_{\text{stp}} e^{-\frac{h}{h_0}} \quad (2.14)$$

where h is the altitude and h_0 is the scale height. Since the Lorentz factor (γ) is related to β by:

$$\gamma = \frac{1}{\sqrt{1 - \beta^2}} \quad (2.15)$$

Particle	Threshold Energy
electrons	21MeV
muons	3.4GeV
Pions	5.6GeV
Protons	38GeV
He Nuclei	151.5GeV

Table 2.1: Table indicating the threshold energy for Cherenkov photon production at sea level for different particle species

Then using β_{\min} , γ_{\min} can be found:

$$\gamma_{\min} \sim \frac{1}{\sqrt{2\eta}} \quad (2.16)$$

as long as η remains small. The threshold kinetic energy below which no particle has the energy to produce Cherenkov radiation is therefore:

$$E_T = mc^2 \left(\frac{1}{\sqrt{2\eta}} - 1 \right) \quad (2.17)$$

As table 2.1 indicates, electrons and positrons are far and away the most numerous producers of Cherenkov light in EAS, as they are the most numerous particles in EAS and have the lowest threshold energy. It is also possible using the full quantum mechanical treatment of Frank and Tamm (1937) [62] to calculate the yield (N) per unit path length (dx (in cm)) of photons with wavelengths between λ_1 and λ_2 assuming that the refractive index is constant between these wavelengths:

$$\frac{dN}{dx} = 2\pi\alpha \left(\frac{1}{\lambda_1} - \frac{1}{\lambda_2} \right) \sin^2\theta_{\max} \quad (2.18)$$

Here α is the fine structure constant ($1/137$). If we assume small angles, such that $\sin\theta_{\max} \sim \theta_{\max}$ and for a wavelength range from 280 and 640 nm, then:

$$\frac{dN}{dx} = 921\theta_{\max}^2 \sim 780\eta \quad (2.19)$$

At STP this corresponds to approximately 0.2 photons per cm. These wavelengths are appropriate for discussions of the atmospheric Cherenkov technique, as the lower bound is

limited by the atmospheric attenuation of the Cherenkov signal, and the upper bound is set by the quantum efficiency of the photomultiplier tubes in the camera of a Cherenkov telescope.

Using simple gas laws we may also relate the quantities calculated here to the macroscopic variable, gas density (ρ).

$$E_T \propto \frac{1}{\sqrt{\rho}} \quad (2.20)$$

$$\frac{dN}{dx} \propto \sqrt{\rho} \quad (2.21)$$

$$\theta \propto \rho \quad (2.22)$$

The relationship between altitude, Cherenkov threshold energy and photon yield is illustrated in figure 2.6. (It should be noted that the energy losses to the charged particles due to Cherenkov radiation production are much smaller than those due to bremsstrahlung.)

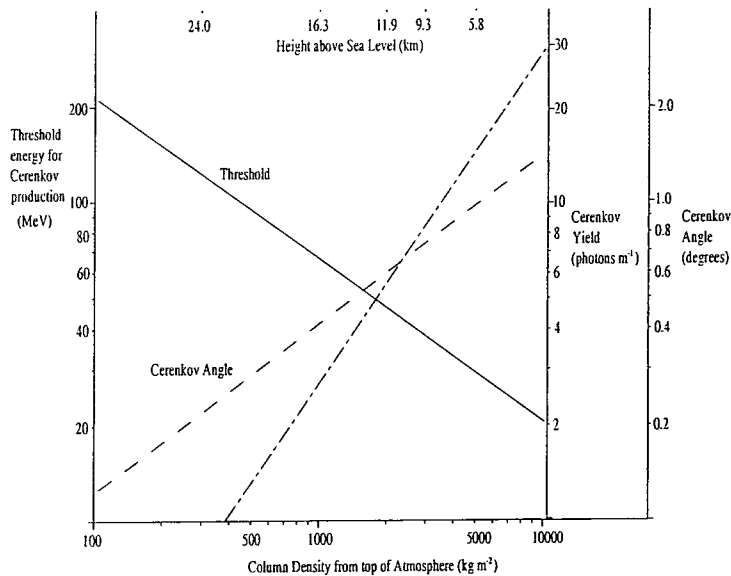


Figure 2.6: Illustration of changes in Cherenkov threshold energy and Cherenkov photon yield with changing altitude of production. Taken from [169].

As the Cherenkov photons pass through the atmosphere several attenuation mechanisms are important, these include; Rayleigh scattering, ozone absorption and aerosol (Mie) scattering (all discussed in detail in Chapter 7). Also the progenitor electrons and positrons can have their trajectories affected by the geomagnetic field, which can cause shifts in image of the Cherenkov light pool taken with Cherenkov telescopes, which again

is discussed in Chapter 7.

As a result of these processes only about half of the Cherenkov light produced in an EAS in the wavelength interval between 300 and 500nm actually reaches ground level. As a result of the low refractive index of air, the Cherenkov photons almost catch up with the particles that emit them. The photons arrive at ground level in a short pulse, within a time approximately given by:

$$\Delta t = \frac{d}{c} \left(\frac{n-1}{n} \right) \quad (2.23)$$

i.e. d is the path length over which photons are emitted. Since d is typically a few kilometres, Δt is typically of the order of nanoseconds. The lateral spread of the Cherenkov photon light pool can be estimated given the maximum Cherenkov angle θ_{\max} . For a 300 GeV gamma-ray, shower maximum is about 9 km a.s.l. and $\theta_{\max} \sim 1^\circ$. This would suggest a light pool of ~ 190 metres radius. As we shall now see, the temporal and lateral distributions of the photons within the Cherenkov light pools are the key to discrimination between gamma-ray and hadron initiated EAS.

2.6 Differences in Cherenkov Emission from Nucleon and Photon Initiated EAS

As mentioned before the Cherenkov light pool represents an image of the overall history of the shower development and as such contains information not only about the primary particle's direction and energy, but also about any atmospheric attenuation mechanisms. Before discussing each type of light pool in detail, the differences between the two types of EAS are recalled.

The Cherenkov Image of EAS

As can be seen from figure 2.7 gamma-ray initiated EAS are long narrow columns of electrons and positrons. The short interaction length of gamma-rays (37 g cm^{-2} at 300 GeV), means the showers develop high in the atmosphere. Except for showers generated by the most energetic gamma-rays (\sim few TeV), most gamma-ray showers die out a few kilometres above sea level when ionisation losses become great ($\sim 4\text{km}$ for 300 GeV gamma-ray showers).

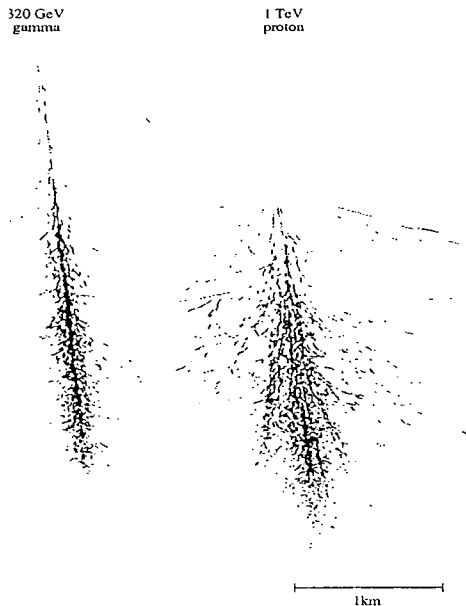


Figure 2.7: Illustration of tracks of electron and positrons in an EAS produced by a 320 GeV gamma-ray and 1 TeV proton simulated with MOCCA. It should be noted that vertical scale is much greater than horizontal scale. The total vertical scale covers approximately 20-30 kilometres for the cases presented here.

Cosmic ray particles, on the other hand, have a much longer interaction length and so penetrate deeper into the atmosphere than gamma-rays (83 g cm^{-2} for a 1 TeV proton). In terms of Cherenkov radiation, a cosmic ray generated shower can be thought of as a series of smaller electromagnetic showers originating at different altitudes and pointing in different directions. The large transverse momenta of the pions results in a large lateral spread of the showers. Many of the muons produced in the shower may also penetrate to ground level.

2.6.1 The Gamma-Ray Initiated EAS Cherenkov Light Pool

The Cherenkov angle (θ) reduces with increasing altitude of photon emission, thus leading to a focussing effect on the Cherenkov light pool (as seen in figure 2.8).

As can be seen in figure 2.8 the lateral density profile consists of a plateau near the shower axis, which rises to a bump about 120 metres from the shower axis, before falling away (as $1/r^2$); this is again illustrated (this time in 3-D) in figure 2.9.

The plateau is formed by particles in the tail of the shower nearest the observer, thus the plateau may show large shower-to-shower fluctuations. If the shower was produced by

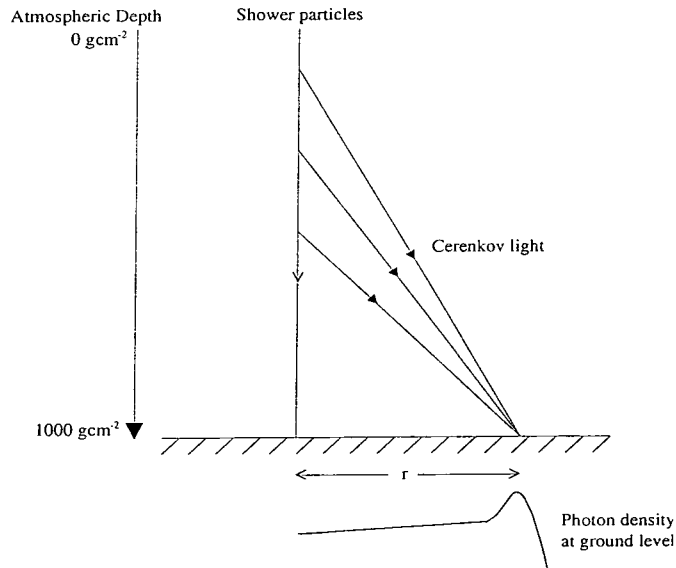


Figure 2.8: Illustration of focusing effect of varying θ with altitude on lateral Cherenkov light density distribution.

a gamma-ray of several TeV then the electrons may penetrate to ground level and cause localised Cherenkov light peaks within the plateau. Light in the bump comes from high energy (1GeV) electrons, which travel along parallel non-deviated tracks, the radius of the bump being related to θ and the altitude of emission. The $1/r^2$ nature of the light density beyond the bump is due to low energy electrons deflected by multiple Coulomb scatterings. The amount of deflection is given by [64] and the equation below:

$$\langle \delta\theta \rangle^2 = \left(\frac{E_s}{E} \right)^2 \delta t$$

Where E_s is 21 MeV, δt is the distance travelled (in radiation lengths) and E is the particle energy.

2.6.2 The Cosmic Ray Initiated EAS Cherenkov Light Pool

Compared to the Cherenkov light pool of gamma-ray initiated EAS, the cosmic ray light pool is more unevenly distributed, due to the more complex nature of the EAS, and leads to the image of the shower being wider than its gamma-ray counterpart. In addition other peaks due to pions with large transverse momenta and very localised intense peaks due to highly penetrating muons are present. This leads to a highly uneven lateral light distribution, compared to that due to gamma-ray initiated EAS, as shown if one compares figures 2.10 and 2.9.

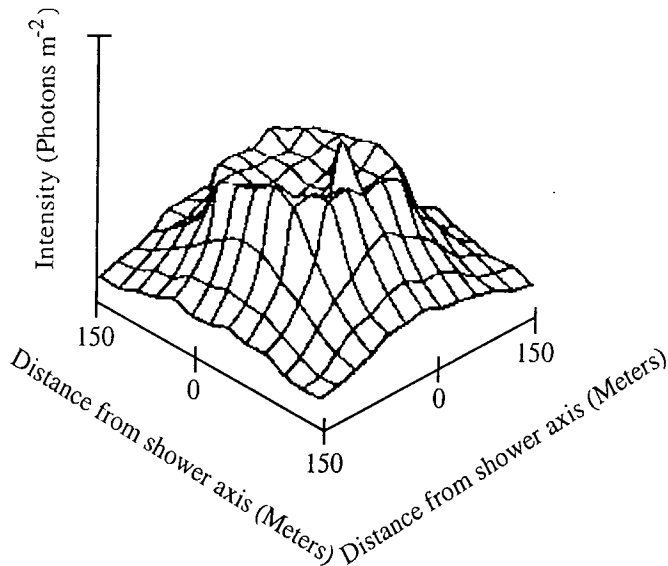


Figure 2.9: Illustration of 3 dimensional lateral photon density distribution from gamma-ray initiated EAS

2.6.3 Time Profiles of Gamma-Ray and Cosmic Ray EAS Cherenkov Light Pulses

It should be noted that some active research exists where the temporal differences in the Cherenkov light pools between gamma-ray and cosmic ray initiated EAS are used as part of the main discriminator [60]. Figure 2.11 a simulated time profile for the Cherenkov light pulse from a gamma-ray and proton initiated EAS is shown (in this case we consider the time profile 80 metres from the core location). The earliest arriving photons are those produced by the tail of the shower nearest the observer. Therefore for gamma-rays one can see that the shower maximum occurs later than for cosmic rays, corresponding to the more penetrating nature of cosmic rays. This early peak of the cosmic ray light pulse may also be due to deeply penetrating muons that produce Cherenkov light near to the telescope mirror. The cosmic ray light pulse has a longer tail, due to the larger transverse momenta of the particles in the EAS, which results in photons from larger lateral distances taking longer to arrive at the telescope mirror. For a single energy, the cosmic ray shower as expected has an overall smaller number of Cherenkov photons than the gamma-ray shower. It should be noted that the results shown here are merely photons incident on a 42m^2 mirror, and that no telescope simulation is included, and that this would only reduce the clarity of the differences. It is therefore clear that from these simple simulations presented herein it would appear as though the spatial differences between

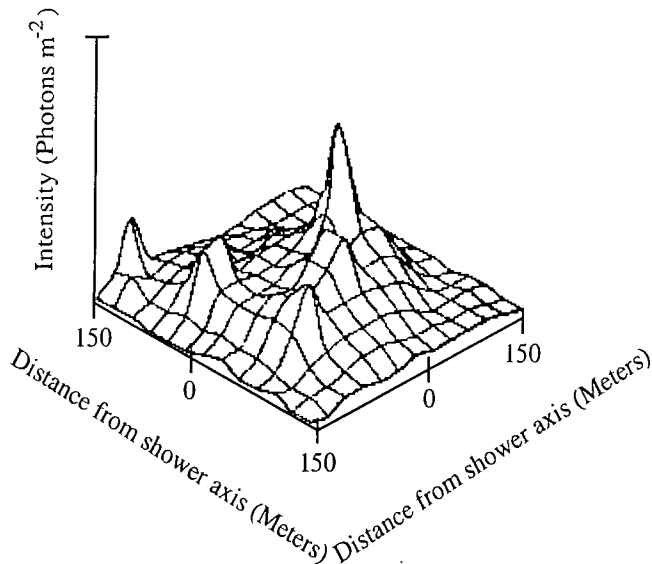


Figure 2.10: Illustration of the 3 dimensional lateral Cherenkov light distribution from a proton initiated EAS.

the two types of Cherenkov light pool would prove to be a more powerful discriminator than the temporal differences, which shall indeed be confirmed in the next chapter.

2.7 Summary

In this chapter a detailed discussion has been presented concerning the development of EAS produced when VHE gamma-rays and cosmic rays interact with particles in the upper atmosphere. The basics of Cherenkov light production and, details of how Cherenkov light may be produced by the secondaries from both hadronic and gamma-ray EAS have been addressed. The chapter then concluded by mentioning the spatial and temporal differences of the Cherenkov light pool at ground level, and indicating that these differences may be used to discriminate between the two kinds of shower.

The physics of the Cherenkov light formation suggests a few requirements for any system used to study VHE gamma-rays (and discriminate against cosmic rays). We require:

- Large flux collectors (as the photon yield after atmospheric absorption is low at the low end of the VHE spectrum) of reasonable optical quality on a steerable mount.
- This system should be preferably placed at high altitude (to minimise atmospheric absorption, and minimise the amount of lateral spread of the light pool).
- The detector should have a high gain, and (due to the short nature of the pulse) a rapid response time (\sim a few ns).

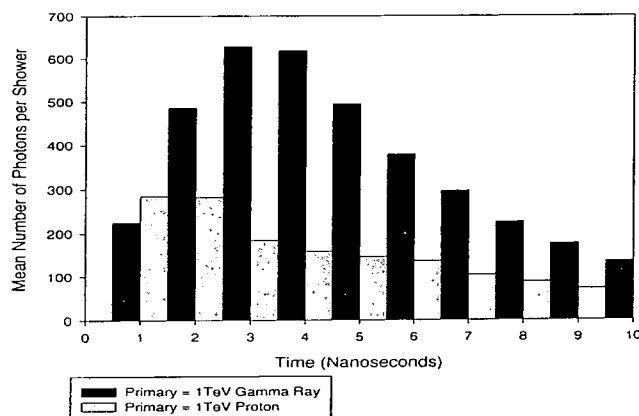


Figure 2.11: Illustration of the time profile of the Cherenkov light pulse produced by 1TeV gamma-ray and proton initiated EAS. Source is a MOCCA [87] simulation and calculates the time profile of photons arriving at a point 80m from the shower core, taken as an average over 100 showers (note large shower to shower fluctuations will make the standard deviation large).

-The detector must be optimised to work in the near UV and optical wavebands. – It also should be able to discriminate against not only the natural background starlight (of which the VHE gamma-ray signal is approximately 1/10000), but also the Cherenkov light pool of hadronic EAS.

In the next chapter, after a brief discussion of the history of the field, a review of the current generation of VHE telescopes and how they meet these physical requirements is given.

Chapter 3

Imaging Atmospheric Cherenkov Astronomy

3.1 Introduction

In this chapter an outline of the current status of ground-based Cherenkov astronomy is made by: discussing its history, outlining the milestone discoveries, and studying the inherent problems of trying to measure the gamma-ray Cherenkov signal given the large backgrounds due to the night sky (NSB) and the Cherenkov signal from hadron initiated showers. An investigation is then made of the imaging atmospheric Cherenkov technique, focussing on one of the last generation of Cherenkov telescopes, the Durham Mark 6 telescope. The current status of Cherenkov telescopes is addressed with particular reference to the importance of stereoscopy, and the H.E.S.S. Cherenkov telescope array is discussed as an example. This chapter will conclude by briefly drawing together future plans for ground-based imaging VHE gamma-ray astronomy around the world, before an investigation of the sources known to emit at TeV energies is made in the next chapter.

3.1.1 History

The first detection of light pulses from EAS was made in 1953 by Galbraith and Jelley [66]. This experiment for the first time overcame the difficulties in extracting the Cherenkov signal from the NSB. This is an extremely difficult task as the Cherenkov signal accounts for only $\sim 10^{-4}$ of the NSB. Although this is a small fraction of the total flux, large numbers of Cherenkov photons from a single shower arrive within a few nanoseconds at ground level. Due to the rapid response time needed for measurements of the light pulse, the standard technique is to use photomultiplier tubes (PMT) mounted at the focus of

a mirror. Thus the Cherenkov signal S_c detected by a PMT at the focus of a mirror is simply given by:

$$S_c \propto \eta A_m \quad (3.1)$$

where A_m is the area of a mirror ($\pi D^2/4$) of diameter D and η is the product of the quantum efficiency of the PMT and the reflectivity of the mirror ($0 < \eta \leq 1$). Of course this simple equation takes no account of the background light signal. If, for instance, the same detector is exposed to the NSB for a time t , there will be a mean signal S_{NS} , due to NSB starlight:

$$S_{NS} \propto \Omega A_m \eta \Phi t \quad (3.2)$$

where Φ is the photon flux from the NSB ($\sim 2 \times 10^{12}$ photons $s^{-1} sr^{-1} m^{-2}$ [153]), and Ω is the solid angle subtended by the detector on the sky. The fluctuations in S_{NS} can be taken to be Poissonian, therefore the noise (σ_{NS}) is the square root of the signal, i.e.:

$$\sigma_{NS} \propto \sqrt{\Omega A_m \eta \Phi t} \quad (3.3)$$

Fast electronics allow the detector to image the light from an individual shower above the signal from the NSB. The minimum signal threshold is the inverse of the signal to noise threshold, namely:

$$S_{min} \propto \sqrt{\left(\frac{\Omega t \Phi}{A_m \eta}\right)} \quad (3.4)$$

Galbraith and Jelley used a single PMT mounted at the focus of a 25cm diameter parabolic mirror. The detection of local EAS particles by an array of Geiger tubes was also used to rule out the photons originating from distant lightning or meteor shower trails. It was postulated at this time that a gamma-ray signal could be detected by looking for anisotropy in the Cherenkov signal from hadronic air showers.

Then in 1959, the suggestion that a VHE signal should be observable from the Crab Nebula was made by Cocconi [44]. This stimulated research in VHE astronomy. In particular, a group in the Lebedev Institute in Moscow built an array of 12 simple telescopes

each with a 1.5m^2 collection area. Although the group measured no signal from the Crab, their research prompted others to join the field. A new model for TeV emission from the Crab was proposed in 1965 by Gould [70]. During the 70's and 80's no observations of the Crab were successful; however, many techniques for hadron/gamma-ray signal separation were suggested. These included: the presence of penetrating particles [73], the ultraviolet excess [188] and the shape of the image [87].

The most powerful and successful of these techniques was the imaging atmospheric Cherenkov technique. This technique, that which is discussed in detail later in this chapter, improved the ability to select gamma-ray events from the hadronic background, by parameterising the images produced by the Cherenkov photons in an array of PMTs at the focus of a large mirror. This technique that was examined in a very rudimentary way by Hill and Porter in 1961 [83], was brought to fruition by the work of Hillas [87] in the mid 1980's.

This work, directly led the Whipple group (a US/Irish/UK Collaboration) to observe a steady flux of TeV photons from the Crab Nebula in 1989 [201]. This discovery brought the field of TeV astronomy to maturity.

3.2 Physical Specifications of an imaging atmospheric Cherenkov telescope (IACT)

As mentioned before, the Cherenkov light signal makes up only a small fraction of the NSB; therefore it is normal operating procedure not to run IACT systems during times when the moon is visible in the sky. In addition, the trigger system of the telescope must be designed to only operate for light signals on the time scale of a few nanoseconds, such that only Cherenkov events and calibration events are recorded. Before going on to discuss the design and use of actual telescope systems, some applicable parameters for IACT comparison are defined, namely the effective sensitive area (ESA), field of view (FOV) and threshold energy (E_T).

3.2.1 Effective Sensitive Area (ESA)

The ESA of an IACT is far greater than its physical size, and is a combination of detector efficiency and sensitive area. The sensitive area is related to the light density function of the Cherenkov light pool, as described in section 2.6.1. For a VHE gamma-ray produced air shower falling vertically, the Cherenkov photons typically fall within an area of $> 10^5$

m^2 . As the fluxes of primary photons at TeV energies are very low ($\leq 10^{-11}$ photons $\text{cm}^{-2} \text{sec}^{-1}$) the large ESA of a ground-based telescope is vital for statistically significant studies of TeV emission from astrophysical sources.

The detector efficiency, as detailed in Section 3.1.1 is a function of collection area, mirror quality, detector quality and environmental parameters, such as the NSB light level and the sky transparency.

However, the ESA is also dependent on the zenith angle of observation, as shown in figure 3.1. This is because the distance between the telescope and the shower maximum becomes larger with zenith angle, and so the light evolves and spreads over wider distances. In normal operation, most IACT's are used at small zenith angles, in order to keep the threshold energy as low as possible.

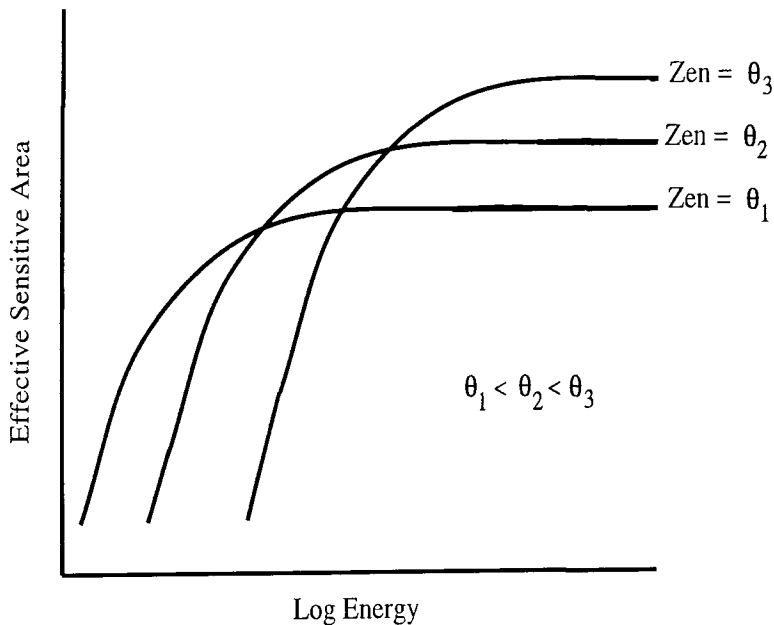


Figure 3.1: Graph illustrating zenith angle and energy dependence of ESA, for zenith angles θ_i .

3.2.2 Field of View (FOV)

The FOV of an imaging Cherenkov telescope must be large enough to record images of showers with impact parameters up to the radius of the Cherenkov light pool of a gamma-ray initiated EAS. However, as the expense of the system increases as the square of the FOV, IACT systems must also have a limited FOV, but if too small the FOV may exclude parts of gamma-ray Cherenkov images.

In the simplest case, for a vertical gamma-ray induced EAS, the optimum FOV (Γ) is given by geometrical constraints, namely:

$$\Gamma = \tan^{-1} \left(\frac{2r}{h} \right) \approx \frac{2r}{h} \quad (3.5)$$

provided $h \gg r$, where r is the typical radius of the Cherenkov light pool, and h is the approximate height of shower maximum ($\sim 11\text{km}$). This gives an optimum FOV of roughly 3° . Some modern IACT systems have larger FOV's [91], to allow the study of emission from extended sources such as supernovae remnants and also when surveying the galactic plane.

3.2.3 Threshold Energy (E_T)

The threshold energy of an IACT is dependent on the ESA of the telescope and the intrinsic differential energy spectrum of the source of VHE gamma-rays. The energy threshold is defined as energy where the peak of the function created by multiplying the ESA by the intrinsic differential energy spectrum occurs. (More useful, when flux calculations are involved is the threshold energy derived from the ESA of the system for useable gamma-ray events, or threshold energy for imaging, which will be discussed in detail in chapter 6.) For example, figure 3.2 shows the ESA for triggering of the Durham Mark 6 telescope (represented by the bar chart) and the convolution of this function with a differential energy spectrum of $E^{-2.6}$ (represented by the plotted curve). This particular example was used in the study of the active galactic nucleus PKS 2155-304 [13], which will be covered in chapter 6. As can be seen, the threshold energy for triggering of this telescope for this spectrum at 30° zenith angle was $E_T \sim 0.7$ TeV.

The most popular and successful technique for hadron/gamma-ray discrimination, namely Cherenkov shower imaging, is now detailed at length.

3.3 The Imaging Atmospheric Cherenkov Technique

It has already been mentioned that up to 1989, the field of ground-based gamma-ray astronomy was struggling to observe the detected DC signal from the Crab Nebulae. Other objects such as pulsars ([52]) were seen before this point however, due to their periodic VHE signal, which made them easier to pick out from the isotropic cosmic ray showers. However, as previously mentioned, the incorporation of the imaging technique and its use

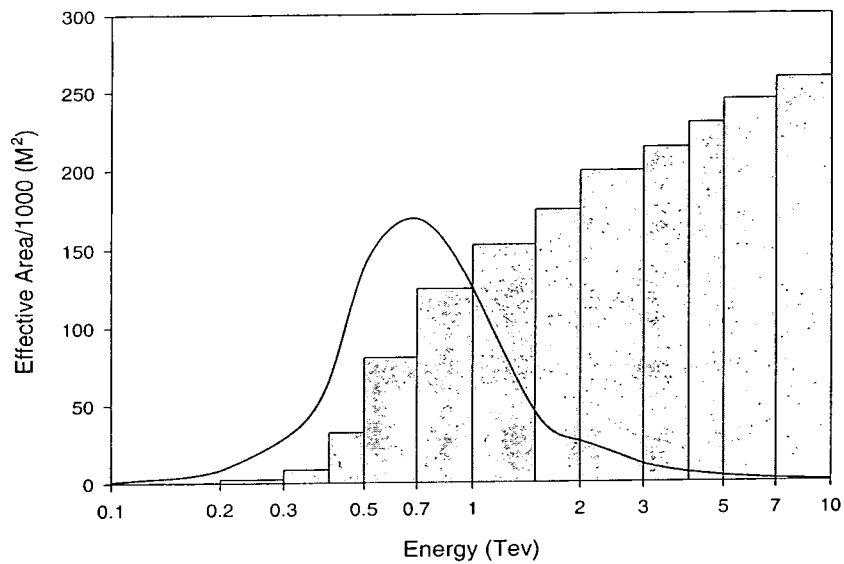


Figure 3.2: The histogram gives the variation of the effective area of the telescope with energy for gamma-ray showers. The curve, having a vertical scale in arbitrary units, shows the form of the triggering spectrum for a power law differential source energy spectrum of index -2.6 . Taken from [13]

by the Whipple Collaboration to first observe the Crab did represent a maturation of the field, therefore the technique will now be discussed in detail.

Given the small lateral extent of an EAS and the point source nature of the source, the Cherenkov image of a gamma-ray shower formed in a camera composed of many PMTs at the focus of a large mirror is best described by an ellipse. However, the position in the field of view and appearance depend on the core location and the energy of the shower. The width of the ellipse is related to the lateral development of the shower. The length is also a function of the shower development and can be attributed to the position of the core with respect to the telescope as indicated in figure 3.3.

The long axis of the ellipse points towards the source of the initiating particle, allowing the identification of the point source of VHE gamma-rays. The signal to noise ratio of ground-based gamma-ray telescopes is greatly improved if the gamma-ray and hadron initiated showers can be separated by using the recorded images. This requires the ability to identify Cherenkov photons over the NSB, and the parameterisation of the image in such a way that images may be easily analysed. The method of moments is covered in the next section, as a means to generating useful parameters to describe each ellipse (i.e.

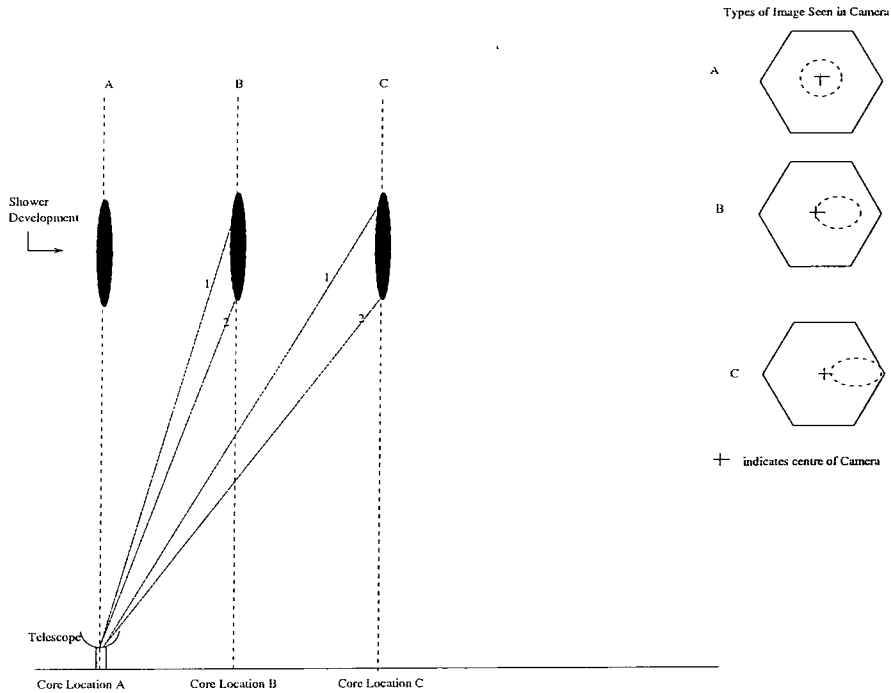


Figure 3.3: Schematic diagram illustrating the relationship between image length and core distance for a gamma-ray initiated EAS, landing at position A,B and C from the telescope. 1,2 indicate the paths of Cherenkov light emission from the top and bottom of the Cherenkov light producing part of the EAS. The diagram also indicates that in a real world application the three images would not all reach the centre of the camera, but would all possess similar widths.

width, length etc) that are called Hillas parameters.

3.3.1 The Moments Technique

The moments technique involves calculating the moments (induced about the origin) of a body, made up of i elements with densities ρ_i and coordinates (x_i, y_i) . Moments can give statistical estimators such as the mean, based on the axis of the coordinate systems. The r th moment of x for a body consisting of N elements is given by:

$$\frac{1}{N} \sum_i x_i^r \quad (3.6)$$

In ground-based gamma-ray astronomy, the following moments are utilised:

$$\Omega = \sum_i \rho_i \quad (3.7)$$

$$\langle x \rangle = \frac{\sum_i \rho_i x_i}{\Omega} \quad (3.8)$$

$$\langle y \rangle = \frac{\sum_i \rho_i y_i}{\Omega} \quad (3.9)$$

$$\langle x^2 \rangle = \frac{\sum_i \rho_i x_i^2}{\Omega} \quad (3.10)$$

$$\langle y^2 \rangle = \frac{\sum_i \rho_i y_i^2}{\Omega} \quad (3.11)$$

$$\langle xy \rangle = \frac{\sum_i \rho_i x_i y_i}{\Omega} \quad (3.12)$$

The variances in x, y and the cross term may be calculated:

$$\sigma_{x^2} = \langle x^2 \rangle - \langle x \rangle^2 \quad (3.13)$$

$$\sigma_{y^2} = \langle y^2 \rangle - \langle y \rangle^2 \quad (3.14)$$

$$\sigma_{xy} = \langle xy \rangle - \langle x \rangle \langle y \rangle \quad (3.15)$$

The point $(\langle x \rangle, \langle y \rangle)$ is known as the centroid of the ellipse, and in a massive system would represent the position of the centre of gravity. In Cherenkov astronomy the technique is applied to the elliptical images within the camera, where the array of PMTs gives the density measure, proportional to the number of Cherenkov photons per square degree in each PMT. Hillas parameters are functions of the moments (up to second order) and can be used to describe the property of the ellipse. However, there is no reason why higher order moments cannot be used as a means to discriminate between hadron and gamma-ray showers. However, as r increases the error increases rapidly, i.e.:

$$\Delta M_r = r! \Delta M_1 \quad (3.16)$$

where ΔM_1 is the error on the first moment of x , i.e.:

$$\Delta M_1 \approx \sqrt{\sum_i^N \delta x_i^2} \quad (3.17)$$

Some groups have been successful in using some 3rd order moments to distinguish between hadron and gamma-ray events, as discussed elsewhere [202], [158]. The Hillas parameters themselves are now given.

3.3.2 The Hillas Parameters

The technique of parameterising Cherenkov images in order to differentiate between cosmic ray and gamma-ray events is largely due to the simulation work of Hillas [87]. The

Hillas parameters for an ellipse fitted to a Cherenkov image are given by:

$$\text{Distance} = \sqrt{\langle x \rangle^2 + \langle y \rangle^2} \quad (3.18)$$

$$\text{Length} = \sqrt{\frac{\sigma_x^2 + \sigma_y^2 + z}{2}} \quad (3.19)$$

$$\text{Width} = \sqrt{\frac{\sigma_x^2 + \sigma_y^2 - z}{2}} \quad (3.20)$$

$$\text{Miss} = \sqrt{\frac{1}{2} (u \langle x \rangle^2 + v \langle y \rangle^2) - \left(\frac{2\sigma_{xy} \langle x \rangle \langle y \rangle}{z} \right)} \quad (3.21)$$

$$\text{Alpha} = \arcsin \left(\frac{\text{Miss}}{\text{Distance}} \right) \quad (3.22)$$

where the following coefficients are taken from [173], and are given by:

$$d = \sigma_y^2 - \sigma_x^2 \quad (3.23)$$

$$z = \sqrt{d^2 + 4\sigma_{xy}^2} \quad (3.24)$$

$$u = 1 + \frac{d}{z} \quad (3.25)$$

$$v = 2 - u \quad (3.26)$$

The Hillas parameters are shown graphically in figure 3.4. It should of course be noted that the Hillas parameters do not describe the image itself, but are rather a function of the moments collected from the available data.

3.3.3 Hillas Parameters in Action

Before showing how Hillas parameters may be used to discriminate between gamma-ray and hadron EAS, firstly an examination of the definition of the image and its capture in a generic camera is presented.

Triggering and Image Definition

In order to record the image data, a triggering criterion has to be set for the camera. As the Cherenkov light signal from an EAS is spatially and temporally coincident over several tubes, the coincidence of a signal over several tubes viewing the same part of the sky within a few nanoseconds is used as a trigger criteria. The exact triggering specifications (i.e. time window for coincidence, threshold level to be exceeded) vary from telescope to telescope, but all use this general triggering technique. To apply a moments

and must also be neighbouring at least one centre tube. Some example simulated images showing border and centre tubes are given in appendix C. Others groups apply further conditions requiring centre and border pixels to respectively contain a signal greater than specific fractions of the light in the brightest pixel. For example, the Durham group in analysing the Mark 6 data set the fractions at $> 37.5\%$ and $> 17.5\%$ respectively [9].

A simulation of a gamma-ray shower image in the recently constructed H.E.S.S. telescope camera [91] is shown in figure 3.5, the colouring of the tubes in the image simply represents the number of photoelectrons in each tube, and does not represent the actual border and centre conditions.

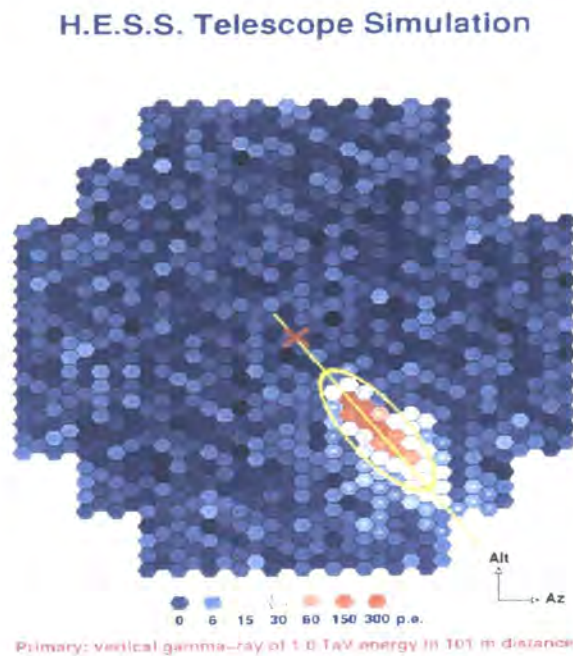


Figure 3.5: Illustration of imaging technique at work within H.E.S.S. camera simulation [91].

Gamma-Ray and Hadron Discrimination

The Crab Nebula has been observed to be a DC source of VHE gamma-rays by several independent IACT systems. This source is now used as the standard candle for VHE gamma-ray astronomy in the northern hemisphere. However, if no known strong source of VHE gamma-rays can be observed with a telescope, it is difficult to predict how the images will appear in the camera. Even the gamma-ray events may be hard to identify given the low signal to noise ratio and similar spectral energy distributions of the source

and background events. Therefore, Monte Carlo simulations of EAS, Cherenkov light absorption in the atmosphere and IACT systems, are used to predict the gamma-ray sensitivity of the telescope. These simulations suggest which Hillas parameters may be used to discriminate between gamma-ray and hadronic events. The shape of the image, as discussed before is dependent on where the shower core landed in relation to the telescope position and the lateral and longitudinal development of the shower. The different development of the hadronic showers makes their images wider than a similar gamma-ray image, and extra light elsewhere in the camera may also be present due to deeply penetrating muons. Also, with reference to the discussions of shower development in the last chapter, gamma-ray shower images tend to be more concentrated than cosmic ray shower images, with the light being concentrated in a smaller number of pixels. As the Mark 6 telescope had three separate cameras, another discriminating parameter could be defined. D_{dist} is the difference in the position of the centroid of the ellipse in the left and right cameras of the telescope. Given the clear definition of shower maximum for gamma ray initiated EAS, one would expect smaller values of D_{dist} for gamma ray showers as compared to cosmic ray showers. This is discussed in detail in [183].

For observations of point sources of gamma-rays, the angle between the image's major axis and the line joining the centroid of the image with the supposed source position (α), has been shown to be a powerful discriminating parameter. The images produced by a telescope pointing at a source of gamma-rays will tend to point towards the source position, and thus have smaller values of α than images from the isotropic cosmic ray background, which may take any value for α . This is brought about by the initialising photons from a point source falling parallel to the detector's optic axis. In Cherenkov astronomy when a potential source is being observed, equal amounts of time are usually spent observing the source and a part of the sky (at a similar zenith angle) with no known source in it. The mean background levels in these two field are adjusted to be the same ('padding'), then the ON and OFF source fields are compared, as if one takes the difference ON-OFF it is possible to subtract the majority of the cosmic ray background events. It is common in the field when detailing the validity of a source to present a histogram of the α -distribution of the ON-OFF dataset. If the source is producing VHE gamma-rays, one should see an excess at low α in the ON-OFF dataset. The significance of such a detection can then be calculated, given N_{ON} on source events, and N_{OFF} off source events:

$$\sigma_{\text{det}} = \frac{N_{\text{ON}} - N_{\text{OFF}}}{\sqrt{N_{\text{ON}} + N_{\text{OFF}}}} \quad (3.27)$$

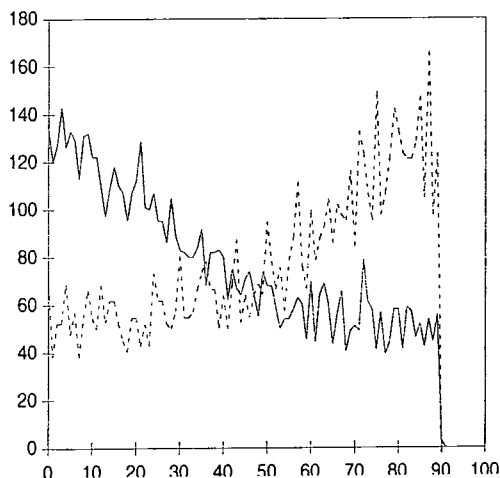


Figure 3.6: Histogram showing differences in α distributions of simulated gamma-ray (solid) and cosmic ray (dotted) spectra images viewed by Durham Mark 6 telescope for EAS produced with MOCCA [87] as illustrated in [13]. Y-axis represents number of events, X-axis represents alpha in degrees.

As can be seen from figure 3.6 the distributions of α from spectra of gamma-rays and cosmic rays are quite different, therefore making α a powerful Hillas parameter for discrimination. However, if one picks events at small α and also cuts for (or picks) events with smaller lengths and widths, the quality factor (or fraction of retained gamma-rays over the square root of the fraction of retained hadrons) is increased even further. Other Hillas parameters (and other parameters based around moments) may be used to discriminate between hadron and gamma-ray events; for instance, the distribution of image SIZE which is the total amount of light in the image tubes (in digital counts), is found to peak at lower values for gamma-rays events and therefore a cut on this parameter can be used to increase the quality factor. Image tubes are defined by the centre and border criteria of section 3.3.3. As mentioned before, the concentration of the light in the images of gamma-ray EAS is greater than an image from a cosmic ray EAS. This can be quantified using the parameter I_{ratio} , defined as:

$$I_{\text{ratio}} = 1 - \frac{\text{SIZE}}{\text{Total Light In Camera}} \quad (3.28)$$

The ‘total light in the camera’ is the sum of digital counts over all the camera tubes. Both this quantity and the SIZE are evaluated after flat-fielding and pedestal subtraction. Smaller values of I_{ratio} correspond to the light in the image being only a sizeable fraction of the total light in the camera, and thus the camera light is mostly concentrated in the image. Modern stereoscopic imaging Cherenkov systems, can provide a hadron suppression factor of $\sim 100\%$ (though this is energy dependent), whilst retaining 60% of gamma-ray showers, giving a quality factor $Q > 6$ [126].

An example of a set of cuts which the Durham group have used can be seen in [38]; these cuts are used in the study of the AGN PKS 2155-304 discussed in chapter 6.

Actual imaging atmospheric Cherenkov telescope systems currently in operation or under construction are now covered in more detail.

3.4 Imaging Atmospheric Cherenkov telescopes

Table 3.1 lists most of the currently operational, or in construction, VHE Cherenkov telescopes. It should be noted that 3 of the systems, STACEE, CELESTE and Solar-2 differ from the generic Cherenkov telescopes described earlier. These systems utilise solar energy research power plants, with their many heliostat mirrors. During the day, light reflected from the mirrors is focussed to a point on a central tower where power is generated; at night a camera of PMTs is placed at the top of the tower and the Cherenkov light reflected there is recorded. This technique tries to discriminate between gamma-rays and hadrons by studying the lateral distribution of Cherenkov light deposited on the solar array mirrors. Table 3.2 shows (among other things) the confirmed or predicted threshold energies for some imaging telescope systems. An examination of two systems, the Durham Mark 6 telescope and stand-alone H.E.S.S. telescopes, is now made.

3.4.1 The Durham Mark 6 Telescope

The Durham Mark 6 telescope operated in Narrabri NSW (altitude 260m), Australia from 1995 to 1999. In this time, it reported observing VHE gamma-ray emission from 4 sources: the AGN PKS 2155-304, pulsar PSR1706-44, X-ray binary Cen X-3 and AGN Markarian 501. The telescope had a unique design, consisting of 3 seven metre diameter parabolic dishes on a single alt-azimuth mount, with a camera of PMT's at the focus of each mirror (see figure 3.7). By demanding a signal in the three cameras in PMT's that were viewing the same part of sky within a time interval of around 10 nanoseconds,

Telescope	Location	Altitude (metres)	Stereo/Stand- Alone
H.E.S.S., [91]	Gamsberg, Namibia	1800	Stereo*
HEGRA, [48]	La Palma, Canary Islands	2200	Stereo
MAGIC, [125]	La Palma, Canary Islands	2200	Stand-Alone*
VERITAS, [203]	Mt. Hopkins, Arizona, U.S.A.	1600	Stereo*
CANGAROOIII, [54]	Woomera, S.A., Australia	160	Stereo*
CAT, [16]	Themis, French Pyrenees	1650	Stand Alone
Whipple, [34]	Mt. Hopkins, Arizona, U.S.A.	2300	Stand Alone
TACTIC, [21]	Mt. Abu, India	1300	Stereo
SHALON, [150]	Tien Shan, Kyrgystan	3338	Stand Alone
GT-48, [107]	Crimea, Ukraine	600	Array
Celeste, [122]	Themis, French Pyrenees	1650	Heliostat Array
Stacee, [60]	Albuquerque, N.M., U.S.A.	1700	Heliostat Array
Solar-2	California, U.S.A.	—	Heliostat Array

Table 3.1: Table showing other currently operational VHE Cherenkov telescopes (with citations where possible). * indicates that these systems are in construction and currently at most only a single telescope is in operation.

the effect of the NSB could be decreased dramatically and triggers from local muons eliminated. The central camera contained 91 1 inch PMT's surrounded by an outer ring of 18 2 inch PMT's. Reflective light cones (Winston cones) were mounted in front of each PMT to limit the light loss from photons falling between the PMT's and so reduce the energy threshold of the telescope.

The centre camera was the main imaging camera of the telescope with the outer two cameras (each with 19 2 inch hexagonal PMT's) taking data to be used for triggering purposes. The reflective surface of the mirrors was made from anodised aluminium which is believed to have a reflectivity of 80% in the range 300 to 500 nm. The mirrors had a focal length of 7.0m and an aperture of $f/1.0$. The point spread function of the mirrors was measured by studying the reflected images of stars in the camera. The physical parameters of the Mark 6 (and their simulation) shall be returned to in detail in chapter 6.

Its low altitude was disadvantageous for the Durham telescope, as indicated in figure

Telescope	No. PMT's/camera	Mirror Size/telescope (metres ²)	Threshold Energy at the zenith (GeV)
H.E.S.S.	960	108	120 [#]
HEGRA	271	8.5	500
CANGAROO III	552	57	200
CAT	548	17.5	300
Whipple	490	74	250
SHALON	244	12.5	1000
GT-48	37	3.8	1000
TACTIC	349*	9.5	600

Table 3.2: Table showing physical parameters of some of the currently operational Cherenkov telescopes applicable to studies of TeV produced EAS. * indicates that the TACTIC array has 349 tubes in the central telescope, the outer telescopes, spaced approximately 20m from the inner, have lower resolution cameras with only 58 PMTs each. # indicates that the threshold energy given for the first stand-alone H.E.S.S. telescope is yet to be verified from real data.

3.8. Here the simulated lateral Cherenkov photon light density at the Narrabri site is compared with the H.E.S.S. Namibian site. The atmospheric profile believed to be correct for each site is used, and the correct geomagnetic field for each site is applied. One finds that, due to altitude, for the same energy primary there are roughly half as many photons at the Narrabri site. This will be important for the next generation CANGARAOO III telescope that is being constructed at a site with a similar altitude and geomagnetic field to the Durham Mark 6 telescope site.



Figure 3.7: The Mark 6 telescope.

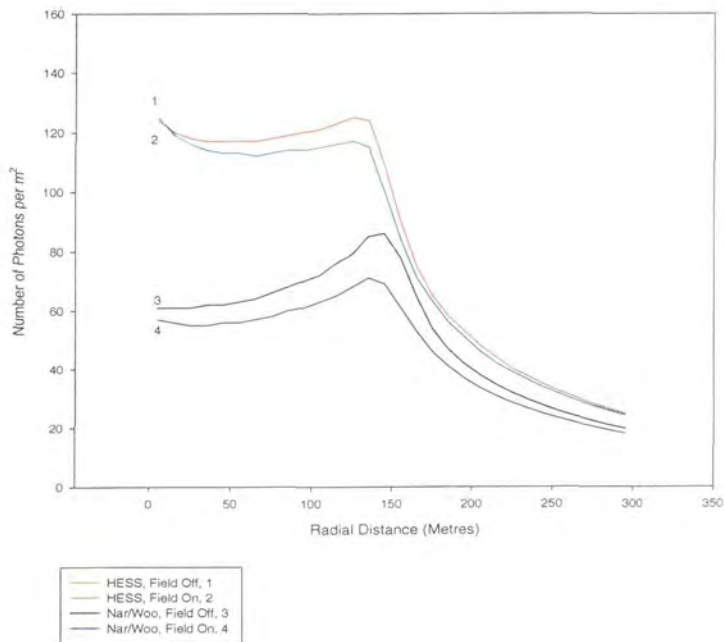


Figure 3.8: Lateral Cherenkov photon density from 1TeV gamma-ray primaries simulated with MOCCA for assumed Narrabri and Namibian Atmospheres, with and without geomagnetic fields.

3.4.2 H.E.S.S.

The H.E.S.S. telescope is an array system of initially 4 (and eventually 12-16) telescopes, currently under construction in Namibia at an altitude of 1800m. The H.E.S.S. site was short listed for the European Southern Observatory, but lost out for political reasons to Chile. The site is considered to have some of the best astronomical viewing conditions in the world. The H.E.S.S. system is a generation more advanced than the Durham Mark 6 telescope, as is indicated by table 3.3. Currently only the first telescope is operational, but by the end of 2003, three more telescopes should be completed. Each telescope is composed of 380 60 cm diameter mirrors in a Davies Cotton design, with a camera of 960 29 mm PMT's at its primary focus. The focal length is 15 m.

	H.E.S.S.	Mark6
PMT's	960 (FOV 5° diameter)	91 Central (FOV 2.5° diameter)
Mirror Area	106m ²	42m ²
Mirror Type	Segmented Davies-Cotton	Single Parabola
Point Spread Function (r.m.s.)	0.03-0.06°	0.18-0.24°
Trigger	2/4 Telescopes	4 Fold (3 detectors)

Table 3.3: Table showing physical specifications of the Durham Mark 6 and first four telescope H.E.S.S. array.

Currently only one stand-alone H.E.S.S. telescope is in operation. Simulations have been performed for this telescope and these form the subject of chapters 6 and 7. For now, however the effective sensitive area of the telescope to gamma- ray spectrum with a -2.45 differential spectrum of showers coming from 30° zenith angle with energies from 0.05 to 30 TeV is shown in figure 3.9. It can be seen that the threshold energy for triggering at 30° zenith angle is about 130 GeV. Before concluding the chapter, the importance of stereoscopy is discussed.

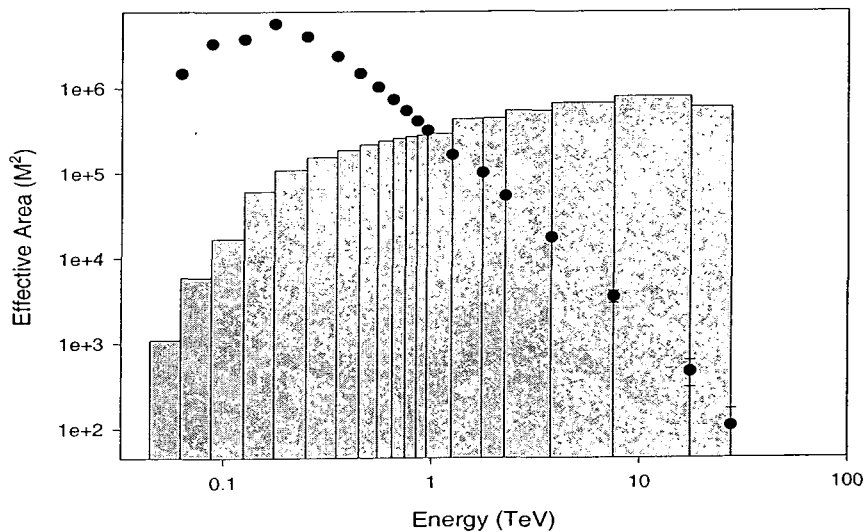


Figure 3.9: Diagram illustrating the effective sensitivity of a stand-alone H.E.S.S. telescope to a Crab gamma-ray spectrum at 30° zenith angle, with differential slope -2.45 , consisting of 100,000 showers spread over a circular area of radius 500m and ranging in energies from 0.05 to 30 TeV. Showers were simulated with MOCCA, and telescope response with CameraHESS simulation code. The circular points indicate the convolution of the effective area with an $E^{-2.6}$ spectrum, and show, on a proportionate logarithmic scale, the number of showers per TeV which trigger the system. They indicate the peak response of the system for triggering, which is commonly quoted as the energy threshold for triggering.

3.4.3 Stereoscopy

The principle of using more than one telescope to view the shower, or stereoscopy has many advantages as the HEGRA collaboration has shown [115]. Firstly, viewing the shower by more than one telescope with a coincidence trigger system increases the gamma/hadron rejection ability. Data that pass the trigger in the system can be used to make a stereo image of a Cherenkov event. This allows a three dimensional reconstruction of the EAS to be made which provides an accurate calculation of the shower angle, the core location and the altitude of shower maximum [115]. Figure 3.10 illustrates the reconstruction of the core location for a gamma- ray initiated EAS with respect to the four telescope H.E.S.S. system.

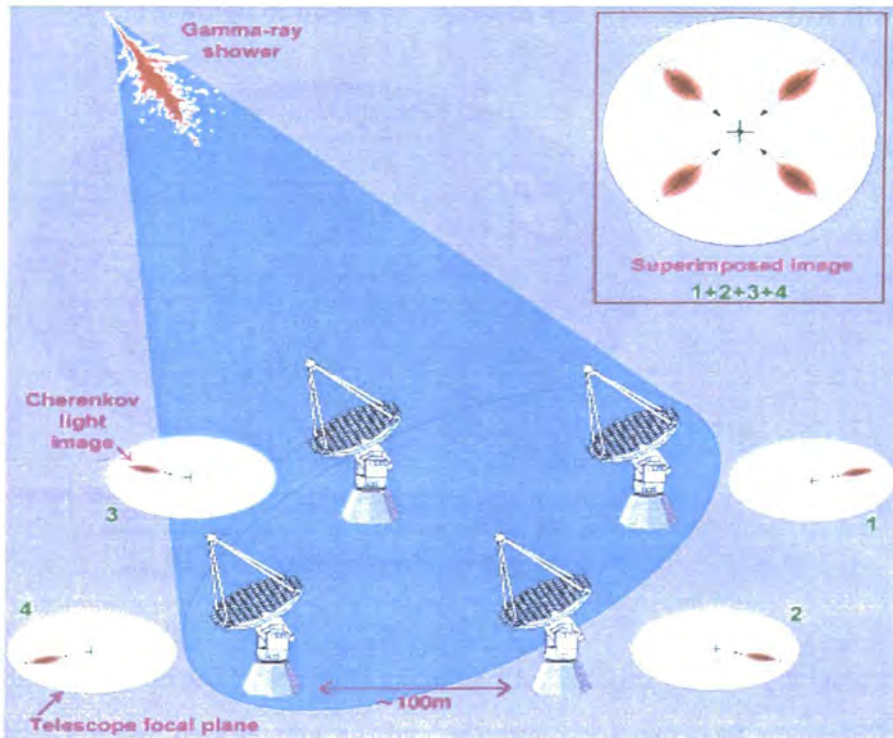


Figure 3.10: Diagram illustrating how viewing a shower with multiple telescopes allows the x,y location of the core to be calculated. This information, along with the SIZE of the image, allows the energy of the primary to be estimated. The particular layout here is for the first 4 H.E.S.S. telescopes.

The altitude of emission is a further discriminator as hadronic primaries tend to penetrate further than gamma-ray primaries. The core location, combined with image brightness allows the energy of the primary to be calculated, with a resulting improvement in energy resolution. This chapter is now concluded with a brief discussion of the current status and future prospects for astrophysics experiments in the GeV/TeV energy window.

3.5 Future Prospects for Ground Based Gamma-Ray Astronomy

The next 3-4 years should see the completion of a 12-16 element H.E.S.S. telescope array in the southern hemisphere, and a 7-element array of Cherenkov telescopes at the Whipple Base Camp ($\sim 1600\text{m}$), called VERITAS, in the northern hemisphere. These two systems will give an almost 95% sky coverage, as shown in figure 3.11.

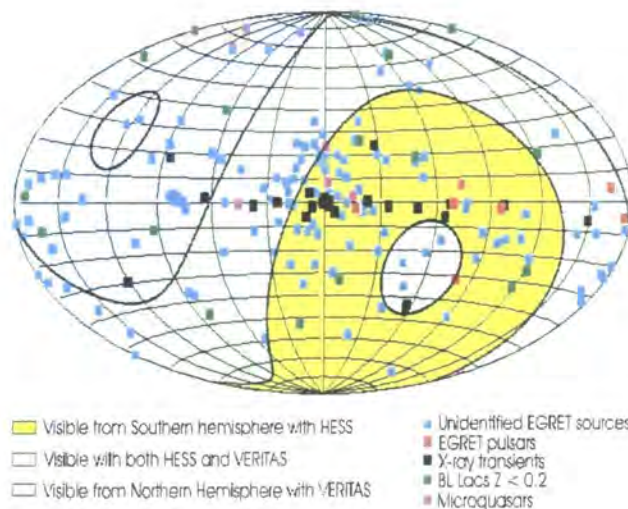


Figure 3.11: Diagram illustrating the sky coverage of the new generation of ground-based Cherenkov telescope array systems, and the sources seen by the EGRET instrument.

Capable of seeing sources emitting fluxes at the milli-Crab level (some 10^{-14} photons $\text{sec}^{-1} \text{cm}^{-2}$), these systems also possess threshold energies low enough to bridge the gap between satellite based experiments at high energies and ground-based particle experiments at ultra high energies, as indicated in figure 3.12. The systems are also capable of angular resolution at the arc-minute level, and therefore should be able to identify the unknown EGRET sources.

Other systems underway include MAGIC [125], a single telescope system with a 230m^2

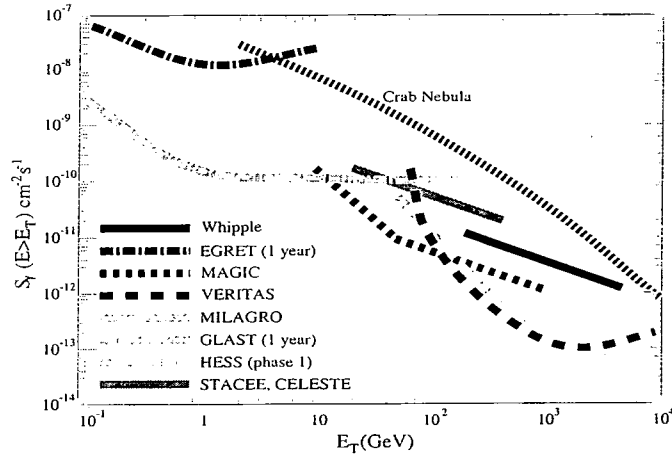


Figure 3.12: Sensitivity curves of the main proposed and existing gamma-ray Cherenkov observatories. Figure shows integral flux versus energy based around 1 year's observation for EGRET and GLAST, and 50 hours for the Cherenkov detectors. In all cases a 5σ detection is required, along with the additional requirement that the signal contain at least 10 photons. Those detectors listed are: Whipple [34], EGRET [108], MAGIC [125], VERITAS [203], MILAGRO [140], GLAST [68], H.E.S.S. [91], STACEE [60] and CELESTE [122].

mirror area, at the HEGRA site on La Palma with a calculated threshold energy of around 15 GeV. CANGAROO III sited in Australia, will be a 4- element array consisting of 10m diameter mirrors, and should be in operation by the end of 2003. This is very important in its own right, and as a system with which H.E.S.S. results may be compared, though as detailed earlier this system will suffer from its low altitude. These altitude problems which trouble Cherenkov astronomy have led to the proposal for a 3rd generation system to be placed at an altitude of 5km, with an estimated energy threshold of 5 GeV [2]. Such systems will truly overlap with the next generation of satellite systems, in particular the NASA GLAST Satellite [68], due for launch in 2006, which has a calculated upper energy limit of order 100 GeV. This will allow high-resolution spectroscopic and angular studies of sources in an energy range hitherto unavailable for study. The nature of these sources is the subject of the next chapter.

Chapter 4

TeV Astrophysics

4.1 Introduction

In this chapter a discussion is presented of the different classes of astrophysical objects that emit, or have been theorised to emit, gamma-rays at very high energies. The chapter begins with a presentation of the general astrophysics motivations behind imaging atmospheric Cherenkov astronomy, and then continues with a review of the different sources believed to produce VHE gamma-rays. An outline of the physical models believed to be at work (where appropriate and with reference to chapter 1,) is made whenever possible during the discussions presented.

4.2 Physics Motivation

VHE gamma-ray astronomy investigates the non-thermal Universe. This part of the Universe (probed by astronomy at X-rays wavelengths and smaller) contains matter and radiation with energy distributions that have no characteristic scale attributive to a temperature. The best known component of the non-thermal Universe are the cosmic rays, which have an energy spectrum governed by power-law distributions up to energies of 10^{20} eV. As discussed in chapter 1, the presence of a VHE gamma-ray signal from a source is believed to indicate that the source might also produce a hadronic cosmic ray signal. Therefore, due to the galactic magnetic field creating an isotropy of charged cosmic rays, gamma-ray astronomy is the tool of choice for studying the source (and mechanisms of production) of cosmic rays.

The space-based detector that has observed the most sources of gamma radiation was the EGRET instrument aboard the now decommissioned Compton Gamma-Ray Obser-

vatory [75]. In its 8 year lifetime, EGRET (capable of detecting events between 30 MeV to 30 GeV) observed 271 distinct sources of gamma-rays [76]. At higher energies, results have come from ground-based imaging Cherenkov telescopes. Thus far the best established sources of VHE gamma-rays are the Crab Nebula, the plerion of pulsar PSR1706-44 and the AGNs (Active Galactic Nuclei) Mkn 421, Mkn 501 and 1H1426+528, which have all been detected independently by two or more groups. With new telescope systems that can work at the milli-Crab level, the number of sources should grow rapidly. However, it is believed that most of the sources seen thus far are not of the type responsible for the bulk of the cosmic rays in the energy region up to the knee (the first break in the cosmic ray spectrum at around 2×10^{15} eV). Therefore, the investigation of further sources is of vital importance.

However, discovering the origin of hadronic cosmic rays is only one of the physics uses for imaging atmospheric Cherenkov telescopes, others include:

- Using the next generation of Cherenkov telescopes with their lower energy thresholds and better energy resolution, a statistically significant number of objects of different astronomical classes should be seen in the VHE gamma-ray window, allowing morphological comparisons. Also, spectroscopic analysis of such sources could be done in a relatively short time. These classes of objects include; pulsar nebulae, black holes in our galactic neighbourhood and relatively nearby AGN.

- Predicted sources like supernovae remnants and molecular clouds may be studied. Although these sources have not been detected by the current generation of IACTs this may be because they are too spatially extended or too faint. Other possible sources yet to be studied include starburst galaxies, nearby clusters of galaxies and compact binary systems in our own galaxy.

- Extragalactic sources may exhibit attenuation due to the TeV gamma-ray signal pair producing electron-positron pairs, with cosmic infra-red background photons (as mentioned briefly in chapter 1). The optical depth due to these pair production interactions is a function of energy and redshift ($\tau(E, z)$), and is dependent upon the spectral energy distribution of the cosmic infra-red photons. Therefore, by studying VHE gamma-ray emitting AGN at different distance scales a study of the form of the infra-red background

may be possible. In particular gamma-ray halos around strong AGN have been proposed, (again due to infra-red background absorption). If these halos could be studied spatially and spectroscopically, more could be learned about the infra-red background, and limits could be placed on source distances, with important implications for cosmology.

-Other ideas have been postulated as mechanisms for VHE gamma-ray production, these include: collapse of topological defects in the early Universe and the annihilation of supersymmetric dark matter particles.

As can be seen from the above argument there is much physics to be explored in the VHE gamma-ray window, and with the soon to go online next generation telescopes (like H.E.S.S., MAGIC and VERITAS) many new sources of TeV radiation should be observed. Each type of source is now taken in turn, and a discussion of any reported observations and the acceleration mechanisms theorised to be at work is presented.

4.3 Astrophysical Sources

4.3.1 Plerions

Plerions form when a relativistic wind from a pulsar is confined by a more slowly expanding shell of the surrounding supernova remnant. The two plerions observed in the VHE gamma-ray window are the Crab and PSR1706-44, and both are known to possess a relatively young neutron star with high spin down energy. The energy of the pulsar is dissipated in a shock that accelerates ambient particles. The production of X-ray synchrotron emission from the source implies the presence of electrons with energies around 100 TeV. Gamma-rays are believed to be produced by inverse Compton scattering of the synchrotron photons from their progenitor electrons (the synchrotron-self-Compton model (SSC)). Models of SSC applied to the Crab Nebula agree well with available data, as shown in [88]. A double peaked light curve from the pulsar has been observed at a pulse period of 33 ms over a spectral range from ≈ 100 MHz to a few GeV.

The first clear steady VHE signal from the Crab nebula was detected in 1989 by the Whipple group [201]. Since then the Crab has been studied extensively by many northern hemisphere groups and found to be a remarkably constant source. A recent measurement by the Whipple group set the integral flux above 1TeV at $\approx (2.1 \pm 0.2_{\text{stat}} \pm 0.3_{\text{syst}}) \times 10^{-11} \text{ cm}^{-2} \text{ s}^{-1}$ [90]. The differential spectral slope of the source was calculated to be $-2.49 \pm$

$0.06_{\text{stat}} \pm 0.04_{\text{syst}}$ in the TeV energy domain, however a differential spectral slope of $-2.44 \pm 0.06_{\text{stat}} \pm 0.04_{\text{syst}} - 0.151 \log(E)$ was found to be more appropriate in the GeV energy region. The significance of this source detection is $> 20\sigma$. The steady nature of the Crab emission has allowed it to be used as a standard candle, which has proved invaluable for the calibration of ground-based detectors in the northern hemisphere. The integral spectrum of the Crab as measured by several systems working in the VHE regime is given in figure 4.1.

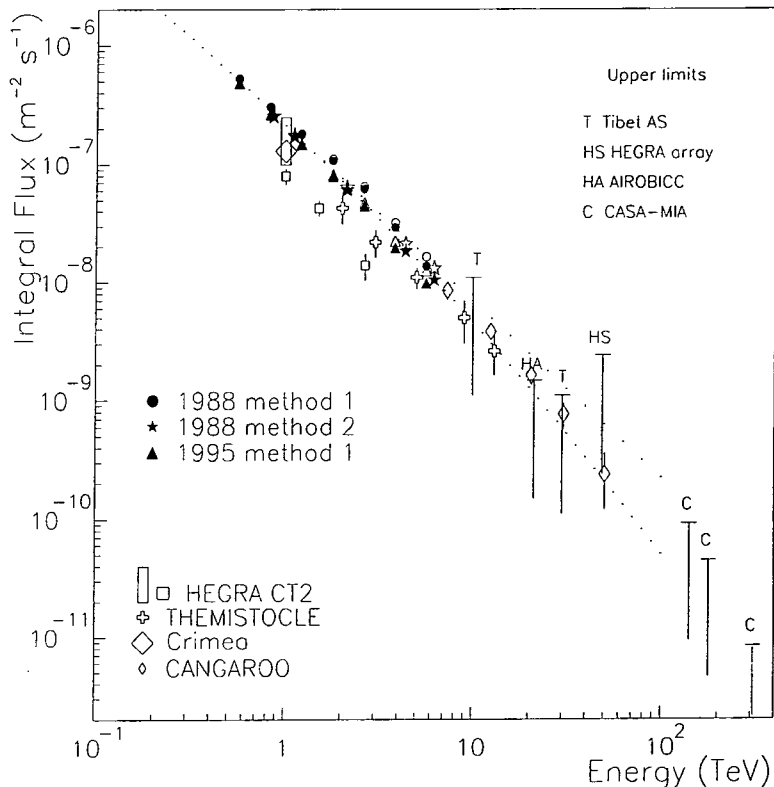


Figure 4.1: Integral flux of photons from Crab Nebula obtained by various groups. Upper dotted line: Power-law fit to the Whipple points (i.e. $\log(\text{flux})$ is linear in $\log(E)$); lower dotted line: quadratic fit in $\log(E)$, taken from [88].

Most plerions are older than the Crab and predictions of SSC fluxes, indicate they would be unobservable at TeV energies. However, inverse Compton scattering of other sources of soft photons (e.g. infra-red radiation and the Cosmic Microwave Background) by the highly relativistic electrons may produce detectable fluxes of gamma-rays from older plerions. Given the use of the Crab as the standard candle for northern hemisphere Cherenkov telescope systems, it is hoped that PSR1706-44 will be use able as a standard candle for the next generation southern hemisphere Cherenkov systems, such as H.E.S.S.

and CANGAROO III.

4.3.2 Isolated Pulsars

Pulsars were first discovered in 1967 [82], and to date around 600 have been detected (usually via pulsed radio emission). Signals at these energies are very regular with pulse length ranging from a few milliseconds to several seconds. EGRET was capable of detecting seven pulsars emitting gamma-rays between 20 MeV and 30 GeV, however only three pulsars (the Crab, Vela and PSR1706-44) have so far been seen in the TeV energy regime, and all produced unpulsed signals, which are believed to be due to their plerionic nature. It is believed that the pulsed signal from the pulsar itself is dominated at TeV energies by the signal from the interaction of the shockwave. The new generation of Cherenkov telescopes possess the angular resolution to correctly check this hypothesis. The acceleration mechanisms believed to be at work behind this underlying pulsed TeV signal is now outlined.

A pulsar consists of a spinning neutron star in a magnetosphere (the region of space dominated by the neutron star's strong magnetic fields ($\sim 10^{12}$ G) shown in figure 4.2). The magnetosphere is highly conducting along field lines, but not perpendicular to them. The magnetic and rotational axes of the pulsar are not aligned, and hence the rotating magnetic dipole causes the emission of a regular electromagnetic wave that is detected at the pulsar's period. This is the major source of energy loss from the pulsar, as pulsars that are not been accreted onto, show a lengthening of pulsar period, indicative of a loss of rotational energy. The magnetic fields co-rotate with the neutron star out to a radius r_c , from the spin axis beyond which the velocity of rotation exceeds the speed of light. This distance defines the light cylinder, within which the magnetic field lines are closed. This cylinder contains a high density of electrons and ions drawn from the surface of the neutron star by strong electric fields. The net charged density in the magnetosphere has the opposite sign as the scalar product of the rotation and magnetic field vectors, $\underline{\Omega} \cdot \underline{B}$ (as shown in figure 4.2) and discussed in [127]. The equatorial and polar regions are separated by a line joining the points where $\underline{\Omega} \cdot \underline{B} = 0$, the so called "null charge surface" and are populated by charges of opposite sign. Two popular models of particle acceleration by pulsars are now described:

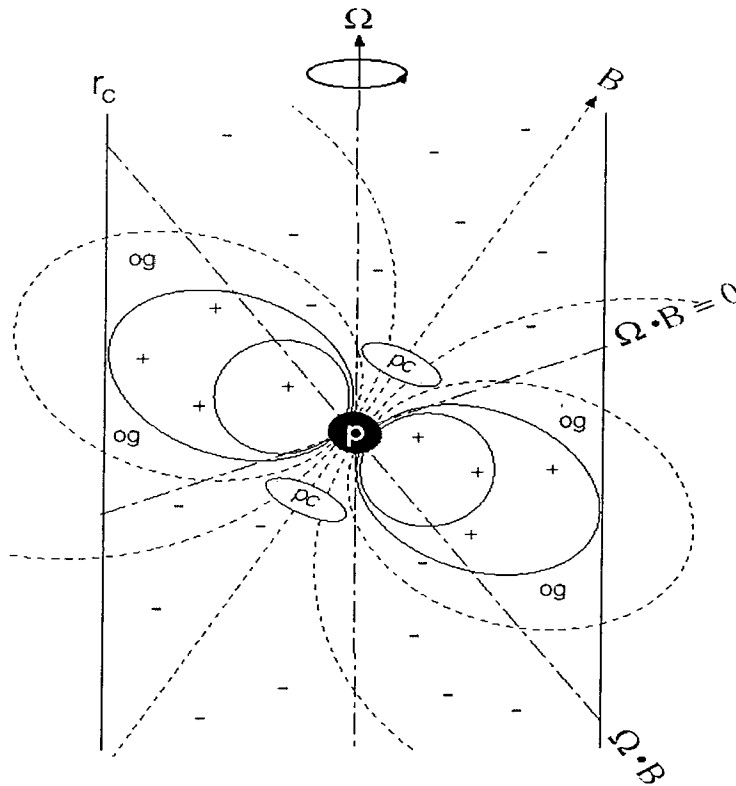


Figure 4.2: The geometry of a pulsar, indicating the closed (solid) and open (dotted) magnetic field lines. Charge separation occurs on either side of the null surfaces (dot-dashed), where the magnetic field and rotation vectors are orthogonal. The indicated regions show the outer gap (og) and polar cap (pc) where particle acceleration might take place.

Polar Cap Model

The circular region at the poles defined by the last closed field line is known as the polar cap [127], as indicated by 'pc' in figure 4.2. Above the polar cap electrons are highly constrained by the field lines, and move in a beam a few degrees wide. It is believed that these electrons produce the radio emission seen from Earth, by synchrotron radiation (as discussed in chapter 1). As the rotation of the pulsar causes the rotating beam of electrons only to pass the observer's line of sight periodically, so a modulated signal at radio energies is seen. The energies of the emitted photons depend on the magnetic field strengths, with the highest energies only possible in the lower magnetosphere. Gamma-rays may also be emitted by curvature radiation processes (as highlighted in chapter 1), close to the stellar surface. However, due to electrons and positrons created at higher altitudes falling back to the surface, it is believed a gamma-ray opaque region of thermal

photons will exist, possibly blocking out any signal from TeV curvature radiation.

Outer Gap Models

The outer gaps (or ‘og’ in figure 4.2) are near the light cylinder radius and are bounded by the null charge surface and the last closed field line. Only pulsars possessing both a short spin period and a large magnetic field may possess an outer gap, and their sizes are heavily dependent on the alignment of the magnetic and spin axis and the field strength. The drop in potential along \underline{B} may be as large as 10^{15} V in the Vela and Crab pulsars.

Many models for pulsed emission of photons from this region have been proposed, but here only that due to Cheng, Ho and Ruderman from 1986 is reviewed [40].

Gamma-rays produced lower in the magnetosphere may traverse the gap and may interact with lower energy photons or the transverse magnetic field to produce electron-positron pairs. These pairs may be accelerated along the field lines, and may in turn produce gamma-rays up to a few GeV by curvature radiation interactions, or by inverse Compton scattering off lower energy infra-red radiation. Even if this emission extended to a few hundred GeV by secondary emission processes, it would be immensely difficult to detect given absorption via pair production with the magnetospheric magnetic field or infra-red photons.

It is important to note that the next generation of Cherenkov telescopes with their lower energy threshold, should be able to determine which model (og or pc) is applicable. If the polar cap model is correct, photons with energies approximately ≥ 50 GeV are liable to pair produce on the strong magnetic fields present. One would therefore expect a cut-off in the photon energies seen by a ground-based Cherenkov telescope, as compared to the outer gap model, as although pair production in the outer gap model is possible with soft X-rays, the cut-off is liable to be slower than for the polar cap case [95].

Up to this point intermittent pulsed signals in the TeV energy region have been reported from the Vela ([20],[31]) and Crab pulsars ([1], [35]). However, since imaging became the tool of choice for ground-based Cherenkov telescopes, no multiply confirmed pulsed signals from isolated pulsars have been seen.

4.3.3 Supernova Remnants

Due to the severe energy losses that occur to cosmic ray electrons via Compton scattering in the intergalactic medium, cosmic ray electrons with energies greater than 100 GeV must have originated from sources within our Galaxy. It is well established from observations of

synchrotron nebulae and the GeV-TeV emission from plerionic remnants that supernovae remnants accelerate electrons to high energies, but due to the different mass to charge ratio of hadrons, it is difficult to say whether hadrons are accelerated at the same sites. It is a widely held belief however that supernova remnants should be the sources of cosmic rays up to energies of $\sim Z \times 10^{14}$ eV, where Z is the nuclear charge [104]. Hadrons and electrons are therefore both thought to be accelerated across the expanding shock wave of a supernova remnant (SNR) via the first order Fermi mechanism discussed in Chapter 1.

Synchrotron emission in the shells of SNRs has been detected at radio, and X-ray wavelengths. The CANGAROO group have observed several shell type SNR at TeV energies including: SN1006 [190] and RXJ1713-39 [53]. In particular their work on SN1006 shows a significant signal from the north-east rim, an area previously seen by the ASCA satellite in X-rays, which are believed to originate from synchrotron emission [120]. The TeV signal is thus believed to come from gamma-rays produced by inverse Compton scattering of synchrotron photons by their progenitor electrons (the so called synchrotron-self Compton model). However this result has not been independently verified, and this will have to wait until H.E.S.S. can observe it. Hadronic models for TeV photon production also exist. Collisions of accelerated nuclei with the interstellar medium outside the SNR might result in the production of neutral pions, which would subsequently decay into gamma-rays at MeV-GeV energies [96] and [65]. The detection of a TeV signal of hadronic origin from a shell type supernova would provide evidence for the shock acceleration of hadronic cosmic rays in SNR shells, and solve the mystery of the origin of most galactic cosmic rays. However, the possibility that such a signal may originate from an electron-based mechanism complicates matters significantly. Some interesting evidence has been given by the HEGRA group, who spent 232 hours viewing the remnant Cassiopeia A. The source was seen to emit gamma-rays with a significance of 5σ . The observed spectrum of Cas-A seen by HEGRA is however consistent with both electron and hadron based acceleration models, or a mixture of both [3]. Hopefully future work with the next of generation of Cherenkov telescopes will allow the discovery of supernovae remnants with an obviously hadronic gamma-ray production process, which would finally help solve the mystery of the source of galactic cosmic rays.

4.3.4 Accreting Binary Systems

This class of objects covers several potential TeV gamma-ray emitting sources, including; high/low mass X-ray binary systems, cataclysmic variables and microquasars.

High/Low Mass X Ray Binary Systems

High mass X-ray binary (HMXRB) systems are believed to consist of a massive OB super giant star and a compact object (usually a neutron star). They generally have a high X-ray luminosity ($\sim 10^{37}$ erg sec $^{-1}$ [172]). Matter is transferred from the super giant to the compact object through a strong stellar wind, which is thought to eject $\sim 10^{-4} M_{\odot}$ per year as discussed in [27] and [50]. The X-ray luminosity is given by the rate the accreting material loses gravitational potential energy, with the maximum luminosity from accretion being given by the Eddington luminosity L_{Ed} (the point at which the gravitational forces on the accreting material are balanced by the outward radiation pressure). For spherically symmetric accretion, this is:

$$L_{\text{Ed}} = \frac{4\pi GMm_p C}{\sigma_T} \quad (4.1)$$

where M is the mass of the compact object, m_p is the proton mass, σ_T is the Thompson cross-section and c is the speed of light. A small accretion disk may exist due to the small angular momentum of the stellar wind, but the super giant itself dominates the optical emission. The X-rays are often pulsed as the compact object's strong magnetic field directs the accreting material on to the magnetic poles that maybe (as in the case of isolated pulsars) displaced from the spin axis. The X ray emission is only seen when a pole is orientated towards the observer ([163]), giving a 'lighthouse' effect.

Low mass X ray binary (LMXRB) systems on the other hand are generally associated with older population II stars. They are characterised by faint optical emission and unpulsed steady X-ray emission of a slightly lower luminosity than that of the high mass systems, but with occasional bursts. They are thought to consist of a cool, late-type star less massive than the Sun which has filled its Roche lobe, and which is transferring matter on to a neutron star through the inner Lagrangian point as shown in figure 4.3 and discussed in [81].

This matter carries a large angular momentum, which causes the formation of a large accretion disk around the compact object, which may be occasionally observed optically. The X-ray emission from the neutron star is basically unpulsed as the magnetic fields

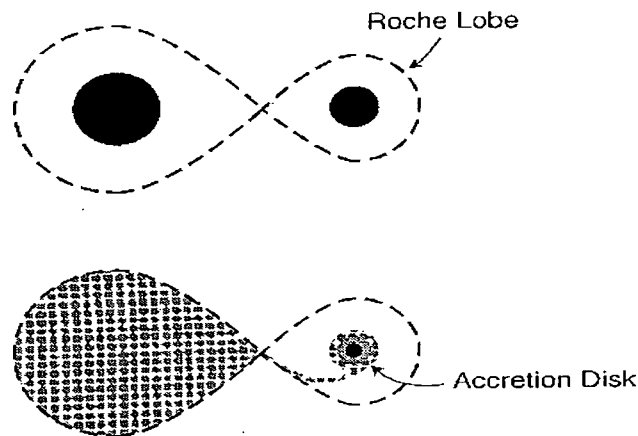


Figure 4.3: The standard model of a matter accretion in low mass X-ray binary systems.

associated with these older objects have significantly decayed, although quasi-periodic oscillations (QPO's) are sometimes seen due to interactions between the accretion disk and the remnant magnetic field [113]. Unstable thermonuclear burning of Helium on the surface of the neutron star may also produce bursts of X-rays.

X-ray binary systems were popular TeV pulsed source candidates in the 1980's and many detections of varying significance were reported (including Cygnus-X3 [36] and Hercules X-1 [200]). However, since the advent of imaging, no X-ray binary source has been confirmed by two separate groups, with significance greater than 5σ . Detections have been made however, and the Durham group recently claimed a detection from the HMXRB system Cen-X3 with their Mark 6 telescope at a significance level $> 4\sigma$ [12].

Many models for TeV photon production exist, although due to insufficient data none have been multiply confirmed. All fall into two broad categories depending on whether the accelerated charged particles are taken to be electrons or hadrons. However both models suffer from problems, if the production site of TeV photons is close to the compact object. Electrons are not favoured in these models because their acceleration is curtailed by inverse Compton scattering in the fields of intense X-ray regions surrounding accreting neutron stars. Hadronic models, where gamma-rays come from hadronic interactions producing π_0 and subsequent π_0 decay also suffer problems, as electron-positron pair production is also possible with UV photons from the companion (this is particularly significant in HMXRB systems, where the peak emission is in the UV). Though, as the hadron signal is only believed to be partially attenuated, some emission may still be seen due to the mechanisms outlined in [41]. Some new models attempt to overcome these potential

problems, by suggesting that the accretion disks of both types of X-ray binary system may form jets and that TeV photon production could occur within the jets in a manner analogous to blazar emission, which shall be discussed later in this Chapter. In particular this theory has been applied to the observations of emission seen from Cen X-3 by the Durham group [12].

Cataclysmic Variables

Cataclysmic variables are binary systems in which the compact object is a white dwarf, rather than a neutron star, and are not as bright as X-ray binaries at X-ray frequencies. The companion stars are usually late-type stars that transfer matter onto the white dwarf by Roche lobe overflow and accretion disk formation. The optical and UV emission can be highly variable, and in some systems, where the companion star is a dwarf star, the accretion disk may be observed directly. Outbursts of periodic pulsed VHE gamma-ray emission have been observed from the cataclysmic variable AE Aquarii indicating particle acceleration at locations tied to the rotating white dwarf during periods of enhanced accretion [28], [139]. No single cataclysmic variable has been seen at the $> 5\sigma$ level by more than one group in the TeV domain.

Microquasars

Microquasars are binary objects where one of the binary pair is a black hole. They possess accretion disks and collimated relativistic jets along the rotational axis of the black hole. To date, no microquasar has been seen at TeV energies. Two objects that are predicted to produce VHE radiation are GRS1915+105 and SS433, although the latter is technically not a microquasar, given that it possesses a neutron star and not a black hole. Aharonian and Atoyan argue for the production of TeV gamma-rays by the inverse Compton scattering of CMB photons, by jet accelerated electrons produced at the eastern jet termination point of SS433 [6]. However, the HEGRA system has not yet seen emission from SS433 and is only able to constrain the models of Aharonian and Atoyan with an upper limit on the flux from SS433 [178].

Possible TeV emission from GRS1915+105 is predicted from shock waves within the jet itself [11], and although this source has not been seen directly at TeV energies it was observed to be emitting at wavelengths covered by OSSE (50 keV to 10 MeV) [195]. Episodic periods of more intense emission from this source have been seen at longer wavelengths, and it is argued that both inverse Compton scattering of external photons

or SSC models both suggest that it may be possible to observe this object emitting in the TeV region at this time [11]. A discussion of actual and possible extragalactic sources of VHE gamma-ray radiation forms the subject of the next section.

4.3.5 Active Galactic Nuclei (AGN)

Active galaxies are those galaxies whose luminosities are much larger than can be accounted for by thermal emission from the stars in the galaxy. The power source responsible for driving the non-thermal processes is thought to be accretion into a black hole ($\sim 10^8 M_{\odot}$) at the centre of the galaxy. There are many classifications of AGN, based on for example, their spectra, their flux variability at different wavelengths and the presence of emission lines. One classification system is based around the observation angle as shown in figure 4.4. Although the population of AGN is diverse, a general description is given in [196].

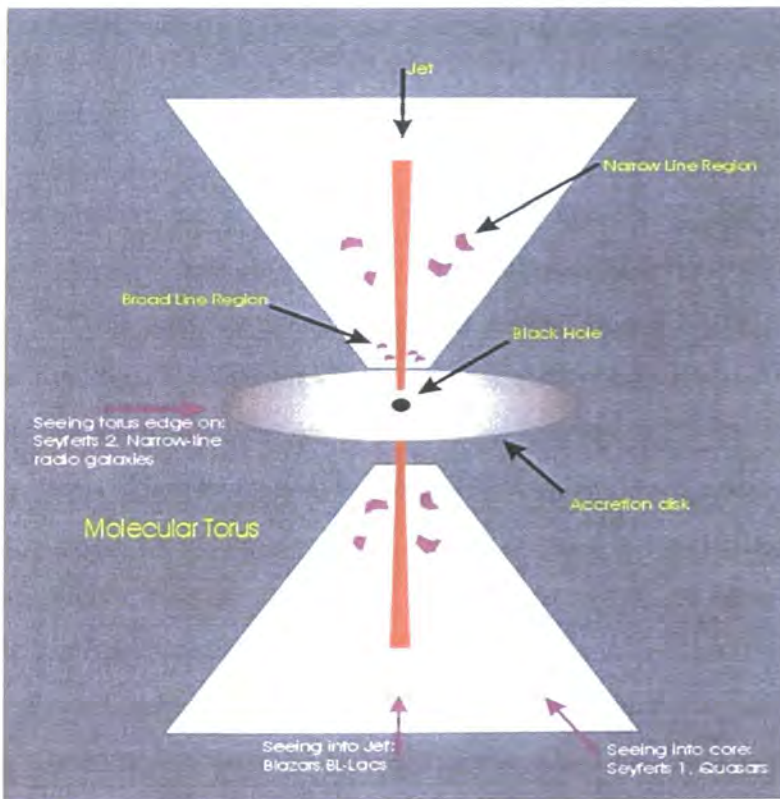


Figure 4.4: Schematic diagram of general AGN structure, showing different classification systems and how they relate to observation angle.

A subset of AGN known to emit at TeV energies is flat spectrum radio-loud quasars (FSRQs) or blazars (those with jets pointing along the line of sight, as shown in figure

4.4). Blazars are powerful radio sources that emit a continuum of emission that has been measured from radio frequencies to VHE energies. Blazars are characterised by high time variability, high luminosity ($> 10^{38}$ watts at most wavelengths) and high optical polarisation. Table 4.1 shows the current set of blazars seen at TeV energies by more than one Cherenkov telescope, at a level greater than 5σ . However, several other blazars have so far only been seen by 1 group. In chapter 6, for example, the emission seen by the Durham group with the Mark 6 telescope from the AGN PKS 2155-304 [38] will be discussed in detail.

Source	Discovered	Redshift	Reference
Markarian 421	1992	0.031	[166]
Markarian 501	1995	0.034	[167]
1H1426	2001	0.129	[92]

Table 4.1: Observed GeV/TeV AGN gamma-ray sources at or above 5σ threshold by more than one group.

The spectral energy distributions (SEDs) of all blazars show a double peak [61]. The location and spacing of the peaks varies from object to object, with the first appearing anywhere in the infra-red to soft X-ray, and the second in X-ray to hard gamma-ray region. The time variability of blazar emission is extremely unpredictable, and flux variations or flares of activity may last from periods as short as an hour to several days. The short timescale and high luminosity of the flares, indicates that emission from blazars is due to non-thermal processes in the relativistic jets of electrons. Shock fronts formed by the plasma in the jets are capable of accelerating electrons to extremely high energies by the first order Fermi mechanism as illustrated in chapter 1. The physical processes producing emission at different wavelengths are clearly linked, as multi-wavelength studies of flaring blazars have shown a correlation between the flux increases at different energies [135], [105]. Figure 4.5 shows this in multi-wavelength observations of Markarian 501 made during April 1997 when a flare occurred [33].

Although the low energy component of the emission is believed to arise from the incoherent synchrotron emission of relativistic electrons in the jets [24], there exist many models for VHE photon production.

In SSC models the gamma-rays are produced through inverse Compton scattering of low energy synchrotron photons by their progenitor electrons [26]. Given this model, SSC

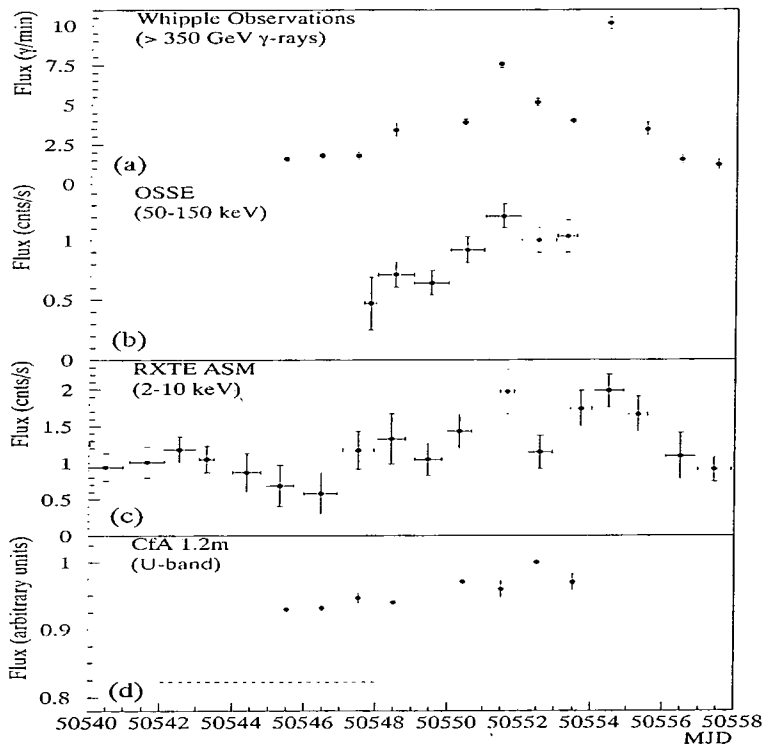


Figure 4.5: Multi-wavelength emission from Mkn 501: (a) VHE gamma-ray emission (WHIPPLE), (b) 50 keV - 150 keV (OSSE), (c) 2 - 10 keV and (d) U-band optical light curves for period 2 April (MJD 50540) to 20th April 1997 (MJD 50558). Dashed line indicates average Uband flux in March 1997. Taken from [33].

emission should occur at some level in all blazars, but models in which the gamma-ray emission occurs predominantly from inverse Compton scattering of seed photons that arise from outside the jet, fit observed data well [186]. Multi-wavelength observations of AGN allow the determination of which inverse Compton model is correct. If the synchrotron-self Compton model is correct, then the TeV photons and X rays are produced by the same electron population, and one should expect to see flaring in X-rays and gamma-rays at the same time. Any uncorrelated flaring may rule out the SSC model. However, as discussed before, there currently seems to be a good correlation between flares in the different wavebands. In particular a large amount of correlated multi-wavelength data exists for the Markarian sources (421 and 501) [33].

Other models exist based around the shock acceleration of protons to extremely high energies. The ultra high energy protons interact with lower energy photons to produce VHE photons by neutral pion decay, electrons (and positrons) from charged pion decay

(and neutrons and neutrinos) [133]. The photons from neutral pion decay have $\sim 10\%$ of the energy of their progenitor protons, therefore photons up to energies of a few hundred TeV are created. If the TeV photons are produced near the central source $\gamma - \gamma$ interactions with softer photons are possible, which would attenuate the TeV signal. However, the electrons and positrons produced may then lose their energy via inverse Compton scattering and synchrotron emission, with the resulting photons going onto produce further cascades, and hence more gamma-rays. The variability on short timescales can be explained using this model, with relativistic shocks moving down a relativistic flow with embedded inhomogeneities [134].

Current TeV (and multi-wavelength) observations do not rule out either model. The different Compton models predict different multi-wavelength behaviour, while the proton models do not suggest any correlated multi-wavelength behaviour, however they suggest that neutrino emission should be simultaneous with TeV flares. If neutrinos from flaring AGN could be observed, current Compton models would be ruled out.

Before moving onto cosmological uses of TeV astronomy one should mention the discovery of emission from the AGN PKS 2155-304 by the Durham Group with the Mark 6 Cherenkov telescope. This AGN at a redshift (similar to that of the AGN 1H1426, [92]) of ~ 0.119 was observed between 1996 and 1997. The strongest emission was seen from the source in November 1997, when the object was producing a significant flux of high-energy X-rays and was seen as a source of gamma-rays of energy greater than 100MeV by EGRET [198]. The TeV emission was first reported in 1998 [38]. The fluxes quoted at this time were based around simplistic simulations, and more recent work (which will be discussed in chapter 6) using the air shower code MOCCA ([87]), and a refined telescope simulation code have allowed the effective sensitive area and threshold energy of the telescope to be recalculated.

Indirectly Measuring the Cosmic Infra-Red Background with TeV gamma-Rays

As discussed earlier in this chapter, pair production can occur at TeV energies with photons from the cosmic infra-red background leading to an energy (and redshift) dependent attenuation of the TeV signal. Studying a large set of GeV/TeV emitting AGN at varying redshifts, would then allow constraints on the infra-red background to be made. This is significant as the structure of the infra-red background gives us valuable information about the epoch of galaxy formation and the composition of dark matter in the Universe

[129].

However, at this time the number of TeV emitting AGN is modest. A recent paper [99] from de Jager and Stecker suggests a semi-empirical model for the infra-red background obtained by integrating luminosity dependent infra-red spectra of galaxies over their luminosity and redshift distributions. The optical depth as a function of redshift and energy is shown as figure 4.6.

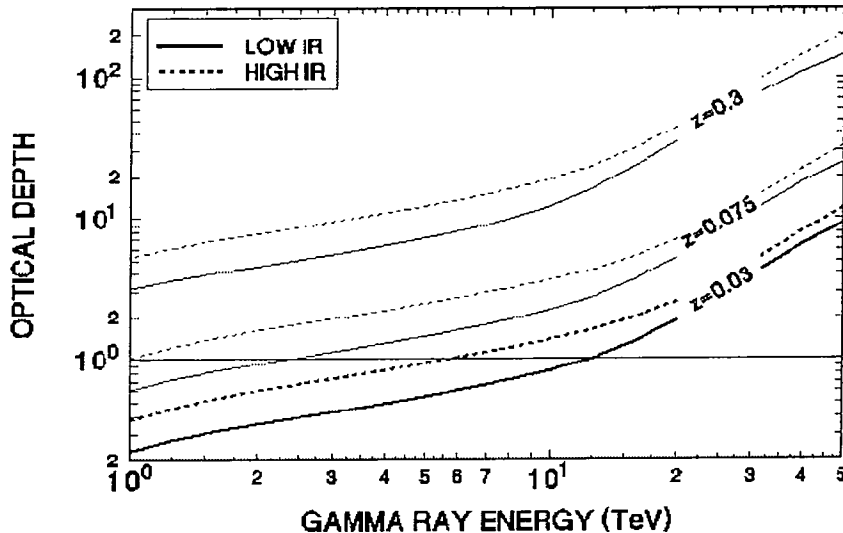


Figure 4.6: Optical depth versus energy for gamma-rays originating at various redshifts obtained from [97]. The low and high infra-red lines correspond to the optical depths predicted by assuming two different spectral energy distributions for the infra-red background taken from [131].

The model is then applied to measurements of AGN at TeV energies, and the intrinsic spectrum of the source is computed and compared with other model predictions. This work has been performed on Markarian 501 [99], as shown in figure 4.7.

A similar model [4] has also been applied to 1H1426, which is at a much greater redshift, and should have a much more attenuated signal as indicated in figure 4.8.

Unfortunately the Durham Mark 6 telescope was unable to observe the source PKS 2155-304 spectroscopically, so a study of the attenuation due to cosmic infra-red background interactions is not possible. However, the next generation of Cherenkov telescopes should be able to study many other AGN, and a catalogue of sources may be compared against current infra-red background models.

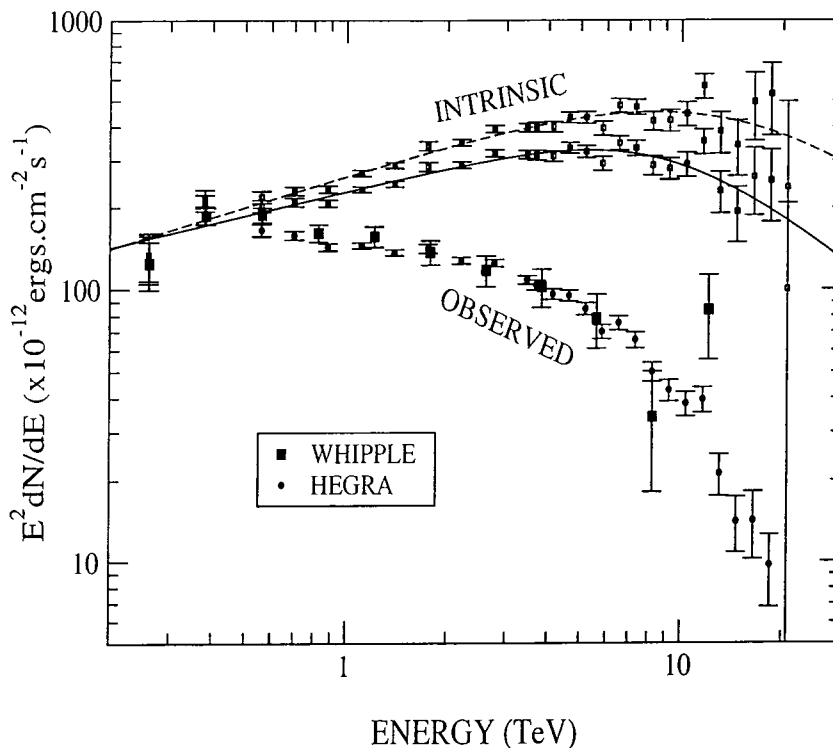


Figure 4.7: The observed spectrum and derived intrinsic spectrum of Mkn 501. The observed spectral data are as measured by HEGRA (solid circles) and Whipple (solid squares). The upper points are the absorption corrected data points (marked 'Intrinsic') using 2 separate models given in [99].

4.3.6 Gamma-Ray Bursts

The sources and mechanisms for producing gamma-ray bursts (GRBs) remains unknown. EGRET detected an 18 GeV photon from the direction of a GRB more than 90 minutes after BATSE had detected the burst [94]. This suggests that high energy gamma-rays play a role in the energetics of GRBs. This source had a redshift $Z < 3$ which would avoid complete intergalactic absorption [99]. Also, as the high energy emission seems to be delayed, so in the future GeV/TeV emission can be followed when information from lower frequency bands indicates that a GRB has occurred. Recently, the Milagro collaboration [140] reported the weak detection ($\sim 3\sigma$) of approximately ≥ 7 TeV gamma-rays from a GRB [10]. This field therefore requires further study of GRB's with future Cherenkov telescopes, in particular MAGIC [125], has an estimated extremely rapid slew time (< 30 seconds) with predicted low energy threshold (~ 15 GeV), and therefore would be an ideal instrument for studying GRBs using the imaging Cherenkov technique.

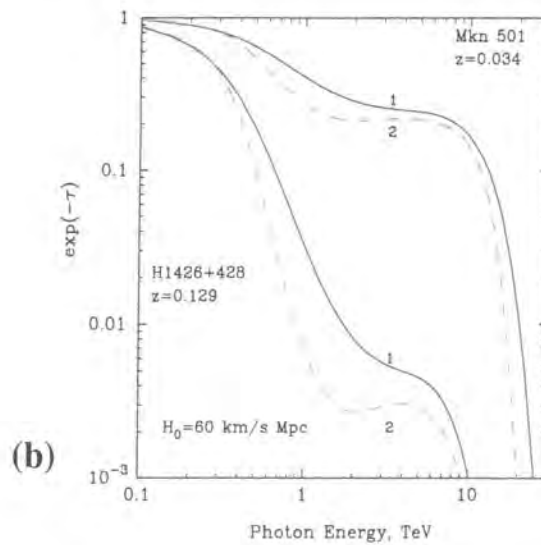


Figure 4.8: The spectrum correction factors from Mkn 501 and 1H1426 ($\exp(-\tau(E))$, where τ is the optical depth) based on 2 models of the cosmic infra-red background. Model 1 fits the data due to [161], and model 2 fits the data due to [137].

4.3.7 Cosmological Uses

No definite cosmological source of TeV photons has yet been seen, so what follows is a discussion of some possible sources of TeV radiation.

Neutralino Annihilation In the Galactic Centre

Most current dark matter models, appear to require a cold dark matter (CDM) contribution to Ω of 0.3, where Ω is the ratio of the total density of the Universe to that required to create a flat Universe, [67] & [162]. The lightest stable super-symmetric particle is the neutralino and is believed to be a strong candidate for CDM, however neutralinos (and any other super- symmetric particles for that matter) remain undetected. Cosmological constraints, and lower limits from large accelerator experiments set the constraints for the neutralino mass between 30GeV and 3TeV. If neutralinos do constitute at least part of the CDM, and if they are found near the centre of extremely massive bodies, such as the centres of galaxies, then their direct annihilation to gamma-rays should produce a unique signal. This signal would be at the frequency corresponding to the neutralinos mean energy, and would therefore be related to its rest mass. GLAST [68] and the new generation of Cherenkov telescopes (covered in Chapter 3) should allow the energy region believed to contain neutralino emission to be studied carefully. A current model suggests that the intensities of gamma-rays produced by this method, would make the annihilation

line visible by GLAST and the new Cherenkov telescopes [146].

Quantum Gravity

By making observations across the high frequency electromagnetic spectrum up to TeV energies of emission from high energy sources, it is possible to place lower limits on E_{QG} the energy at which quantum gravity is believed to couple to the electromagnetic force. This is due to quantum fluctuations within the vacuum of space having a dispersive effect on photons. The Amelino-Camelia [8] formulation relates the dispersive time delay (δT) of a photon of energy E , relative to the light travel time over a distance L to E_{QG} .

$$\delta T = \frac{\xi EL}{cE_{\text{QG}}} \quad (4.2)$$

where ξ is a model dependent factor, taken to be approximately equal to 1. The analysis of a strong VHE emitting flare from Markarian 421 by the Whipple group, has placed a lower limit on E_{QG} which is four times higher than that expected from theory [22].

Primordial Black Holes

Primordial Black Holes (if they exist) should emit a burst of radiation in the final stages of their evaporation [154]. In the standard model of particle physics, the last burst of radiation should release 10^{23} J in 1 second, at energies around 1TeV. This therefore remains another predicted source for exploration in the VHE regime. This chapter will now be concluded with a discussion of the current status of TeV astronomy with respect to observed sources.

4.4 Current Status

As this chapter has shown, many classes of object are possible sources for TeV gamma radiation, however the current number of multiply confirmed sources is still relatively low (around 5 or 6). These and other singly confirmed sources are shown in table 4.2. In particular if one compares table 4.2 with figure 3.11 from chapter 3, one can see that the chances of many of the new lower energy threshold systems detecting many more sources of TeV/GeV radiation are very large indeed. In the next chapter the simulation codes that exists for air shower development will be compared, and in chapter 6 telescope simulation and flux derivation will be covered. Chapter 7 will concentrate on the importance of the atmospheric structure to the results of simulations of ground-based VHE astronomy, and hence fluxes and spectral calculations.

Source/type	Discovered	Reference	Comments
CRAB/plerion	1989	[201]	$\gg 10\sigma$, seen by \geq nine groups
PSR1706/plerion	1995	[111]	$> 10\sigma$, seen by two groups
VELA/plerion	1997	[206]	$> 6\sigma$, seen by one group
SN1006/SNR	1998	[190]	$> 6\sigma$, seen by one group
Cas A/SNR	1999	[164]	$\sim 5\sigma$, seen by one group
RXJ1713/SNR	1999	[143]	$> 5\sigma$, seen by one group
Mkn 421/AGN	1992	[166]	$\gg 10\sigma$, seen by \geq three groups
Mkn 501/AGN	1995	[167]	$\gg 10\sigma$, seen by \geq seven groups
1H1426/AGN	2001	[92]	$> 5\sigma$, seen by two groups
1ES2344/AGN	1998	[32]	$\sim 5\sigma$, seen by one group
PKS 2155/AGN	1999	[38]	$> 6\sigma$, seen by one group
3C66/AGN	1998	[148]	$\sim 5\sigma$, seen by one group
1ES1959/AGN	1999	[151]	$\sim 7\sigma$, seen by one group
BL-LAC/AGN	2001	[149]	$> 5\sigma$, seen by one group (*)

Table 4.2: Observed GeV/TeV gamma-ray sources seen at or above 5σ threshold. This table is transcribed from [126], with source 1H1426 added. (*) indicates that although the title of this paper ([149]) relates to ultra high energies, a closer study reveals a claimed integral flux above 1TeV.

Chapter 5

Simulations of Extensive Air Showers

5.1 Introduction

Ground-based VHE gamma-ray astronomy requires the simulation of the Cherenkov light produced indirectly by a spectrum of gamma-ray primaries and (for off source purposes) a spectrum of cosmic ray primaries. The effects of atmosphere, the elevation of the telescope site, the telescope design and how data are processed must be applied to the simulations to make them comparable with real data. The simulation occurs in two stages. EAS simulation, traces the particle interactions occurring for a given primary, and the paths of Cherenkov photons down to predefined telescope position, recording data for only those photons that are incident upon a mirror. The second stage is the simulation of the telescope itself, where quantum efficiency and mirror reflectivity are applied, so that the Cherenkov photons may be expressed as photoelectrons. These are then traced through the system and applied to the trigger of the telescope (which shall be discussed in the next chapter).

In this chapter the history of simulations of EAS is discussed, and comparisons made of three of the most commonly utilised codes in the field, namely: ALTAI, CORSIKA and MOCCA. The techniques used within the three codes are studied, and the differences these produce in the spatial and temporal profiles of the Cherenkov light created for mono-energetic primary particles (both gamma-rays and protons) are revealed. At the end of the chapter the differences in terms of Hillas parameter distributions for spectra simulated with the three codes for gamma-ray and cosmic ray primaries are outlined.

5.2 A History of EAS Simulation

Early shower simulations were analytical in nature, as the computing power requirement to perform detailed Monte Carlo simulations has only been available since the advent of modern computing technology. The first notable analytical calculations were performed by Zatsepin and Chudakov, and concerned the lateral distribution of Cherenkov light from gamma-ray and proton primaries, [207], [208]. They were successful in reproducing data that can be compared to more modern results. Their data for gamma-rays for instance, show a plateau within 100m radial distance of the core, with an enhancement at 120m radial distance, and a r^{-2} decrease in light density at distances greater than 120m. Their data for protons were found to be in agreement with experimental results of the time. With the advent of increases in computing power, large-scale Monte Carlo simulations became possible, which took account of other effects on EAS formation such as ionisation losses and multiple scattering. These codes then allowed the user to make a statistically large data set for comparison. Simulations of gamma-ray showers were then performed by Rieke [174]. These data were found to be comparable to those produced by Zatsepin and Chudakov, when lateral light densities were contrasted, see figure 5.1.

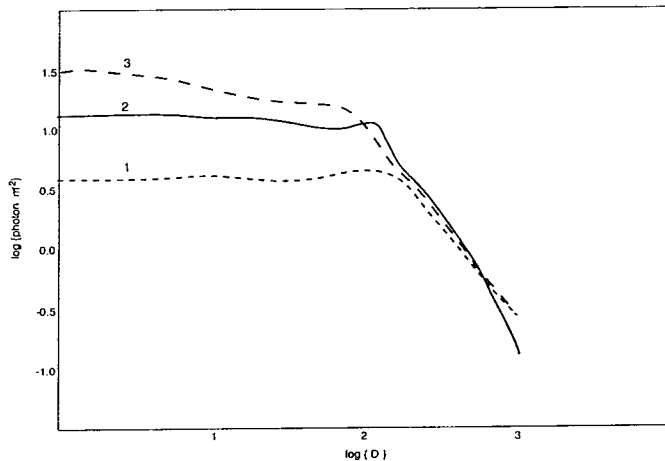


Figure 5.1: Diagram illustrating the simulated lateral distribution of Cherenkov light from gamma-ray initiated EAS. Curve 1 is due to Zatsepin and Chudakov [207] and was calculated for the light pool at sea level, curve 2 is that due to Rieke [174] was calculated for the light pool at 2320m and curve 3 is as given by Zatsepin and Chudakov [208] for the light pool at an altitude of 3860m. All taken from [174].

The presence of large shower to shower fluctuations in gamma-ray induced EAS was first seen by Browning and Turver in 1977 [29], which had not been seen in the earlier

work of Rieke [174]. Their work also suggested that the angular distribution of Cherenkov light from electromagnetic cascades would be so distorted by fluctuations that use of it as a discriminator between hadronic and gamma-ray showers would be questionable. Turver and Weekes [193] compared light profiles for mono-energetic gamma-ray and hadronic showers of 0.1, 1 and 10 TeV and found that the Cherenkov light yield for gamma-ray showers was much greater than for hadronic showers of the same energy. At 10 TeV their work suggested a factor of 2 differences, while at 0.1 TeV a factor of 14 difference was calculated. Their early work proposed that an array of two telescopes separated by 100m with a detector of 37 PMT's at the focus of each telescope could achieve a ~ 0.1 TeV energy threshold. Although their estimates may have been a little optimistic, this work represents the first suggestion that an array of large mirror telescopes, with a camera of PMT's at each focus, would be the tool of choice for ground-based VHE gamma-ray astronomy.

Imaging itself came into the picture in the mid 1980's, and was strongly influenced by the results of Monte Carlo simulations. For example Plyasheshnikov and Bignami carried out simulations of gamma-ray and nucleonic (proton only) showers in the ranges 0.1 to 2 TeV, which were used as a source of simulations for the Whipple 10m telescope. However, their work suggested that the angular dimensions of the images from both types of shower would be quite similar, thus they suggested that imaging would not be a useful technique for hadron rejection. However, this work was later shown to be in error by Hillas [87].

Hillas used the Monte Carlo technique to determine the behaviour of shower particles given a non-isothermal atmosphere. A thinning approximation was used to reduce computing time, where a weighting factor was attached to each particle to take account of low energy particles that were not followed in their entirety. Although thinning is no longer needed at GeV/TeV energies, it was a useful tool at the time and allowed Hillas to produce a significant database of events for comparison. After applying simulation of the 37 PMT Whipple telescope to this database, it was found that imaging parameters could be used to discriminate between hadronic and gamma-ray showers, and the Hillas parameters (as described in Chapter 3) were created [87].

5.3 Monte Carlo EAS Simulation Codes

There are currently many different codes available for producing data on Cherenkov photons from EAS. Those compared herein are: CORSIKA (COsmic Ray SIMulations for

KASCADE) [45], MOCCA (MONte Carlo CASCade) [87] and ALTAI (Atmospheric Light Telescope Array Image) [116]. Before presenting the results of simulations, the subtle differences in techniques used within the three codes are described.

5.3.1 Gamma-Ray Initiated EAS

First, the differences in procedures used in ALTAI, CORSIKA and MOCCA with respect to gamma-ray initiated EAS will be discussed. It should be noted that the differences are small compared to hadronic interactions, as the interaction cross-sections can be calculated very precisely from quantum electrodynamics. The particle interactions important in the gamma-ray initiated EAS include: electron-positron pair production, Compton scattering for primary photons, Bremsstrahlung, ionisation losses and Coulomb scattering for the electrons and positrons.

In particular one finds that the key differences lie in the way each of the three codes deals with the phenomenon of multiple Coulomb scattering of electrons and positrons. Firstly, the importance of multiple Coulomb scattering is discussed, and then its implementation in the three codes is covered.

Multiple Electron/Positron Scattering

The elastic scattering of an electron of energy E (and momentum p) from atoms is characterised by the Rutherford scattering cross-section. It is complicated only at very small angles, of the order of:

$$\theta_{min} = \alpha Z^{1/3} \frac{m_e c}{p} \quad (5.1)$$

where for angles of the order of magnitude of θ_{min} screening of the nucleus by atomic electrons occurs. For angles greater than this, we can calculate an effective interaction length in g cm^{-2} , i.e. the length an electron can travel before being scattered. In [177] this is defined as X_c and is given by:

$$\frac{1}{X_c} = \frac{4\pi}{\alpha^2} N \frac{Z^{4/3} r_e^2}{A\beta^2} \quad (5.2)$$

For highly relativistic particles $\beta = v/c \approx 1$, and to take account of the field of the atomic electrons one should replace Z^2 with $Z(Z+1)$, then:

$$\implies \frac{1}{X_c} = 4\pi Z(Z+1) \frac{N_A r_e^2}{A} \alpha^{-2} Z^{-2/3} \quad (5.3)$$

Here r_e represents the classical radius of the electron ($e^2/m_e c^2$), and N is Avogadro's constant. A and Z represents the atomic mass and atomic number of the scattering media respectively, α is the fine structure constant, m_e is the mass of an electron and c is the speed of light .

The X_c parameter for air equates to around $8.08 \times 10^{-5} \text{ g cm}^{-2}$. This represents the shortest characteristic scale length relevant in EAS development, and therefore this interaction occurs more than any other for the charged particles produced, and is particularly important for electrons and positrons given their large number and low mass. If one tried to simulate every single Coulomb interaction, it would be extremely computational intensive, therefore it is assumed that an electron traverses a straight line along a path length (typically for all these codes $\leq 5 \text{ g cm}^{-2}$), the total deflection is then applied to the electron in either the middle or at the end of the path segment. One standard technique in Monte Carlo code for EAS is to use a Gaussian approximation to simulate the angular distribution of scattered electron velocities [47]. The application of this Gaussian approach depends on the number of scattering events that occur, and does not depend on the length of the track segment or the particle's energy. In the case of low energy electrons, produced further down in the atmosphere, when the Gaussian approximation is used, the trajectories of the electrons become discontinuous, as after just a few collisions the electron's path has been altered dramatically. To track such an electron continuously, the path segment would have to be reduced, dramatically reducing the number of scattering interactions per segment, but also invalidating the Gaussian approach, as the impact of individual scattering events increases. Thus this technique is best at high energies.

The applicability of this model for the three codes is now discussed, and in doing so particular attention is paid to the angular displacement of the velocity incurred by particles undergoing multiple Coulomb scattering.

Angular Deflection

Each of the three codes has a somewhat different approach to angular scattering. MOCCA works in a simplistic, though (as will be seen later) extremely physically descriptive way [86]. Each segment has a length $0.1\text{-}3 \text{ g cm}^{-2}$. For each track segment, a critical angle ϕ is set, such that on average one would expect 0.4 scattering events producing an angular deflection greater than ϕ . The RMS scattering expected from all individual scatters up to

Where with reference to figure 5.3, Θ is defined as $\arccos(\vec{\Omega}_1 \vec{\Omega}_2)$. T_o and T_1 represent the energy of the electron before and after scattering, Δl is the path length used in the calculation (between 1 and 5 g cm⁻² for ALTAI). β is defined as:

$$\beta_1 = \beta_I + \beta_R \quad (5.8)$$

and represents the mean energy loss per unit path length due to the inelastic collisions of a charged particle by production of low energy secondaries via ionisation (I) and bremsstrahlung (R). χ_c is defined by the Coulomb scattering cross-section ($W_c(T, \theta)$) as defined in [116] as:

$$W_c(T, \theta) = \frac{2\chi_c^2}{(\theta^2 + \chi_a^2)^2} \quad (5.9)$$

Parameter B is dependent on energy and material thickness, and can be found by the solution of the transcendental equation $B - \ln B = \ln(0.856(\bar{\chi}_e/\chi_a))$. Functions $f_n(\tilde{\Theta})$ where $n = 0, 1, 2$ are calculated via:

$$f_n(\tilde{\Theta}) = \int_0^\infty \left(\frac{u^2 \ln u}{4} \right)^n e^{-\frac{u^2}{4}} J_0(\tilde{\Theta}u) u du \quad (5.10)$$

where J_0 is a Bessel function of order zero. ALTAI solves for B (which defines the shape of $P(\Theta)$) numerically and CORSIKA follows a similar approach [45].

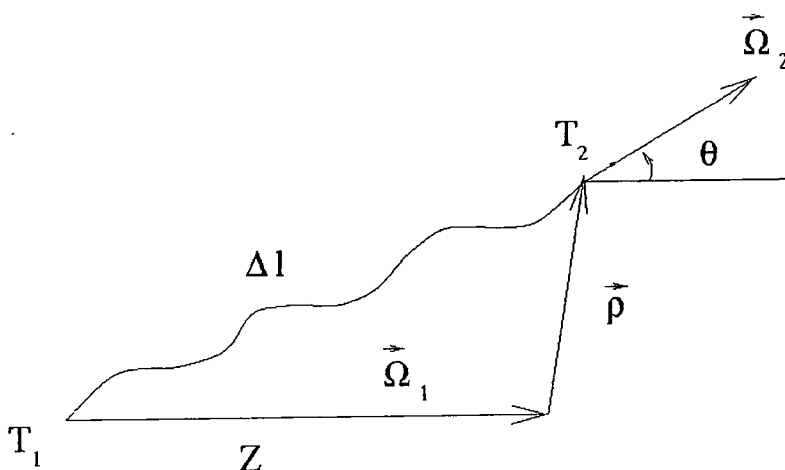


Figure 5.3: Multiple scattering diagram, taken from [116]. Figure shows the transform of phase co-ordinates at the multiple scattering segment.

However unlike ALTAI, CORSIKA (using routine EGS-IV) sets the lateral displacement of the particle at the end of the multiple scattering segment to zero, and therefore must set the longitudinal displacement to $Z = \Delta l$. This means that for correct simulation the step size used in CORSIKA is much smaller than that used in ALTAI, and as discussed before, this is of vital importance to simulation run-time. ALTAI uses step sizes around $1\text{-}5 \text{ g cm}^{-2}$ [116]. Figure 5.4 shows a histogram of the step size distribution for a TeV gamma-ray shower produced with CORSIKA and MOCCA. The histogram is normalised such that the same number of events is used for both MOCCA and CORSIKA, as given CORSIKA's smaller step size, many more calls are made to its multiple scattering routines. As can be seen, the mode step size for the two routines is $\sim 0.4 \text{ g/cm}^2$ for CORSIKA as compared to $\sim 2 \text{ g cm}^{-2}$ for MOCCA.

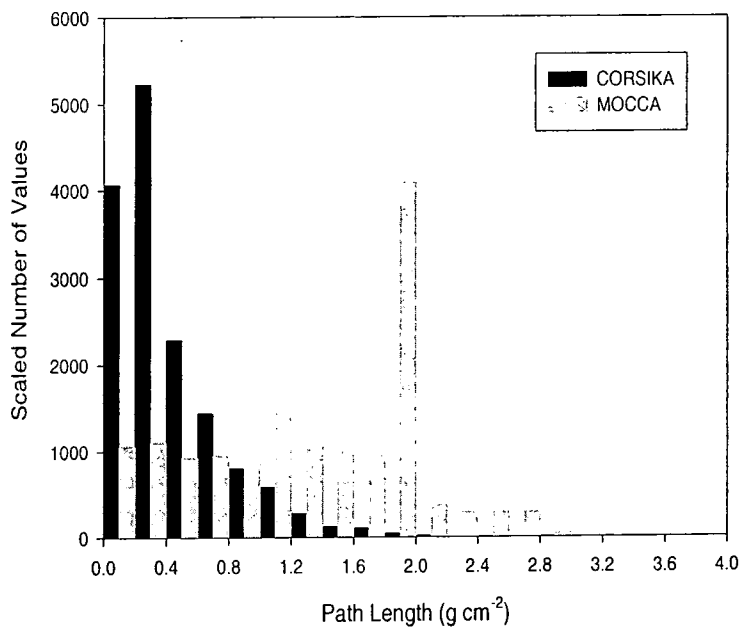


Figure 5.4: Scaled histogram showing size of multiple scattering segments for CORSIKA and MOCCA production of a 1TeV gamma-ray shower.

Conclusion - Differences in Multiple Scattering Treatment

As shown, the treatment of multiple Coulomb scattering in the three codes is slightly different. The result of this in terms of computing power requirements can be seen in figure 5.5. This figure shows the differences in run time when a database of 0.3 TeV gamma-ray showers is produced on the same machine using ALTAI, CORSIKA and MOCCA. The

differences that can be seen are due to the aforementioned differences in the application of multiple scattering, and the fact that the random number generator used in CORSIKA is a factor of three times slower those used in the other two codes. The step size used for multiple scattering in CORSIKA may however be easily changed by the user, which would greatly reduce the differences in run time between the three codes. Later in the chapter, the effects of these differences on the spatial and temporal profiles of the Cherenkov light will be covered. However, firstly the differences in hadronic EAS generation are addressed.

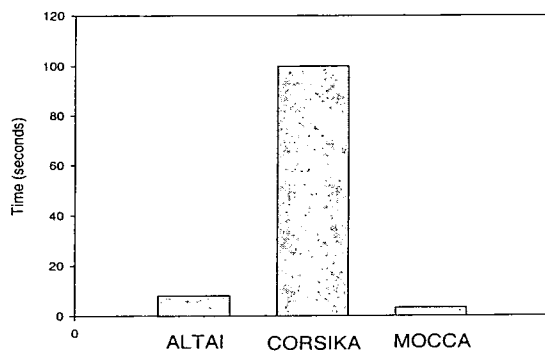


Figure 5.5: Average amount of time taken in seconds to generate a 0.3 TeV gamma-ray initiated shower with ALTAI, CORSIKA and MOCCA.

5.3.2 Hadron Initiated EAS

Given the more complex particle interactions involved, the different models used in hadronic EAS generation are liable to produce more significant differences in Cherenkov photon spatial and temporal profiles than in the case of gamma-ray initiated EAS. The general techniques used for simulations of EAS (given the primary energies are just beyond the capabilities of today's modern particle accelerators) will be discussed, by concentrating on three main topics; the treatment of transverse momenta, heavy nucleus fragmentation and energy deposition. In doing this, the differences in approximations made by the three codes are reviewed.

Yen/Radial Scaling

In 1974, Yen suggested that the invariant cross-section $E \frac{d^3\sigma}{d^3p}$ for the process $a+b \rightarrow C+X$ should approach a limiting function of x and p_t at high energies (E), namely

$$\lim_{s \rightarrow \infty} E \frac{d^3\sigma}{d^3p} \rightarrow \sigma f_{abc}(x, p_t) \quad (5.11)$$

for fixed x and p_t , where p_t are the transverse momenta and where:

$$x = \frac{E^*}{E_0^*} \sim \frac{2E^*}{\sqrt{s}} \quad (5.12)$$

Here E^* and E_0^* are the energy of C and the initial total energy in the centre of mass frame respectively. This is the Hypothesis of Limiting Fragmentation (HLF). Among others, Hillas in 1974 [84] fitted functional forms of f for various particle interactions at low energies and interpolated the transverse momenta distributions.

Application of Yen Scaling

Yen scaling is used to derive forms for the transverse momenta distributions of secondaries for various particle interactions, given measured cross-sections at lower energies.

To reiterate:

$$\lim_{s \rightarrow \infty} E \frac{d^3 \sigma(ab)}{dp_c^3} = \sigma_{ab} f_{abc}(x, p_t) \quad (5.13)$$

Fits to $f_{abc}(x, p_t)$ can be found experimentally [84]. If the HLF holds then fits to graphs of $E_c \frac{d^3 \sigma_{ab}}{dp_c^3}$ versus x at fixed p_t for relatively low energy $a + b \rightarrow c + X$ may be applied at higher energies. These measurements have been made for proton-proton primaries, with many possible permutations of c (neutral and charged pions, nucleons etc).

Hillas (1979) produces many results of the fits for $A(x)$, $B(x)$ and $C(x)$ for many particle species [84], where:

$$f(x, p_t) = A \exp -(B(x)p_t^C) \quad (5.14)$$

If Lorentz transforms are performed on the centre of mass energy spectrum to obtain spectra in the lab frame, the following modified scaling law may be used to fit the data:

$$x \frac{dN}{dx} = F_{abc}(x) H_c(E) \quad (5.15)$$

$H_c(E)$ is a correction factor which tends to 1 at high energies of the secondary particles (10's of GeV). $F_{abc}(x)$ is the function obtained by integrating $f(x, p_t)$ over p_t in the centre of mass frame at very high beam energies, i.e.:

$$F_{abc}(x) = \int f(x, p_t) 2\pi p_t dp_t \quad (5.16)$$

The basic functions for $F_{abc}(x)$ and $H_c(E)$ for various primaries and secondaries, used in ALTAI calculations and are given below:

$$F_{(p,n) \rightarrow \pi^\pm} = F_{(p,n) \rightarrow \pi^0} = 1.22(1 - x)^{3.5} + 0.98e^{-18x} \quad (5.17)$$

$$F_{\pi^\pm \rightarrow \pi^0} = 1.3 \left(1 + \frac{x}{0.45}\right)^{-3} \quad (5.18)$$

$$F_{\pi^\pm \rightarrow \pi^\pm} = F_{\pi^\pm \rightarrow \pi^0} + 0.57e^{4(x-1)} \quad (5.19)$$

$$H_{(p,n) \rightarrow (\pi^\pm, \pi^0)} = \left[1 + \frac{0.4}{E + 0.14}\right]^{-1} \quad (5.20)$$

$$H_{\pi^\pm \rightarrow (\pi^\pm, \pi^0)} = 1 - 0.88e^{-1.8x} \quad (5.21)$$

MOCCA uses slightly different forms for these equations as it makes simplifying assumptions concerning Lorentz transformations.

The functions F and f give the number of particles emerging per inelastic collision. In order to obtain the actual cross-sections, one requires the overall inelastic cross-section as a function of energy, which must be derived from accelerator experiments at much lower energies as discussed in [84] for instance. For comparison, figure 5.6 shows the mean free path (in $g \text{ cm}^{-2}$) used for proton-air interactions within MOCCA and ALTAI versus primary energy (in GeV). As can be seen, the mean free path for cosmic rays in ALTAI is greater than in MOCCA, which suggests that there will be slightly more Cherenkov light associated with cosmic ray EAS generated with ALTAI as compared to MOCCA, as the EAS produced in ALTAI will develop further down in the atmosphere and therefore have more efficient Cherenkov light production and less atmospheric light attenuation.

ALTAI and MOCCA make use of the radial scaling with energy, however CORSIKA (using the VENUS algorithm at least) works slightly differently. The phenomenological model used in ALTAI and MOCCA differs from that used in VENUS, which extends up to energies of 2×10^4 TeV, whilst ALTAI and MOCCA are only applicable up to around 50 TeV for hadrons. Below a few hundred GeV, CORSIKA replaces VENUS with GHEISHA, a package whose cross-section and interaction models are heavily interpolated and extrapolated from available accelerator data. The presently implemented version of VENUS uses Gribov-Regge theory and its exchange of pomerons as the basis for hadron-hadron interactions (a pomeron is considered to be a cylinder of gluons and quark loops) [72]. Particle production refers to cutting pomerons, i.e. producing colourless hadrons

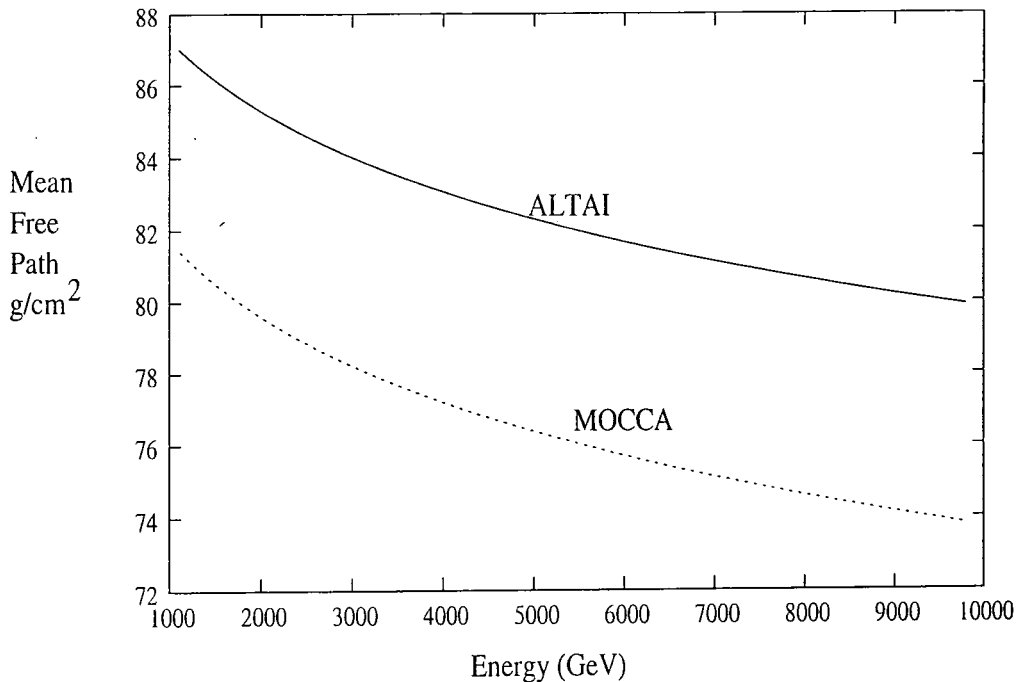


Figure 5.6: Plot of mean free path of primary cosmic ray proton in air in g cm^{-2} versus energy (in GeV) for MOCCA and ALTAI.

by fragmenting the gluon-quark loops. In CORSIKA, hadronic interactions are therefore treated in a more complex fashion than in either ALTAI or MOCCA; however when the increased run-time of CORSIKA is considered, ALTAI and MOCCA are found to be preferable given current computational power. Next another important part of the hadronic interaction is covered, namely the treatment of the fragmentation of cosmic ray nuclei.

Heavy Nucleus Fragmentation

The fragmentation of a highly relativistic cosmic ray nucleus upon interaction with an air molecule is another important source of complications of the physical process of hadronic EAS formation. In ALTAI, all the nucleons of the projectile nucleus have the same energy (determined by E_0/A , where E_0 is the energy of the projectile nucleus and A is the atomic number of the projectile nucleus). Each cosmic ray nucleus is modelled as having an even mass number (as in MOCCA), defined as twice the charge of the particle. For large cosmic ray nuclei, all nucleons of the cosmic ray nucleus that overlap with the target interact independently of each other. The non-overlapping part of the nucleus decays into individual nucleons and heavier fragments. The energies of the fragments (with

atomic number A^*) are $E_f = (A^*E_o)/A$. The fragmentation treatment in ALTAI follows the probability of the channels derived from table 5.1.

	Z>10	C,N,O,F	Li,Be,B	He
Primaries				
Z>10	0.17	0.29	0.26	1.34
C,N,O,F	-	0.11	0.24	1.00
Li,Be,B	-	-	0.15	0.51

Table 5.1: Mean number of fragments created by different nuclei, taken from [116] and originally [144].

In MOCCA the number of freed protons/neutrons is always even, and thus, given that all nuclei are modelled as an equal combination of neutrons and protons, the larger fragments all have even numbers of nucleons. The precise number of freed protons/neutrons depends on the initial nuclei and obeys different functions for mass numbers in the range <15 , >15 and >23 (the limits are slightly different to those in table 5.1). For the nuclei remaining after collision (i.e. after considering the loss of protons and neutrons) of mass number >15 , one alpha particle will be produced in MOCCA and for mass numbers >23 two alpha particles are produced. In addition, all nuclei of mass number = 8 are broken up into two alpha particles, simulating the behaviour of the unstable Beryllium-8 isotope. The kinetic energy of the initiating particle is divided equally between all of the nucleons in the resultant nuclei, whether they are individual protons/neutrons, within alpha particles or larger nuclear fragments.

CORSIKA has two run options, either complete nuclear fragmentation occurs or alternatively all non-interacting nucleons remain together; in both cases the produced particles go on to further interactions. Simulations presented herein are run with complete nuclear fragmentation.

Energy Deposition

The splitting of the energy of the primary into the fragments and particles produced is of course key to the amount of Cherenkov light they will produce. The basic energy splitting algorithm (HSA) used in early versions of MOCCA [84], is:

- (i) Split the total energy available into two parts, A and B.

- (ii) Assign energy A to the leading nucleon.
- (iii) Further subdivide energy B randomly into J=4 parts.
- (iv) Subdivide each J=4 energy fragments randomly into two parts A' and B' .
- (v) Assign A' as the energy of a pion.
- (vi) Subdivide B' and assign one energy fragment as the energy of another pion.
- (vii) Continue in this fashion until the energy remaining is less than some predefined threshold value (the energy threshold will depend on the problem at hand, but must at least be as large as the rest mass energy of a pion, m_π).

This model has been refined so that the energy of the leading nucleon is picked according to the best available fit to proton-nucleus interaction data, as described in [85], and results in the elasticity of the nucleon-nucleon collision being reduced to $\sim 41\%$ from $\sim 50\%$. The energy assignment for fragments is then derived by randomly splitting the total energy available into J fragments, and selecting the number of energy fragments that will become pions using the following expression: $\text{INT}(3 + (4.35 * R_a))$ where R_a is a random number in the range 0 to 1. This ensures that at least three pions are produced per interaction. On average, 58.75% of the initiating particle's available energy will be converted into pions. An analytical form of the energy distribution of the pions resulting from the original splitting algorithm (seen in [84]), derives from:

$$F_{N-\pi} = x_\pi \frac{dn_\pi}{dx_\pi} = x_\pi 2^N \left[\frac{1}{x_\pi} - \sum_{n=1}^N \frac{(\ln \frac{1}{x})^n}{n!} \right] \quad (5.22)$$

where 2^N pieces of energy are available to be split into pions, x represents the fraction of energy available after n splittings, and x_π is the momentum fraction of the produced pion. A review of this function may be found in [64].

A different scheme is used within ALTAI. For each inelastic hadron interaction the energy of the leading particle (be it p , n or π^\pm) is sampled, these energies being uniformly distributed within the region $(0, E_0)$ where E_0 is the energy of the primary interacting particle. The total inelasticity is defined as:

$$\kappa = 1 - E/E_0 \quad (5.23)$$

The type of secondary particle is randomised assuming that π^0 forms on average, for one third of all pions generated in hadronic interactions. The energy spectrum is derived

from Yen scaling as discussed earlier. The fragmentation stops when the total energy of all fragments exceeds the energy of the primary, the energy of the last simulated particle renormalized to conserve the total energy in each inelastic interaction.

A recent paper on very and ultra high energy hadronic interactions, sheds light on the differences between the approach taken in ALTAI and MOCCA to that taken in CORSIKA [114]. As mentioned previously the models used in CORSIKA are based around pomeron exchange, and in some senses maybe thought of as more theoretically realistic. However, in the 50 GeV-1TeV energy range (which includes the threshold energies of the Mark 6 and H.E.S.S. stand-alone telescopes), the difference between these more complicated models and the MOCCA/ALTAI approach is quite small. In later chapters, where the effects of atmosphere on the triggers of the H.E.S.S. telescope at energies below 100GeV are discussed, the differences in all hadronic models are also small, given that at these energies, ALTAI, MOCCA and GHEISHA are all based around measured data.

The production of Cherenkov light and its deposition on the mirrors of a telescope system is now discussed.

5.3.3 Cherenkov Light Deposition

ALTAI

The production of Cherenkov light was discussed in detail in Chapter 2; here the treatment of light produced by air showers from production to landing on a telescope mirror is discussed. At this stage the photons undergo no atmospheric attenuation; this is applied in the telescope simulation part of the code, which shall be discussed in chapters 6 and 7. In ALTAI the multiple scattering segments Δl are small, so Cherenkov emission is assumed to come just from the middle of the segment. As will be recalled from Chapter 2, the Cherenkov angle is small $\lesssim 1^\circ$, thus a schematic for the Cherenkov light deposition from a segment Δl is shown in figure 5.7.

To good approximation, the intersection of the Cherenkov light cone with the plane perpendicular to the shower axis forms a circle of radius r_o , which is calculated as:

$$r_o = (Z - Z_{\text{obs}})\theta_c \quad (5.24)$$

Where Z and Z_c are the height of emission and observation respectively, and θ_c is the Cherenkov angle. With reference to figure 5.7, the number of photons hitting the telescope mirror ($\langle \tilde{n}_{ph} \rangle$) is given by:

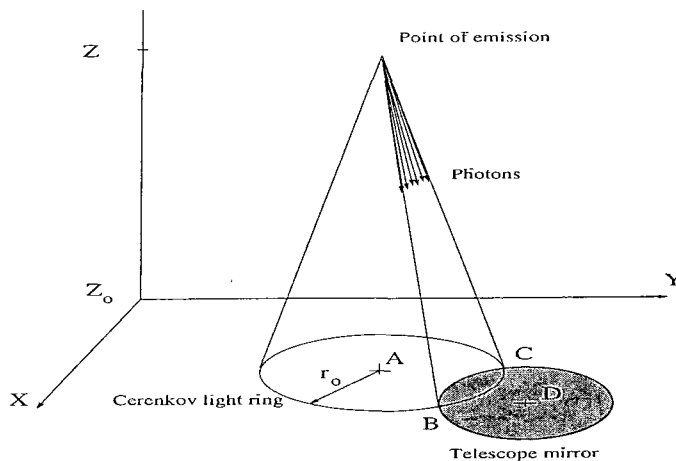


Figure 5.7: Diagram illustrating Cherenkov light deposition as treated with ALTAI [116]. Coordinates are Cartesian, with Z along shower axis, and X and Y perpendicular to it.

$$\langle \tilde{n}_{ph} \rangle = \frac{\Delta L}{2\pi r_c} (1 - p(Z, Z_{obs})) \langle n_{ph} \rangle \quad (5.25)$$

Where $\langle n_{ph} \rangle$ is the number of photons emitted, and ΔL is the length of the circle arc between points B and C. $p(Z, Z_{obs})$ is the probability of atmospheric attenuation, discussed in greater detail in the next two chapters. Finally, one uses the Poissonian distribution function in order to simulate the random number of photons hitting a telescope, which are distributed smoothly over the circle arc BC. In all three codes for each shower several randomly positioned telescopes are placed with a radius R of the core, to recreate the fact that the core location is random. Also for all three codes; for each photon a set of 7 parameters are kept, namely: x, y the position of the photon with respect to the centre of the mirror, θ_x, θ_y the x and y incidence angles of the photon on the mirror, Z_0 the height (in $g\text{ cm}^{-2}$) of photon emission, t , the time of arrival at the detector and 'id' the particular telescope (given several are simulated at once) that the photon was incident upon.

CORSIKA

CORSIKA operates in a slightly different manner to ALTAI and MOCCA with respect to Cherenkov light deposition. The routines to allow CORSIKA to be used with imaging atmospheric Cherenkov telescopes have been adapted by K. Bernlöhner [19]. Here the detector configuration is surrounded by a sphere (see figure 5.8). Only photons that intersect the sphere are considered, and then ray tracing is performed from the sphere

surface to the surface of the mirrors on this subset of photons.

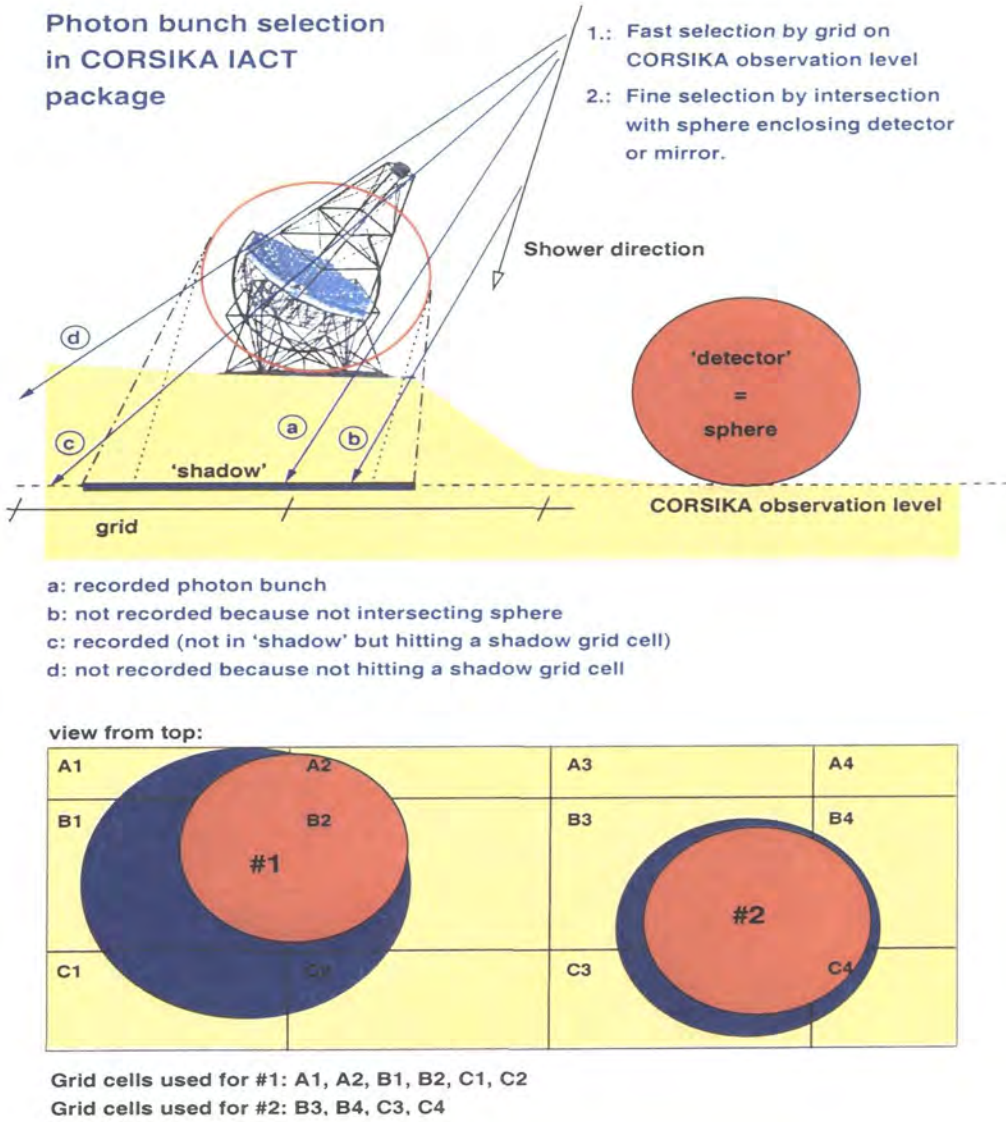


Figure 5.8: Scheme of selection of photon bunches for output in the CORSIKA IACT package.

MOCCA

MOCCA works in a similar fashion to ALTAI with respect to Cherenkov light deposition. The Cherenkov photon output of the codes is now compared.

5.4 Simulation Comparisons

5.4.1 Mono-energetic Simulations

In order to study the effect of the outlined differences, a series of 10,000 simulations for mono-energetic primaries (protons and gamma-rays) at 0.1 TeV (0.3 TeV in the case of the proton primary, given the smaller Cherenkov flux produced by a 0.1 TeV hadronic primary) and 1 TeV have been performed, and studies of the Cherenkov light deposited on a 42m^2 (Mark 6) mirror placed at 80,120,160,200 and 240 metres from the core location using ALTAI, CORSIKA and MOCCA have been made. The mirror was placed at 1800m altitude, and the simulations were subject to a US standard atmospheric profile, with corresponding atmospheric light attenuation (the effects of this attenuation will be discussed in detail in chapter 7).

0.1 TeV Gamma-Ray

As can be seen in figure 5.9 the differences in the 3 codes are greatest outside the Cherenkov ring (at 120m from core), while within and on the ring the differences are $< 10\%$.

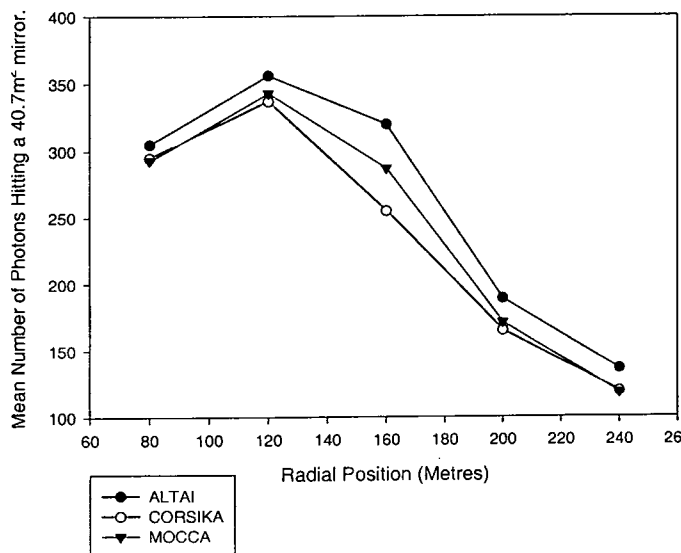


Figure 5.9: Plot of mean number of photons hitting a central Mark 6 mirror, with atmospheric absorption, for a US Std atmospheric profile at an altitude of 1800 metres for a 0.1TeV photon primary for ALTAI, CORSIKA and MOCCA at fixed radial distances.

Proton Primary

As can be seen in comparing figures 5.9 and 5.10, as expected (given the complexity of hadronic interaction models) the differences in proton based showers are much larger than for gamma-ray showers, with ALTAI giving at most 150% of the CORSIKA photon flux. As expected from earlier discussions, ALTAI and MOCCA are very similar in their hadronic modelling and Cherenkov photon deposition, and thus have a very similar Cherenkov photon flux.

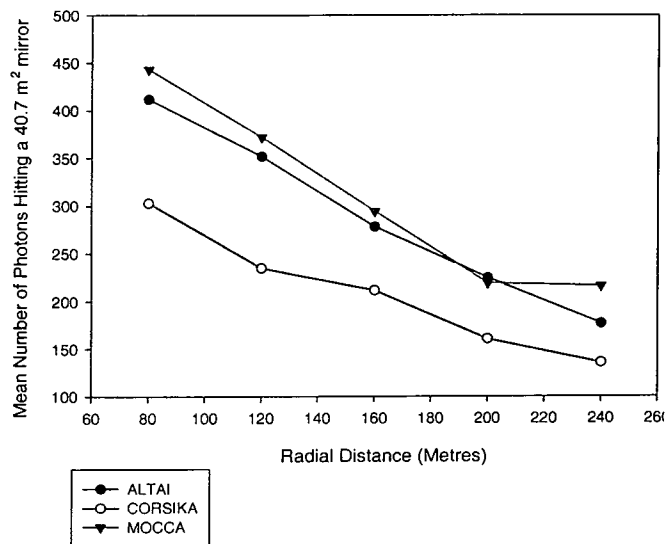


Figure 5.10: Plot of mean number of photons hitting a central Mark 6 mirror, with atmospheric absorption, for a US Std atmospheric profile at an altitude of 1800 metres for a 0.3 TeV proton primary for ALTAI, CORSIKA and MOCCA at fixed radial distances.

1 TeV Gamma-Ray

Again, in this case (figure 5.11) the differences between the 2 codes are quite small, and at the ring are much less than 7%. Again, for gamma-ray primaries, ALTAI gives a somewhat larger photon flux throughout, whilst MOCCA and CORSIKA are very similar.

1 TeV Proton Primary

The differences in the hadronic models are clearly evident in figure 5.12. ALTAI and MOCCA are closely linked, however CORSIKA appears to have almost half as much light as ALTAI within 100m of the core.

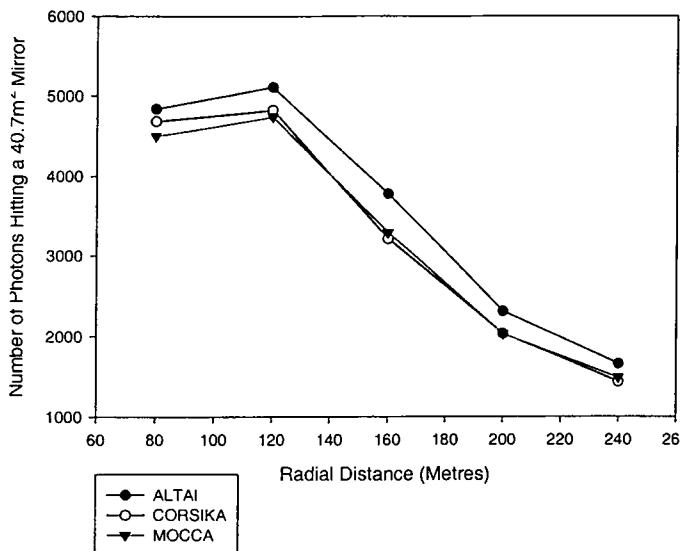


Figure 5.11: Plot of mean number of photons hitting a central Mark 6 mirror, with atmospheric absorption, for a US Std atmospheric profile at an altitude of 1800 metres for a 1TeV photon primary for ALTAI, CORSIKA and MOCCA at fixed radial distances.

5.4.2 Conclusion of Spatial Cherenkov Deposition Study

As can be seen from figures 5.9-5.12, MOCCA is generally intermediate in photon number to the other two codes. CORSIKA is clearly seen to produce much smaller amounts of light for hadronic primaries than the other two codes. Given that MOCCA has a runtime which is $> 30\times$ faster than CORSIKA, and $> 3\times$ faster than ALTAI, and is generally intermediate in photon flux, MOCCA is used throughout our spectral studies of sources for both the Mark 6 and H.E.S.S. stand-alone telescopes. However, as the temporal profile of the light is the other important factor in the triggering of a Cherenkov telescope, the temporal spread of the light produced with the three codes has also been studied, for the primaries given above. Our work shows no great difference in the normalised temporal profile of the Cherenkov light produced for either gamma-ray or hadron showers for any of the three codes. The results in figures 5.13 and 5.14 are wholly representative of this (in each case one should focus on the overall shape of the temporal distribution and not the exact photon numbers at each moment).

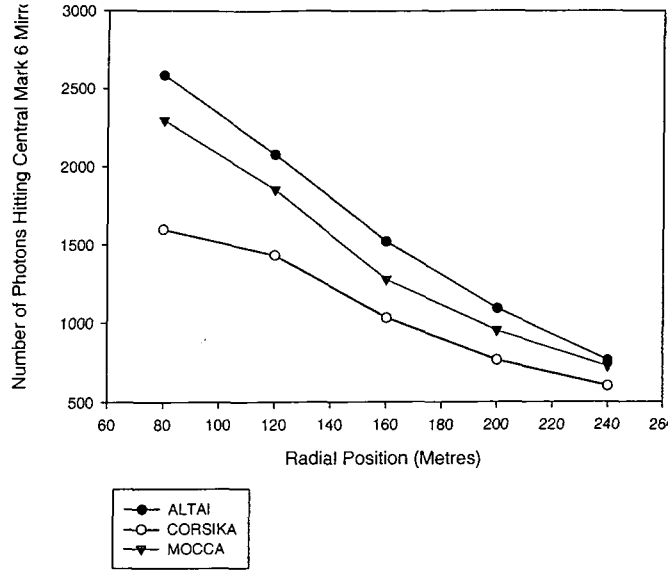


Figure 5.12: Plot of mean number of photons hitting a central Mark 6 mirror, with atmospheric absorption, for a US Std atmospheric profile at an altitude of 1800 metres for a 1TeV proton primary for ALTAI, CORSIKA and MOCCA at fixed radial distances.

5.5 Higher Order Differences

Results of the simulation of spectra of cosmic rays and gamma-ray EAS with ALTAI, CORSIKA and MOCCA are now presented, and the differences in the Hillas parameter distributions seen with the Mark 6 telescope (discussed earlier in Chapter 3, and in greater detail in the next Chapter), when viewing showers at 30° zenith angle are highlighted.

5.5.1 Gamma-Rays

A spectrum of 50,000 gamma-ray showers with energies ranging from 0.1 to 30 TeV and a differential spectral slope of -2.45 was simulated for the three codes. Each shower was sampled by 5 Mark 6 telescopes, positioned randomly within 300 m radially of the core. The simulations were then fed through the Mark 6 simulation package (as discussed in great detail in the next chapter), and the results of the three codes are compared below. It should be noted that although the length and width distributions of the images would be of greatest interest, the point spread function of the Mark 6 mirrors is significant, and therefore any true variation in width and length may not be apparent. Also, in this comparison the run parameters for the Mark 6 are set slightly differently for each code, so that all satisfy as closely as possible the triggering rate for cosmic rays during the Mark 6 studies of the AGN PKS 2155-304 (this will be discussed in the next chapter). The result

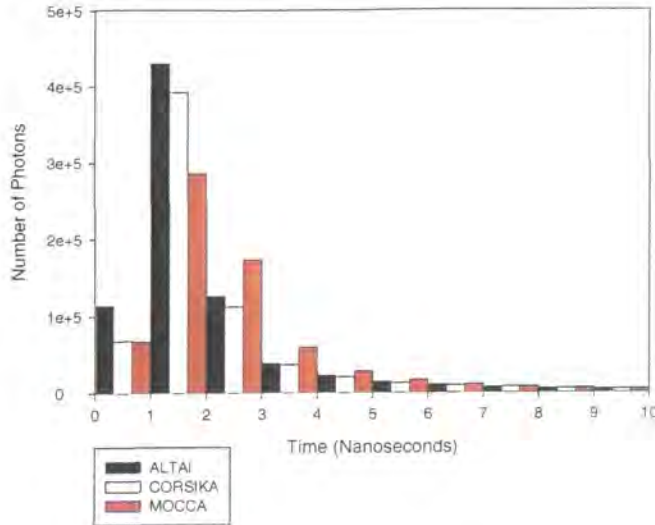


Figure 5.13: Number of photons incident on central Mark 6 mirror placed at a radial distance of 80 metres from core location versus relative arrival time with ALTAI, CORSIKA and MOCCA for 1 TeV gamma-ray primaries.

of this again, is that any inherent differences within the codes will be minimised.

Figure 5.15 and 5.16 show the results for comparisons between MOCCA and ALTAI, and between MOCCA and CORSIKA respectively.

5.5.2 Cosmic Rays

A spectrum of cosmic rays was produced with each of the three codes for the Mohanty cosmic ray spectrum [141], as discussed in great detail in the next chapter. For the moment, however, the importance is placed on the relative differences between the three codes for the simulation of a given spectrum of cosmic rays. Each shower was again sampled by 5 randomly placed Mark 6 telescopes, sited within 300 m of the core. To simulate correctly the isotropy of cosmic rays, the light was also shifted around randomly 4 times within the camera's field of view. Figures 5.17 and 5.18 show the results of comparisons between MOCCA and ALTAI, and between MOCCA and CORSIKA respectively. One important point to note for CORSIKA, is that given the significantly smaller Cherenkov flux for hadronic showers compared to ALTAI and MOCCA, the telescope discrimination level (as discussed in the next chapter) had to be lowered significantly to match the real off source data, as compared to the other two codes. When comparing CORSIKA with real data this led to an extremely poor fit to the width, camsum and Ntubes distributions.



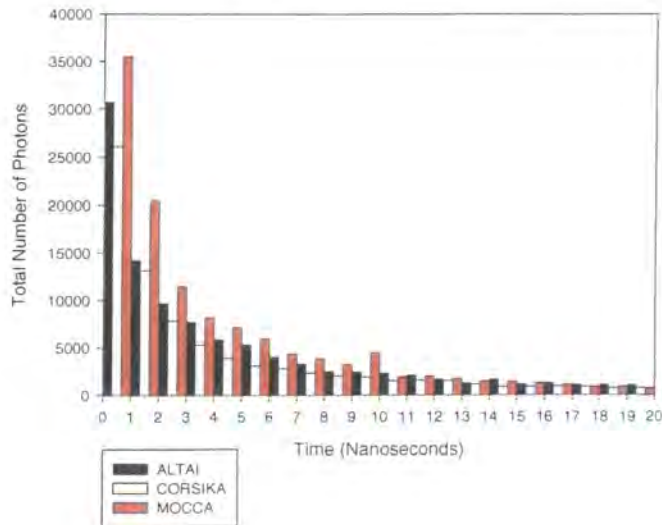


Figure 5.14: Number of photons incident on central Mark 6 mirror placed at a radial distance of 80 metres from core location versus relative arrival time with ALTAI, CORSIKA and MOCCA for 1TeV proton primaries.

5.5.3 Results

In table 5.2 below, the mean values for the width and length for the gamma-ray and cosmic ray Hillas parameter distributions produced with ALTAI, CORSIKA and MOCCA are listed. As one will recall from figures 5.9- 5.12, MOCCA was generally intermediate in Cherenkov light density to the other two codes, and this is carried forward into this Hillas parameter study, where again MOCCA is intermediate in both length and width for cosmic and gamma- rays.

5.6 Conclusion

In this chapter the differences in particle models used within the three codes (ALTAI, CORSIKA and MOCCA) have been covered, with particular reference to the physics at work in the development of an EAS. Details of mono-energetic comparisons of simulations of Cherenkov flux for gamma-ray and hadronic primaries have been given, and studies of the Hillas parameter distributions produced for spectra of gamma-rays and cosmic rays using ALTAI, CORSIKA and MOCCA and a simulation of the Durham Mark 6 telescope have been presented. The results of all this work show that MOCCA is generally intermediate in photon flux and Hillas parameters to the other two codes, and given its

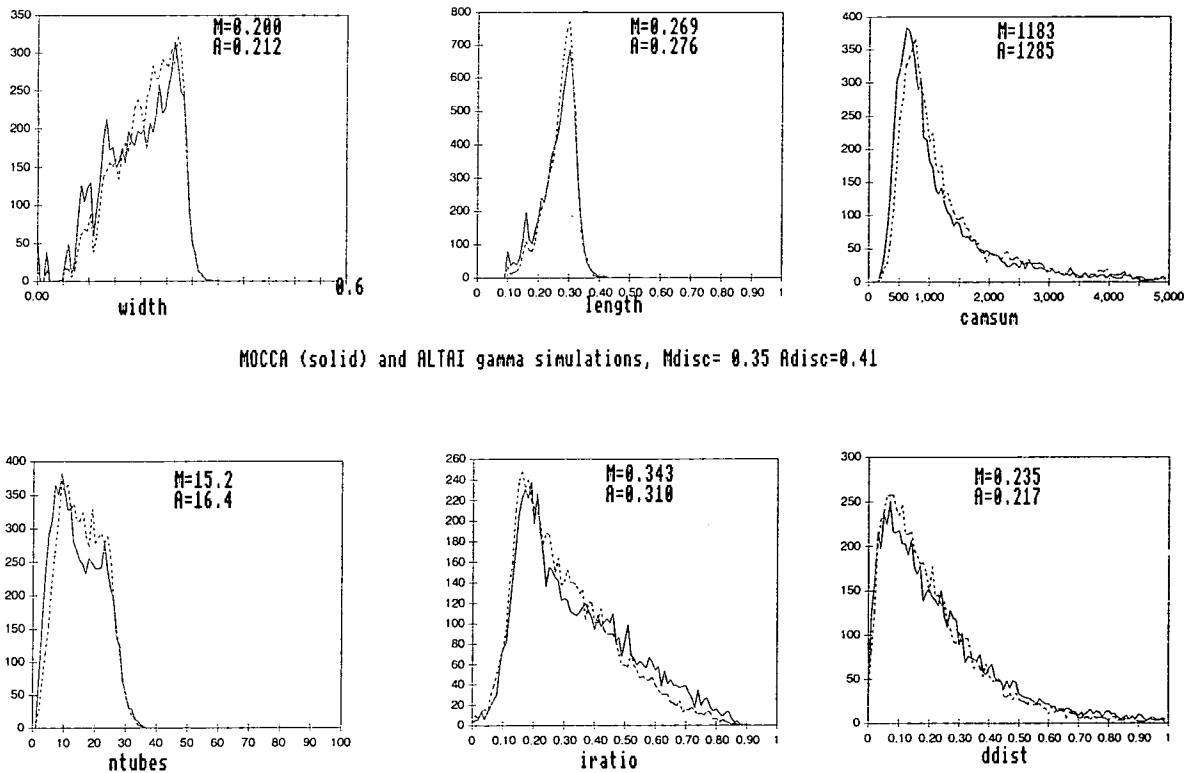
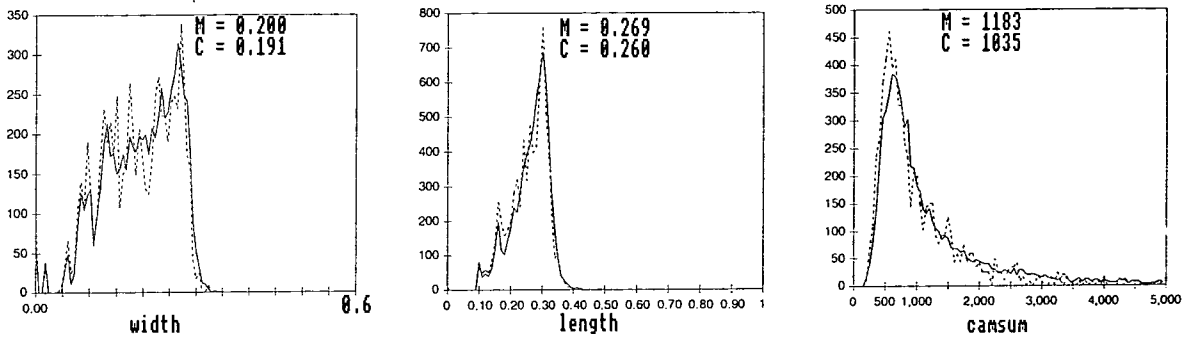


Figure 5.15: Comparisons of distributions of width, length, camsum (SIZE), Ntubes, Iratio and ddist for gamma-ray spectral simulations with MOCCA and ALTAI using the Durham Mark 6 telescope. The means of the distributions for each code are shown within each subplot. Each curve is normalised to the same number of events, although each code required a slightly different discriminator to match the off source trigger rate of $8.38 \text{ events sec}^{-1}$.

appreciably quicker run-time MOCCA will be used for all future simulations. It should be noted that as large databases of events are required (due to shower to shower fluctuations), program computing power requirements are currently an important issue for simulations of Cherenkov telescopes.

In the next chapter the general simulation of the Durham Mark 6 and H.E.S.S. stand-alone telescopes is discussed, and the response of these telescopes to simulated cosmic ray and gamma-ray spectra produced with MOCCA is shown. In particular, the calculations of the flux of the AGN PKS 2155-304 with the Mark 6 telescope are covered.



MOCCA (solid) and CORSIKA (CERSIZ=1) Gamma simulations, M-Disc=0.35, C-Disc=0.25

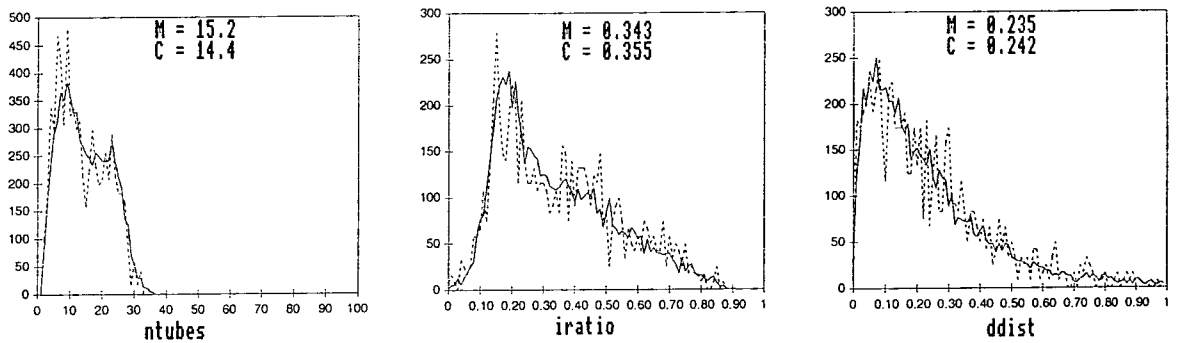


Figure 5.16: Comparisons of distributions of width, length, camsum (SIZE), Ntubes, Iratio and ddist for gamma-ray spectral simulations with MOCCA and CORSIKA using the Durham Mark 6 telescope. The means of the distributions for each code are shown within each subplot. Each curve is normalised to the same number of events, although each code required a slightly different discriminator to match the off source trigger rate of $8.38 \text{ events sec}^{-1}$.

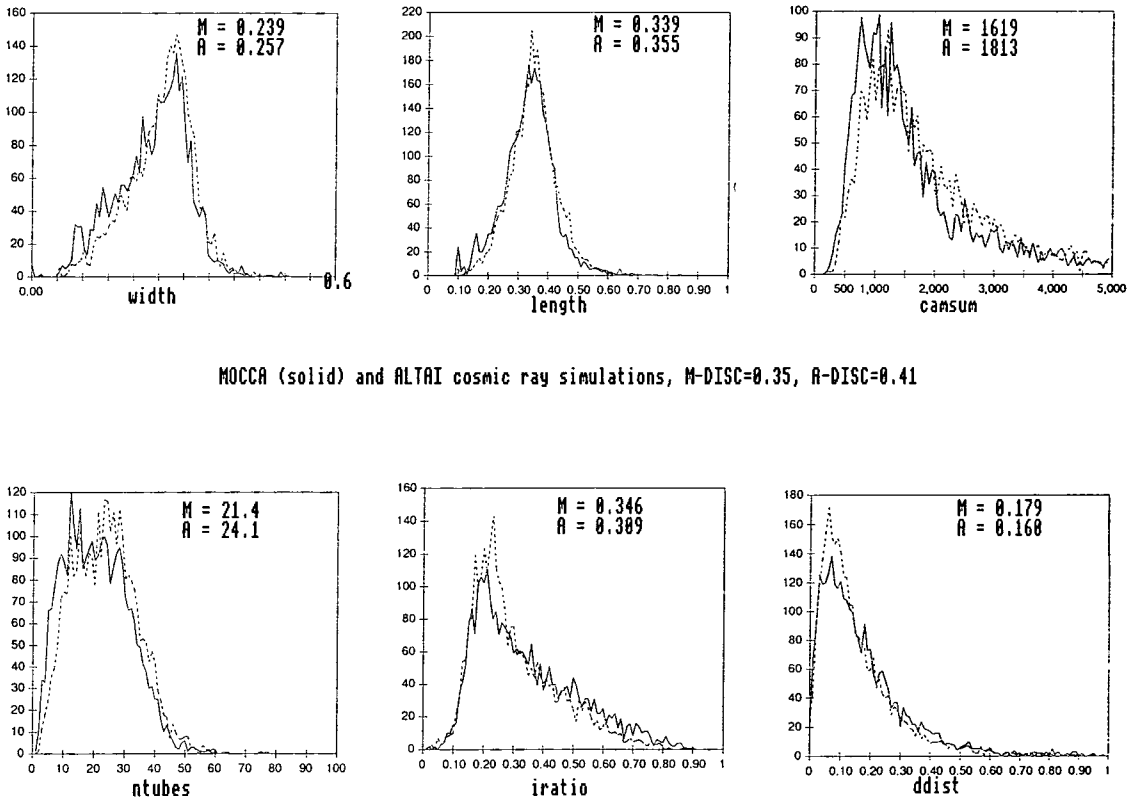


Figure 5.17: Comparisons of distributions of width, length, camsum (SIZE), Ntubes, Iratio and ddist for cosmic ray spectral simulations with MOCCA and ALTAI using the Durham Mark 6 telescope. The means of the distributions for each code are shown within each subplot. Each curve is normalised to the same number of events, although each code required a slightly different discriminator to match the off source trigger rate of $8.38 \text{ events sec}^{-1}$.

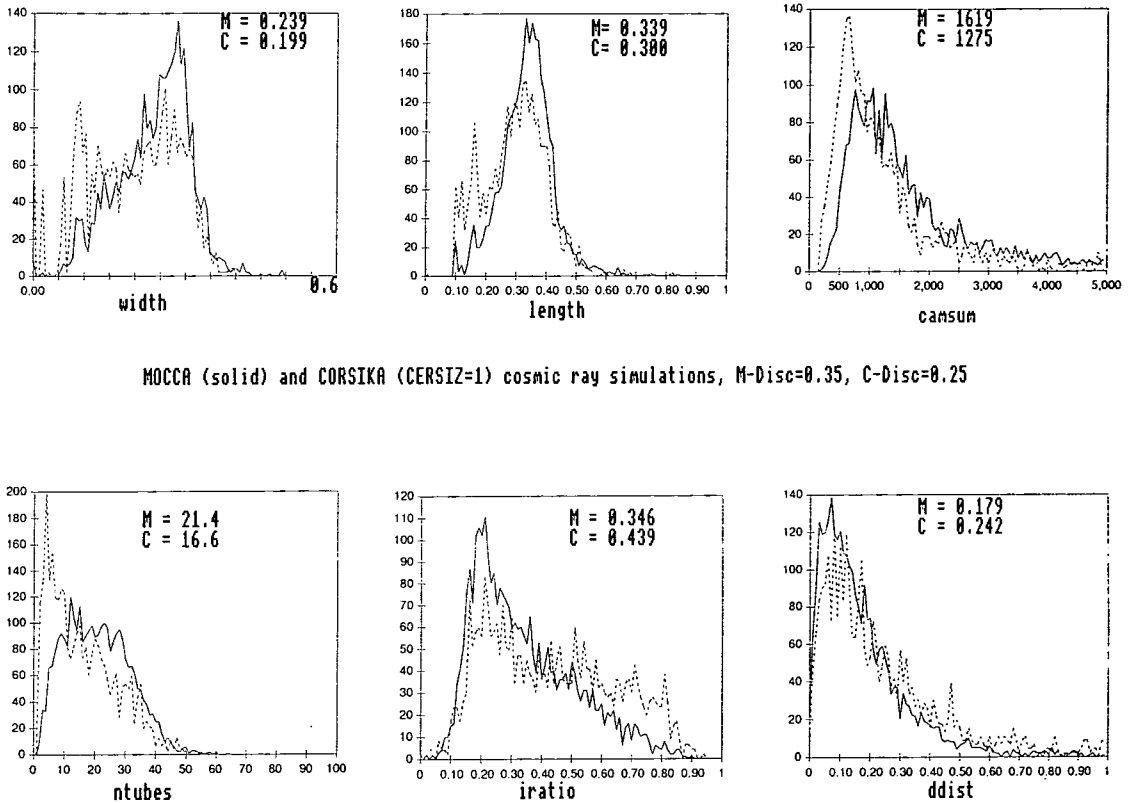


Figure 5.18: Comparisons of distributions of width, length, camsum(SIZE), Ntubes, Iratio and ddist for cosmic ray spectral simulations with MOCCA and CORSIKA using the Durham Mark 6 telescope. The means of the distributions for each code are shown within each subplot. Each curve is normalised to the same number of events, although each code required a slightly different discriminator to match the off source trigger rate of $8.38 \text{ events sec}^{-1}$.

Code	Spectrum Type	Mean Length	Mean Width
ALTAI	Gamma-Ray	0.276	0.212
CORSIKA	Gamma-Ray	0.260	0.191
MOCCA	Gamma-Ray	0.269	0.200
ALTAI	Cosmic Ray	0.355	0.257
CORSIKA	Cosmic Ray	0.300	0.199
MOCCA	Cosmic Ray	0.339	0.239

Table 5.2: Comparisons of mean values of width and length for cosmic ray and gamma-ray spectra produced by ALTAI, CORSIKA and MOCCA, and passed through a simulation of the Durham Mark 6 telescope, with discrimination levels set to match real off source data trigger rates in each case.

Chapter 6

Simulations of Imaging

Atmospheric Cherenkov Telescope

Response

6.1 Introduction

The last chapter dealt with the production of Cherenkov light by EAS, and its arrival on the mirrors of a Cherenkov telescope system. By contrast, this chapter will deal with the next step in the journey for that light and will therefore discuss how simulations of imaging atmospheric Cherenkov telescope systems are performed. The chapter begins with a simplistic outline of the simulation of two such systems, the Durham Mark 6 and the first stand-alone H.E.S.S. telescope. Following this, the practical use of the simulations is covered with particular reference to the derivation of the flux from the AGN source PKS 2155-304, using the Durham Mark 6 telescope. The chapter concludes with a brief study of the simulated responses for the first stand-alone H.E.S.S. telescope. In the next chapter, the responses of this system under different assumptions about atmospheric structure will be detailed.

6.2 Simulations of the Telescope System

6.2.1 Photon Attenuation

It has been found that applying the atmospheric attenuation model within the telescope simulation code is a more satisfactory way to work, given that one has only to simulate one set of showers, and then apply a number of different atmospheric attenuation

models as required. Therefore, the attenuation due to atmosphere, quantum efficiency and mirror reflectivity are all applied within this code. The photons are read from the simulated shower file and given the form of the Cherenkov spectrum ($\propto \lambda^{-2}$), they are assigned wavelengths accordingly. Given a wavelength and their altitude of emission, the atmospheric attenuation is calculated. This is then multiplied by the necessary quantum efficiency and mirror reflectivity, followed by other attenuating factors, including:

- In the Davies Cotton design of H.E.S.S., 380 spherical mirrors of diameter 60cm and focal length 15 m are placed on a spherical mount whose radius of curvature is 15m. The overall area of the mirror mount is $\pi \times 7^2 \text{ m}^2$, however the total geometric mirror area is only 106.08 m^2 , so an attenuating factor of the ratio of these two numbers is applied. This is not required for the single parabolic dishes of the Mark 6 telescope.
- An estimated 10 – 12% reduction due to the shadow cast by the camera mast [18].

Once the overall attenuation factor for a photon is calculated, it is compared with a random number in the range 0 to 1. If the number is less than this factor, the photon (now technically a photoelectron) is written into the next stage of simulation. In this way, the attenuation effects are applied via the Monte-Carlo method, and therefore, given the large number of photons incident upon the system, the simulations should realistically approximate the real world situation. No ray tracing is performed. Given the angle of incidence of the photon with respect to the plane of the mirror system, the position on the camera is calculated taking the mirror to be an ideal imager of appropriate focal length. A smearing of the light by a sampling for each photon of the the measured point spread function of the mirrors is then applied. After this point, the position of the photon on the camera is converted into a PMT number, so that each photoelectron surviving attenuation is associated with one PMT.

6.2.2 Triggering

Given that the stand-alone H.E.S.S. telescope and the Mark 6 telescope are very different physically, the triggering methods are quite different and are now discussed separately.

Mark 6

As discussed in Chapter 3, the Mark 6 telescope consisted of 3 flux collecting mirrors with a camera at each focus. The central camera consisted of 91 central (1 inch diameter)

PMT's with a tube separation of 0.25° , surrounded by an outer ring of 18 (2 inch diameter) PMT's. A typical event is shown in figure 6.1.

The trigger condition of the Mark 6 required that if a signal was recorded in 2 neighbouring PMT's in the central camera, and 1 PMT within both the left and right cameras that were all viewing a similar part of the sky, within 10ns of each other, then a signal was recorded [9].

For the simulation, the time of arrival of the first photon is subtracted from the arrival time of each photon, so that the times are counted from the arrival time of the first photon. The pulse profile for the response of the PMT to a single photoelectron, liberated from the photocathode is read from file. This pulse profile, along with the triggering criteria, are key to the operation of the simulation, and thus the single photoelectron pulse for the Mark 6 is given in figure 6.2, and may be compared with a similar figure for the H.E.S.S. telescope (figure 6.3).

For a PMT to record a signal in the telescope a discriminator level is set by matching the trigger rate of real off source cosmic ray data to a simulated cosmic ray spectrum, and a time gate of 40 nanoseconds is set. If the sum of single photoelectron pulses passes the discriminator level within the time gate, then the data are recorded. In addition to the single photoelectron pulses (SPP's) resulting from Cherenkov photons, there is a probability that NSB photons will create noise, in the form of additional SPP's arriving at random intervals. If the discriminator level is reached, or exceeded, in tubes corresponding to those looking at the same patch of sky in all 3 cameras within 10 nanoseconds, then the telescope system triggers. The responses of each of the PMT's to all the non-attenuated photons arriving at them will be summed. These PMT responses will be in units of photoelectrons. They are then subject to a conversion factor (due to the fast charge digitisers used) from photoelectrons to digital counts, which is measured for the Mark 6 telescope to be approximately 4.5 digital counts per photoelectron (see p 116). At this point the images may be directly compared with real data, and conclusions may be drawn.

H.E.S.S.

Simulations of the first stand-alone H.E.S.S. telescope follow a similar pattern to those used for the Mark 6, though with slightly differences. The package used is that due to A. Konopelko, namely CameraHESS [118]. A random scaled time delay is added to the arrival time of each photon, given that the Davies- Cotton geometry of the mirrors introduces a delay in arrival time. Again the photons are allocated to individual PMT's,

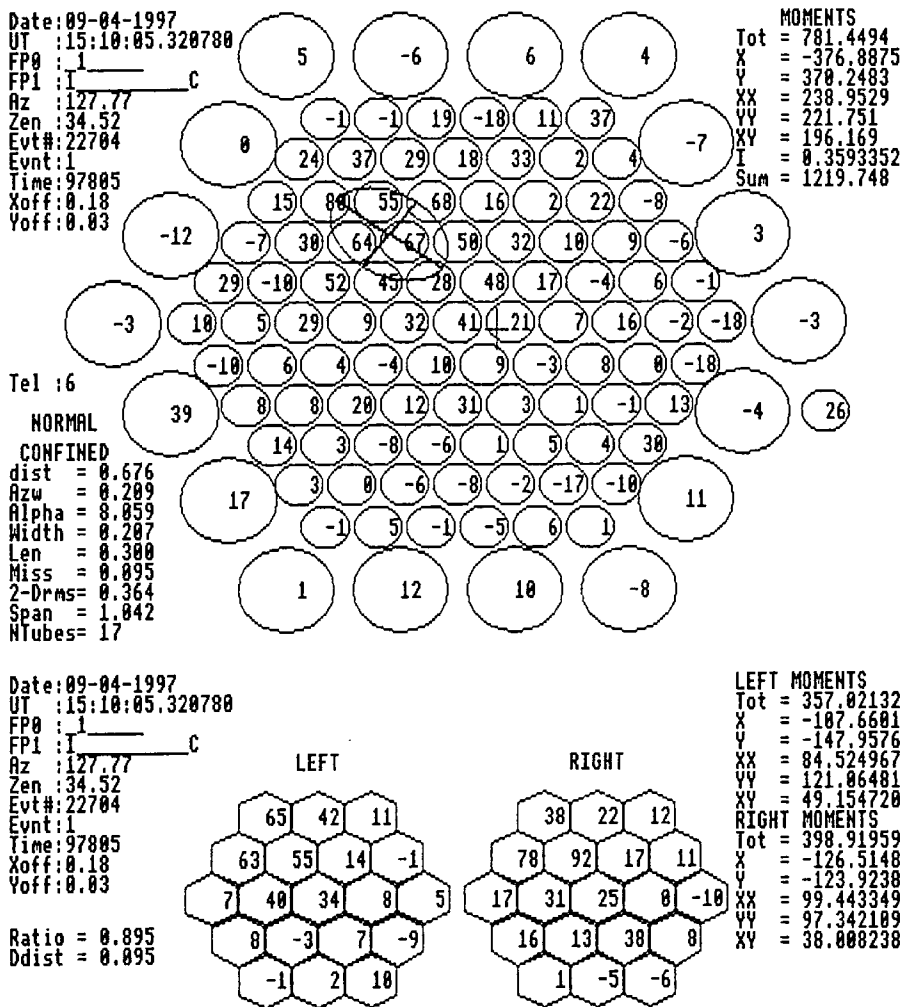


Figure 6.1: A typical image recorded with the Mark 6 telescope. Shown are the image recorded with the central camera and the two images recorded with the left and right detectors. The left and right detectors cover the same area of sky as the 91 PMT's of the central camera. Taken from [9].

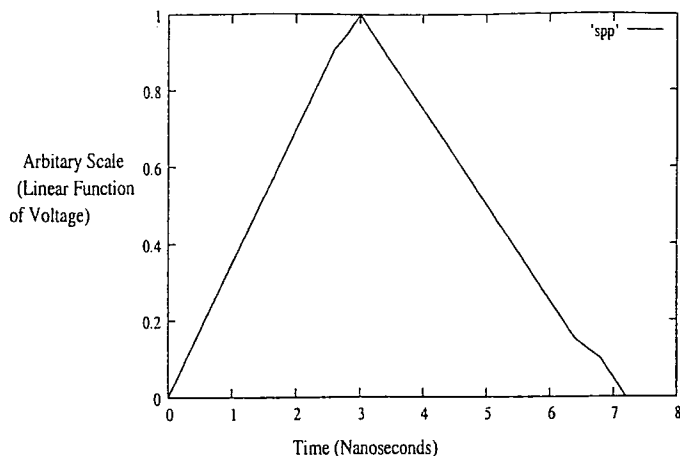


Figure 6.2: The single photoelectron pulse profile adopted for use the Mark 6 telescope simulation

and the responses of the PMT's are decided based upon a given SPP. However, as can be seen from figure 6.3, the H.E.S.S. telescope simulations are performed with a much more realistic SPP function than that used for the Mark 6.

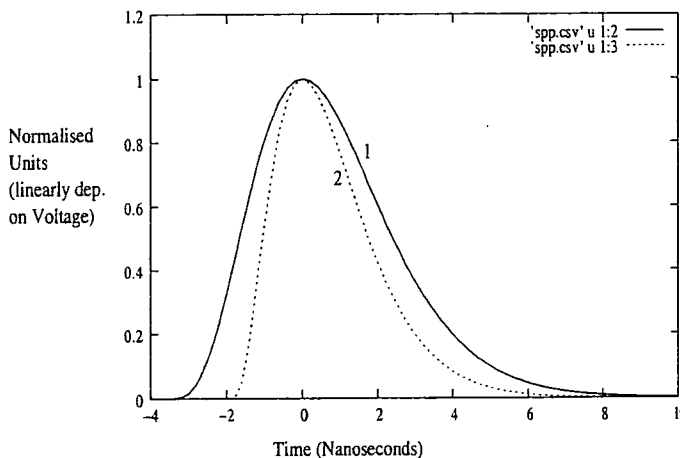


Figure 6.3: The single photoelectron pulse profile for the PMT's of the stand-alone H.E.S.S. camera. Curve 1 shows the first approximation, whereas curve 2 shows the currently used value, which is adopted in this thesis.

The triggering criteria for the stand-alone H.E.S.S. telescope is if 4 tubes in 1 sector have a signal greater than 4 photoelectrons, the system triggers. The camera is defined by 38 overlapping sectors as shown in figure 6.4. Again the NSB flux is applied to the trigger, using values measured at the H.E.S.S. site [180]. The results of simulations of the stand-alone HESS telescope will be presented later in this chapter and in the next

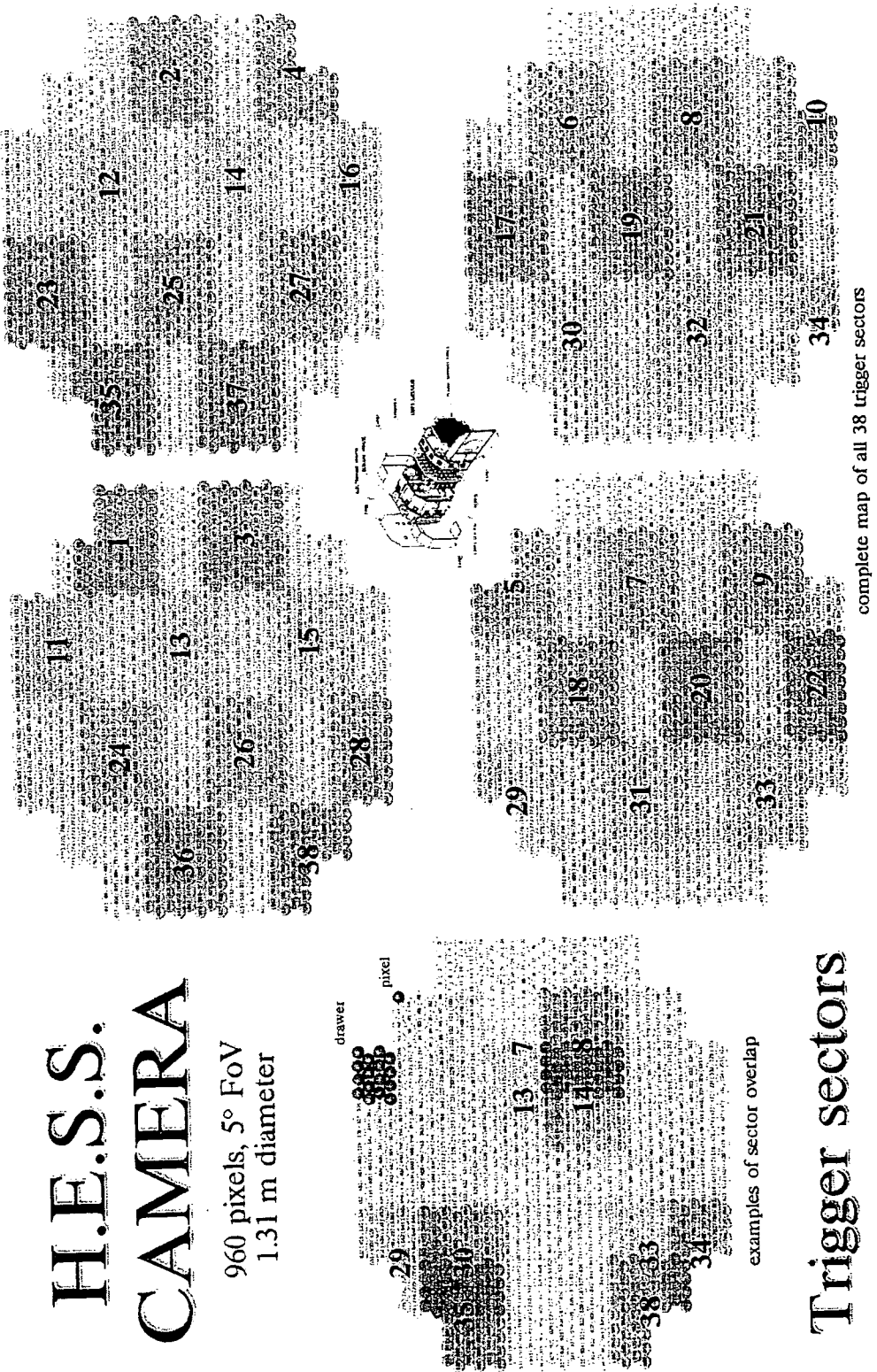


Figure 6.4: Map of H.E.S.S. trigger sectors in camera.

chapter. For the moment however the derivation of the flux of the AGN PKS 2155-304 as seen with the Mark 6 telescope is outlined to show how real data and simulation are combined to calculate the physical properties of a source.

6.3 Simulations in Practice

6.3.1 Shower Simulation

Cosmic Ray EAS

EAS were generated at an observing angle of 30° from the zenith, for a spectrum of gamma-ray and cosmic ray primaries with MOCCA. This angle was chosen as it best represents the mean observing angle used in measurements of the AGN PKS 2155-304. Furthermore, a subset of 30 off-source data segments, each of 15 minutes length, and possessing a zenith angle between 25° and 35° , was compared to simulation, as opposed to the complete data set. This dataset contains a total of 203,602 cosmic ray events, representing 1/5 of the total background data below 45° zenith angle. Figure 6.5 shows that this subset is representative of the entire data set in the range $0^\circ < Z_A < 45^\circ$. Each shower was sampled by 5 Mark 6 telescopes placed randomly within a radius of 300 m of the core and each image was shifted randomly 4 times within the camera.

Two separate spectra of cosmic rays were used, one due to Mohanty et al. [141], and the other due to Wiebel et al. [204]. Both had a power law fit for each species of the form:

$$\Phi(E) = \Phi_o \left(\frac{E}{TeV} \right)^{-\gamma} (\text{m}^2 \text{ sec sr TeV})^{-1} \quad (6.1)$$

In the power laws presented herein it should be noted that for gamma-rays Φ_o has the units of $\text{m}^{-2} \text{s}^{-1}$, whereas for cosmic rays the units are $\text{m}^{-2} \text{s}^{-1} \text{sr}^{-1}$. This follows, given the isotropic cosmic flux and point source nature of the gamma-ray emission. In each instance, and as discussed before, the discriminator level is set so that each simulated cosmic ray spectrum gives the same trigger rate as the subset of the off source data for the PKS 2155-304 observations, namely $\sim 8.38\text{Hz}$, whilst maintaining the best fit for the image parameters. The differences between the two spectra are shown in table 6.1.

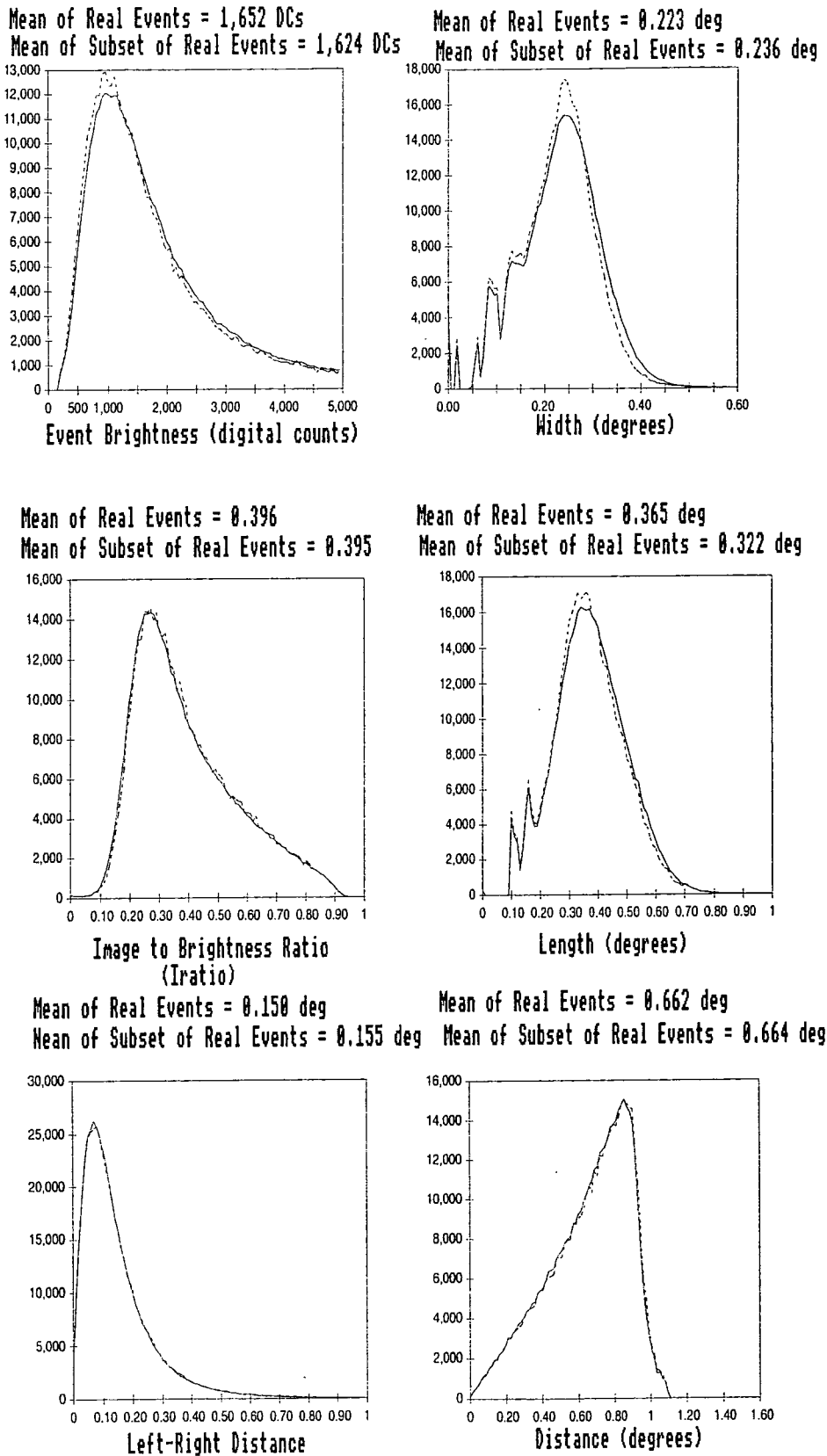


Figure 6.5: The observed differences in image parameter distributions between off source cosmic ray observations made between 25° and 35° zenith angle (dotted line) and all zenith angles below 45° (solid line). These graphs have been normalised so that both curves have the same area.

Species	Φ_o Mohanty	Φ_o Wiebel	γ Mohanty	γ Wiebel
Proton	0.1244	0.1091±0.0032	2.77	2.75±0.02
Alpha	0.0773	0.0660±0.0015	2.66	2.62±0.02
Oxygen Group	0.0655	0.0522 ± 0.0013	2.63	2.67±0.02
Iron Group	0.0303	0.0252±0.005	2.62	2.60±0.02

Table 6.1: Comparison of cosmic ray fluxes due to studies by Mohanty [141] and Wiebel [204]. Here elements with atomic mass in the range 11 to 28 are in the Oxygen group, and those with masses between 32 and 56 are in the Iron Group.

Gamma-Ray EAS

A simulation of a spectrum of 150,000 gamma-ray showers at 30° zenith angle was undertaken. The showers were simulated between 0.1 and 30 TeV with a Crab type spectral slope of -2.45. For each shower the light deposited on 5 randomly placed Mark 6 telescopes situated within 300 m radial distance of the core was recorded.

6.3.2 Refined Telescope Simulation

The mechanics of the telescope simulation were discussed in detail earlier in this chapter. Here the actual physical parameters used within the Mark 6 telescope simulation are now reviewed in greater detail.

Optics

The point spread function (PSF) of the mirror, as discussed earlier, causes a smearing of the images. The PSF of the central Mark 6 mirror is best fit with an equation composed of two Gaussian functions, of the form:

$$f(x) = A \exp\left(-\left(\frac{x^2}{a^2}\right)\right) + B \exp\left(-\left(\frac{x^2}{b^2}\right)\right) \quad (6.2)$$

where x is the angular displacement of the photon. Here the angular size of each component of the PSF can be found from the standard deviation, e.g. $\sigma_a = |\sqrt{a/2}|$. The PSF is measured by studying the central cross-section of a star image formed upon the focal plane using a CCD. A closer inspection of measurements made in 1996 show that one Gaussian should be highly peaked in the centre of the field of view ('peak') and the other should be a much wider and less peaked function ('skirt'). The peak has an angular

size of $0.18 \pm 0.03^\circ$, whereas the skirt has an angular size of $0.45 \pm 0.05^\circ$ and contains 66% of the light. There is also likely to be some diffuse light scattered in reflection, however, as the skirt is large, this is considered to be negligible in comparison. This combination of numbers 0.18/0.45/66 defines the response of the optics of the Mark 6 telescope.

Analogue to Digital Conversion (ADC)

As discussed earlier, in the simulations a digital counts (dc) to photoelectron (pe) ratio is defined, such that images may be converted into digital signals and compared with the real events. Estimates of this ratio may be obtained by exposing a PMT to a photon pulse of known intensity and measuring the response in terms of digital counts after the signal has passed through the appropriate electronics. Measurements of this kind have been performed using radioactive material ($0.02\mu\text{Ci}$ of Am^{241}) embedded within a 10mm diameter pill of scintillating material and placed upon the front surface of a PMT. Results from this experiment suggest values for the dc/pe conversion ratio of ~ 4 . Results from simulations, found by comparing the means of the simulated and observed brightness distributions is dc/pe ~ 4.5 , which is within the error of the experimental result.

Noise

The amount of NSB light incorporated within the simulations can affect the images seen within the camera. The effect of noise is to add extra SPP's to the convolved Cherenkov pulse profile at random intervals, and at a level that must be derived iteratively by comparing the simulated parameter distributions with the observed cosmic ray data. Noise is added in a Poissonian manner to the Cherenkov pulse profile, the equation for the mean noise rate for a particular tube being:

$$R_n = \text{NSB}_{\text{noise}} \times \text{NSB}_{\text{ratio}} \times A \times R \times \phi_{\text{tube}} \times C_{\text{cone}} \times S_{\text{tube}} \quad (6.3)$$

here $\text{NSB}_{\text{noise}}$ is the average NSB level ($\sim 7.7 \times 10^{11} \text{ pe s}^{-1} \text{ m}^{-2} \text{ sr}^{-1}$) and $\text{NSB}_{\text{ratio}}$ is the scaling to the actual level of NSB, set by iteration and matching of simulation to real cosmic ray data. A and R are the area and reflectivity of the mirror, ϕ_{tube} is the solid angle subtended by each tube and C_{cone} is an enhancement factor, due to the additional light collected by the Winston cones. S_{tube} is the ratio of the sensitivity of the tube to the sensitivity of the central imaging tubes. The mean number of photoelectrons in a time

window Δt is thus $M = R_n \Delta t$. The probability of getting n photoelectrons within this time window is therefore:

$$P(n) = \frac{M^n e^{-M}}{n!} \quad (6.4)$$

Noise is then fed into the trigger. This is computed by taking the 40 nanosecond signal integration time window and dividing it into 200 0.2 nanosecond bins. Δt is thus set to 0.2 nanoseconds. As $M \ll 1$ for this Δt , we calculate $P(n > 0) = 1 - P(0)$ and ignore the small possibility that there could be 2 photoelectrons within the 0.2 nanosecond time bin. The SPP is then added into each bin based upon this probability. Noise is also added to the integrated signal from each PMT. In this case $\Delta t = 40$ nanoseconds and so $M \approx 5$. This noise is randomly added to the signal from each PMT using a Poissonian distribution with this mean.

Relative Tube Sensitivities

Two other factors in the simulation, are the sensitivity of the guard ring compared to the main imaging tubes, and the sensitivity of the left and right camera tubes, as compared to the main imaging tubes:

Guard-Ring Sensitivity: The sensitivity of the guard ring PMT is expressed as a relative sensitivity as compared to the central camera imaging tubes. The value is optimised by comparison of the distance distributions in both observed and simulated hadronic events.

Left-Right Sensitivity: In a similar fashion to the guard-ring sensitivity, this is set relative to the central camera imaging tubes. It has a strong effect on those imaging parameters that utilise information from the left and right cameras, and in addition it has a strong effect on the telescope trigger.

6.3.3 Result

Triggering

The rate of triggering for cosmic rays and gamma-rays is calculated by:

$$R_{trig} = \frac{N_{trig}}{N_{show}} A \Omega \frac{\Phi_o}{\gamma - 1} \left(E_L^{1-\gamma} - E_H^{1-\gamma} \right) \quad (6.5)$$

Here N_{trig} and N_{show} are the number of showers which trigger the telescope, and the total number of showers simulated respectively (in actuality this is $20\times$ the number of showers simulated for cosmic rays and $5\times$ the number of showers simulated for gamma-rays, given the multiple sampling). A represents the area over which the telescopes were randomly scattered (i.e. $\pi \times r^2$, where $r = 300$ m). Φ_o and γ are the previously defined power law variables, applicable here to either the Mohanty/Wiebel data, or the gamma-ray spectrum. E_L and E_H are the lower and upper energy limit of the simulations in TeV, namely 0.1 and 30 TeV for gamma-rays and 0.3 and 30 TeV for cosmic rays. Ω is the solid angle of a cone of half angle 2° within which the 4 random shifts of cosmic ray source direction were confined. For gamma-rays this factor is ignored, given their point source origin.

For each cosmic ray spectrum (i.e. both Mohanty and Wiebel), the discriminator level, NSB_{ratio} , digital counts per photoelectron, PSF, guard ring and left right sensitivities are all changed within the limits of measurement, where possible, so that both the trigger rate of the system and the cosmic ray image parameters match the real data.

Both spectra give results which lie near the limits of experimental and statistical error of the observed cosmic ray trigger rate of 8 ± 1 Hz. Wiebel is slightly below the mean value of real trigger rate at 7.6 ± 0.1 Hz and Mohanty is slightly higher at 9.1 ± 0.1 Hz. A closer fit is not possible, as changes in the physical parameters used, tends to disturb the fits for the image parameters. During our research it was decided by the H.E.S.S. collaboration that the Wiebel spectra would be used for cosmic ray simulations for H.E.S.S. and therefore it was decided to concentrate on Wiebel simulations in future analysis.

As mentioned the simulations are matched against data taken between 25° and 35° degrees zenith angle. It has been shown that the real data in this range are representative of the real data for all zenith angles $< 45^\circ$. However the real trigger rate for all the off source data included in the published results for PKS 2155-304 is 10.7 Hz. The physical parameters of the simulation must then be altered (within the experimental error bounds set where possible by measurement) to match this rate. Therefore table 6.2 shows two sets of physical parameters. Fit 1 correspond to those which best fit the trigger rate of the system between 25° and 35° zenith angle and fit 2 matches the trigger rate for all zenith angles $< 45^\circ$. Fit 1 is used for the meantime, and a discussion of the differences

caused by using fit 2 is discussed later with respect to systematic errors.

Physical Parameter	Fit 1	Fit2
Discriminator Level	0.43	0.35
Point Spread Function	0.20°,0.40°66%	0.25°,0.45°66%
Photoelectrons per Digital Count	4.5	4.5
Sky Noise Factor	0.3	0.25
Guard Ring Sensitivity	0.58	0.4
Left/Right Sensitivity	0.31	0.30

Table 6.2: Physical parameters which best match the trigger rate and image parameters of the observed off source cosmic ray data taken for PKS 2155-304, based on, Fit 1: 25° to 35° degrees zenith angle, and Fit 2: < 45° zenith angle.

These fit 1 factors are applied to the gamma-ray simulations, and values of effective sensitive area as a function of energy are produced. Image tubes are then identified by the significance of the signal in the tube compared to the assumed mean nightsky background level. The images are then ‘tidied’. This involves discarding those images that have less than 200 digital counts, and/or less than two image tubes. Also those events that have a brightest pixel in the outer ring of tubes are discarded, as it is conceivable that the light density in the image would continue to grow beyond the edge of the camera. Thus the Hillas parameters calculated from such unconfined events would be incorrect. This removes around 50% of both the real and simulated cosmic ray events from the data set, and around 25% of the simulated gamma rays.

Image Parameters

The resultant fits are shown in figure 6.6 for the image parameters of real and simulated cosmic ray data. As can be seen from the parameter distributions there is a significant disparity in the simulated length and I_{ratio} distributions compared to the observed distributions. Looking at real data, one sees that the length distribution is thrown off due to some events possessing two significant and separated patches of light within the camera. The secondary patch is believed to be due to the Cherenkov light coming from deeply

penetrating muons, which changes the ellipse fitting procedure and increases the length of the primary image. This however is not seen to such an extent within the simulated data set. I_{ratio} is defined as:

$$I_{\text{ratio}} = 1 - \frac{\text{Light in Image}}{\text{Total Light in Camera}} \quad (6.6)$$

Therefore, as the real data consists of two deposits of Cherenkov light, only one of which is counted in the image, the ratio of image light to total light will be smaller. Hence I_{ratio} will be bigger than when only one image exists in an otherwise empty camera. One other possibility for the differences seen is the poor simulation of the flat fielding procedure of the camera. In the simulations the same noise level is applied to all the tubes, which will obviously not be the case in real life. Although, as discussed in Chapter 3, the on and off source data are corrected so that the total brightness in both datasets is similar, there may be more subtle second order effects, which produce the disparity between real and simulated events. This may lead to an underestimation of the mean of the length distribution.

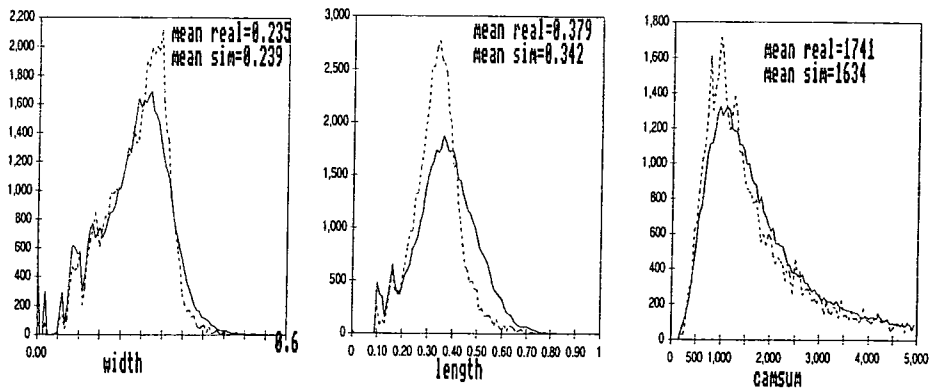
If the disparity is due to sub-shower development of muons, then it will not be present in the gamma-ray data, however if it is due to the simulation of the noise-level then this may introduce a systematic bias into the simulation of the telescope response to gamma-ray showers. The simulated gamma-ray image parameter distributions produced are compared with real hadronic data in figure 6.7. This again shows the discriminatory power of the imaging technique. These data are now used in flux calculations for PKS 2155-304.

6.3.4 Flux Derivation in Principle

The gamma-ray spectrum produced with MOCCA is fed through the telescope simulator, using the physical parameters that gave the best fits to the cosmic ray parameters, assuming the Wiebel spectra. The data are then pre-processed in the same way as real data, and the number of events surviving the tidying process is given in table 6.3. Image parameter cuts are applied to the data, in the same fashion as in [38].

In the analysis of the PKS 2155-304 data, the events were grouped into 5 image SIZE bins as detailed in table 6.7.

After cutting, the number of simulated events as a function of energy in each SIZE bin is given in table 6.4. If the threshold energy of the system is defined as the energy of



q03 off source (solid) and simulated cr, Hiebel mix, USS atmos, sesfin params, disc=0.43

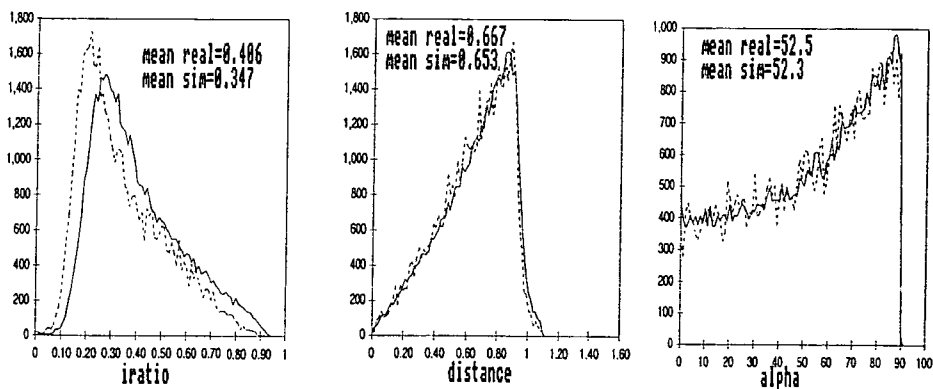


Figure 6.6: Comparisons of distributions of width, length, camsum (SIZE), iratio, distance and alpha for cosmic ray spectral simulations with MOCCA and real off source data taken during observation of PKS 2155-304 using the Durham Mark 6 telescope. The means of the distributions for each code are shown within each subplot. The simulations have been scaled such that they match the off source trigger rate of 8.38 s^{-1} as closely as possible.

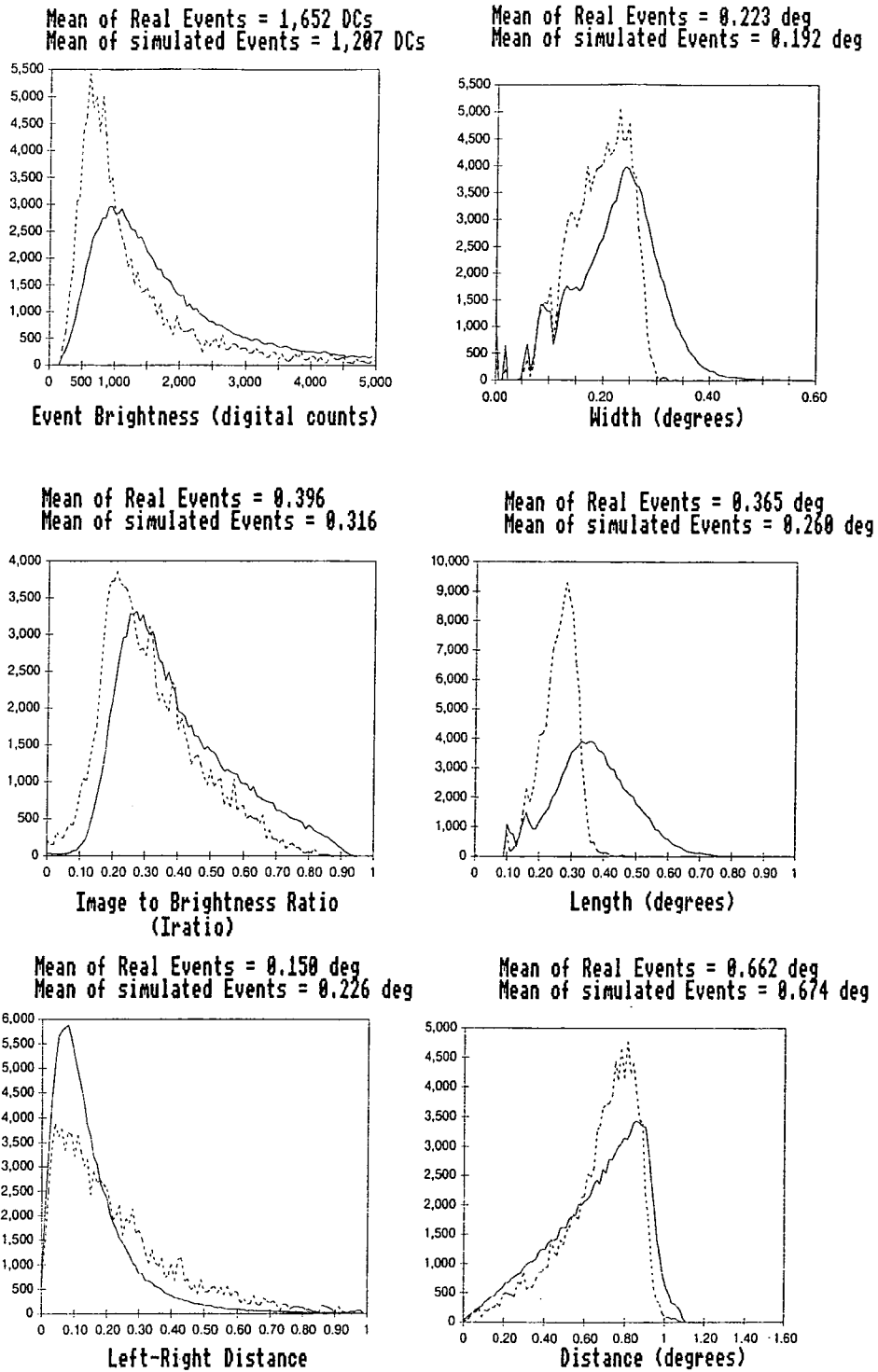


Figure 6.7: Comparisons of distributions of width, length, camsum (SIZE), distance, Iratio and ddist for gamma-ray spectral simulations with MOCCA (dotted line) and real off source data taken below 45° zenith angle during positive observations of PKS 2155-304 (solid line) using the Durham Mark 6 telescope [38].

Energy Bin (TeV)	Number Simulated	Number Triggering	Number After Tidying
0.1-0.3	588,790	64	46
0.3-0.4	53,830	248	192
0.4-0.5	28,775	527	444
0.5-0.7	29,690	2428	2186
0.7-1.0	19,700	4760	4413
1.0-1.5	12,885	5323	4630
1.5-2.0	5,465	2793	2105
2.0-3.0	4,760	2821	1749
3.0-4.0	2,130	1440	731
4.0-5.0	1,155	842	378
5.0-7.0	1,255	981	390
7.0-10.0	695	572	199
10.0-15.0	465	416	133
15.0-20.0	195	172	49
20.0-30.0	210	204	57
Total	750,000	23591	17702

Table 6.3: The number of simulated gamma-ray images surviving the tidying process as a function of energy.

peak response per unit energy after these cuts then, for a $E^{-2.6}$ differential spectrum, one obtains a threshold energy of around 1.5 TeV, which is much higher than the threshold energy derived from triggering or tidied events alone. The response curves for an $E^{-2.6}$ spectrum for these three cases are shown in figure 6.8. In the past the Durham group has used the triggered events to define an energy threshold, as the triggering behaviour of the three dish system is distinctly different from a normal stand-alone telescope. This can be seen if one compares figures 3.2 and 3.9, ie the effective area plots for the Mark 6 and H.E.S.S. stand-alone telescopes. At low energies the Mark 6 is seen to have a much less inclined slope than the H.E.S.S. telescope. However, if one considers the total number of events in the bins, it becomes clear that the efficiency of the system below 1.5 TeV is very poor. Thus the threshold energy for flux calculation for the Mark 6 is set as 1.5 TeV.

By considering the mode energy for each bin one can set an approximate SIZE to

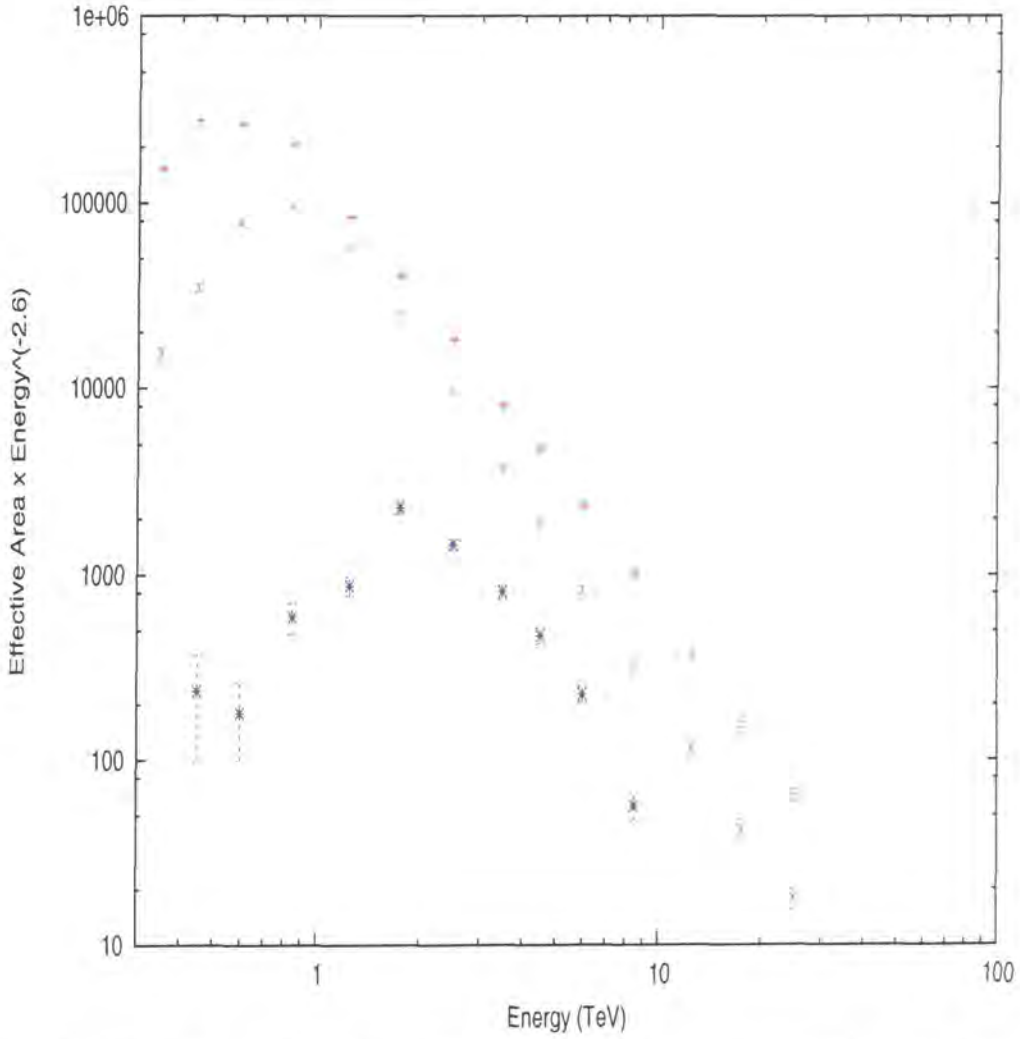


Figure 6.8: Histograms of the effective area for gamma-ray showers of the Mark 6 telescope, using ‘Fit 1’ parameters, convolved with an $E^{-2.6}$ spectrum for triggered (red), tidied (green), and cut (blue) events. Errorbars are 1σ poissonian noise on the number of triggered events within a bin. The threshold energy for triggered events ≈ 0.5 TeV. Tidying increases it to ≈ 0.7 TeV while for cut events, it is still higher, namely ≈ 1.5 TeV. The Y axis is in $\text{m}^2 \times (E/\text{TeV})^{-2.6}$.

Energy Bin (TeV)	Number Simulated	Number Selected				
		Bin 1	Bin 2	Bin 3	Bin 4	Bin 5
0.1-0.3	588,790	0	0	0	0	0
0.3-0.4	53,830	0	0	0	0	0
0.4-0.5	28,775	2	1	0	0	0
0.5-0.7	29,690	3	0	1	1	0
0.7-1.0	19,700	5	15	2	4	1
1.0-1.5	12,885	3	3	12	44	9
1.5-2.0	5,465	0	0	8	126	56
2.0-3.0	4,760	0	0	0	54	212
3.0-4.0	2,130	0	0	0	0	159
4.0-5.0	1,155	0	0	0	0	96
5.0-7.0	1,255	0	0	0	0	106
7.0-10.0	695	0	0	0	0	36
10.0-15.0	465	0	0	0	0	0
15.0-20.0	195	0	0	0	0	0
20.0-30.0	210	0	0	0	0	0
Total	750,000	13	19	23	229	675

Table 6.4: The number of simulated gamma-ray images surviving the image parameter cuts as a function of energy for each of the image SIZE bins.

energy relation as given in table 6.5.

SIZE Bin Number	1	2	3	4	5
Approximate Mean Energy (TeV)	0.75	0.9	1.2	1.5	3.0

Table 6.5: Approximate energy of each bin, based around peak in number of events in each bin for cut data.

If we consider bin 3 for a moment then, by making a small change in the telescope parameters, as given in table 6.2, one reduces the number of simulated events in bin 3 to 2. The events in bins 4 and 5 being typically reduced by only $\approx 20\%$. It therefore seems sensible to use only bins 4 and 5 in calculations of flux or spectral index. The variable $f_i(E)$ is then defined as the fraction of simulated gamma-ray showers of energy E , which are accepted and placed in size bin i . Each $f_i(E)$ is then folded with an $E^{-\gamma}$

trial spectrum and integrated over the energy range for which gamma-ray simulations have been made, to derive $F_i(\gamma)$. Therefore:

$$F_i(\gamma) = \int_{0.1\text{TeV}}^{30\text{TeV}} f_i(E) E^{-\gamma} dE \quad (6.7)$$

The spectral index that best fits the observed data is found when $F_i(\gamma)$ is divided by N_i , the number of excess events observed in SIZE bin i , is the same within error for each bin. In our case (with only bins 4 and 5), this gives simply:

$$\frac{N_4}{N_5} = \frac{F_4(\gamma)}{F_5(\gamma)} \quad (6.8)$$

To reduce the systematic errors incurred in deriving $F_i(\gamma)$, in binning over large energy intervals, a curve is fitted to the histogrammed data for $f_i(E)$ to provide a tabulated function, into which is folded the $E^{-\gamma}$ spectrum. A numerical integration is then performed over the curve to derive a value for $F_i(\gamma)$. The flux S_γ above a threshold energy E_{th} is then given by:

$$S_\gamma(E_{th}) = \frac{N}{T} \frac{E_{th}^{-(\gamma-1)}}{\gamma-1} \left(A \sum_{i=4}^5 F_i(\gamma) \right)^{-1} \quad (6.9)$$

Where N and T are the number of excess on source events and the time of observation. A is the target area for the simulated showers (i.e. $\pi \times 300^2 \text{ m}^2$).

This therefore incorporates real measurements, simulations, estimations and selected limits as shown in figure 6.9. In the following calculations only the PKS 2155-304 data which was taken between the zenith angles of 0° and 45° is included, as simulations at larger zenith angles have not been performed.

6.4 Flux Derivation for PKS 2155-304

6.4.1 Observations

As detailed in Chapter 4, the AGN PKS 2155-304, was observed with the Durham Mark 6 telescope whilst in a high state in 1996/1997 [38]. Simultaneously X-ray emission was seen with RXTE and low energy gamma-ray emission with EGRET [198]. The observational data taken with Mark 6 is given in table 6.6. This data was then cut, according to the cuts outlined in table 6.7, where the number of events surviving the cuts is also given.

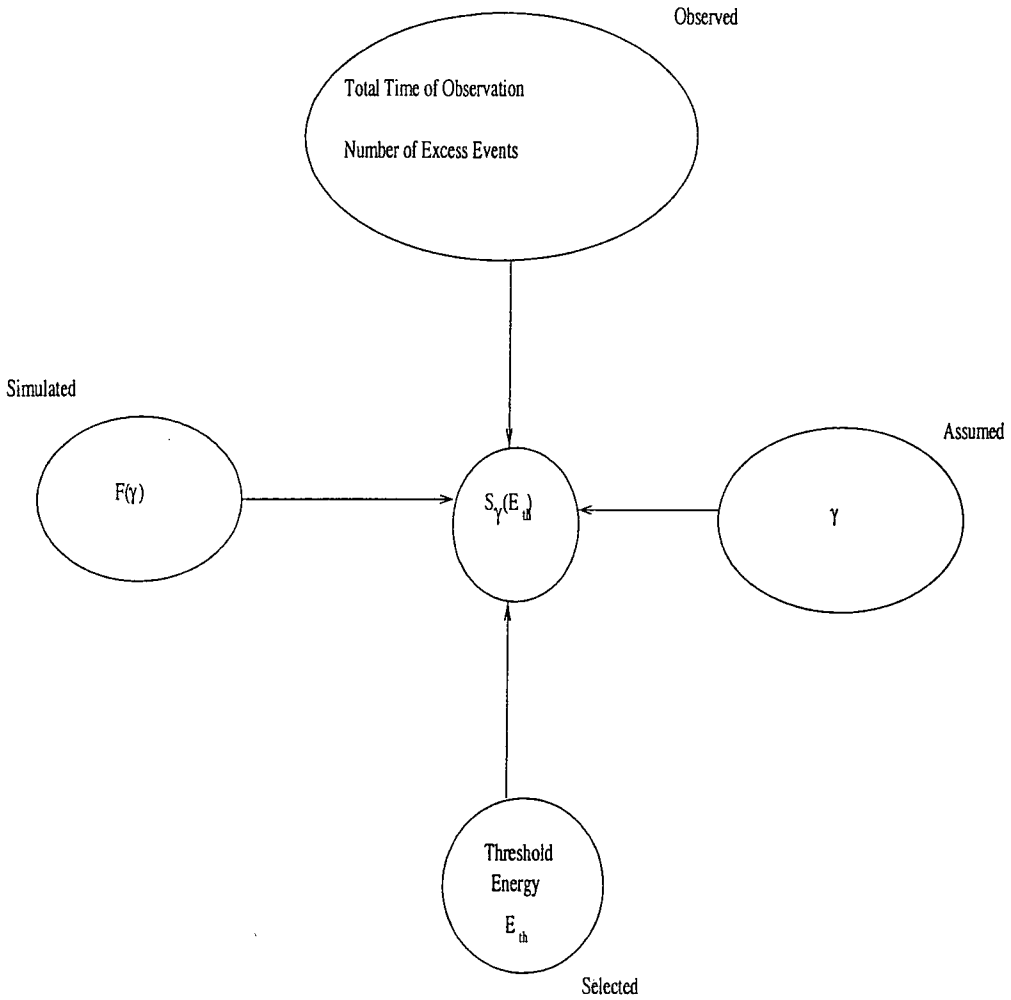


Figure 6.9: A guide to the factors which play a part in the determination of the flux $S_\gamma(E_{th})$.

Events	On	Off	Difference	Significance (σ)
Number of Events	10121083	1023280	-2197	-1.5
Number of SIZE and Distance Selected Events	6000856	598733	2123	1.9
Number of Shape, SIZE and Distance Selected Events	37125	36151	974	3.6
Number of Shape, SIZE, Distance and α Selected Events	6099	5370	729	6.8
Number of Shape, SIZE, Distance and α Selected Events between 0 – 45° zenith angle	5163	4619	544	5.5
Number of Shape, SIZE, Distance and α Selected Events between 0 – 45° zenith angle in top two SIZE bins	3946	3588	358	4.1

Table 6.6: Observed data for AGN PKS 2155-304 taken from [38]. Last row shows data used in simulation work, i.e. data cut according to table 6.7 from less than 45° zenith angle, in the top two SIZE bins (i.e. between 1500 and 10000 digital counts).

Before calculating the flux seen, it will be shown that it may be possible to give an indication (based around the ratio of the number of events in bins 4 and 5) of the spectrum of PKS 2155-304.

6.4.2 Finding the Spectral Index

Recalling equations 6.24 and 6.25, and given the number of real excess events which have survived the cut procedure, i.e.:

$$N_4 = 138 \pm 57 \quad (6.10)$$

$$N_5 = 220 \pm 65 \quad (6.11)$$

$$(6.12)$$

One may then run a simple code to numerical integrate $f_i(E)E^{-\gamma}$ using a Simpsons rule integration for various values of γ and ascertain, which value produces the closest fit

Parameter	Ranges	Ranges	Ranges	Ranges	Ranges
<i>SIZE</i> (d.c.)	500 – 800	800 – 1200	1200 – 1500	1500 – 2000	2000 – 10000
<i>Distance</i> (deg)	0.35-0.85	0.35-0.85	0.35-0.85	0.35-0.85	0.35-0.85
<i>Eccentricity</i>	0.35-0.85	0.35-0.85	0.35-0.85	0.35-0.85	0.35-0.85
<i>Width</i> (deg)	<0.10	<0.14	<0.19	<0.32	<0.32
<i>Iratio</i>	<0.80	<0.70	<0.70	<0.35	<0.25
<i>D_{dist}</i>	<0.18	<0.18	<0.12	<0.12	<0.10
α (deg)	<22.5	<22.5	<22.5	<22.5	<22.5
0-60° Zenith Angle					
<i>Excess on-source</i>	50	98	138	169	274
<i>Off-source Events</i>	250	433	529	1752	2406
0-45° Zenith Angle					
<i>Excess on-source</i>	29	74	83	138	220
<i>Off-source Events</i>	227	371	433	1546	2042

Table 6.7: The image parameter cuts applied, and the results of the application of the image parameter cuts to the PKS 2155-304 data [38]

to that slope seen in the real data. Taking the data from bins 4 and 5, a reasonable differential spectral slope of ≈ -3.2 is arrived at. This is similar to the spectral slope of 1H1426, derived from Whipple measurements outlined in [157]. This similarity is plausible, given the similar redshifts of the two sources. If we included both a systematic error (due to telescope input parameters), and a statistical error (based on the poissonian fluctuations in the number of events in bins 4 and 5, and an estimation of the functional form to a Gaussian), then the result is:

$$\gamma = 3.2 \pm 0.3_{\text{sys.}} \pm 0.6_{\text{stat.}} \quad (6.13)$$

6.4.3 Calculation of Flux

The simulated data for SIZE bins 4 and 5 is cut according to the image cuts defined in table 6.7 and the surviving fractions, as a function of energy, are shown in table 6.4.

The fractional values of $f(E)$ are combined for bins 4 and 5, and plotted. As discussed earlier, a curve is fitted to the points and an interpolated set of $f(E)$ points are computed,

this was repeated for several possible curves (at the $\pm 1\sigma$ of bin excess level) to compute possible errors. The points are then folded with a function of the form $E^{-2.6}$, and $F(\gamma)$ is determined by a Simpson's rule integration. The result is:

$$F(2.6) = 0.015 \pm 0.002 \tag{6.14}$$

Given the discussed equation for $S_\gamma(E_{th})$, $N = 358$ and $T = 32.5$ hrs, then the integral flux above 1.5 TeV for PKS 2155-304 was seen to be

$$2.5 \times 10^{-7} \text{ m}^{-2} \text{ s}^{-1}.$$

6.4.4 Sources of Error

Statistical - The simple Poissonian error of $\sigma = \sqrt{N}$ is applicable to the number of simulated events throughout the appropriate equations and procedures. The major contribution comes from statistical error on the number of observed excess events in bins 4 and 5, namely 358 ± 87 events. There will also be a statistical error on $F(\gamma)$ due to the error on the number of simulated events surviving the cuts, at the 1σ level this corresponds to $\Delta F(\gamma) \sim 0.002$. These two statistical errors, give an overall statistical error in the flux of:

$$\Delta_{\text{statistical}}[S_{2.6}(1.5\text{TeV})] = 0.7 \times 10^{-7} \text{ photons m}^{-2} \text{ s}^{-1} \tag{6.15}$$

Systematic Error - Atmosphere and Count Rate: Over the wavelengths of Cherenkov light collection Rayleigh scattering, ozone scattering and aerosol scattering are liable to introduce a significant source of error. Rayleigh scattering is the dominant mechanism and is governed by the column density of the atmosphere over the telescope site, which is related to barometric pressure. Although the majority of ozone in the atmosphere is at altitudes greater than shower maximum, ozone extinction will still be significant at lower altitudes and will reduce transmission for wavelengths below ~ 300 nm. In addition aerosol scattering in the lower layers of the atmosphere will introduce light attenuation, which will be highly variable given the constantly changing aerosol density.

Although all measurements of PKS 2155-204 were taken under apparently clear and stable atmospheric conditions, variations of around $\pm 10\%$ are seen in the background count rate at a given zenith angle. Given that the Mark 6 telescope was sited at a relatively low altitude (260m a.s.l.), aerosol concentration is likely to have had a large effect on count rate. This will be discussed in much greater detail in the next chapter, where studies of the effects of changing aerosol structure on simulations of the first stand-alone H.E.S.S. telescope will be presented.

Systematic Error - Telescope Simulation Input Parameters: The differences in the physical parameters which best model the telescope system when matching real off source data from either $25^\circ < Z_A < 35^\circ$ (fit 1) or $< 45^\circ Z_A$ (fit 2) were given in table 6.2. For the flux calculation so far fit 1 has been used, however fit 2 leads to a 15% higher flux than that derived previously. This suggests that the systematic error due to the sensitivity of the final flux to input parameter changes is likely to be around 15%.

Systematic Effects - Differences in EAS simulation: The differences in EAS simulation and the predicted Cherenkov fluxes, were shown in the last chapter. For hadronic showers, CORSIKA showed a large discrepancy in Cherenkov light level as compared to ALTAI and MOCCA ($> 20\%$ at 0.3 TeV). In order to match the cosmic ray trigger rate for hadronic showers, and maintain a good fit for the image parameters, the photoelectron/digital counts conversion ratio would have to be changed from 4.5 to 6. Such a value is higher than that suggested by experiment but cannot be excluded. The trigger probability of the gamma-ray showers would thus increase, leading to a reduction in inferred flux by a factor of 0.6.

Overall Systematic Error: The 10% error due to atmospheric attenuation and the 15% error due to differences in telescope simulation input parameters, can be considered as \pm errors, i.e. possible errors in either direction. ALTAI and MOCCA agree quite well, although CORSIKA gives a flux which is 60% of that predicted using MOCCA. Therefore the complete systematic error should be:

$$+\Delta[S_{2.6}(1.5\text{TeV})] = 0.5 \times 10^{-7} \text{ photons m}^{-2} \text{ s}^{-1} \quad (6.16)$$

$$-\Delta[S_{2.6}(1.5\text{TeV})] = 1.6 \times 10^{-7} \text{ photons m}^{-2} \text{ s}^{-1} \quad (6.17)$$

6.4.5 Conclusion

The overall flux seen by the Durham Mark 6 telescope for the AGN PKS 2155-304, is calculated to be:

$$S_{2.6}(1.5\text{TeV}) = (2.5 \pm 0.7_{\text{stat}} \pm \frac{0.5}{1.6_{\text{syst}}}) \times 10^{-7} \text{ photons m}^{-2} \text{ s}^{-1} \quad (6.18)$$

This may be converted to Jy Hz using the assumed differential spectral index of $\gamma = 2.6$, and is thus shown on the spectral energy distribution for PKS 2155-304 in figure 6.10. The value plotted at 1.5 TeV ($3.63 \times 10^{26} \text{ Hz}$) is:

$$(9.6 \pm 2.7_{\text{stat}} \pm \frac{1.9}{6.1_{\text{syst}}}) \times 10^{12} \text{ JyHz} \quad (6.19)$$

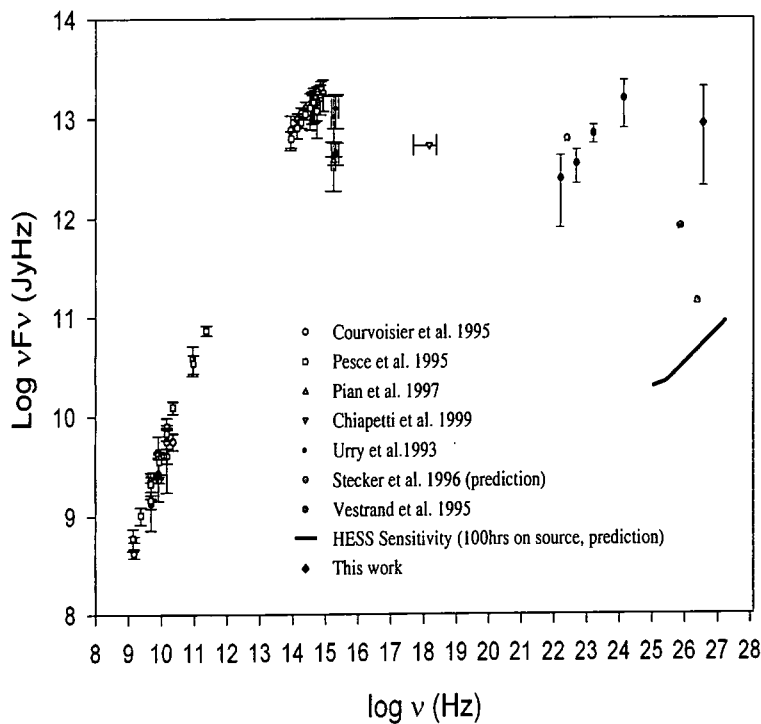


Figure 6.10: Spectral energy distribution of PKS 2155-304 in High State. Other points due to Courvoisier et al (1995) [46], Pesce et al. (1997) [156], Pian et al. (1997) [159], Chiapetti et al. (1999) [43], Stecker et al. (1996) [187] and Vestrand et al. (1995) [197]. Also shown is the sensitivity of the 4 telescope H.E.S.S. array.

6.5 Spectral Simulations for H.E.S.S. Stand Alone Telescope

As the first stand-alone H.E.S.S. telescope is yet to go into full and stable operation, a similar comparison to that performed between real data and simulation is not possible. However, some simulated results are presented, and discussion of the inferred trigger rates of the system can be given.

Simulations of a gamma-ray spectrum of 56,700 showers, with energies ranging from 0.05 to 30 TeV, with a differential spectral index of -2.45, have been made for the stand-alone H.E.S.S. system using MOCCA. These showers have been simulated at an observation angle of 20° zenith angle, using the standard H.E.S.S. atmospheric attenuation model (as discussed in the next chapter). For each shower the light is sampled by 4 stand-alone H.E.S.S. telescopes, placed randomly within 300 metres of the core for primary energy <1 TeV, or within 500 metres of the core for primary energy >1 TeV.

Simulations of 31,140 cosmic ray showers have been made. These use the cosmic ray spectra derived by Wiebel [204]. The cosmic ray species used, number of EAS generated and spectrum power law used, are detailed in table 6.8.

Primary	Number of EAS generated	Φ_0	γ
Proton	15000	$(10.91 \pm 0.32) \times 10^{-2}$	2.75 ± 0.02
Alpha	7265	$(6.60 \pm 0.15) \times 10^{-2}$	2.62 ± 0.02
Oxygen	3427	$(2.86 \pm 0.06) \times 10^{-2}$	2.67 ± 0.02
Magnesium	2767	$(2.43 \pm 0.07) \times 10^{-2}$	2.64 ± 0.03
Iron	2682	$(2.52 \pm 0.05) \times 10^{-2}$	2.60 ± 0.03

Table 6.8: Cosmic ray showers generated for H.E.S.S. simulation

As for gamma-rays, each cosmic ray shower is sampled by four stand-alone H.E.S.S. telescopes within a radius of 300 m from the core. In addition the light in each camera is shifted in the field of view 5 times randomly within a cone of half angle 4°, so that any simulated triggers match the true isotropy of the cosmic ray flux.

6.5.1 Results

The result for the gamma-rays in terms of the effective sensitive area for triggering can be seen in figure 3.9 for an observation angle of 30° zenith angle (the results for 20°

zenith angle will be presented in chapter 7). For the gamma-rays, concentrating on the region below 0.5 TeV, we see that the peak in the plot of effective sensitive area convolved with an $E^{-2.45}$ energy spectrum occurs at approximately 130GeV. We define this as the threshold energy of the stand-alone H.E.S.S. telescope. The rate of triggering for cosmic rays and gamma-rays is calculated as in equation 6.5. The trigger rates for cosmic rays incident upon the H.E.S.S. telescope at 20° zenith angle (as calculated in chapter 7) is:

$$R_{\text{cos}} = 439 \pm 28_{\text{syst}} \pm 6_{\text{stat}} \text{ Hz} \quad (6.20)$$

For a gamma-ray source of strength equal to that of the Crab Nebula (as given in [141]), the trigger rate at 20° zenith angle would be:

$$R_{\gamma} = 0.71 \pm 0.34_{\text{syst}} \pm 0.04_{\text{stat}} \text{ Hz} \quad (6.21)$$

Here the systematic errors are those given for the spectra published in [204] and [141], and the statistical errors are simply the 1σ levels given by the square root of the number of triggers.

6.6 Conclusion

In this chapter the general simulation of the Durham Mark 6 and H.E.S.S. stand-alone telescopes have been detailed, and the responses of these telescopes to simulated cosmic ray and gamma-ray spectra produced with MOCCA have been shown. A review of the deduction of astrophysical flux values has been presented and has been applied to calculate the flux of the AGN PKS 2155-304 seen with the Durham Mark 6 telescope. It has been noted that a significant error in the flux calculation may be due to the uncertainties over the level of atmospheric attenuation of Cherenkov light. Therefore in the next chapter, these spectra are taken and studies of the differences that occur in telescope behaviour given different models for the attenuation of Cherenkov light due to the atmosphere are presented for the first stand-alone H.E.S.S. telescope. A discussion of the actual systems used at the H.E.S.S. site to monitor atmospheric quality is also given.

Chapter 7

Atmospheric Effects on the Cherenkov Light Deposition

7.1 Introduction

In chapter two, the formation of EAS produced by VHE gamma radiation and charged cosmic rays was discussed. It was shown that some of the secondary charged products of these showers travel faster than the speed of light in air and produce Cherenkov radiation. The intervening chapters have discussed; how the differences between the spatial and temporal characteristics of the Cherenkov light pool measured with a ground-based Cherenkov telescope for gamma-ray and cosmic ray initiated EAS may be used to largely separate the gamma-ray events from cosmic ray events, in order to perform ground-based VHE gamma-ray astronomy. It should be noted however that the atmosphere is the detector in this form of astronomy, and that the Cherenkov telescope is a secondary detector. Understanding the atmosphere is vital for understanding the nature of both the formation of the EAS and the propagation and attenuation of the Cherenkov light. Therefore the application of the correct atmospheric model is necessary for the derivation of fluxes of astrophysical sources measured with ground-based Cherenkov telescopes.

In this chapter the effects of different atmospheric models on EAS formation and the various mechanisms for Cherenkov light attenuation are discussed. Details are given of atmospheric radiosonde measurements made near the sites of the Durham Mark 6 telescope and the H.E.S.S. system, which allow us to study the atmospheric structure, and these measurements are compared with the models available within the standard MODTRAN4 atmospheric simulator (these are detailed in appendices A and B). Other tools for atmospheric study in conjunction with Cherenkov telescopes will be covered, namely; mid

infra-red radiometers (for sky clarity), multi-wavelength LIDAR (for aerosol structure), robotic optical telescopes and studies of calibrated light sources situated on hills distant from the telescope (to study low-level light attenuation by aerosols). Simulations under different atmospheric and aerosol structures of both cosmic ray and gamma-ray initiated EAS, and their measurement in a stand-alone H.E.S.S. telescope are presented in terms of triggering effective area functions. The chapter concludes with two separate studies for the image parameter distributions of the stand-alone H.E.S.S. telescope, namely, a study of the effects of aerosol concentration and a study of the effects the Namibian geomagnetic field.

7.2 Atmospheric Profile

As shown in chapter 2, that the number of Cherenkov photons emitted per unit path length in a wavelength range λ_1 to λ_2 is given by:

$$\frac{dN}{dx} = 2\pi\alpha \left(\frac{1}{\lambda_1} - \frac{1}{\lambda_2} \right) \sin^2\theta \quad (7.1)$$

for a singly charged particle. More generally, for any charged particle the equation is:

$$\frac{dN}{dx} = 2\pi\alpha z^2 \int_{\lambda_1}^{\lambda_2} \left(1 - \frac{1}{(\beta n(\lambda))^2} \right) \frac{1}{\lambda^2} d\lambda \quad (7.2)$$

where α is the fine structure constant ($\sim 1/137$), z is the charge number, $\beta = v/c$, $n(\lambda)$ is the refractive index and θ is the angle of Cherenkov emission. Obviously particles with $\beta < 1/n(\lambda)$ cannot emit Cherenkov light at wavelength λ . This (as discussed in chapter two) sets a threshold energy for Cherenkov light production (see table 2.1). The amount of light emitted above threshold is dependent on the refractive index, as is the opening angle (θ_c) of the Cherenkov light cone, i.e.:

$$\cos \theta_c = 1/n\beta \quad (7.3)$$

which at limit, for $\beta = 1$ and for $(n-1) \ll 1$ is $\theta_c \sim \sqrt{2(n-1)}$ radians. Taking different atmospheric models from MODTRAN [63], results in different refractive index profiles near shower maxima, and therefore in different amounts of Cherenkov light emitted. In the profile of the lateral density of the Cherenkov light from a gamma-ray initiated EAS

(see 7.1), the light arriving less than 120 metres from the core is emitted near or after shower maximum and is therefore most grossly effected by changes in the refractive index profile between different atmospheric models. The same model for light absorption is used in each case.

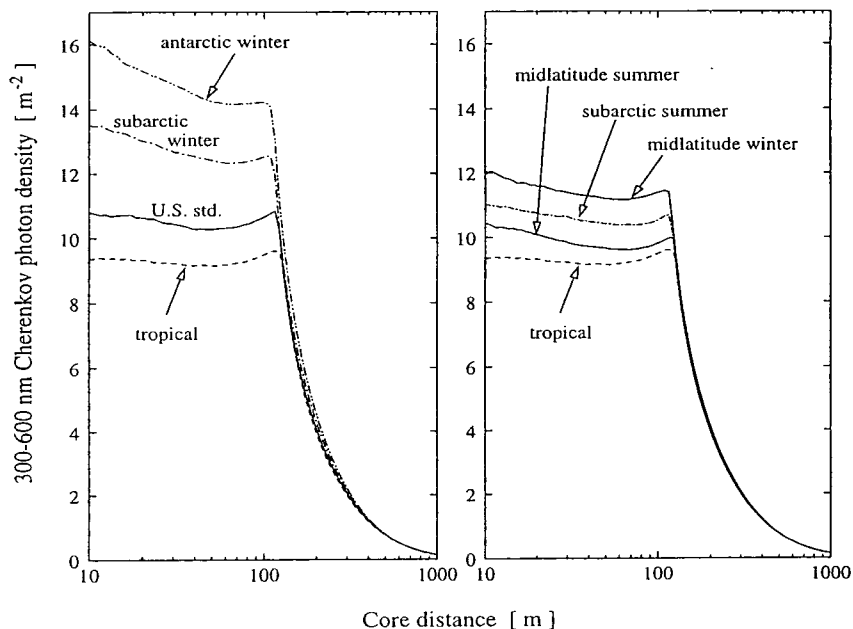


Figure 7.1: Average lateral distributions of Cherenkov light photons in the wavelength range 300 to 600nm for vertical 100 GeV gamma-ray showers produced with CORSIKA 5.71 simulations with different atmospheric profiles (2000 showers simulated for each profile). Absorption of Cherenkov light is taken into account assuming a US standard atmosphere with rural haze. Observation altitude is 2200 metres above sea level. Taken from [17].

Near the core, a 60% greater light density is seen for the Antarctic profile than the tropical. However, doing ground-based Cherenkov astronomy with large flux collectors at high altitude near the South Pole would be prohibitively expensive. At more moderate latitudes a more realistic difference of between 15-20% between light densities is seen. Most ground-based imaging Cherenkov experiments to date have simply used the US standard atmospheric profile. However, the use of inappropriate atmospheric profiles could lead to systematic errors in flux calculations.

The atmospheric profile is not only important for the light density at small distances from the core, but also for the radial fall off in light density further out. At multi-TeV

energies the radial fall off can be used as a discriminator between hadron and gamma-ray initiated EAS, and can be used to estimate the cosmic ray mass composition. Therefore, simulations with incorrect atmospheric profiles could lead to systematic errors in both these cases.

The reasons for the difference in lateral density with different atmospheric profile become apparent if instead the longitudinal development of the air shower for different profiles is studied, as shown in figure 7.2. For profiles with lower temperatures in the lower stratosphere and troposphere, the maximum of Cherenkov emission is shifted down, to a region with higher density (and therefore higher refractive index), leading to a higher Cherenkov efficiency, over profiles with higher temperatures at these altitudes.

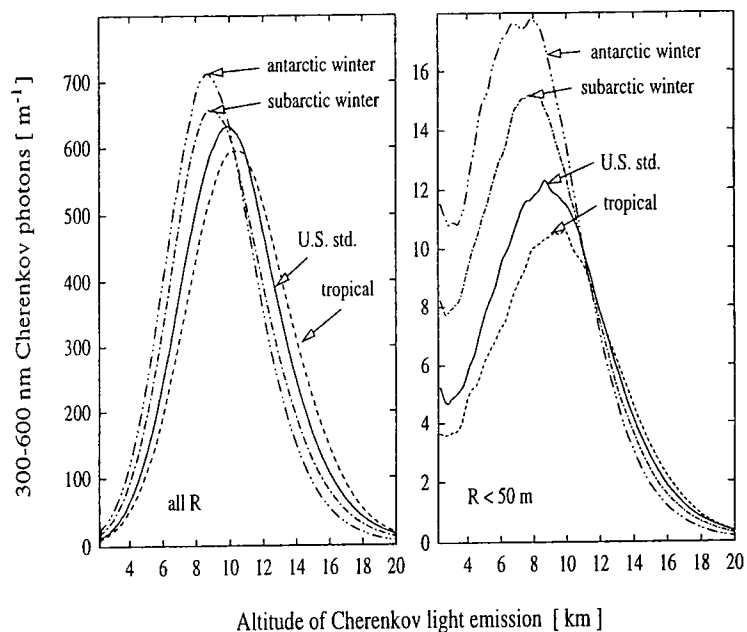


Figure 7.2: Average Cherenkov light emission along the shower axis for vertical 100 GeV gamma-rays with different atmospheric profiles. Left: all emitted photons; right: photons that would arrive within 50m from the core at an observation level of 2200m. No absorption is applied here. Taken from [17].

The amount of Cherenkov light within 500m radially from the core is proportional to $(n-1)$ at the shower maximum, with about 15% difference between tropical and Antarctic winter. If light arriving extremely far from the shower core is included, the difference is even smaller. Close to the core, however, differences are substantial for many reasons. As the amount of Cherenkov light is roughly proportional to $(n-1)$ at median altitude

h_{med} of Cherenkov emission (or shower maximum), then with increasing $(n-1)$ at h_{med} the Cherenkov cone opening angle is increased and the light is spread over a greater area, decreasing the central light density. Also with decreasing h_{med} the distance between shower maximum and observer is decreased, increasing the central light density. For Cherenkov light near the core the median height of emission h_{med}^* is typically 1-1.5Km below that of all Cherenkov light, emphasising therefore the geometrical factor even more.

One can estimate the central light density ρ_c for vertical showers as:

$$\rho_c \propto \frac{n_{\text{med}} - 1}{(n_{\text{med}} - 1)(h_{\text{med}}^* - h_{\text{obs}})^2} = (h_{\text{med}}^* - h_{\text{obs}})^{-2} \quad (7.4)$$

where h_{obs} is the observation level altitude. The numerator accounts for the Cherenkov emission, the denominator for the area of the light pool. As can be seen the dominating factor is geometrical, the difference in altitude between the height of median light production and the observation level. Since for increasing energy h_{med} approaches the height of observation, the geometrical factor becomes increasingly important.

7.2.1 Profile Calibration

A radiosonde is a set of atmospheric monitoring equipment mounted on a Helium filled balloon. The system possesses a radio transmitter, and a base station on the ground records the atmospheric data as the balloon rises. Typically a radiosonde has a thermometer, barometer and hygistor (a humidity sensor). Radiosonde measurements of temperature and pressure close to sites of Cherenkov telescopes are being increasingly compared with the atmospheric profile models used in the simulations of EAS.

As can be seen from figure 7.3, the tropical atmosphere fits most closely the atmosphere believed to exist above the H.E.S.S. site. The H.E.S.S. group intends to launch regular radiosonde equipment in order to maintain a constant check on the atmospheric profile.

The Durham group did some work on trying to understand the atmospheric profile which best suited its former site in New South Wales. Data from a nearby radiosonde stations has been compared with the MODTRAN US standard and Tropical atmospheric profiles, to see which represented a better fit. This is shown below in figures 7.4 and 7.5. As can be seen, the atmosphere above the Durham Mark 6 telescope site is believed to possess a profile that at shower maximum was intermediate to these two models in temperature and pressure.

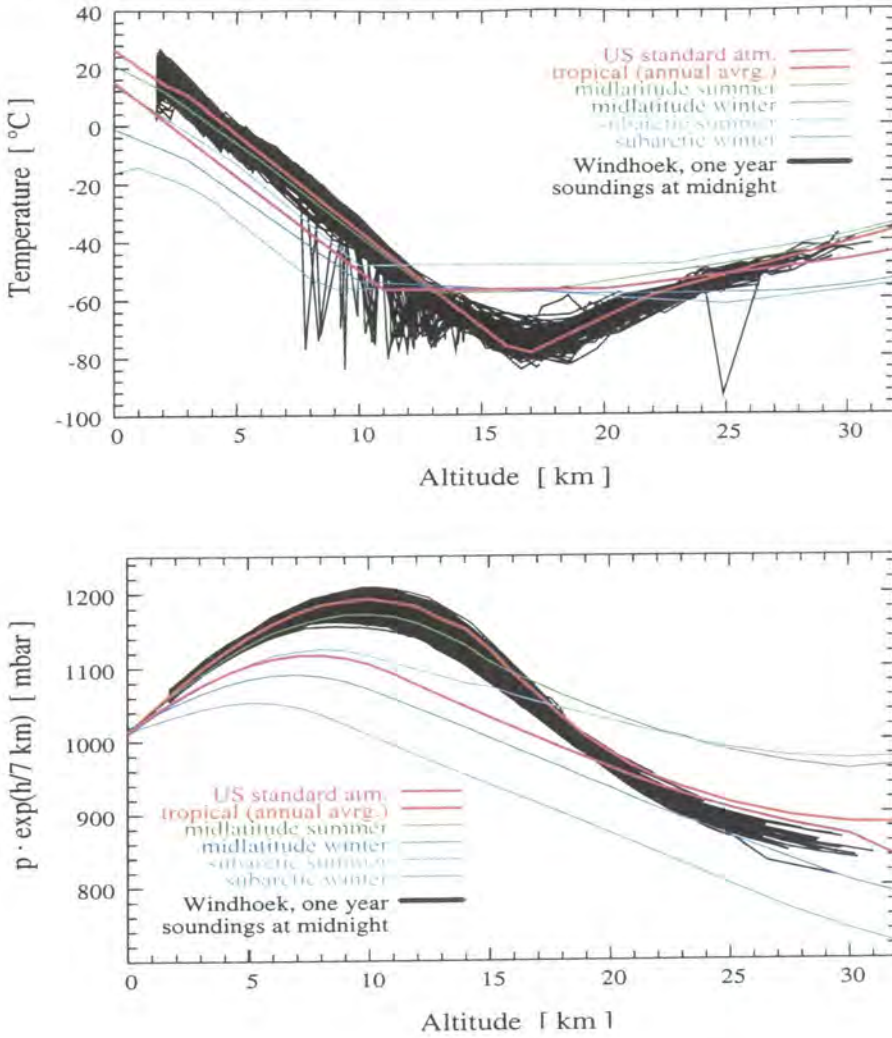


Figure 7.3: Measurements of sky temperature and pressure taken from Namibian capital of Windhoek, some 100km from H.E.S.S. site, as compared to simulated atmospheric profiles produced with MODTRAN [63].

7.3 Attenuation of Cherenkov Light

As mentioned in chapter 2, the atmospheric attenuation of the Cherenkov light is another source of possible error for energy calibration of ground-based Cherenkov telescopes and also possibly for the Hillas parameter imaging technique. Several sources of extinction exist, namely: absorption bands of several molecules, molecular (Rayleigh) scattering and aerosol scattering and absorption; see figure 7.6. However, most Cherenkov light in the PMT sensitive range is lost by molecular and aerosol (Mie) scattering. Unlike Rayleigh scattering, which may be estimated given atmospheric measurements of tem-

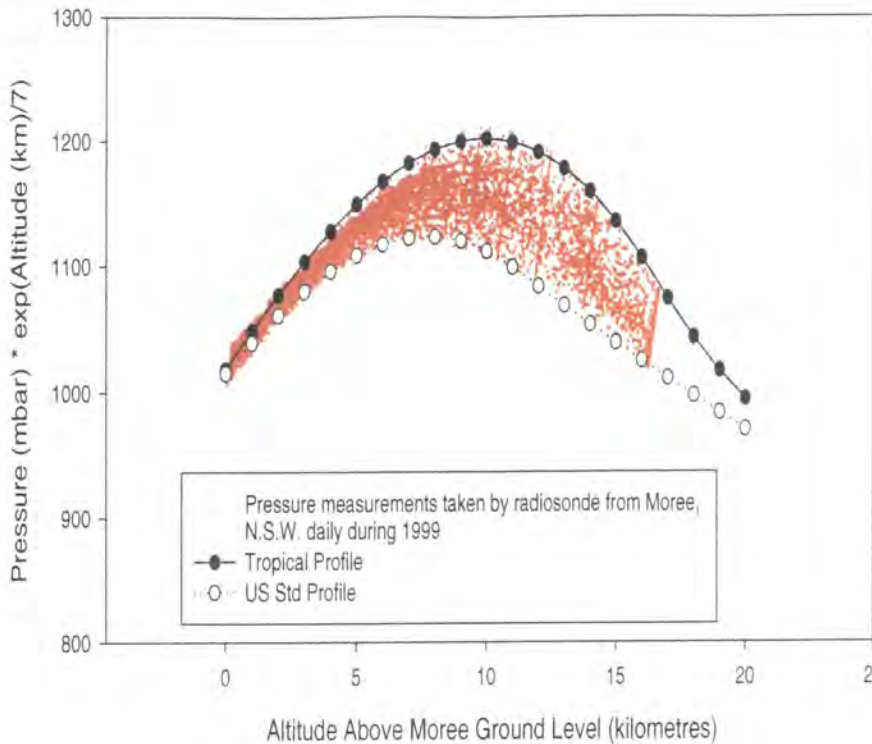


Figure 7.4: Measurements of atmospheric pressure taken from Moree [168] approximately 100 km from the Mark 6 telescope site. As can be seen, around shower maximum the results lie mainly between the MODTRAN US standard and Tropical models.

perature and pressure, Mie scattering is dependent on the structure and composition of aerosol molecules, and thus these must be measured directly, as shall be discussed later. Although some light may be scattered into the viewing angle, telescope triggering and imaging make this light unimportant, and to this extent scattering can be thought of as an attenuation process. While molecular scattering is easily predictable and almost constant at any given site, aerosol scattering is site dependent and time variable. The largest day to day aerosol variations are likely to be limited to the 'boundary layer', typically the first 1-2.5Km above the surrounding terrain where the dependence on ground material and wind speed is greatest. In the boundary layer, the heating of the ground due to solar radiation leads to rapid exchanges of dust and air. However, it should be noted that, aerosols occur even in the stratosphere due to meteoric and volcanic dust.

One can measure the extinction of star light optically (as the H.E.S.S. group do at their Namibian site); this is fitted to the function:

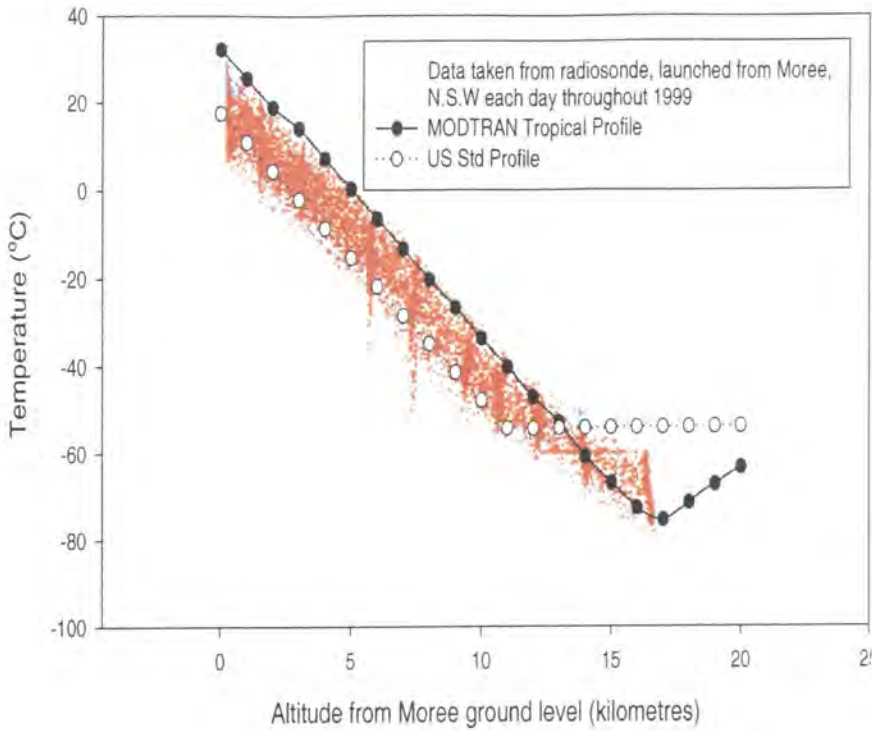


Figure 7.5: Measurements of atmospheric temperature taken from Moree [168] approximately 100 km from Mark 6 telescope site. As can be seen, around shower maximum the results lie mainly between the MODTRAN US standard and Tropical Models.

$$\ln I(\lambda) = \ln I_0(\lambda) - \tau_1(\lambda) \sec z \quad (7.5)$$

In this equation I is the measured Intensity, I_0 the actual intensity, τ the optical depth and z is the zenith angle. By measuring one or many sources at different zenith angles, z and τ can be fitted closely. However, the vertical structure of the absorbing particles is not taken into account by this formula. Even at mountain altitudes, different assumptions on the vertical structure of the aerosols can lead to a 10 – 15% difference in Cherenkov light density; at sea level these differences can be as much as 30%. For example, often the density of aerosols is taken to be proportional to the air density. This can however lead to overestimates of between 4 and 8% in Cherenkov light density at mountain altitudes, even if the measured star light extinction is taken into account. This is because the Cherenkov light is produced approximately half way down in the atmosphere, implying 50% of the star light extinction using this simplistic model. However, actually 80- 90% of the light extinction occurs below the average Cherenkov photon production altitude.

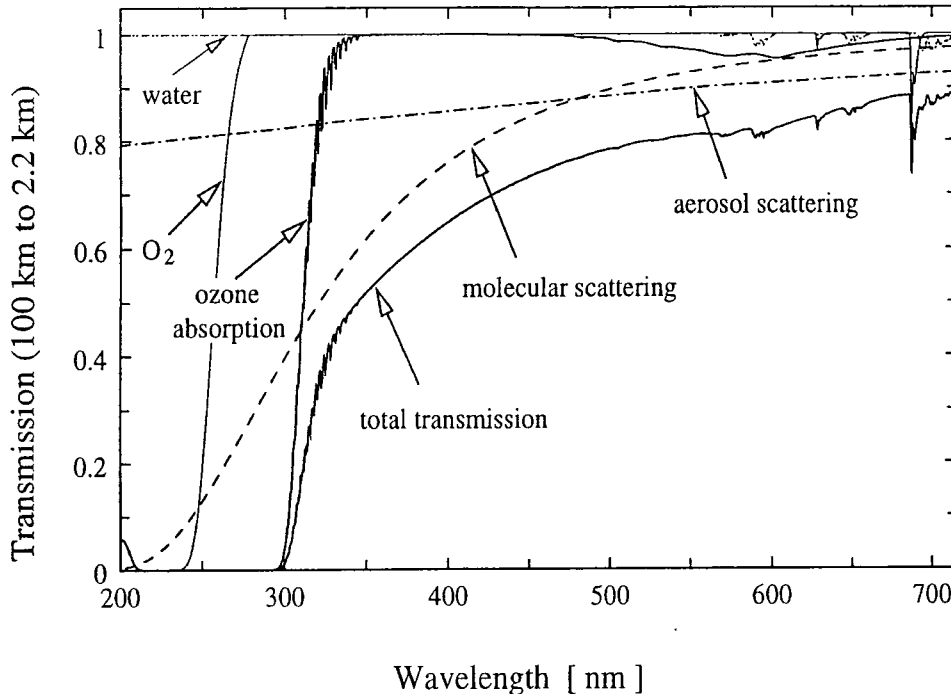


Figure 7.6: Direct transmission of light from space (here 100km altitude) along a vertical path to an altitude of 2.2km, as calculated with MODTRAN. The impact of the most important absorbers and scatterers are shown. Taken from [17].

A more realistic version of aerosol vertical structure is found in the MODTRAN program [63]. Figure 7.7 shows the transmission curves for light emitted from different altitudes arriving at a ground level of 2200m (the HEGRA site) using a MODTRAN US standard profile, with a low-level rural haze model with 23km horizontal visibility.

The task now is to compare these models with data taken at the sites of the new generation of Cherenkov telescopes.

7.4 Mapping the Aerosol Structure

The Durham group is operating a LIDAR system at the H.E.S.S. site. LIDAR (Light Detection and Ranging) is a system that produces pulses of light via a LASER, the light scattered back from aerosols is then recorded by a detector mounted paraxially. The time between signal departure and backscatter arrival allows the altitude of the scattering aerosols to be calculated. The group also maintains a paraxial and all-sky monitoring mid infra-red radiometer to study high level cloud above the H.E.S.S. site. Finally, the

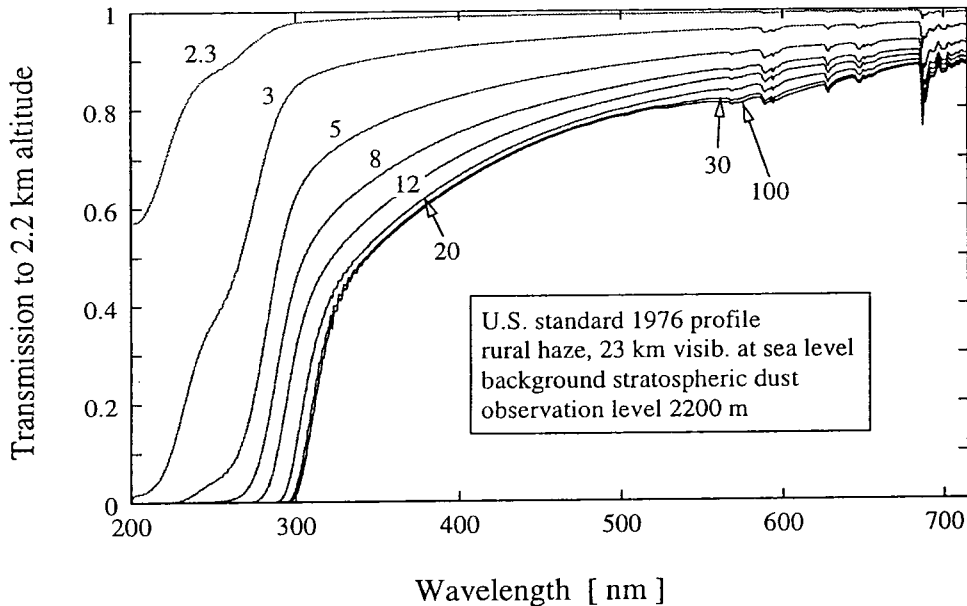


Figure 7.7: Direct transmission of light along vertical paths from different altitudes (in km), to an observation level of 2200m. Transmission was modelled with MODTRAN for US Standard atmospheric profile, rural haze with 23km sea level horizontal visibility, and background stratospheric dust. Taken from [17].

group will also be in charge of a system to monitor very low-level aerosol populations, by studying the transmission of light from calibrated light sources at the H.E.S.S. site whose light reflects off corner reflectors placed on hills near the H.E.S.S. site. The theory behind these different techniques is now briefly discussed.

7.4.1 Horizontal Extinction Length Monitor

The goal of studying light attenuation from calibrated sources on distant hills is to determine the combined Rayleigh and Mie low-level extinction length, $\Lambda(\lambda)$:

$$\frac{1}{\Lambda(\lambda)} = \frac{1}{\Lambda_M(\lambda)} + \frac{1}{\Lambda_R(\lambda)} \quad (7.6)$$

This should be measured at several wavelengths comparable to Cherenkov photon wavelengths (in the range 280 to 640 nm). The planned instrument, includes a calibrated pulsed LASER light source on the site. The instrument shines onto a remote corner reflector, the returned light is then detected by a photodiode at the focus of an optical

telescope. The system is placed in a phase locked loop, which allows the signal to be determined, even if only a relatively small flux of photons returns. In some senses, this is similar to the instrument detailed in [138].

7.4.2 Optical Depth Monitor

The optical depth above the H.E.S.S. site is monitored by a single wavelength Vaisala CT25K LIDAR system. The LIDAR consists of a pulsed 905nm LASER and an avalanche photodiode receiver. The receiver measures the intensity of the photons as a function of time, which is of course equivalent to the intensity of photons versus distance to the point of back scattering. The observed intensity is then given by (taken from [138]):

$$I(z, \alpha) = I_o T_{out} T_{back} \left(\frac{1}{\Lambda_M(z)} \frac{1}{\sigma_M} \left(\frac{d\sigma_M}{d\Omega} \right) + \frac{1}{\Lambda_R(z)} \frac{1}{\sigma_R} \left(\frac{d\sigma_R}{d\Omega} \right) \right) \Delta s \Delta \Omega \quad (7.7)$$

Here I_o is the outgoing LIDAR beam intensity, T_{out} and T_{back} are the transmission factors for out-going and incoming light respectively. $\Lambda(z)$ are the extinction lengths at altitude z , $\Delta s = c\Delta t/2$ is the length of the scattering region (set by the LIDAR time bins). $\Delta \Omega$ is the solid angle subtended by the LIDAR mirror, and $\frac{1}{\sigma_M} \left(\frac{d\sigma_M}{d\Omega} \right)$ is the Mie phase function and $\frac{1}{\sigma_R} \left(\frac{d\sigma_R}{d\Omega} \right)$ is the Rayleigh phase function, with σ being the corresponding cross-section. By studying ratios of backscattered LIDAR measurements ($I(z, \alpha)$) for the same altitude (z), but at different angles (α), the phase function and extinction lengths (which are not known for the case of aerosol scattering) cancel and the sum of the Rayleigh and Mie optical depths is obtained.

In addition, the Durham group plans to construct a multi-wavelength LIDAR system. Given that Mie Scattering is dependent on wavelength, one may probe the composition of the aerosols, and by incorporation of best fitting MODTRAN model in EAS simulation, study this as a function of Cherenkov light attenuation. Current work on multi-wavelength LIDAR has been performed by a group at the University of Hawaii in studying marine aerosol concentrations, as detailed in [123].

The results so far have indicated a very clear and stable atmosphere above the H.E.S.S. site. For instance, the optical depth profile taken in June 2002 at the H.E.S.S. site with the Vaisala CT25K LIDAR system is shown below in figure 7.8. Each bin represents 30 metres in altitude above the H.E.S.S. site, and thus the limit of the LIDAR system, as shown in figure 7.8 is 7.5km above ground level. The optical depth here is calculated by taking the back scattered light within a bin and calculating the fraction returned. Thus

Figure 7.8 indicates a perfectly clear atmosphere with optical depth being almost linearly related to altitude. Aerosols are doubtless present within the atmosphere, however their densities are below those recordable with the LIDAR system.

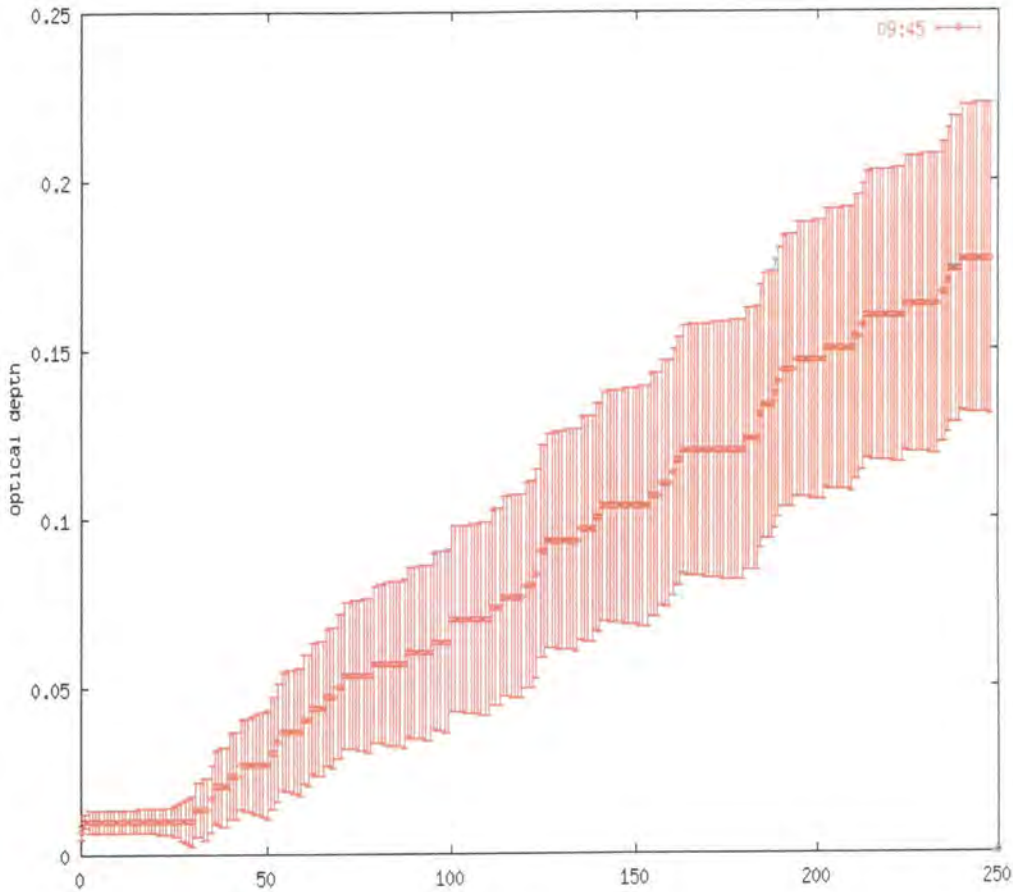


Figure 7.8: Results taken from with the CT25K Vaisala LIDAR system at the H.E.S.S. site in June 2002, prior to the stand-alone H.E.S.S. telescope first light.

7.4.3 Sky Clarity using a mid Infra-Red Radiometer

The Durham group have worked on their own, as well as with the HEGRA and H.E.S.S. collaborations, in mounting an infra-red radiometer paraxially with a Cherenkov telescope, to measure the infra-red signal between 12 and 14 microns integrated along the line of sight to the source. This basically gives a sky temperature, and as clear sky is colder than sky containing high level aerosols, the presence of high level clouds (invisible to the naked eye at the low background light levels required for Cherenkov astronomy) can be mapped with the radiometer. This becomes useful, if when studying a rapidly flaring AGN, one sees a dip in the TeV signal, one needs to ascertain whether this was

an effect from the source or simply due to the presence of high level aerosol scattering. The Durham group (both at Narrabri, and at the HEGRA site on La Palma) was able to show an anti-correlation between off source cosmic rate trigger rate and sky temperature. As can be seen from figures 7.9 and 7.10 as the sky temperature increases as cloud drifts into the field of view, so the off source cosmic ray trigger rate drops.

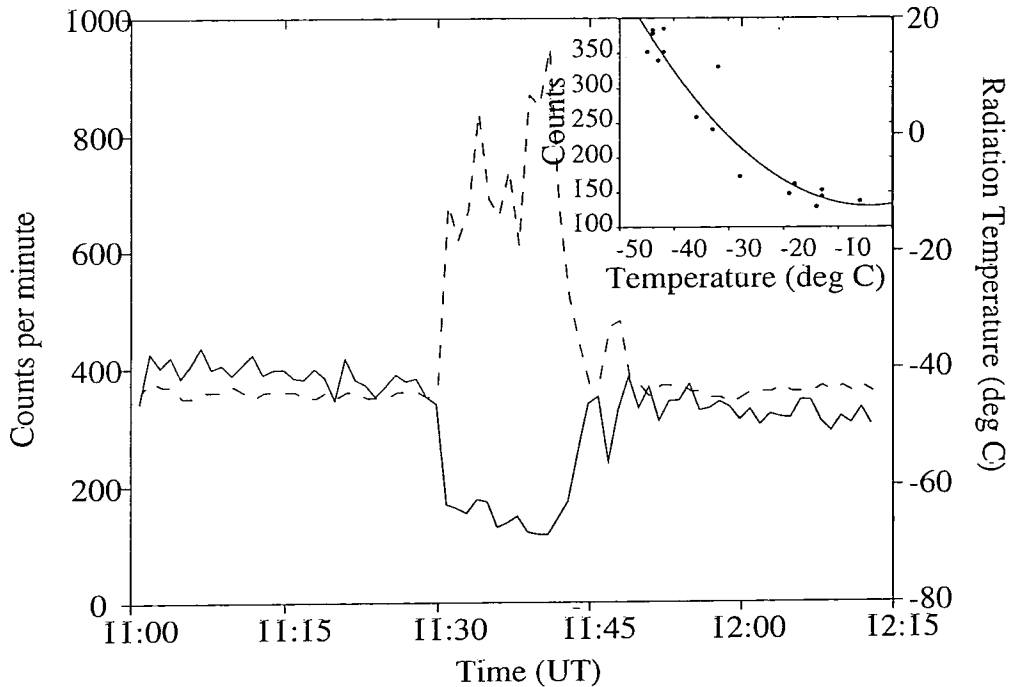


Figure 7.9: Dotted line showing variation of sky temperature as measured by mid infra-red radiometer, versus solid line indicating cosmic ray trigger rate for the Durham Mark 6 telescope. Taken from [194]

7.4.4 Stellar Photometry Measure

In addition the H.E.S.S. collaboration possess several robotic optical telescopes at the site to perform stellar photometry on many stars known to emit in the UV and optical wavebands with a given flux. This gives another measure of light extinction; however, as mentioned before, it is an integrated study and therefore altitude independent.

7.5 Further Simulation Studies of Atmospheric Effects

In an earlier section of this chapter, general arguments for the atmospheric attenuation were presented. These discussions are now continued, in particular with a look at the

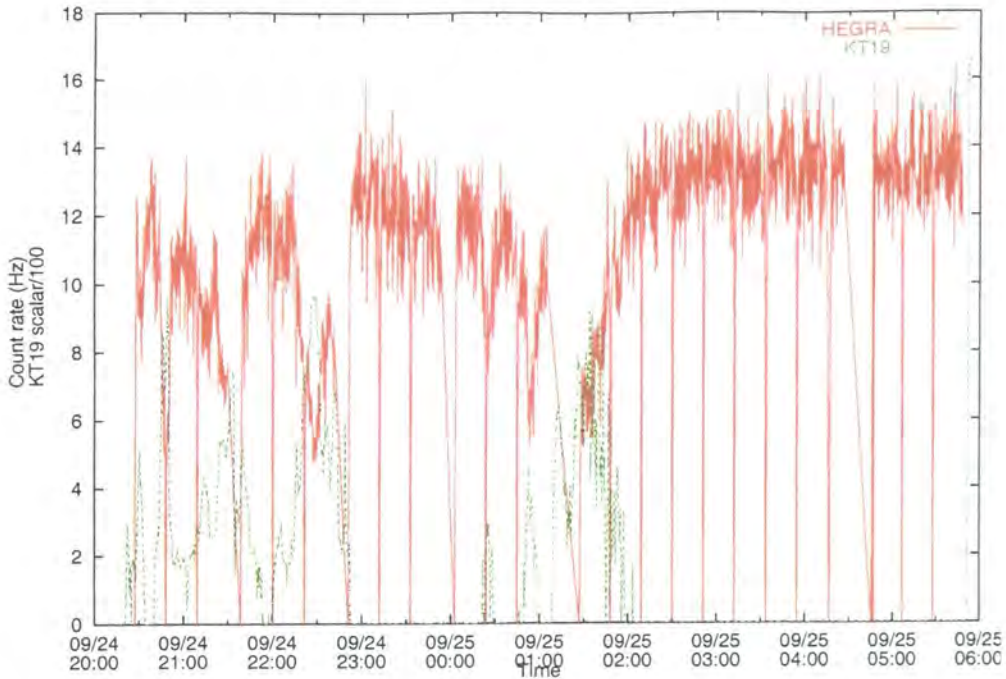


Figure 7.10: Green line showing scaled variation of sky temperature as measured by mid infra-red radiometer, and red line indicating cosmic ray trigger rate for on and off source for HEGRA CT6 telescope plotted against time for night of September 24th 2000.

differences these effects have on hadronic and gamma-ray initiated EAS by using simulations performed with MOCCA. As before, the telescopes are randomly placed within 300 m of the core for cosmic ray and gamma-rays below 1 TeV, and 500 m for the gamma-rays above 1 TeV. This leads to a small systematic flattening of the gamma-ray response at 1 TeV, which may be ignored in all future plots. This work serves as a test of the performance of next generation Cherenkov telescope systems in different atmospheres, and studies the effects of atmospheric structure on effective sensitive area.

As a first attempt at matching the aerosol structure at the Namibian site, the absorption tables for different aerosol structures have been applied to a database of 20,000 gamma-ray showers and 31,000 cosmic ray showers produced with MOCCA. The gamma-ray showers have energies ranging from 0.05 to 30 TeV and are distributed with the spectral slope as according to [201] (differential value -2.45). The cosmic rays range between 0.1 and 10 TeV and follow the spectrum described in [204] and in table 6.8. The aerosol models applied were produced with MODTRAN4, [63], and are further detailed in appendix B. Unless stated all showers develop using the tropical profile model. In the following sections, the effects of the various different aerosol models applied, and the results

of the simulations with respect to the effective area of the stand-alone H.E.S.S. telescope are discussed. Throughout, a test case ('sim0'), of simulations without any atmospheric attenuation whatsoever is used.

7.5.1 Ground at Different Levels

When simulating aerosol structure at the H.E.S.S. site with MODTRAN4, the first important question is how to define the boundary layer (the layer between ground level and 2 km above this). The HEGRA group, whose telescopes were on a coastal mountain top, found good agreement by placing the ground level at sea-level, even though their telescope was at 2200 m. In effect their atmospheric attenuation simulations include no part due to local haze whatsoever. However, if one places the ground level at the telescope altitude, the atmospheric aerosol density is increased slightly as one scales the structure of the first 100 km to (100 km-telescope altitude), i.e. ~ 98 km for the H.E.S.S. site. Putting the ground level at sea level corresponds to the most optimistic case, where light attenuation in all but the uppermost 200 m of the boundary layer is ignored. Putting the ground level at the telescope altitude corresponds to the most pessimistic case with a significant amount of low-level attenuation. However, it is unknown at the moment which is the best case for the H.E.S.S. site of a Namibian plateau at 1800 m; this ultimately depends on the terrain and wind speed [19]. The effects on the sensitive area for cosmic rays and gamma-rays are shown below.

Gamma-Rays

Figure 7.11 shows the effective area for gamma-rays in both cases. Here the current H.E.S.S. standard aerosol structure is assumed, this consists of a maritime haze model from 0 to 2 km, with a tropospheric spring-summer model from 2 to 10 km and default stratospheric dust. Also included for comparison is sim0. As can be seen due to the greater attenuation, the effective area of the telescope is lower when the ground level is placed at the telescope altitude. This is more pronounced at lower primary energies, because the photon yield from the shower at these energies is smaller, and therefore the effects of attenuation are more noticeable. The effect at 0.05 TeV is to introduce a difference of a factor of 5/2 in effective area dependent upon where the boundary layer is placed.

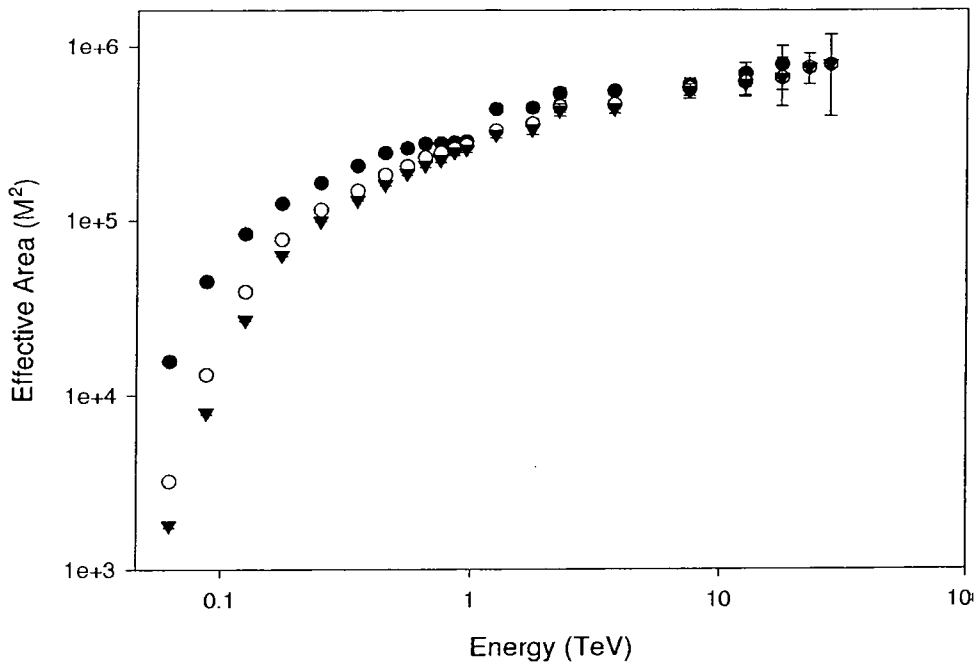


Figure 7.11: The effective sensitive area of a stand-alone H.E.S.S. telescope to the discussed spectrum of gamma-rays, given a tropical atmospheric profile, and with zero aerosol attenuation (sim0 - represented by filled circles), and aerosol attenuation with ground level at 0m a.s.l. (white circles) and 1800m a.s.l. (triangles).

Cosmic Rays

As shown in chapter 2, cosmic ray initiated EAS produce less Cherenkov light than gamma-ray initiated EAS with the same primary energy, as a large fraction of the energy goes into π^+ and π^- sub-cascades which may decay to produce muons, which produce much less Cherenkov light than electron-positron cascades as shown in table 2.1. Therefore, the effective area for cosmic rays is much less than for gamma-rays. Also, as cosmic rays are more penetrating than gamma-rays, the overall effect of atmospheric attenuation is slightly less, as shown if one compares figures 7.11 and 7.12. As one can see from figure 7.12, for these reasons, the overall effect of the atmospheric model changes on the effective area is smaller for cosmic rays than gamma-rays, though as in the gamma-ray case, the attenuation is most significant at the lowest energies. It should be noted that at the lowest energies simulated (0.1 TeV), the difference in ground level leads to approximately the same ratio difference in telescope effective area as for gamma-ray EAS. Given that this directly affects the trigger rate, it is an important number for the data acquisition for the H.E.S.S. system. Therefore, a ground level at sea level is used to make estimations of

computing power requirements, and unless stated this assumption is used in the following presented simulations.

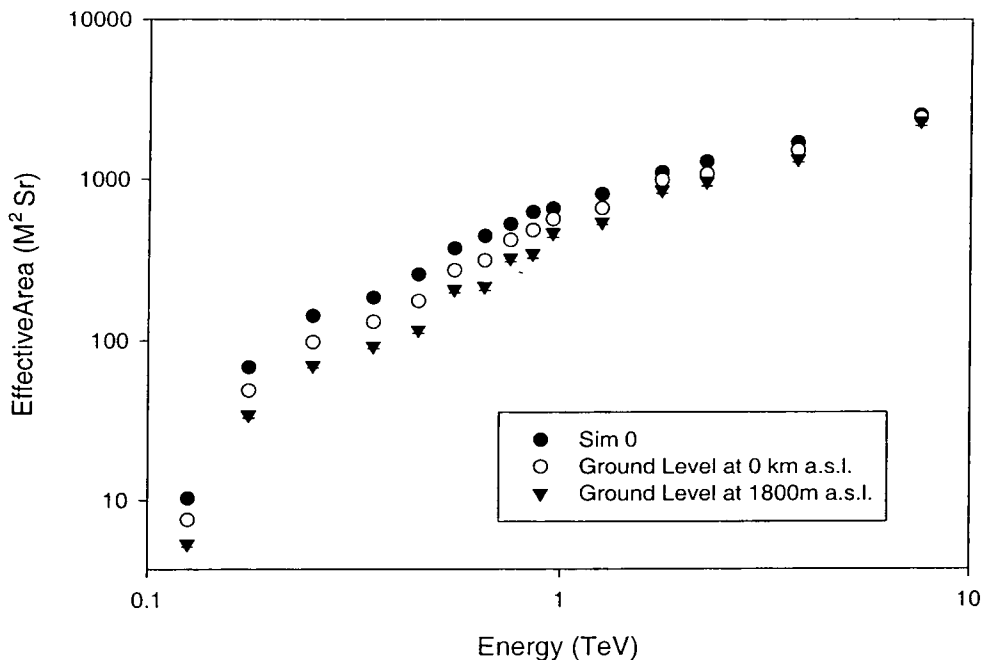


Figure 7.12: The effective sensitive area of a stand-alone H.E.S.S. telescope to the discussed spectrum of cosmic rays, given a tropical atmospheric profile, and with zero aerosol attenuation (sim0), and aerosol attenuation with ground level at 0m a.s.l. and 1800m a.s.l.

7.5.2 Aerosols at Different Levels

The second set of simulations study which parts of the atmospheric aerosol structure have the most dramatic effect on the Cherenkov light seen at the H.E.S.S. site. To the simulated Cherenkov light produced by spectra of cosmic rays and gamma-rays, absorption tables based on:

- Zero attenuation (sim0)
- A tropospheric dust model (with spring summer assumptions (see appendix B) from 2-10 km only.
- A tropospheric model (with spring-summer assumptions from 2-10 km) and a low-level (0-2 km) rural haze model.

are then applied, and a comparison for gamma-rays and cosmic rays is presented.

Gamma-Rays

The effects on the effective sensitive area of the stand-alone telescope based on these three aerosol models are shown in figure 7.13. As can be seen the tropospheric dust attenuates the signal highly at the lowest energies reducing the number of triggers by a factor of $\sim 1/5$, the low-level aerosols then further reduces the trigger number by a factor of $\sim 1/1.5$. Thus although the tropospheric model (which may be probed by a multi-wavelength LIDAR) is dominant, this plot shows that the low-level light (monitored by the lights on distant hills system) must be monitored too.

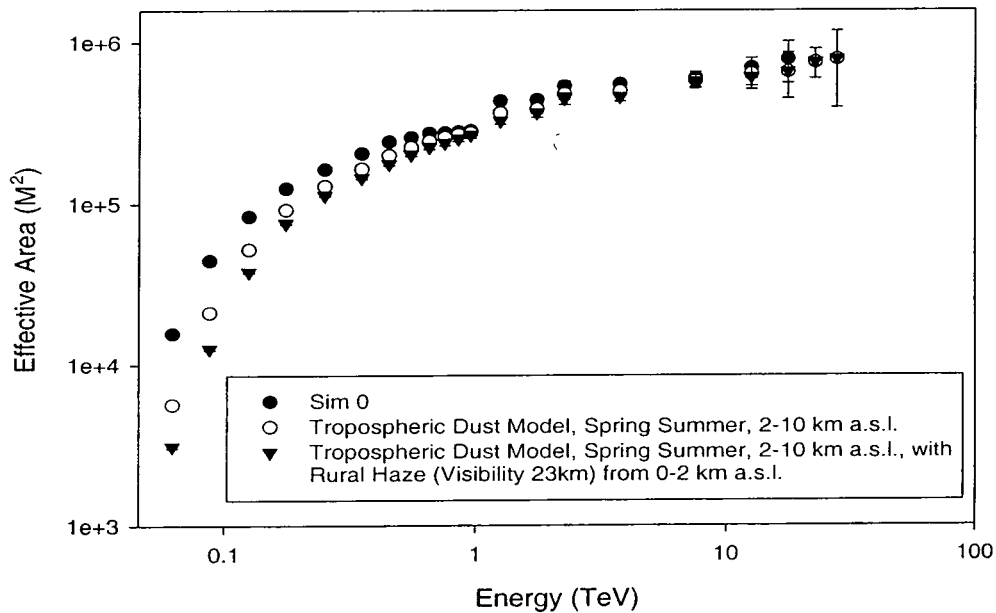


Figure 7.13: The effective sensitive area of a stand-alone H.E.S.S. telescope to the discussed spectrum of gamma-rays, given a tropical atmospheric profile, with zero aerosol attenuation (sim0), and attenuation due to higher level (2-10km) with tropospheric dust and also with tropospheric and low-level (0-2km) rural haze attenuation models applied.

Cosmic Rays

Figure 7.14 shows the same response for cosmic rays. It indicates again that cosmic rays are less sensitive to changes in aerosol structure. At the lowest energy simulated again, the tropospheric model dominates the attenuation, reducing the trigger number by a factor

of $\sim 1/2$, with the addition of aerosols further reducing the trigger number by a further $\sim 4/5$.

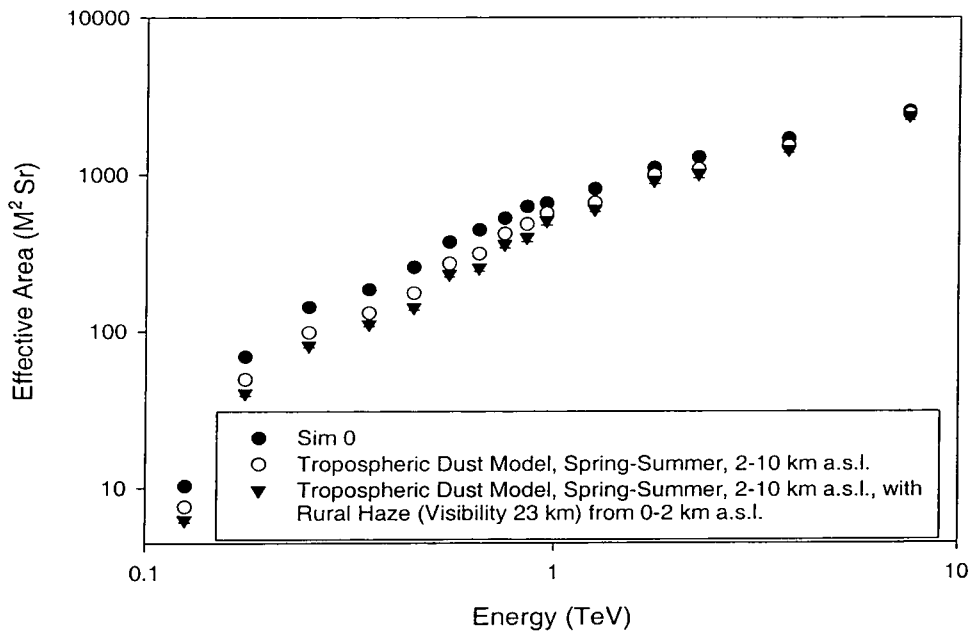


Figure 7.14: The effective sensitive area of a stand-alone H.E.S.S. telescope to the discussed spectrum of cosmic rays, given a tropical atmospheric profile, with zero aerosol attenuation (sim0), and attenuation due to higher level (2-10km) with tropospheric dust and also with tropospheric and low-level (0-2km) rural haze attenuation models applied.

7.5.3 Different Aerosol Structures

The actual constituents of the low-level aerosol part of the atmospheric model may be changed. The default horizontal visibilities available within MODTRAN are: 5 km (a far too high attenuation for Cherenkov astronomy), 23 km (the case used so far) or 50 km. The results for gamma-rays and cosmic rays are presented.

Gamma-Rays

It is no surprise if figure 7.15 is considered, that increasing the visibility to 50 km increases the sensitive area of the Cherenkov telescope. Again of course as in all these cases, the lower energy events are more effected than those above 0.3 TeV.

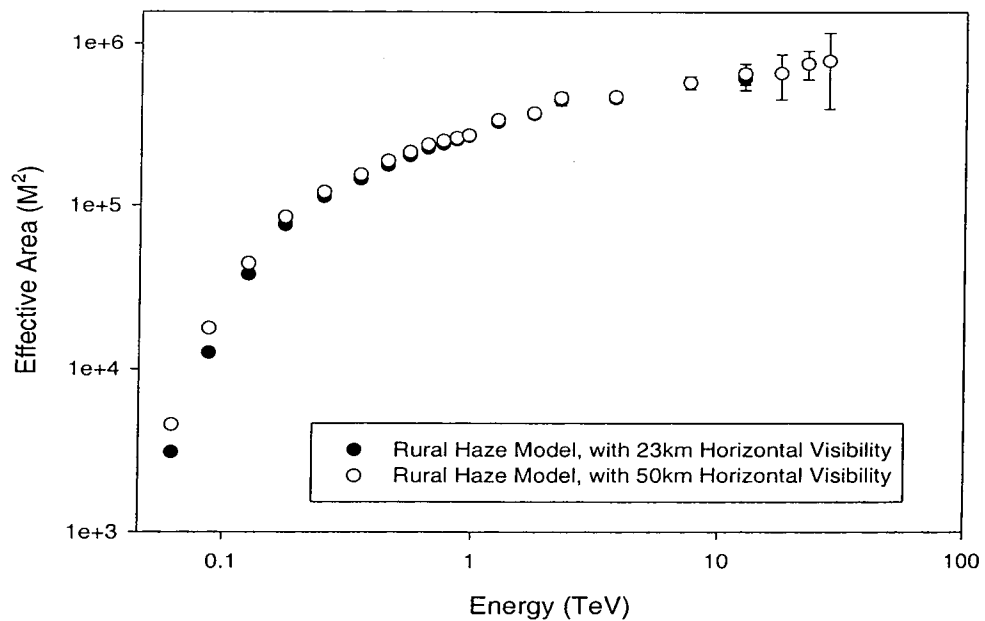


Figure 7.15: The effective sensitive area of a stand-alone H.E.S.S. telescope to the discussed spectrum of gamma-rays, given a tropical atmospheric profile, and with aerosol attenuation due to low-level (0-2km) rural haze, with 23km and 50km horizontal visibility applied.

Cosmic Rays

As figure 7.16 shows the cosmic rays are barely effected by changes in the low-level aerosol model, even compared to the small response of gamma- rays to this effect.

7.5.4 Changes in Tropospheric Model

One may also change the type of tropospheric model used. The suggested atmosphere for Namibia is the spring-summer tropospheric model; however the result may be compared with the result given for effective sensitive area using the autumn-winter profile.

Gamma-Rays

Only the result for gamma-rays is presented here in figure 7.17, as the cosmic ray result is very similar, with no significant differences between the two atmospheric models.

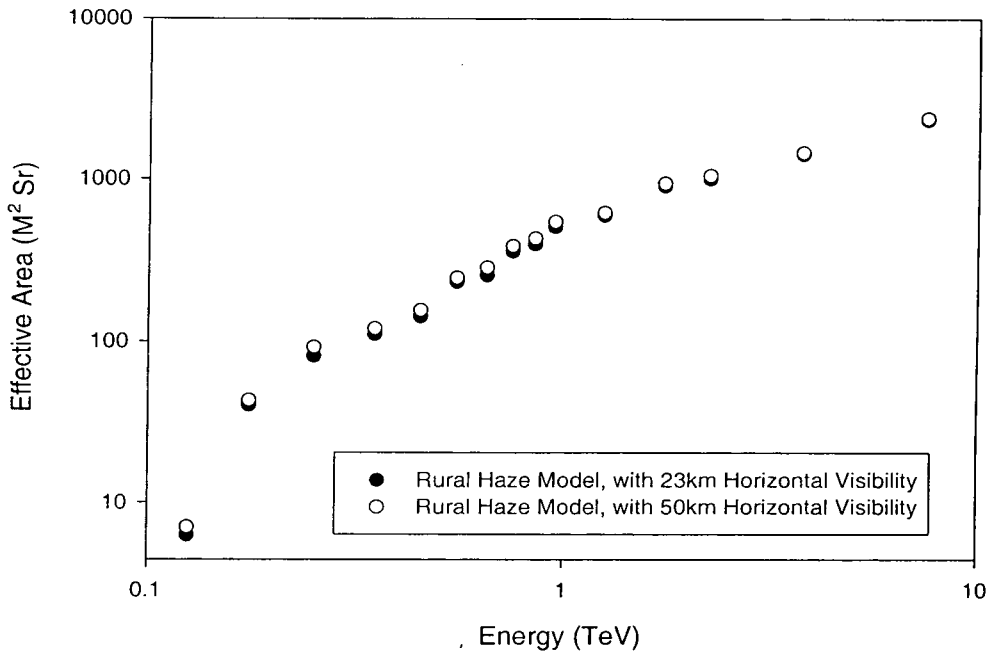


Figure 7.16: The effective sensitive area of a stand-alone H.E.S.S. telescope to the discussed spectrum of cosmic rays, given a tropical atmospheric profile, and with aerosol attenuation due to low-level (0-2km) rural haze, with 23km and 50km horizontal visibility applied.

7.5.5 Current Standard Model

The current standard atmospheric attenuation model for the H.E.S.S. site, is to use a maritime haze model for 0-2km, with tropospheric spring-summer model from 2-10km and a layer of default stratospheric dust, with the ground level set at sea level, not at the H.E.S.S. site altitude of 1800m. The coastal maritime haze model has no real reason for application (the site being over 100km from the coast). This low-level aerosol model is less attenuating than the rural haze model as indicated in figure 7.18.

Given these investigations into the effects of aerosol attenuation on the gamma-ray Cherenkov signal, it can be seen that changes in aerosol distributions have the largest effect for events with primaries at or under 0.3 TeV. The most likely cause for day to day variation in the effective area (and therefore trigger rate) of the telescope, are changes in aerosol structure in the first 2 km above the H.E.S.S. site. A further investigation of the effects of increasing the aerosol concentration in this region, with particular reference to Hillas parameters, will follow later in this chapter. In the next section however, the data taken from radiosonde measurements made at the Namibian capital (Windhoek) will be

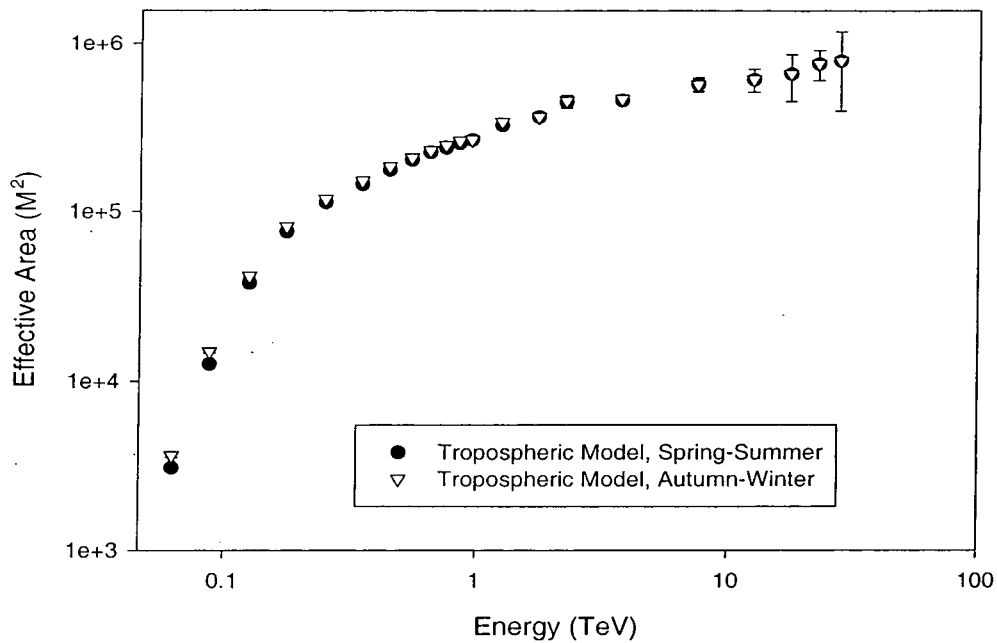


Figure 7.17: The effective sensitive area of a stand-alone H.E.S.S. telescope to the discussed spectrum of gamma-rays, given a tropical atmospheric profile, and with aerosol attenuation due to low-level (0-2km) rural haze at 50km horizontal visibility. Attenuation due to spring-summer and autumn-winter tropospheric models are applied separately.

used to generate atmospheric profiles and absorption models based around these measurements. By utilising these atmospheric profiles when generating cosmic and gamma-ray showers with MOCCA, the effects of taking the Windhoek winter and summer measurements, as opposed to the tropical profile, on the effective area of the stand-alone H.E.S.S. telescope will be shown.

7.5.6 Atmospheric Profile Effects

In studying the H.E.S.S. site, the data shown in figure 7.3 indicates that the tropical atmosphere is representative of the average atmosphere above the Namibian capital Windhoek. Assuming this atmosphere is identical to that at the H.E.S.S. site (some 100km away), the differences in effective sensitive area which occur if one uses the maximum Windhoek profile and minimum Windhoek profile as opposed to the tropical profile are now discussed. To achieve this, we take the temperature profile, and fit it with linear sections, i.e. for one linear section $T(h) = T_0 - \Gamma h$, where h is the altitude. Given the ideal gas and the hydrostatic equation, i.e:

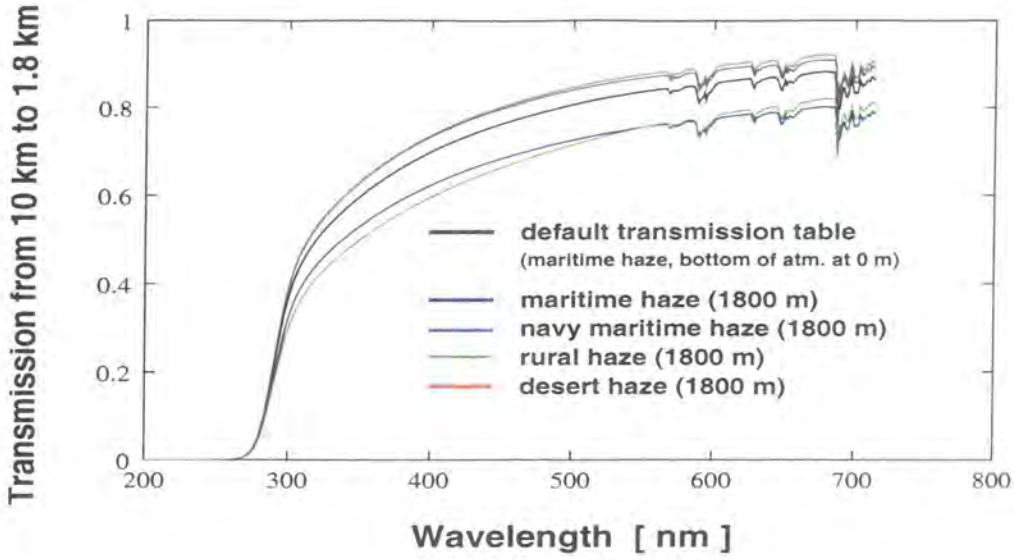


Figure 7.18: The transmission from 10 to 1.8 km a.s.l. in the Cherenkov wavelength range given different low-level (0-2km) aerosol attenuation model.

$$P = \frac{R}{\mu} \rho T \quad (7.8)$$

$$\frac{dP}{dh} = -g\rho \quad (7.9)$$

where P is pressure, ρ is gas density, T is temperature, R is the molar gas constant, μ is the mean molecular weight of air, and g is the acceleration due to gravity. If we consider each section independently then we may take the altitude of the bottom of each section to be 0. Thus the following relation may be derived for each atmospheric section:

$$\frac{P}{P_o} = \exp \left(-A \int_0^h \frac{dh}{T(h)} \right) \quad (7.10)$$

where P_o is the pressure at the lower atmospheric boundary, and $A = \mu g/R$.

Therefore:

$$\frac{P}{P_o} = \left(1 - \frac{\Gamma}{T_o} h \right)^{\frac{A}{\Gamma}} \quad (7.11)$$

or more simply:

$$P = P_o(1 - ah)^b \quad (7.12)$$

Given the atmospheric boundaries suggest by the temperature profile, we fit this function to the pressure profile, and calculate the depth in g cm^{-2} for various height in metres above sea level. As can be seen from figure 7.19, this approach fits the models well, though it must be noted that the temperature above 20km is extrapolated and not actually radiosonde recorded.

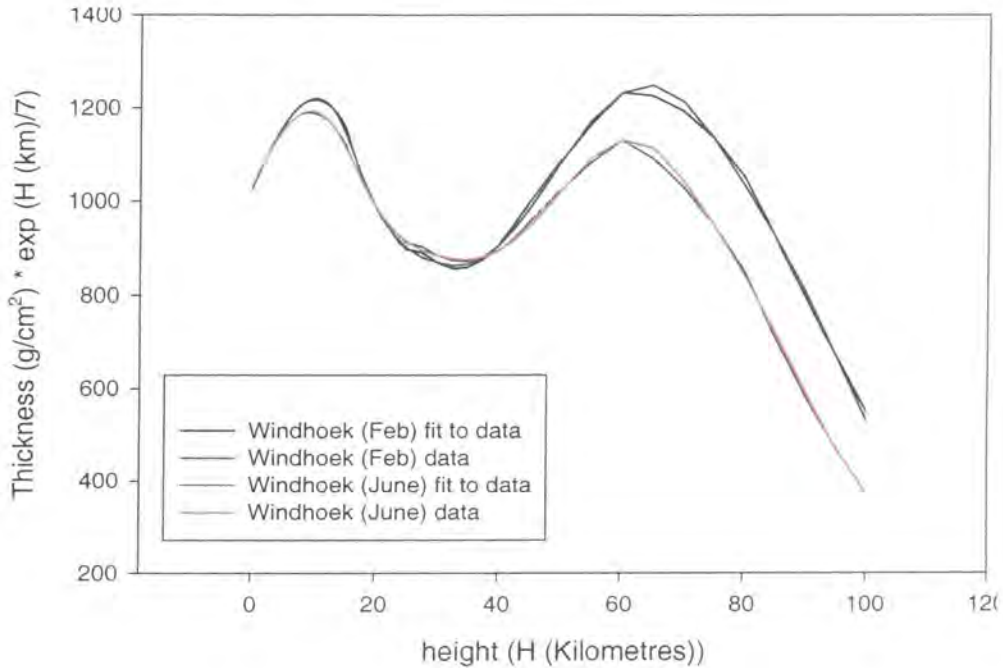


Figure 7.19: Figure shows atmospheric thickness measurements for Windhoek in February and June 1999, and the fits used with MOCCA [87] in the shower simulation.

These two slightly different atmospheric profiles are used to perform simulations of the spectra of gamma-rays and cosmic rays with MOCCA (with identical random number seeds). In the telescope simulation, atmospheric attenuation produced with MODTRAN based around these measurement is applied, as outlined in appendix B. Figure 7.20 and 7.21 show the effect of the two profiles on the effective sensitive area for the stand-alone H.E.S.S. telescope for gamma-rays and cosmic rays. This is only a small effect, as one can see from figure 7.19 there are only small differences between the two profiles around shower maxima; therefore there is a tiny difference in the effective area of the telescope. Any differences above 40km are unimportant as the densities of air are such that the material traversed is much less than the gamma-ray or cosmic ray interaction lengths, as discussed in chapter 2.

Also shown on the plots (7.20 and 7.21) is the effective area due to the tropical model

(and default H.E.S.S. absorption model), which as expected shows excellent agreement with the Windhoek minimum and maximum data.

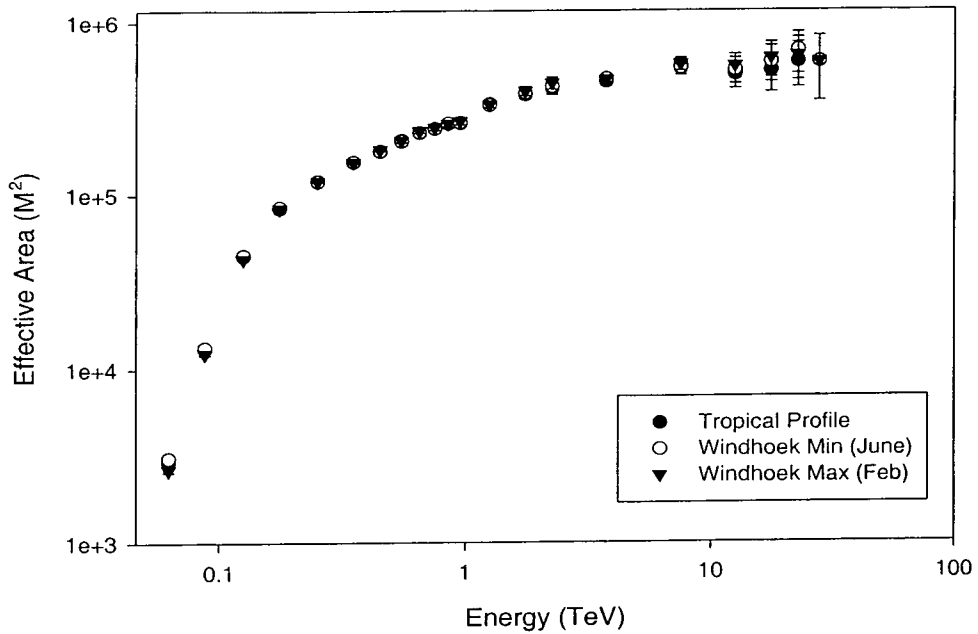


Figure 7.20: Figure showing the effective area of a stand-alone telescope in reference to a crab spectrum of TeV gamma-rays at a zenith angle of 20° , assuming tropical, Windhoek maximum and minimum atmospheric profiles.

7.5.7 Conclusion

The most likely and normal day to day difference in effective area is probably due to the changes in the density and composition of the aerosols in the first 2 kilometres above the telescope site. For example, the effects on the trigger rates due to the placement of the ground level and the resultant scaling in aerosol density are shown in table 7.1. Although this is only a preliminary study of what may happen to the trigger rate of the first stand-alone H.E.S.S. telescope, given the current lack of a large database atmospheric data for the H.E.S.S. site, these two cases (for ground level at 0 and 1.8 km) are revisited, and further explored by looking at the simulated Hillas parameter distributions for gamma-rays and cosmic rays.

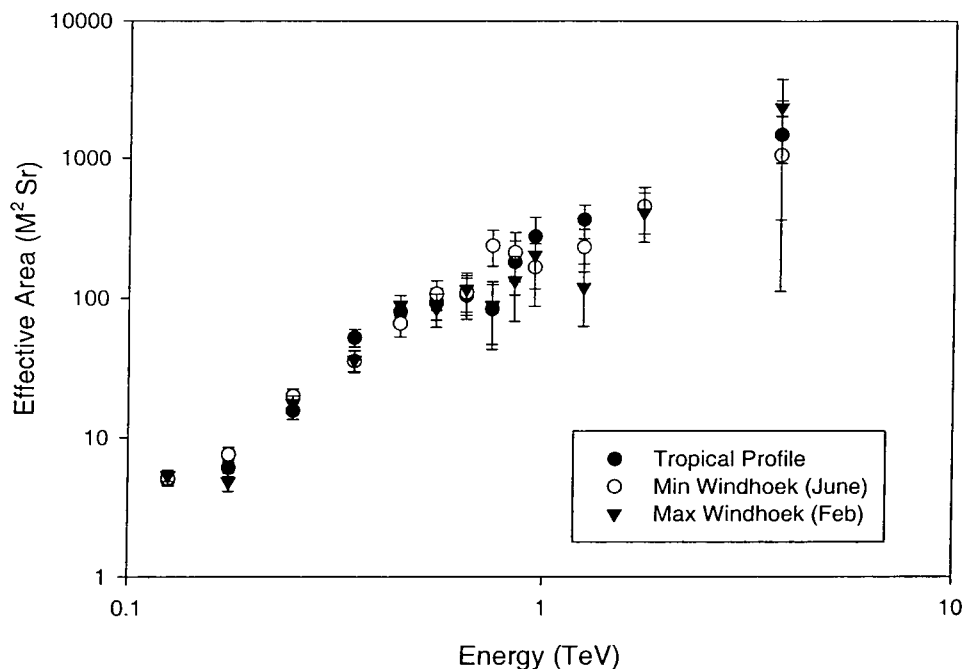


Figure 7.21: Figure showing the effective area of a stand-alone telescope in reference to a Wiebel spectrum of TeV cosmic rays at a zenith angle of 20° , assuming tropical, Windhoek maximum and minimum atmospheric profiles [204].

7.6 Hillas Parameter Changes

As seen the amount of low-level aerosols (dependent upon where the ground level is placed) has a dramatic effect on the effective sensitive area of the first H.E.S.S. telescope at low energies. This is important as the H.E.S.S. telescope sits near the edge of a plateau at an altitude of 1800m, and thus a mixing of aerosols from the nearby lower altitude regions may occur dependent upon wind direction. Given a lack of low-level aerosol measurements for the H.E.S.S. site at this time, the difference the Hillas parameter distributions which occur by moving the ground level from sea level to the telescope altitude will be naively investigated. It is not exactly clear at this stage, what effect this change might have on the image distributions.

H.E.S.S. Hillas Parameter Distributions

As the image definition (i.e. the amount of light above the NSB noise required within a tube for it to form part of the image) for the H.E.S.S. telescope tubes was being varied at the time of writing, the analysis of the data is based on a simplistic image definition technique, where the image tubes possess a signal greater than 4.25σ of the NSB, and the

Species	Count Rate (Hz) with Ground Level at 0 km a.s.l.	Count Rate (Hz) with Ground Level at 1.8 km a.s.l.
Gamma-Rays	$0.71 \pm 0.34 \pm 0.04$	$0.58 \pm 0.32 \pm 0.05$
Proton	$405 \pm 26 \pm 4$	$305 \pm 20 \pm 4$
Alpha	$22.2 \pm 1.6 \pm 1.1$	$17.7 \pm 1.0 \pm 1.2$
Oxygen	$5.5 \pm 0.3 \pm 0.5$	$4.0 \pm 0.2 \pm 0.5$
Magnesium	$3.6 \pm 0.2 \pm 0.1$	$2.5 \pm 0.2 \pm 0.4$
Iron	$2.2 \pm 0.2 \pm 0.1$	$1.6 \pm 0.2 \pm 0.1$
Total Simulated CR	$439 \pm 28 \pm 6$	$331 \pm 22 \pm 6$

Table 7.1: Table showing trigger rate of simulated H.E.S.S. telescope to spectra of cosmic rays and gamma-rays with atmospheric attenuation based on the ground level at 0km a.s.l. and the telescope altitude. Errors are: systematic (given first) and based upon errors in power laws taken from [204] and [141], and statistical (given second) at the 1σ level.

border tubes (which must neighbour an image tube) possess a signal of greater than 2.25σ of the NSB. NSB light is included in the same fashion as discussed in Chapter 6, scaled such that the mean noise was in agreement with that used for the H.E.S.S. site [180], a mean value of typically 4 photoelectrons per tube per event, or 300 digital counts with a Poissonian distribution (this assumes a digital counts to photoelectron conversion of 75 digital counts per photoelectron [118]). The mean was then subtracted to give an overall fluctuation of the noise around zero. However, one should note that no changes to the NSB light incurred by the changes in atmospheric model have been included. Some sample images for gamma-ray and cosmic ray events are given in appendix C. A distance cut was placed on the data, and only events whose centroid was between 0.3° and 2.0° from the centre of the camera were studied. This removed circular events, whose alpha was unclear, and those events towards the edge of the camera that may have been unbounded. As a first cut to the data, this still includes regions where either cosmic rays or gamma-rays dominate, as shown in figure 7.22. The data was also cut such that only events with 4 tubes or more were studied, and only events with greater than 40 photoelectrons (or 3000 digital counts) were included. It should be noted that these cuts will tend to minimise the effects of any atmospheric changes. For instance, any outlying events that may have

a greater attenuation dependence will be ignored by the distance cut. Also, those small SIZE events (< 30 photoelectrons), which may also be highly affected by atmospheric changes are ignored. However, this is in keeping with the current state of data taking at the actual first stand-alone H.E.S.S. telescope [118]. A bin size for each parameter is used as given in the H.E.S.S. analysis software [136].

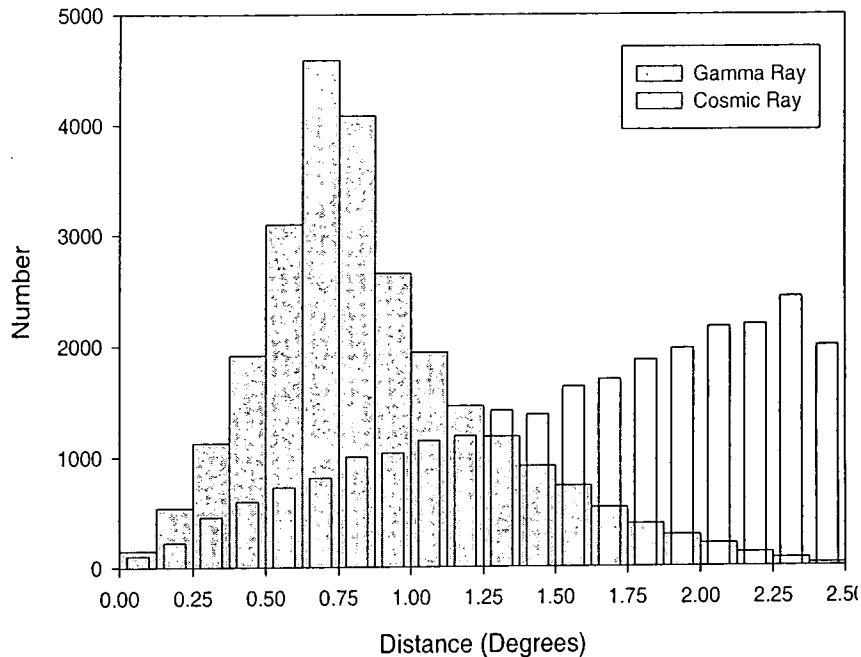


Figure 7.22: Image distance histograms for simulated cosmic ray and gamma-ray spectra using atmospheric model with ground level at 0km a.s.l. No cuts are applied to data at this point. This suggests a cut of $< 1.2^\circ$ to maximise gamma-ray signal and minimise cosmic ray signal. A cut of $> 0.3^\circ$, is also placed to rule out circular events whose alpha is undefined.

In addition, as the earlier results of this chapter show an energy dependence upon the effects of atmospheric attenuation, Hillas parameter distributions for all energies simulated, and for a subset of energies have been produced. For gamma-rays those events with energy equal to or below 0.1 TeV were considered, and for cosmic rays this value was changed to 0.3 TeV (given the smaller amount of light in cosmic ray showers). All the produced plots (for length, width, SIZE, concentration (1-Iratio), alpha and distance) are given in appendix D, and a small subset is shown in the next discussion section.

7.6.1 Discussion

The parameter plots given in appendix D (figures D-1 to D-20), show the differences in Hillas parameter distributions caused by calculating atmospheric attenuation tables based on moving the ground layer from sea to level to the H.E.S.S. telescope altitude of 1800 metres. The cuts placed on the data are as previously discussed. Before discussing the results, one may suggest what might be expected in terms of Hillas parameter changes given two atmospheric models, with differing attenuation. Figure 7.23 shows a schematic of the system under consideration, namely a single Cherenkov telescope subject to atmospheres with different clarities.

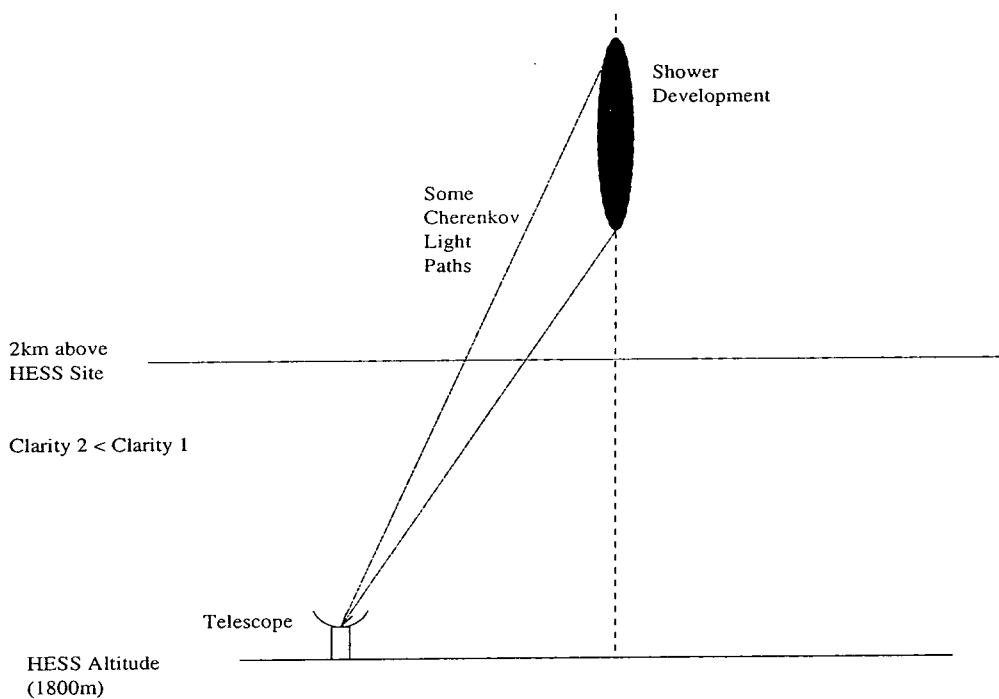


Figure 7.23: Schematic diagram of stand-alone H.E.S.S. telescope and typical EAS being measured, not to scale. Two atmospheres are suggested for the area up to 2 km above the H.E.S.S. site, with clarities 1 and 2, such that atmosphere 1 is clearer than atmosphere 2.

The possible effects on each individual Hillas parameter for gamma-ray showers are given below:

Length - As discussed in chapter 3, length is directly related to core location, and therefore one expects that for a more attenuating atmosphere, showers with cores which are more distant to the telescope will be attenuated more than those nearer. Therefore, one might expect the more attenuating atmosphere to have a length distribution that has

fewer large events.

Width - Width is related to the lateral development of the shower. The effect on width of the change between the two atmosphere models under consideration, is however, likely to be negligible. The development of the shower is of course altitude dependent on the atmospheric profile used and this will indicate where shower maxima is likely to occur, and the maximum opening angle of the shower, and hence the width. Attenuation will also be important, as for the more severe case more light will be lost, leading to a decrease in width. Therefore, it is possible that for the more severe case that the width distribution will be slightly shifted towards smaller events.

Number of Image Tubes - Here simply a more attenuating atmosphere will lead to less light and fewer tubes in the image.

Alpha - It is unlikely that α (the pointing angle of the ellipse) will be affected very much by the atmospheric changes. Only a severe change which would alter the shape of the tail of the ellipse from the upper parts of the shower, might change α , but even the effect here is likely to be small.

Distance - Distance (the distance from the centre of the camera to the centroid of the ellipse) is another geometrical term, which is unlikely to have its distribution affected much by subtle changes in the atmospheric attenuation.

SIZE - Image SIZE (in digital counts) is likely to be smaller for the more attenuating atmosphere given that more light is lost from the image.

Concentration - Concentration (or amount of light in image/total amount of light in camera (or 1-Iratio)) is more difficult to predict. This is because although for certain the image SIZE should go down, the total light in the camera is made up of the image light + Cherenkov light which didn't pass the 4.25σ and 2.25σ image/border criteria + NSB light (with pedestal subtracted so that it fluctuates around zero). The Cherenkov light not in the image is also likely to be less for a more attenuating atmosphere. The NSB however will be reduced, but as it is isotropic, and unlike the Cherenkov light is not peaked in the blue/UV, it is therefore not subject to as great an attenuation effect. This is liable to lead to a greater decrease in the denominator than the numerator, and hence the concentration for the more attenuated case should go down.

If a net difference for a parameter is defined as a difference in the distribution beyond the 1σ level for 2 or more neighbouring bins, then no significant difference is seen in

terms of the Hillas parameter distributions for any of the results given in appendix D, including all the events cut for low energies, where one expects the atmospheric effect to be greatest given the results from the earlier parts of this chapter. The parameter most likely to be affected by these atmospheric changes, is the image SIZE. If only those events with energies equal to or below 0.1 TeV are considered and the other cuts are applied as discussed, a marginal effect in the SIZE distribution is seen, as indicated for gamma-rays in figure 7.24.

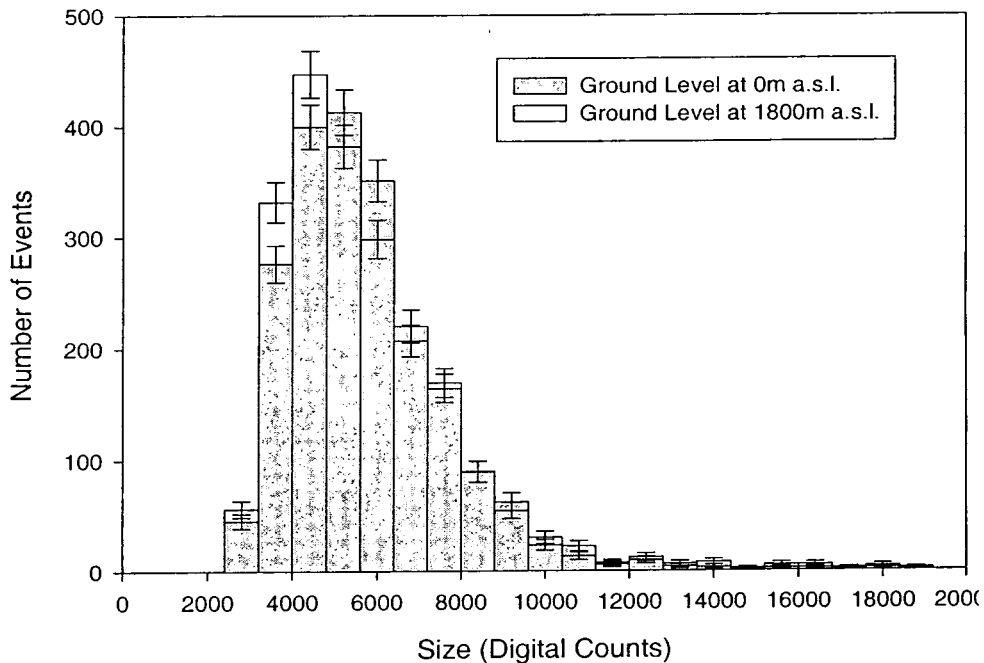


Figure 7.24: Plot shows histogram of the simulated response of the stand-alone H.E.S.S. telescope to a spectrum of gamma-rays (with energies less than or equal to 0.1 TeV), produced with MOCCA, in terms of the SIZE parameter for cut datasets as detailed. The two different plots are for atmospheric attenuation with a ground level set at sea level, and at the telescope altitude. Scaled such that area under both curves is the same.

Here the effect that the more attenuating atmosphere has fewer large SIZE events, and (because of the scaling of the histogram so that the areas underneath match) a larger number of smaller SIZE events can be seen. As expected, a much less pronounced effect is seen in the cosmic ray data given in figure 7.25, in fact there are no differences at all between the two distributions with the bounds of statistical error.

It was discovered that as the cuts on the data were slackened (i.e. changed from 4 image tubes, to 2, and from a minimum SIZE of 30 photoelectrons to a minimum SIZE

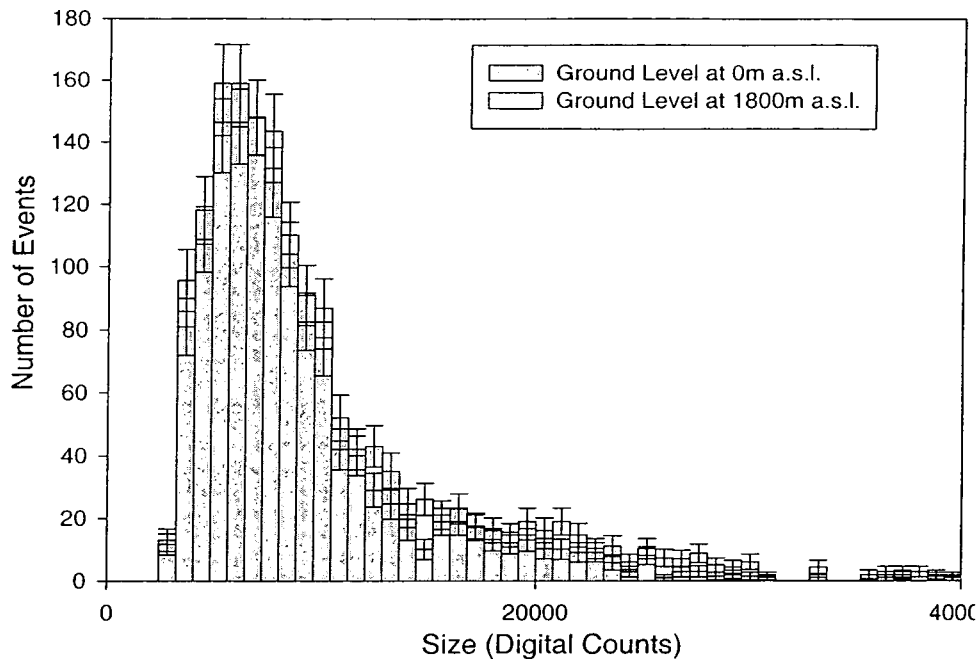


Figure 7.25: Plot shows histogram of the simulated response of the stand-alone H.E.S.S. telescope to a spectrum of cosmic rays (with energies less than or equal to 0.3 TeV), produced with MOCCA, in terms of the SIZE parameter for cut datasets as detailed. The two different plots are for atmospheric attenuation with a ground level set at sea level, and at the telescope altitude. Scaled such that area under both curves is the same.

of 10 photoelectrons), then the differences in the SIZE distribution were enhanced for gamma-ray showers as shown in figure 7.26. No discernible difference was seen with the bounds of experimental error for the cosmic ray SIZE distributions, and also, no great difference is seen in any of the second order parameter distributions after this change, for either primary species. Increasing the upper distance limit to 2.5° for the analysis of these low energy events, yields no extra data, as events with energies less than 0.1/0.3 TeV for gamma-ray/cosmic ray showers fail to trigger the system from this far out.

7.6.2 Conclusion of Study

The results of these simulations indicate that for the atmospheric changes made (i.e. the movement of the ground level), which dramatically increases the low-level aerosol attenuation, the most obvious effect is the trigger rate of the first stand-alone H.E.S.S. telescope, as given in table 7.1. Given a set of preliminary cuts on the data, the only image parameter that is discernibly affected by changes is the overall image SIZE, and the

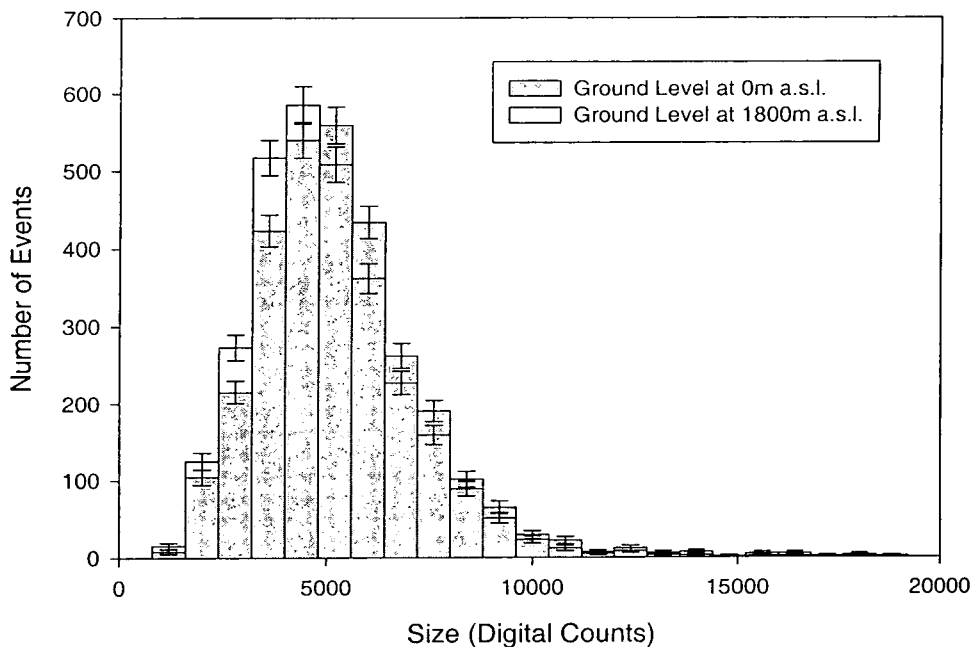


Figure 7.26: Plot shows histogram of the simulated response of the stand-alone H.E.S.S. telescope to a spectrum of gamma-rays (with energies less than or equal to 0.1 TeV), produced with MOCCA, in terms of the SIZE parameter for cut datasets as detailed. The two different plots are for atmospheric attenuation with a ground level set at sea level, and at the telescope altitude. Scaled such that area under both curves is the same.

largest effect, as predicted from figures 7.11 and 7.12 is for gamma-ray showers with small primary energy. No obvious differences between cosmic ray Hillas parameter distributions have been seen within the bounds of statistical error. The main conclusion to draw is that given this simple trigger for the H.E.S.S. stand-alone system, with simplistic image identification algorithms, the effects of atmosphere on second order image parameters is very small indeed. The most discriminatory imaging parameter, alpha, is however affected by the geomagnetic field, as discussed next.

7.7 Other Effects - Geomagnetism

Although not atmospheric but terrestrial in origin, the geomagnetic field can effect the trajectories of the charged constituents of both gamma-ray and hadron initiated EAS and affect the resulting shape of the Cherenkov images seen by ground-based Cherenkov telescopes. Much work has been done in this field by the Durham Group, both in the magnitude of the error caused and correction techniques, [37], [39]. Of particular im-

portance, is the fact that the component of the geomagnetic field perpendicular to the telescope pointing direction may affect the pointing of the elliptical images produced in the camera by gamma-ray showers, therefore affecting the Hillas parameter, α , the most powerful discriminator between gamma-ray and cosmic ray initiated showers.

The Durham group found this particular problem at their Narrabri site, as the perpendicular component of the geomagnetic field was greatest when pointing 180° in Azimuth. In comparison Namibia has almost the lowest field strength value on the planet. The Durham group has performed sets of simulations to study the effect of various field strength values on the Cherenkov images of a gamma-ray initiated shower using an ideal telescope system (with perfect optical performance and zero pixelisation) [14]. The suggestion is that with the new generation of Cherenkov telescopes, with smaller mirror point spread function and finer camera pixelisation, the effect seen may be greater than that seen by the Durham group with their relatively coarse Mark 6 camera.

The effects of the geomagnetic field for the response of a simulated stand-alone H.E.S.S. telescope to a spectrum of gamma-rays subject to no geomagnetic field and the Namibian geomagnetic field are shown in terms of effective sensitive area and the produced α distribution in figures 7.27 and 7.28. The simulation used (produced with MOCCA and CameraHESS) assumes a differential spectral slope of -2.45 , and simulate primary energies between 0.1 and 1.0 TeV, and assumes a pointing angle of 180° in azimuth, which corresponds to the largest effect of the geomagnetic field. The telescopes are pointed at 20° zenith angle, and for each shower they are scattered randomly four times within a 300 metres radius of the core location.

As the geomagnetic field tends to spread out the Cherenkov light more, by deflecting the paths of the electrons and positrons, so figures 7.27 shows the reduced effective area with geomagnetic field applied. The orientation of the image ellipses is rotated slightly due to the geomagnetic deflection of the electrons and positrons. This orientation is dependent on the azimuthal angle in the camera, and dependent upon the telescope pointing angle and the geomagnetic field, the rotation of the images can be in either direction, this leads to a slightly broadened α distribution for $\alpha < 30^\circ$. However, the effects on α (and other Hillas parameters) may be corrected for in data processing.

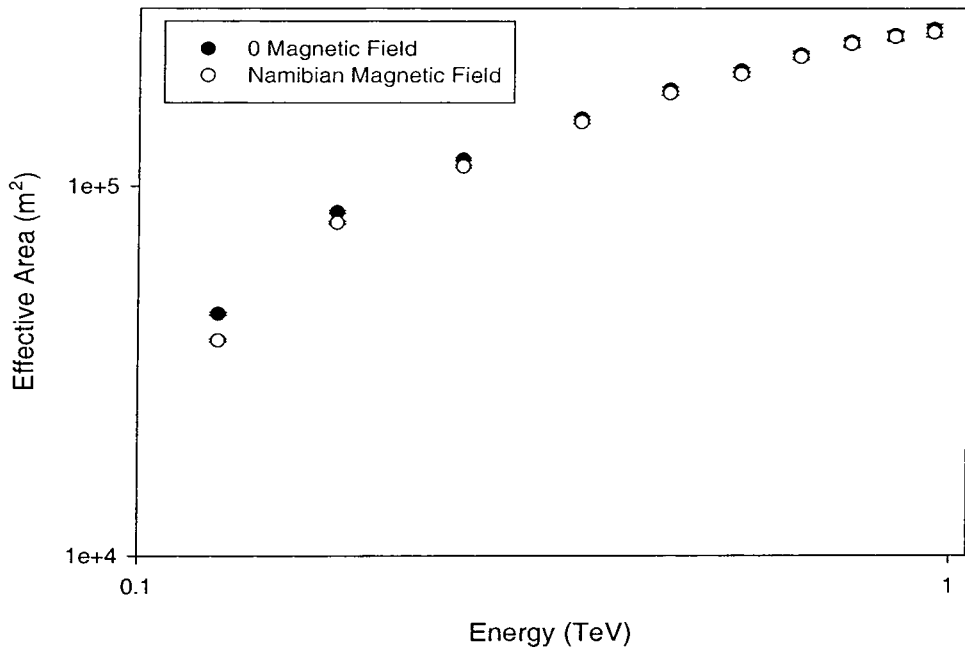


Figure 7.27: Diagram illustrating the effective sensitive area of a stand-alone H.E.S.S. telescope to a spectrum of gamma-ray induced showers with spectral slope of -2.45 and with primary energy between 0.1 and 1.0 TeV. The telescope is pointed at 20° zenith angle, and 0° in azimuth, and the plots shown have no geomagnetic field applied, and the field corresponding the H.E.S.S. site applied.

7.8 Chapter Conclusion

In this chapter discussions have been made for the need for the calibration of the atmosphere in imaging Cherenkov astronomy, given the simulations have suggested that below 300 GeV, atmospheric attenuation of Cherenkov light is an important factor. However, if using multi-wavelength LIDAR one were able to map out the size and position of the low-level (0-2km) aerosols, and given (using distant calibrated light sources) a measure of the very low-level attenuation due to dust blown up from the ground, one may be able to calculate the attenuation due to Mie scattering and apply this to calculations of flux from VHE emitting objects.

The low-level aerosol density changes likely to be caused by wind blown up from the surface, represent only a small change compared to those considered here. However, it has been shown in simulations that the structure of the atmosphere has a definite effect on the trigger rate of the stand-alone H.E.S.S. telescope. In particular, the placing of the ground level (which scales the overall aerosol density) has been shown to have a dramatic effect on

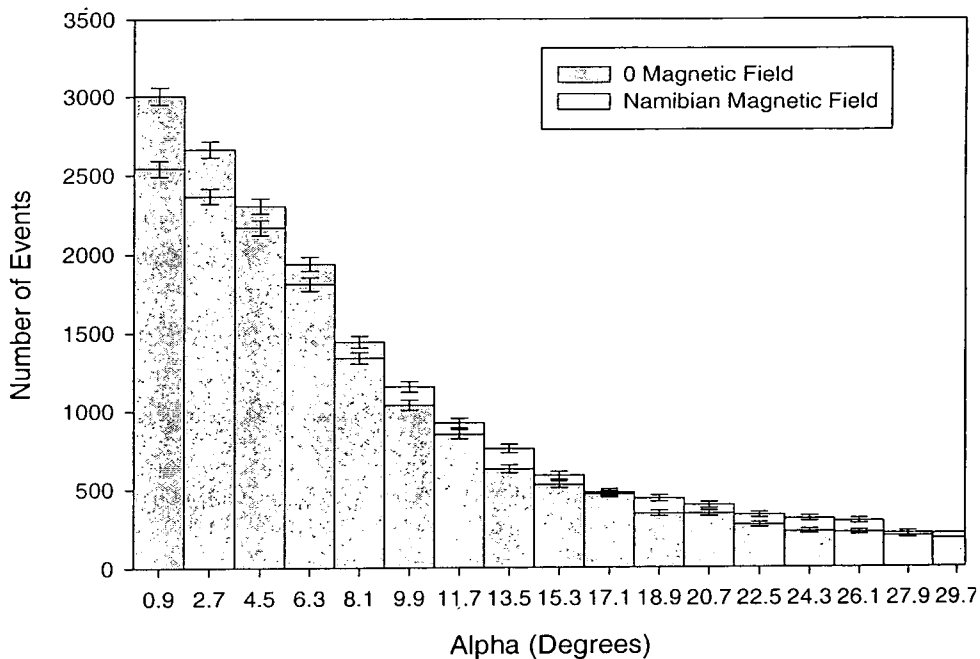


Figure 7.28: Diagram of the α distributions of the gamma-ray showers simulated, for the cases of no and H.E.S.S. site geomagnetic fields. The histograms are normalised such that the area underneath for α ranging from 0 to 90 is the same. The data here shows the area of difference, beyond $\alpha = 30^\circ$ the plots converge as expected. Scaled such that area under both curves is the same. Distance and SIZE cuts as previously outlined in the text are applied.

the low energy events that trigger the H.E.S.S. telescope. Given a simple set of preliminary cuts, the effect is still also seen in the gamma-ray SIZE distribution, though in none of the second order image parameter distributions. The cosmic ray showers appear to be less affected by atmospheric changes, given their larger lateral extent, deeper penetration and isotropic nature.

It is unknown as yet what the likely seasonal and day to day trends in low-level aerosols above the H.E.S.S. site will be, therefore the simulations conducted within this chapter for aerosol distributions are not based around real measured data. However within the next 6 months changes in aerosol concentration will be easily measured by the large array of atmospheric monitoring equipment at the H.E.S.S. site, and on longer time scales with the introduction of a multi-wavelength LIDAR on the site, the actual aerosol composition variations will be easily monitored. The effects of the geomagnetic field on the trigger and imaging capabilities of the first stand-alone H.E.S.S. telescope have also been given.

In the final chapter the discussions of the various chapters will be revisited briefly, and new upper limits will be placed on the AGN sources seen by the Durham Mark 6 telescope. In conclusion, the current status of the first H.E.S.S. telescope will be covered, as will the overall prospects for the field of imaging atmospheric Cherenkov astronomy.

Chapter 8

Conclusion: A New Era in Cherenkov Astronomy

8.1 Introduction

In this thesis a discussion of the current status of VHE gamma-ray astronomy, and the atmospheric monitoring required to make meaningful spectral studies of sources below 0.3 TeV, where atmospheric effects make a large difference to the inferred flux, has been presented. Simulations of atmospheric structure, EAS production and Cherenkov telescope observation have been utilised, in order to investigate these atmospheric effects. A comparison of three specific air shower simulation codes; ALTAI, CORSIKA and MOCCA, and two Cherenkov telescope systems; the stand-alone H.E.S.S. telescope and the Durham Mark 6 telescope has been presented. In astrophysics terms, the current set of observed and possible sources of VHE gamma-ray emission and the possible models of particle acceleration believed to be at work have been discussed. In particular, with reference to the most significant source seen with the Mark 6 telescope (the AGN PKS 2155-304), a new calculation of the flux seen, with greater accuracy than published before, has been presented. This final chapter, shall draw together the discussions of the previous 7 chapters and reach conclusions based upon the research therein. Firstly, the refined telescope simulation for Durham Mark 6 telescope is used to produce upper limits for the AGN sources observed during its lifetime.

8.2 AGN in the Durham Mark 6 Observing Program

In its 4 year lifetime, the Durham Mark 6 telescope was used to observe many potential sources of TeV gamma-rays. The only AGN observed at a significance greater than 5σ was the aforementioned AGN PKS 2155-304. Given the refined telescope simulation code discussed in chapter 6, 3σ upper limits on the other AGN sources observed by the Mark 6 are now calculated. A summary of the observation schedule for these sources is given in table 8.1, which also includes the figures for the calculation of the upper limit discussed below.

Upper Limit Calculation

Recalling the equation for the integral flux of a source given in chapter 6, namely:

$$S_{\gamma}(E_{th}) = \frac{N}{T} \frac{E_{th}^{-(\gamma-1)}}{\gamma-1} \left(A \sum_{i=4}^5 F_i(\gamma) \right)^{-1} \quad (8.1)$$

where S is the integral flux above energy E_{th} , assuming a differential spectral slope of γ , for an excess of N events after cuts, for a time of observation of T seconds, for gamma rays landing within 300 metres radially over the telescope, giving an area $A = \pi \times 300^2$ metres². As derived in Chapter 6, for bins 4 and 5:

$$F_4 + F_5 = 0.015 \quad (8.2)$$

If we take $E_{th} = 1.5$ TeV and $\gamma=2.6$, then to calculate a 3σ upper limit from the emission from a source, one can take $N = 3 \times \sqrt{\text{On} + \text{Off}}$. Therefore given the number of on and off source events, and the time of observation (i.e. number of 14 minute on source segments (n_s) at zenith angles $< 45^\circ$), then S may be defined as:

$$S_{2.6}(1.5 \text{ TeV}) = 2.75 \times 10^{-7} \cdot \frac{\sqrt{\text{On} + \text{Off}}}{n_s} \quad (8.3)$$

The data used in the following calculations is given in table 8.1.

Each of the individual source is now discussed briefly.

Cen A

Cen A (NGC 5128) ($z = 0.008$) is the closest radio-loud AGN to Earth. It was tentatively identified as a source of TeV gamma-rays in the mid 1970's [73], at a flux of $(4.4 \pm 1.0) \times$

Object	Date Month/ Year	n_s	Counts On Source	Counts Off Source	N	$S_{2.6}(1.5 \text{ TeV})$ $\times 10^{-7} \text{ m}^{-2} \text{ s}^{-1}$
Cen A	03/97	27	695	723	113.0	3.8
PKS1514-34	04/96	51	1329	1292	153.6	2.8
1ES2316-423	08 & 09/97	37	1250	1286	151.1	3.7
1ES1101-232	05/98	43	1460	1434	161.3	3.4
RXJ1058-275	03/96	11	611	619	105.2	8.8
PKS0548-322	03/96	95	2273	2271	202.2	2.0
PKS2005-489	96-99	358	12051	11958	464.8	1.2

Table 8.1: Summary of data used in upper limit calculations for AGN measured with the Mark 6 telescope during its lifetime. On source counts are those from bins 4 and 5 combined, as are off source counts.

$10^{-7} \text{ m}^{-2} \text{ s}^{-1}$ at energies $> 300 \text{ GeV}$. Observations of Cen A made with the Mark 6 were taken in March 1997. At this time RXTE observations showed that the AGN was in a low state. No emission was seen with the Mark 6, and an upper flux limit is set at $3.8 \times 10^{-7} \text{ m}^{-2} \text{ s}^{-1}$ above 1.5 TeV.

PKS 1514-24

PKS1514-24 ($z = 0.049$) is a radio selected BL-LAC. The EGRET detector saw no evidence for emission and placed an upper limit of $7 \times 10^{-4} \text{ m}^{-2} \text{ s}^{-1}$ at $E > 100 \text{ GeV}$ [58]. The upper limit presented here is $2.8 \times 10^{-7} \text{ m}^{-2} \text{ s}^{-1}$ above 1.5 TeV.

1ES 2316-423

1ES 2316-423 ($z = 0.055$) is identified in [155], as an AGN whose energy emission could reach TeV energies. However it was not seen by the Mark 6, and an upper limit here of $3.7 \times 10^{-7} \text{ m}^{-2} \text{ s}^{-1}$ above 1.5 TeV is presented here.

1ES 1101-232

1ES1101-232 ($z = 0.186$) is an X-ray selected BL-LAC, however only an upper limit could be placed on the results seen by EGRET (in phase I) at the level of $6 \times 10^{-4} \text{ m}^{-2} \text{ s}^{-1}$ at $E > 100 \text{ MeV}$ [58]. The Durham group's observations of this source were part of a multi-

wavelength campaign with the Beppo-Sax satellite. Beppo-Sax saw a 30% reduced flux compared to their measurements for 1997, during our observations [205]. An upper flux limit for emission above 1.5 TeV on this source of $3.4 \times 10^{-7} \text{ m}^{-2}\text{s}^{-1}$ is set.

RXJ1058-275

RXJ1058-275 ($z = 0.092$) is classified as an X-ray selected BL-LAC [15], but has not been seen with the Durham Mark 6. Therefore a flux limit of $8.8 \times 10^{-7} \text{ m}^{-2}\text{s}^{-1}$ above 1.5 TeV is set.

PKS0548-322

PKS0548-322 ($z = 0.069$) is an X-Ray selected BL-LAC. Observations with EGRET failed to see any gamma-ray emission [76], and none was seen by the Mark 6. An upper limit on the flux above 1.5 TeV of $2.0 \times 10^{-7} \text{ m}^{-2}\text{s}^{-1}$ is set.

PKS2005-489

PKS2005-489 ($z = 0.071$) is another X-Ray selected BL-LAC, which although not listed as a 100MeV gamma-ray source in the 3rd EGRET catalogue [76], is seen as a source of marginal significance in the GeV EGRET catalogue [121]. Our upper limit on the flux above 1.5 TeV is $1.2 \times 10^{-7} \text{ m}^{-2}\text{s}^{-1}$.

8.2.1 Conclusion

The upper limits presented here are unconstraining on most models of AGN behaviour, but all sources should be re-observed with the milli-Crab sensitivity of H.E.S.S., which may yield more interesting results [128]. For example, in comparison with the H.E.S.S. system, it should be noted that if for instance PKS2005-489 were emitting at the upper limit set by the Durham group, and was observed for as long with the first 4 H.E.S.S. telescopes, it should show emission with a signal to noise ratio of $> 400\sigma$ (the normal 5σ limit being exceeded after the first minute). Therefore, even if this source has emission significantly below the upper flux limit set by Durham, it should still be observable in a relatively short time with the H.E.S.S. system. The current status of the H.E.S.S. system is now outlined.

8.3 Status of H.E.S.S.

The first stand-alone H.E.S.S. telescope went online for the first time in late June 2002. At this point, however, it is still undergoing shakedown procedures, and therefore it is not possible to present any results for comparison with the simulations presented herein. In light of future comparisons with simulation, possible discrepancies that may appear are now addressed.

8.3.1 Single Photoelectron Pulse Profiles and Simulation Comparisons

Since the first stand-alone H.E.S.S. telescope was being designed, several groups have been performing simulations of the single telescope, using various telescope and shower simulation packages. Aside from the work presented here with MOCCA, work has been performed with ALTAI, CORSIKA and KASCADE. The results of these different simulations have been compared at several collaboration meetings. Aside from the inherent differences in the EAS simulations codes, another important difference between the work done on H.E.S.S. performance is the use of different single photoelectron pulses. Figure 6.3 shows two of the curves used in simulations. Curve 2 is that in the CameraHESS package, which has been used in conjunction with ALTAI and MOCCA simulations, whereas curve 1 is the single photoelectron pulse used with CORSIKA and KASCADE. Given the complex electronics of the stand-alone H.E.S.S. telescope camera, measurements of the single photoelectron response at the comparator (where signals across the camera are combined) are required. However, the mean photoelectron pulse amplitude cannot be measured directly. This problem arises for several reasons, including:

- The trigger channel is quite noisy for amplitudes of the order of a single photoelectron.
- The oscilloscope used to measure the single photoelectron pulse, has a threshold for pulse selection, which induces a bias which may be difficult to quantify.
- One has to use a probe to reach the signal at the entrance of the comparator, which increases noise and modifies the pulse signal.

However, it is much simpler to measure the PMT anode signal as outlined in [74]. This has been done many times for 16 tubes from the second H.E.S.S. telescope camera (which is identical to the first), and the mean result, along with the scaled curves already pre-

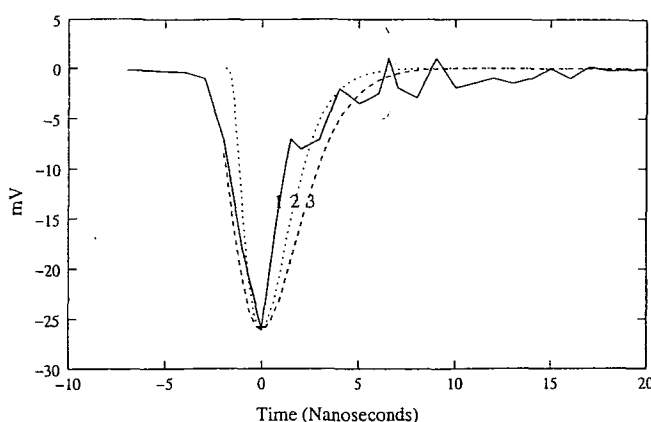


Figure 8.1: The single photoelectron response curve. (1) represents the measured from the anode current as outlined in [74]. (2) is that used in the simulations of the single H.E.S.S. telescope response as detailed herein, and (3) represents that used in simulations of the single H.E.S.S. telescope response to EAS produced with CORSIKA. Results normalised to measured peak amplitude of photoelectron response.

sented in figure 6.3, are shown in figure 8.1. After correction for the probe attenuation, the nominal pulse amplitude at the entrance to the comparator is inferred to be 25.7 ± 1.6 mV (the value used in CameraHESS simulation was 26.7 mV).

It should be noted that to date, no after pulse simulation has been added to the H.E.S.S. telescope simulations presented within this thesis. Given the inherent light differences in the hadronic part of the EAS shower codes, and the dramatic effect of the single photoelectron pulse on telescope response, it is clear that the results of the three codes for cosmic ray trigger rate will differ, in some cases greatly, and that all the simulated results will differ from that seen by the actual telescope. In fact, the matter is more complicated as different groups have used different assumptions about the cosmic ray composition and spectral indices. Therefore, only the results with ALTAI may be realistically compared, as these use the same single photoelectron pulse, telescope simulation package, and the Wiebel cosmic ray spectra [204]. The last quoted cosmic ray and gamma-ray trigger rates at a H.E.S.S. group meeting for ALTAI, for a Crab-type source at the zenith, were: ~ 550 Hz for cosmic rays, and 0.7Hz for gamma-rays. These values are plausible when compared with those given in table 7.1 for a similar source at 20° zenith angle. The difference seen, may be accounted for by the differing zenith angle, and the differences between EAS simulations codes. Some recently presented Hillas

parameter distributions produced with ALTAI, are given below in figure 8.2, they assume a Crab type spectral slope and are based around 0.8 million gamma-ray showers ranging in energy from 0.01 to 30 TeV. They are meant here to be used in comparison with the results presented in appendix D, but also show the effects of altering the triggering criteria on the gamma-ray Hillas parameter distributions. It should be noted, however, that although requiring a large number of tubes in the trigger broadens the image length and width for gamma-ray EAS, it has almost the same effect on cosmic ray initiated EAS and therefore overall the efficiency of separation remains unchanged.

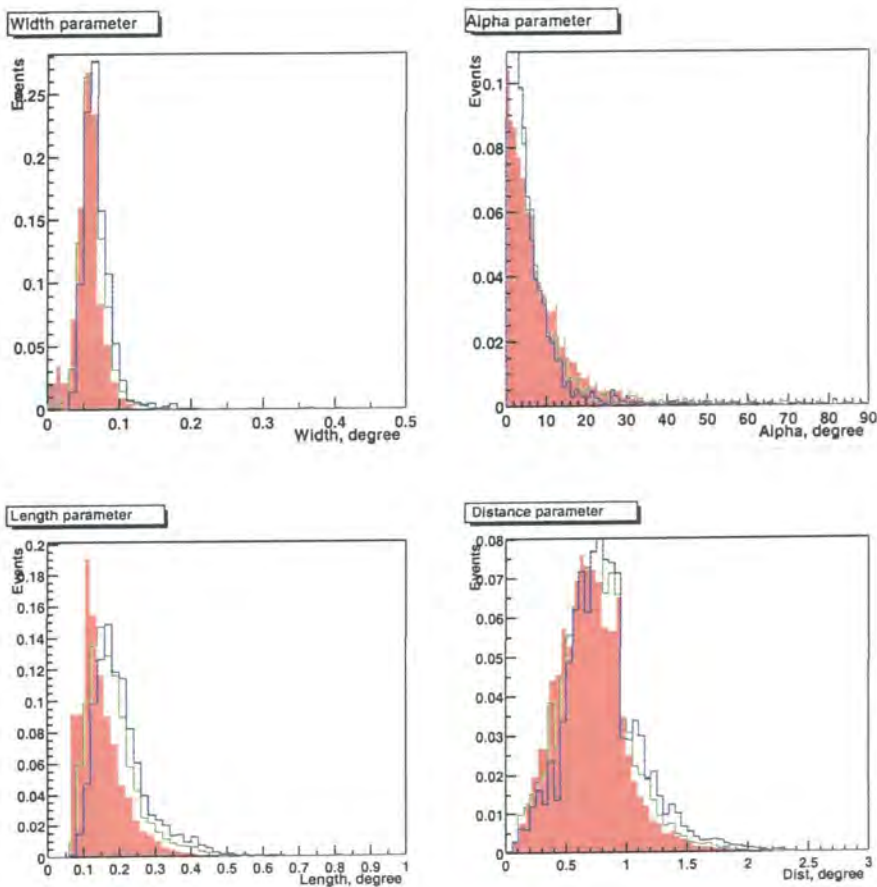


Figure 8.2: Distributions of the standard second order moment image parameters of the γ ray induced showers for the trigger condition $2/960 > 4$ photoelectrons (filled histogram), $3/960 > 4$ photoelectrons (histogram in green) and $4/960 > 4$ photoelectrons (histogram in blue) produced with ALTAI and CameraHESS package as given in [117].

However, both these simulations used a broader single photoelectron pulse than that measured and, give the differences between the single photoelectron pulse profile used

here and the actual one measured as shown in figure 8.1, the actual count rate seen is likely to be smaller still than that derived from either ALTAI or MOCCA simulations. Other important factors, which may need further investigation before any comparison with simulations and real data may be drawn, include:

- The digital counts/photoelectron ratio, which may require further measurements, which is liable to have a large effect on the image SIZE distribution.
- The transit time for an individual PMT (~ 3 ns) has not been definitely measured.
- The trigger currently in use on the first telescope is unlike the one used in any simulations to date, requiring 4 pixels to possess a signal greater than 5 photoelectrons.
- The atmosphere has not been fully calibrated as yet, as seen in chapter 7, this leads to a possible 15-20% difference in light densities, and therefore the trigger rate will be affected.

As mentioned earlier the camera is currently taking data, though still has several shakedown problems, which prevent the data taken from being compared against simulation. Hopefully the atmospheric model comparison made in chapter 7 will form part of the further study of the atmospheric effects on the imaging technique that the Durham group shall be involved with in the future. Therefore, before concluding the discussion of the status of H.E.S.S., the status of atmospheric measurements made at the site is now discussed.

8.3.2 Status of Atmospheric Measurements at the H.E.S.S. Site

The atmospheric monitoring LIDAR on the site has been running since the telescope first light. Most data taken so far has been identical to that shown in figure 7.8, indicating the clear and stable nature of the H.E.S.S. site. However, around the beginning of August, the observers noted a large amount of haze in the lower atmosphere, which was seen to obscure a large amount of light. Observations taken on the at 16:30 and 18:30 UT on the 2nd of August with the ceilometer pointed at the zenith are shown below in figure 8.3. The results, in terms of optical depths at 905 nm, of given MODTRAN models, are also shown. These all assume a tropical atmosphere with different atmospheric attenuation models. These include:

- An atmosphere with only molecular scattering of light included (i.e. purely Rayleigh scattering and no aerosol (Mie) scattering.)
- An atmosphere with a rural haze model with 23km visibility, and spring-summer tropo-

spheric model.

- An atmosphere with a rural haze model with 5km visibility, and spring-summer tropospheric model.
- An atmosphere with only spring-summer tropospheric aerosols included, with 50km visibility, i.e. only tropospheric extinction has any great effect.

The altitudes quoted on the y-axis are above ground level set at 1800m. All MODTRAN data produced assumes a ground level of 1800m, as it is impossible to fit the data with a ground level set at sea-level. Data taken a week after this still shows a sizeable, though much reduced amount of low-level aerosol attenuation.

As can be seen the best fit for this data is the 5 km visibility model, as one would expect given the poor conditions on this day. Obviously, no source data was taken with the stand-alone H.E.S.S. telescope at this time.

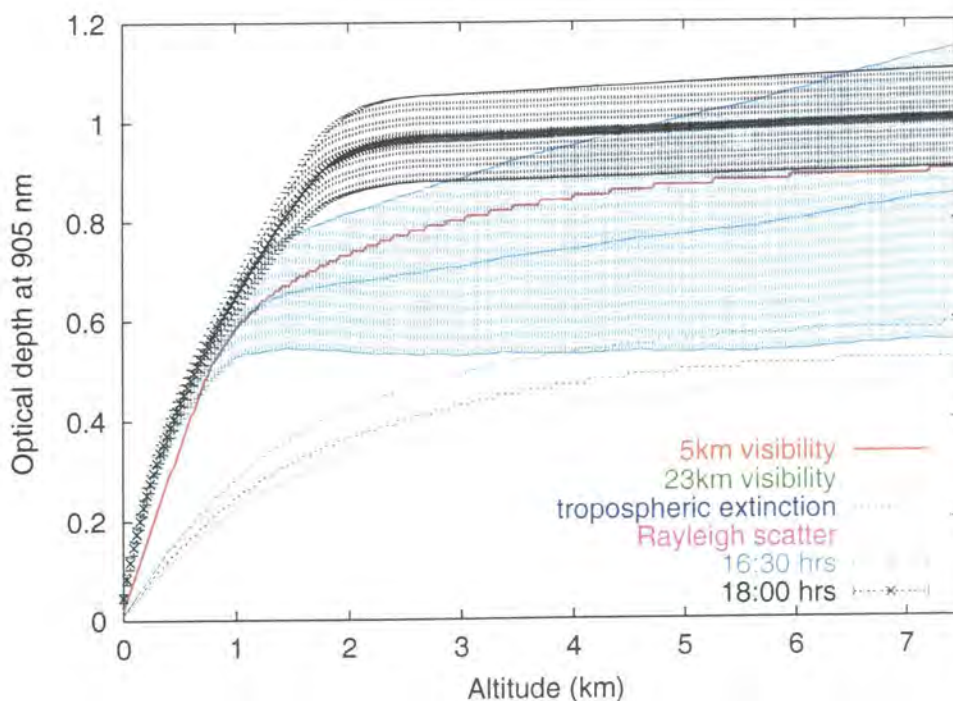


Figure 8.3: Diagram illustrating the optical depth profile at 905nm as inferred from measurements made with the CT25 LIDAR system at 16:30 and 18:30 on the 5th August. Also shown are models fits as described in the text.

However, it would be wrong to infer too much from these results, as yet there is only a small database of atmospheric results for the site. It can be said however, that at times of high obscuration, a ground level of 1800m should be used in MODTRAN simulations.

However, before the period of poor weather, the results from the ceilometer indicate no aerosol presence at all. This is obviously incorrect, which indicates that the aerosol density in the 7.5km above the H.E.S.S. site was below the signal to noise resolution of the ceilometer due to the signal digitisation. Given a tunable multi-wavelength LIDAR, and the fact that the backscatter intensity is proportional to $\sim \lambda^{-1}$ for Mie scattering and λ^{-4} for Rayleigh scattering, then by tuning the LIDAR to a lower wavelength, this problem would be easily overcome. Given that in the winter the atmosphere is likely to be more clear and stable than in the Namibian summer, it may be that first light has coincided with a particularly clear period and that after this point, more useful ceilometer results will be taken. Hopefully after the first year, a clear idea of the seasonal trend and typical daily variations in aerosol concentration will be known. Also, given time, data will be seen which correspond to atmospheric conditions which permit observations with the telescope, but which also possess a significant and measurable aerosol and molecular scattering component. At this point comparisons of real data with EAS and telescope response simulations will be possible.

The project to build a system to measure the low-level light signal that is returned from a corner reflector sited on a distant hill is currently, underway and the multi-wavelength LIDAR system is still in the planning/funding stage. These systems, along with the mid infra-red radiometers and optical telescopes, and TOMS satellite data [192], should give a continuous record of any subtle changes in the atmosphere above the site. In particular the corner reflector project and LIDAR data may in time highlight changes in the composition of the lower part (first 2 kilometres) of the atmosphere that could be used in a comparison with the simulated work presented in this thesis.

However, fortunately as chapter 7 indicates, within the scope of the errors of the simulations presented, the Hillas parameter distributions are not affected much by the changes in the atmospheric model in scaling the ground level from 0m a.s.l. to 1800m a.s.l. due to the selective nature of the telescope trigger. This work requires further study, however it means that for the interim it may be difficult to use Hillas parameter distributions of the background noise of the cosmic ray generated EAS as a direct measure of atmospheric clarity, though of course the trigger rate of the telescope is still an applicable measure of atmospheric quality. The future prospects for imaging Cherenkov astronomy are now covered again briefly.

8.4 The Future of Cherenkov Astronomy

8.4.1 Analysis and Simulation Refinement

Through this thesis the maturation of the field of ground-based VHE gamma-ray astronomy has been conveyed. This began in chapter 1 with the discussion of the discovery by Hess of cosmic rays, and has ended by reviewing the H.E.S.S. telescope system, which may at last answer the hundred year mystery of the origin of at least a significant fraction of the cosmic rays. However, as also shown gamma-ray astronomy has many other possible uses, both in terms of astronomy and particle physics. This maturation of the field is largely due to the imaging technique for hadron discrimination. Although other possible techniques have been suggested for hadron rejection ([30]), given modern computing requirements, and the large trigger rate of systems such as H.E.S.S, the Hillas parameter still remain the tool of choice [87]. Though their applicability is somewhat less useful at energies $< 80\text{GeV}$ for systems such as H.E.S.S., because here the amount of Cherenkov light falling within the image is very small, and below this point the main sources of interest for H.E.S.S. and VERITAS are likely to be pulsating, which makes background rejection simpler.

Given that modern particle accelerators are fast approaching the energies requirement to check the assumptions made about cross-section scaling (as discussed in Chapter 5), it may be possible to refine our simulations of EAS formation to a greater level of accuracy than possible before.

There still remains however a fundamental difference between the process studied in accelerator experiments and those of most importance in EAS development. Events measured at accelerators are generally those with high momentum transfer. They are well defined by QCD, but they constitute only a tiny part of the overall reaction rate ($< 10^{-6}$). Interactions with low momentum transfer (so called soft processes) produce particles with small transverse momenta, which mostly escape undetected in the beam pipe. Of most relevance to EAS models are the diffractive dissociation events, which originate from peripheral accelerator collisions, where only a small fraction of the energy is transferred to secondary particles. These mostly unstudied accelerator collisions, are vital for EAS development as they allow the energy to be carried further down into the atmosphere, and thus drive the air shower development. If this is combined with the fact that most energetic accelerators (with energies of $E_{lab} = 900\text{GeV}$) are proton-proton colliders, and that the nucleon-nucleus and nucleus-nucleus interactions vital for EAS

development are only studied at lower energies, it becomes easy to see why the hadronic models for TeV EAS development are uncertain. A full review of this can be found in [114].

However, at low energies ($\sim 100\text{GeV}$) there seems to be fairly good agreement between hadronic models. This is important, as at these energies the atmospheric fluctuations have a large impact on the H.E.S.S. trigger rate. Thus a continuous regime of atmospheric measurements at the sites of the Cherenkov telescope system, (using: multi-wavelength LIDAR, radiosondes, infra-red radiometers and horizontal extinction monitoring systems), will allow the simulations of EAS and telescope response to reach unprecedented levels of precision. This will in turn, increase the energy resolution and improve the errors on flux calculation (as discussed in Chapter 6) tremendously.

8.4.2 New Instrumentation

Imaging Cherenkov Telescopes

The completion date for the first 4 H.E.S.S. telescopes is the end of 2003, within a year of this the VERITAS system is believed to come online. As discussed before these two array systems give almost full sky coverage in the energy range from just below 100GeV to tens of TeV [91], [203]. Another array system CANGAROO III will soon go online in Australia [54]. As shown, the low altitude of this experiment, gives it a slight disadvantage over H.E.S.S., and its energy threshold is therefore likely to be a little higher than that of H.E.S.S.. However it is another important tool for exploration of the southern skies at GeV/TeV energies, and a comparison of data taken on the same source at similar times with both H.E.S.S. and CANGAROO III will provide unambiguous evidence for source activity.

MAGIC, a single Cherenkov telescope with a mirror area $> 230\text{m}^2$, will soon go online at the HEGRA site on La Palma (altitude of 2200m a.s.l.) [125]. This telescope is predicted to have an energy threshold of around 15 GeV , the lowest ever possible with an imaging Cherenkov telescope. In future years, it is hoped that the PMT camera of MAGIC will be replaced by avalanche photodiodes, which have a much higher quantum efficiency $> 80\%$, and it is claimed given the lightweight carbon fibre frame that MAGIC can be repositioned anywhere in the sky within ~ 30 seconds, making it ideal to study gamma-ray burst activity above 15 GeV . A similar system MACE has been proposed by a group based at the Bhabha Atomic Research Centre in India [119]. In the longer term,

a system has been proposed to place 5 large ($\sim 20\text{m}$ diameter mirror) imaging Cherenkov telescopes at an altitude of 5km , with an estimated threshold energy of 5 GeV [2].

Non-Imaging

The heliostat array systems (STACEE & CELESTE) use wavefront sampling techniques to discriminate against hadrons [60], [122]. The suppression is far less impressive than imaging, though good results have been found for, among other objects, Markarian 421 [122]. These systems have a large mirror area (STACEE $\sim 2300\text{ m}^2$, CELESTE $\sim 2160\text{ m}^2$), and thus a low threshold energy ($\sim 60\text{ GeV}$). At higher energies MILAGRO, is a system consisting of PMT's emerged in a water pool, with an energy threshold $\sim 5\text{TeV}$ [140]. Unlike its imaging counterparts, this system has a high duty cycle, and is operational almost 24 hours a day.

8.4.3 New Physics

If one compares figures 3.11 and 3.12, the countless opportunities for the new telescope systems to elucidate the origin of the gamma-ray emission from the unknown EGRET sources can be seen. The systems discussed in this chapter all help bridge the gap between the GLAST satellite due for launch in 2006 [68], and allow an as yet untapped region of the gamma-ray spectrum to be observed.

In chapter 4 many possible sources for investigation with the new and next generation of systems were reviewed. Some of the proposed questions for exploration included:

- Where do the galactic cosmic rays come from ?
- At what energy does the periodic signal from Pulsars disappear ?

What is the overall shape of the cosmic infra-red background ?

Also given that some of the primary particles producing EAS have been accelerated well beyond the capabilities of today's modern particle accelerators, one would hope that, with increasing confidence thanks to improved EAS simulation and atmospheric quality measurements, one may use the Cherenkov light produced by DC TeV sources as a means to investigating particle interactions at tens of TeV.

8.5 Final Conclusions

The main conclusions of this thesis are:

- The technique of imaging atmospheric Cherenkov astronomy for studying GeV/TeV astrophysical gamma-ray emission has been discussed, and many possible source candidates have been given, along with many theoretical models for emission.
- Sizeable differences have been shown in the spatial Cherenkov light profiles for ALTAI, CORSIKA and MOCCA for hadronic EAS. Some possible suggestions for the differences have been made, though this research does require further study. The effect this has on the Hillas parameter distributions as seen with the Mark 6 telescope has been shown.
- The integral flux of the AGN PKS 2155-304 above 1.5 TeV, assuming a differential spectral index of -2.6, as seen in 1996/1997 with the Durham Mark 6 telescope is found to be

$$S_{2.6}(1.5\text{TeV}) = (2.5 \pm 0.7_{\text{stat}} \pm \frac{0.5}{1.6_{\text{syst}}}) \times 10^{-7} \text{ photons m}^{-2} \text{ s}^{-1}$$

given the refined Durham Mark 6 telescope simulation code detailed in chapter 6.

- The effective area of the stand-alone H.E.S.S. telescope below 0.3 TeV for gamma-ray and cosmic ray EAS is seen to be noticeably altered by the aerosol attenuation model used, though little effect is seen in the Hillas parameter distributions for the data to be analysed. This will in part be due to the trigger and cuts used. As daily variations are likely, particularly in the low-level aerosol density, many devices for atmospheric study are shown to be in operation at the H.E.S.S. site.
- Given the different single photoelectron pulse assumed in simulation and the possible dead time of the system, it is quite possible that the trigger rate of the H.E.S.S. telescope for cosmic ray EAS at 20° zenith angle will be below $439 \pm 28 \pm 6$ Hz.

It is clear that the effects of the atmosphere on the performance of the stand-alone H.E.S.S. telescope require further study, but hopefully given; a large database of simulated events with full cosmic ray and gamma-ray spectra for varying quantities of aerosol density and composition, a large dataset of real measured gamma-ray and cosmic ray events from the first stand-alone H.E.S.S. telescope and a corresponding set of measurements from all the atmospheric monitoring equipment on site (including a multi-wavelength LIDAR for composition studies), it may be possible to perform a detailed study of the effects of small changes in the aerosol composition on events. This may be investigated in terms of overall trigger rates and Hillas parameters. Given time and further study, a possible technique

for using cosmic ray data as an atmospheric measurement tool may be developed.

As these final thoughts are written, the first stand-alone H.E.S.S. telescope begins to become more stable. However, the system is not yet completely stable, but data are available, and one of the observed images is included below for completeness, i.e. figure 8.4.

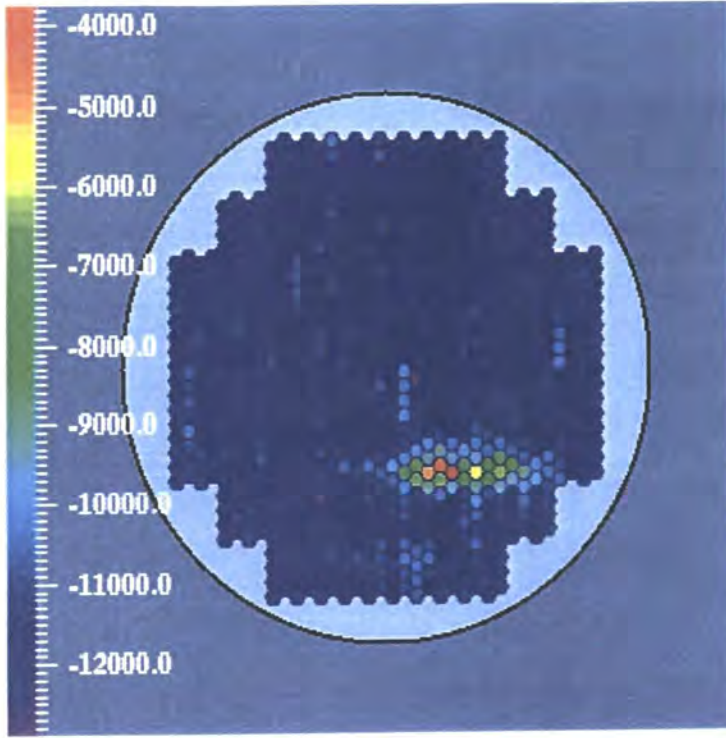


Figure 8.4: First images of cosmic ray data seen with first stand-alone H.E.S.S. telescope. This uncalibrated data, represents the first light seen with the uncalibrated H.E.S.S. Camera.

The calibrations systems for the camera have also gone online, and within the next two months shake-down of the system will occur. Given the sensitivity of the system (figure 8.5), many new sources of the types illustrated in Chapter 4 should become available.

One final thought is that if the AGN PKS 2155-304 were flaring with the same integral flux as derived in this thesis, then the same result at the 5σ measurable with the first 4 telescope H.E.S.S. system would be possible within 2-3 minutes of on source observation, compared with > 30 hours for the Mark 6. This represents a considerable leap in technological capability and shows that the future for the field of imaging atmospheric Cherenkov astronomy is very bright indeed.

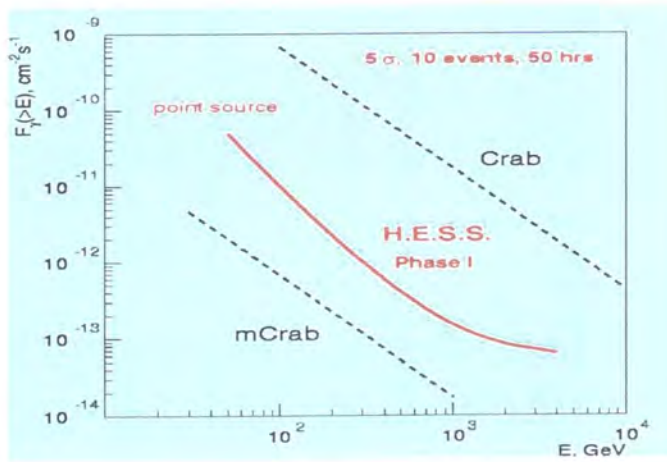


Figure 8.5: Sensitivity of the first 4 H.E.S.S. telescopes represented as flux versus energy. The curve shown represents a 5σ confidence level. Also shown as dotted lines are the Crab energy spectrum, and the milli-Crab confidence level.

Appendix A: MODTRAN Atmospheric Models

This tabular information includes: altitude (km), pressure (mb), density (cm^{-3}), and mixing ratios (ppmv, parts per million volume) for H_2O , O_3 , N_2O , CO and CH_4 . This is given for:

MODEL 1 = Tropical (15N Annual Average)

MODEL 2 = Mid-Latitude Summer (45N July)

MODEL 3 = Mid-Latitude Winter (45N Jan)

MODEL 4 = Sub-Arctic Summer (60N July)

MODEL 5 = Sub-Arctic Winter (60N Jan)

MODEL 6 = U.S. Standard (1976)

For altitudes up to 40 kilometres. All data is taken from [63].

ALT (KM)	PRES (MB)	TEMP (K)	DENSITY (CM ⁻³)	H ₂ O (PPMV)	O ₃ (PPMV)	N ₂ O (PPMV)	CO (PPMV)	CH ₄ (PPMV)
0.0	1.01E+03	299.7	2.45E+19	2.59E+04	2.87E-02	3.20E-01	1.50E-01	1.70E+00
1.0	9.04E+02	293.7	2.23E+19	1.95E+04	3.15E-02	3.20E-01	1.45E-01	1.70E+00
2.0	8.05E+02	287.7	2.02E+19	1.53E+04	3.34E-02	3.20E-01	1.40E-01	1.70E+00
3.0	7.15E+02	283.7	1.82E+19	8.60E+03	3.50E-02	3.20E-01	1.35E-01	1.70E+00
4.0	6.33E+02	277.0	1.65E+19	4.44E+03	3.56E-02	3.20E-01	1.31E-01	1.70E+00
5.0	5.59E+02	270.3	1.49E+19	3.35E+03	3.77E-02	3.20E-01	1.30E-01	1.70E+00
6.0	4.92E+02	263.6	1.35E+19	2.10E+03	3.99E-02	3.20E-01	1.29E-01	1.70E+00
7.0	4.32E+02	257.0	1.21E+19	1.29E+03	4.22E-02	3.20E-01	1.25E-01	1.70E+00
8.0	3.78E+02	250.3	1.09E+19	7.64E+02	4.47E-02	3.20E-01	1.19E-01	1.70E+00
9.0	3.29E+02	243.6	9.78E+18	4.10E+02	5.00E-02	3.20E-01	1.09E-01	1.69E+00
10.0	2.86E+02	237.0	8.77E+18	1.91E+02	5.60E-02	3.18E-01	9.96E-02	1.69E+00
11.0	2.47E+02	230.1	7.78E+18	7.31E+01	6.61E-02	3.14E-01	9.96E-02	1.68E+00
12.0	2.13E+02	223.6	6.90E+18	2.91E+01	7.82E-02	3.10E-01	7.81E-02	1.66E+00
13.0	1.82E+02	217.0	6.07E+18	9.90E+00	9.29E-02	3.05E-01	6.37E-02	1.65E+00
14.0	1.56E+02	210.3	5.37E+18	6.22E+00	1.05E-01	3.00E-01	5.03E-02	1.63E+00
15.0	1.32E+02	203.7	4.69E+18	4.00E+00	1.26E-01	2.94E-01	3.94E-02	1.61E+00
16.0	1.11E+02	197.0	4.08E+18	3.00E+00	1.44E-01	2.88E-01	3.07E-02	1.58E+00
17.0	9.37E+01	194.8	3.48E+18	2.90E+00	2.50E-01	2.78E-01	2.49E-02	1.55E+00
18.0	7.89E+01	198.8	2.87E+18	2.75E+00	5.00E-01	2.67E-01	1.97E-02	1.52E+00
19.0	6.66E+01	202.7	2.38E+18	2.60E+00	9.50E-01	2.53E-01	1.55E-02	1.48E+00
20.0	6.65E+01	206.7	1.98E+18	2.60E+00	1.40E+00	2.37E-01	1.33E-02	1.42E+00
21.0	4.80E+01	210.7	1.65E+18	2.65E+00	1.80E+00	2.19E-01	1.23E-02	1.36E+00
22.0	4.09E+01	214.6	1.38E+18	2.80E+00	2.40E+00	2.05E-01	1.23E-02	1.27E+00
23.0	3.50E+01	217.0	1.16E+18	2.90E+00	3.40E+00	1.97E-01	1.31E-02	1.19E+00
24.0	3.00E+01	219.2	9.92E+17	3.20E+00	4.30E+00	1.88E-01	1.40E-02	1.12E+00
25.0	2.57E+01	221.4	8.41E+17	3.25E+00	5.40E+00	1.76E-01	1.52E-02	1.06E+00
27.5	1.76E+01	227.0	5.62E+17	3.60E+00	7.80E+00	1.59E-01	1.72E-02	9.87E-01
30.0	1.22E+01	232.3	3.80E+17	4.00E+00	9.30E+00	1.42E-01	2.00E-02	9.14E-01
32.5	8.52E+00	237.7	2.59E+17	4.30E+00	9.85E+00	1.17E-01	2.27E-02	8.30E-01
35.0	6.00E+00	243.1	1.78E+17	4.60E+00	9.70E+00	9.28E-02	2.49E-02	7.46E-01
37.5	4.26E+00	248.5	1.24E+17	4.90E+00	8.80E+00	6.69E-02	2.74E-02	6.62E-01
40.0	3.05E+00	254.0	8.70E+16	5.20E+00	7.50E+00	4.51E-02	3.10E-02	5.64E-01

ALT (KM)	PRES (MB)	TEMP (K)	DENSITY (CM ⁻³)	H ₂ O (PPMV)	O ₃ (PPMV)	N ₂ O (PPMV)	CO (PPMV)	CH ₄ (PPMV)
0.0	1.01E+03	294.2	2.49E+19	1.88E+04	3.02E-02	3.20E-01	1.50E-01	1.70E+00
1.0	9.02E+02	289.7	2.25E+19	1.38E+04	3.34E-02	3.20E-01	1.45E-01	1.70E+00
2.0	8.02E+02	285.2	2.03E+19	9.68E+03	3.69E-02	3.20E-01	1.40E-01	1.70E+00
3.0	7.10E+02	279.2	1.84E+19	5.98E+03	4.22E-02	3.20E-01	1.35E-01	1.70E+00
4.0	6.28E+02	273.2	1.66E+19	3.81E+03	4.82E-02	3.20E-01	1.31E-01	1.70E+00
5.0	5.54E+02	267.2	1.50E+19	2.23E+03	5.51E-02	3.20E-01	1.30E-01	1.69E+00
6.0	4.87E+02	261.2	1.35E+19	1.51E+03	6.41E-02	3.20E-01	1.29E-01	1.67E+00
7.0	4.26E+02	254.7	1.21E+19	1.02E+03	7.76E-02	3.20E-01	1.25E-01	1.65E+00
8.0	3.72E+02	248.2	1.08E+19	6.46E+02	9.13E-02	3.20E-01	1.19E-01	1.63E+00
9.0	3.24E+02	241.7	9.71E+18	4.13E+02	1.11E-01	3.16E-01	1.09E-01	1.62E+00
10.0	2.81E+02	235.3	8.65E+18	2.47E+02	1.30E-01	3.10E-01	9.96E-02	1.58E+00
11.0	2.43E+02	228.8	7.69E+18	9.56E+01	1.79E-01	2.99E-01	8.96E-02	1.54E+00
12.0	2.09E+02	222.3	6.81E+18	2.94E+01	2.23E-01	2.94E-01	7.81E-02	1.51E+00
13.0	1.79E+02	215.8	6.01E+18	8.00E+00	3.00E-01	2.86E-01	6.37E-02	1.48E+00
14.0	1.53E+02	215.7	5.14E+18	5.00E+00	4.40E-01	2.80E-01	5.03E-02	1.45E+00
15.0	1.30E+02	215.7	4.36E+18	3.40E+00	5.00E-01	2.72E-01	3.94E-02	1.42E+00
16.0	1.11E+02	215.7	3.73E+18	3.30E+00	6.00E-01	2.61E-01	3.07E-02	1.39E+00
17.0	9.50E+01	215.7	3.19E+18	3.20E+00	7.00E-01	2.42E-01	2.49E-02	1.36E+00
18.0	8.12E+01	216.8	2.71E+18	3.15E+00	1.00E+00	2.17E-01	1.97E-02	1.32E+00
19.0	6.95E+01	217.9	2.31E+18	3.20E+00	1.50E+00	1.84E-01	1.55E-02	1.28E+00
20.0	5.95E+01	219.2	1.96E+18	3.30E+00	2.00E+00	1.61E-01	1.33E-02	1.22E+00
21.0	5.10E+01	220.4	1.67E+18	3.45E+00	2.40E+00	1.32E-01	1.23E-02	1.15E+00
22.0	4.37E+01	221.6	1.42E+18	3.60E+00	2.90E+00	1.15E-01	1.23E-02	1.07E+00
23.0	3.76E+01	222.8	1.22E+18	3.85E+00	3.40E+00	1.04E-01	1.31E-02	9.73E-01
24.0	3.22E+01	223.9	1.04E+18	4.00E+00	4.00E+00	9.62E-02	1.40E-02	8.80E-01
25.0	2.77E+01	225.1	8.91E+17	4.20E+00	4.30E+00	8.96E-02	1.52E-02	7.89E-01
27.5	1.90E+01	228.5	6.05E+17	4.45E+00	6.00E+00	8.01E-02	1.72E-02	7.05E-01
30.0	1.32E+01	233.7	4.09E+17	4.70E+00	7.00E+00	6.70E-02	2.00E-02	6.32E-01
32.5	9.30E+00	239.0	2.82E+17	4.85E+00	8.10E+00	4.96E-02	2.27E-02	5.59E-01
35.0	6.52E+00	245.2	1.92E+17	4.95E+00	8.90E+00	3.70E-02	2.49E-02	5.01E-01
37.5	4.64E+00	251.3	1.33E+17	5.00E+00	8.70E+00	2.52E-02	2.72E-02	4.45E-01
40.0	3.33E+00	257.5	9.37E+16	5.10E+00	7.55E+00	1.74E-02	2.96E-02	3.92E-01

ALT (KM)	PRES (MB)	TEMP (K)	DENSITY (CM ⁻³)	H ₂ O (PPMV)	O ₃ (PPMV)	N ₂ O (PPMV)	CO (PPMV)	CH ₄ (PPMV)
0.0	1.01E+03	272.2	2.71E+19	4.32E+03	2.78E-02	3.20E-01	1.50E-01	1.70E+00
1.0	8.97E+02	268.7	2.42E+19	3.45E+03	2.80E-02	3.20E-01	1.45E-01	1.70E+00
2.0	7.89E+02	265.2	2.15E+19	2.79E+03	2.85E-02	3.20E-01	1.40E-01	1.70E+00
3.0	6.93E+02	261.7	1.92E+19	2.09E+03	3.20E-02	3.20E-01	1.35E-01	1.70E+00
4.0	6.08E+02	255.7	1.72E+19	1.28E+03	3.57E-02	3.20E-01	1.31E-01	1.70E+00
5.0	5.31E+02	249.7	1.54E+19	8.24E+02	4.72E-02	3.20E-01	1.30E-01	1.69E+00
6.0	4.62E+02	243.7	1.37E+19	5.10E+02	5.84E-02	3.20E-01	1.29E-01	1.67E+00
7.0	4.01E+02	237.7	1.22E+19	2.32E+02	7.89E-02	3.20E-01	1.25E-01	1.65E+00
8.0	3.47E+02	231.7	1.08E+19	1.08E+02	1.04E-01	3.20E-01	1.19E-01	1.63E+00
9.0	2.99E+02	225.7	9.61E+18	5.57E+01	1.57E-01	3.16E-01	1.09E-01	1.62E+00
10.0	2.56E+02	219.7	8.47E+18	2.96E+01	2.37E-01	3.10E-01	9.96E-02	1.58E+00
11.0	2.19E+02	219.2	7.27E+18	1.00E+01	3.62E-01	2.99E-01	8.96E-02	1.54E+00
12.0	1.88E+02	218.7	6.23E+18	6.00E+00	5.23E-01	2.94E-01	7.81E-02	1.51E+00
13.0	1.61E+02	218.2	5.35E+18	5.00E+00	7.04E-01	2.86E-01	6.37E-02	1.48E+00
14.0	1.37E+02	217.7	4.58E+18	4.80E+00	8.00E-01	2.80E-01	5.03E-02	1.45E+00
15.0	1.17E+02	217.2	3.91E+18	4.70E+00	9.00E-01	2.72E-01	3.94E-02	1.42E+00
16.0	1.00E+02	216.7	3.36E+18	4.60E+00	1.10E+00	2.61E-01	3.07E-02	1.39E+00
17.0	8.61E+01	216.2	2.88E+18	4.50E+00	1.40E+00	2.42E-01	2.42E-02	1.36E+00
18.0	7.36E+01	215.7	2.47E+18	4.50E+00	1.80E+00	2.17E-01	1.97E-02	1.32E+00
19.0	6.28E+01	215.2	2.11E+18	4.50E+00	2.30E+00	1.84E-01	1.55E-02	1.28E+00
20.0	5.37E+01	215.2	1.80E+18	4.50E+00	2.90E+00	1.62E-01	1.33E-02	1.22E+00
21.0	4.58E+01	215.2	1.54E+18	4.50E+00	3.50E+00	1.36E-01	1.23E-02	1.15E+00
22.0	3.91E+01	215.2	1.31E+18	4.53E+00	3.90E+00	1.23E-01	1.23E-02	1.07E+00
23.0	3.34E+01	215.2	1.12E+18	4.55E+00	4.30E+00	1.12E-01	1.31E-02	9.73E-01
24.0	2.86E+01	215.2	9.63E+17	4.60E+00	4.70E+00	1.05E-01	1.40E-02	8.80E-01
25.0	2.44E+01	215.2	8.21E+17	4.65E+00	5.10E+00	9.66E-02	1.50E-02	7.93E-01
27.5	1.64E+01	215.5	5.53E+17	4.70E+00	5.60E+00	8.69E-02	1.60E-02	7.13E-01
30.0	1.11E+01	217.4	3.70E+17	4.75E+00	6.10E+00	7.52E-02	1.71E-02	6.44E-01
32.5	7.56E+00	220.4	2.48E+17	4.80E+00	6.80E+00	6.13E-02	1.85E-02	5.75E-01
35.0	5.18E+00	227.9	1.64E+17	4.85E+00	7.10E+00	5.12E-02	2.00E-02	5.05E-01
37.5	3.60E+00	235.5	1.10E+17	4.90E+00	7.20E+00	3.97E-02	2.15E-02	4.48E-01
40.0	2.53E+00	243.2	7.54E+16	4.95E+00	6.90E+00	3.00E-02	2.33E-02	3.93E-01

ALT (KM)	PRES (MB)	TEMP (K)	DENSITY (CM ⁻³)	H ₂ O (PPMV)	O ₃ (PPMV)	N ₂ O (PPMV)	CO (PPMV)	CH ₄ (PPMV)
0.0	1.01E+03	287.2	2.54E+19	1.19E+04	2.41E-02	3.10E-01	1.50E-01	1.70E+00
1.0	8.96E+02	281.7	2.30E+19	8.70E+03	2.94E-02	3.10E-01	1.45E-01	1.70E+00
2.0	7.92E+02	276.3	2.08E+19	6.75E+03	3.38E-02	3.10E-01	1.40E-01	1.70E+00
3.0	7.00E+02	270.9	1.87E+19	4.82E+03	3.89E-02	3.10E-01	1.35E-01	1.70E+00
4.0	6.16E+02	265.5	1.68E+19	3.38E+03	4.48E-02	3.08E-01	1.31E-01	1.70E+00
5.0	5.41E+02	260.1	1.50E+19	2.22E+03	5.33E-02	3.02E-01	1.30E-01	1.69E+00
6.0	4.74E+02	253.1	1.35E+19	1.33E+03	6.56E-02	2.91E-01	1.29E-01	1.67E+00
7.0	4.13E+02	246.1	1.21E+19	7.97E+02	7.74E-02	2.82E-01	1.25E-01	1.65E+00
8.0	3.59E+02	239.2	1.08E+19	4.00E+02	9.11E-02	2.76E-01	1.19E-01	1.63E+00
9.0	3.10E+02	232.2	9.70E+18	1.30E+02	1.42E-01	2.70E-01	1.09E-01	1.62E+00
10.0	2.67E+02	225.2	8.61E+18	4.24E+01	1.89E-01	2.65E-01	9.96E-02	1.58E+00
11.0	2.30E+02	225.2	7.40E+18	1.33E+01	3.05E-01	2.60E-01	8.96E-02	1.54E+00
12.0	1.97E+02	225.2	6.36E+18	6.00E+00	4.10E-01	2.55E-01	7.81E-02	1.51E+00
13.0	1.70E+02	225.2	5.47E+18	4.45E+00	5.00E-01	2.49E-01	6.37E-02	1.47E+00
14.0	1.46E+02	225.2	4.69E+18	4.00E+00	6.00E-01	2.43E-01	5.03E-02	1.43E+00
15.0	1.26E+02	225.2	4.05E+18	4.00E+00	7.00E-01	2.36E-01	3.94E-02	1.39E+00
16.0	1.08E+02	225.2	3.47E+18	4.00E+00	8.50E-01	2.28E-01	3.07E-02	1.34E+00
17.0	9.28E+01	225.2	2.98E+18	4.05E+00	1.00E+00	2.18E-01	2.49E-02	1.29E+00
18.0	7.98E+01	225.2	2.56E+18	4.30E+00	1.30E+00	2.04E-01	1.97E-02	1.23E+00
19.0	6.86E+01	225.2	2.20E+18	4.50E+00	1.70E+00	1.82E-01	1.55E-02	1.16E+00
20.0	5.90E+01	225.2	1.89E+18	4.60E+00	2.10E+00	1.57E-01	1.33E-02	1.07E+00
21.0	5.07E+01	225.2	1.63E+18	4.70E+00	2.70E+00	1.35E-01	1.23E-02	9.90E-01
22.0	4.36E+01	225.2	1.40E+18	4.80E+00	3.30E+00	1.22E-01	1.23E-02	9.17E-01
23.0	3.75E+01	225.2	1.20E+18	4.83E+00	3.70E+00	1.10E-01	1.31E-02	8.57E-01
24.0	3.22E+01	226.6	1.03E+18	4.85E+00	4.20E+00	9.89E-02	1.40E-02	8.01E-01
25.0	2.78E+01	228.1	8.83E+17	4.90E+00	4.50E+00	8.78E-02	1.51E-02	7.48E-01
27.5	1.92E+01	231.0	6.03E+17	4.95E+00	5.30E+00	7.33E-02	1.65E-02	6.96E-01
30.0	1.34E+01	235.1	4.13E+17	5.00E+00	5.70E+00	5.94E-02	1.81E-02	6.44E-01
32.5	9.40E+00	240.0	2.83E+17	5.00E+00	6.90E+00	4.15E-02	2.00E-02	5.89E-01
35.0	6.61E+00	247.2	1.93E+17	5.00E+00	7.70E+00	3.03E-02	2.18E-02	5.24E-01
37.5	4.72E+00	254.6	1.34E+17	5.00E+00	7.80E+00	1.95E-02	2.34E-02	4.51E-01
40.0	3.40E+00	262.1	9.40E+16	5.00E+00	7.00E+00	1.27E-02	2.50E-02	3.71E-01

ALT (KM)	PRES (MB)	TEMP (K)	DENSITY (CM ⁻³)	H ₂ O (PPMV)	O ₃ (PPMV)	N ₂ O (PPMV)	CO (PPMV)	CH ₄ (PPMV)
0.0	1.01E+03	257.2	2.85E+19	1.41E+03	1.80E-02	3.20E-01	1.50E-01	1.70E+00
1.0	8.87E+02	259.1	2.48E+19	1.62E+03	2.07E-02	3.20E-01	1.45E-01	1.70E+00
2.0	7.77E+02	255.9	2.20E+19	1.43E+03	2.34E-02	3.20E-01	1.40E-01	1.70E+00
3.0	6.79E+02	252.7	1.95E+19	1.17E+03	2.77E-02	3.20E-01	1.35E-01	1.70E+00
4.0	5.93E+02	247.7	1.73E+19	7.90E+02	3.25E-02	3.20E-01	1.31E-01	1.70E+00
5.0	5.15E+02	240.9	1.55E+19	4.31E+02	3.80E-02	3.20E-01	1.30E-01	1.69E+00
6.0	4.46E+02	234.1	1.38E+19	2.37E+02	4.45E-02	3.20E-01	1.29E-01	1.67E+00
7.0	3.85E+02	227.3	1.22E+19	1.47E+02	7.25E-02	3.20E-01	1.25E-01	1.65E+00
8.0	3.30E+02	220.6	1.08E+19	3.38E+01	1.04E-01	3.20E-01	1.19E-01	1.63E+00
9.0	2.82E+02	217.2	9.44E+18	2.98E+01	2.10E-01	3.16E-01	1.09E-01	1.62E+00
10.0	2.41E+02	217.2	8.06E+18	2.00E+01	3.00E-01	3.10E-01	9.96E-02	1.58E+00
11.0	2.06E+02	217.2	6.89E+18	1.00E+01	3.50E-01	2.99E-01	8.96E-02	1.54E+00
12.0	1.76E+02	217.2	5.89E+18	6.00E+00	4.00E-01	2.94E-01	7.81E-02	1.51E+00
13.0	1.51E+02	217.2	5.03E+18	4.45E+00	6.50E-01	2.86E-01	6.37E-02	1.47E+00
14.0	1.29E+02	217.2	4.30E+18	4.50E+00	9.00E-01	2.80E-01	5.03E-02	1.43E+00
15.0	1.10E+02	217.2	3.68E+18	4.55E+00	1.20E+00	2.72E-01	3.94E-02	1.39E+00
16.0	9.43E+01	216.6	3.15E+18	4.60E+00	1.50E+00	2.61E-01	3.07E-02	1.34E+00
17.0	8.05E+01	216.0	2.10E+18	4.65E+00	1.90E+00	2.42E-01	2.49E-02	1.29E+00
18.0	6.88E+01	215.4	2.31E+18	4.70E+00	2.45E+00	2.17E-01	1.97E-02	1.23E+00
19.0	5.87E+01	214.8	1.98E+18	4.75E+00	3.10E+00	1.84E-01	1.55E-02	1.16E+00
20.0	5.01E+01	214.2	1.69E+18	4.80E+00	3.70E+00	1.62E-01	1.33E-02	1.08E+00
21.0	4.27E+01	213.6	1.45E+18	4.85E+00	4.00E+00	1.36E-01	1.23E-02	1.01E+00
22.0	3.64E+01	213.0	1.24E+18	4.90E+00	4.20E+00	1.23E-01	1.23E-02	9.56E-01
23.0	3.10E+01	212.4	1.06E+18	4.95E+00	4.50E+00	1.12E-01	1.31E-02	9.01E-01
24.0	2.64E+01	211.8	9.06E+17	5.00E+00	4.60E+00	1.04E-01	1.40E-02	8.48E-01
25.0	2.25E+01	211.2	7.74E+17	5.00E+00	4.70E+00	9.57E-02	1.52E-02	7.96E-01
27.5	1.51E+01	213.6	5.13E+17	5.00E+00	4.90E+00	8.60E-02	1.72E-02	7.45E-01
30.0	1.02E+01	216.0	3.42E+17	5.00E+00	5.40E+00	7.31E-02	2.04E-02	6.94E-01
32.5	6.91E+00	218.5	2.29E+17	5.00E+00	5.90E+00	5.71E-02	2.49E-02	6.43E-01
35.0	4.70E+00	222.3	1.53E+17	5.00E+00	6.20E+00	4.67E-02	3.17E-02	5.88E-01
37.5	3.23E+00	228.5	1.02E+17	5.00E+00	6.25E+00	3.44E-02	4.43E-02	5.24E-01
40.0	2.24E+00	234.7	6.92E+16	5.00E+00	5.90E+00	2.47E-02	6.47E-02	4.51E-01

ALT (KM)	PRES (MB)	TEMP (K)	DENSITY (CM ⁻³)	H ₂ O (PPMV)	O ₃ (PPMV)	N ₂ O (PPMV)	CO (PPMV)	CH ₄ (PPMV)
0.0	1.01E+03	288.2	2.54E+19	7.75E+03	2.66E-02	3.20E-01	1.50E-01	1.70E+00
1.0	8.98E+02	281.7	2.31E+19	6.07E+03	2.93E-02	3.20E-01	1.45E-01	1.70E+00
2.0	7.95E+02	275.2	2.09E+19	4.63E+03	3.24E-02	3.20E-01	1.40E-01	1.70E+00
3.0	7.01E+02	268.7	1.89E+19	3.18E+03	3.32E-02	3.20E-01	1.35E-01	1.70E+00
4.0	6.16E+02	262.2	1.70E+19	2.16E+03	3.39E-02	3.20E-01	1.31E-01	1.70E+00
5.0	5.40E+02	255.7	1.53E+19	1.40E+03	3.77E-02	3.20E-01	1.30E-01	1.70E+00
6.0	4.72E+02	249.2	1.37E+19	9.25E+02	4.11E-02	3.20E-01	1.29E-01	1.70E+00
7.0	4.11E+02	242.7	1.22E+19	5.72E+02	5.01E-02	3.20E-01	1.25E-01	1.70E+00
8.0	3.56E+02	236.2	1.09E+19	3.67E+02	5.97E-02	3.20E-01	1.19E-01	1.70E+00
9.0	3.08E+02	229.7	9.71E+18	1.58E+02	9.17E-02	3.20E-01	1.09E-01	1.69E+00
10.0	2.65E+02	223.3	8.60E+18	7.00E+01	1.31E-01	3.18E-01	9.96E-02	1.69E+00
11.0	2.27E+02	216.8	7.58E+18	3.61E+01	2.15E-01	3.14E-01	8.96E-02	1.68E+00
12.0	1.94E+02	216.7	6.48E+18	1.91E+01	3.10E-01	3.10E-01	7.81E-02	1.66E+00
13.0	1.65E+02	216.7	5.54E+18	1.09E+01	3.85E-01	3.05E-01	6.37E-02	1.65E+00
14.0	1.41E+02	216.7	4.73E+18	5.93E+00	5.03E-01	3.00E-01	5.03E-02	1.63E+00
15.0	1.21E+02	216.7	4.05E+18	5.00E+00	6.51E-01	2.94E-01	3.94E-02	1.61E+00
16.0	1.03E+02	216.7	3.46E+18	3.95E+00	8.70E-01	2.88E-01	3.07E-02	1.58E+00
17.0	8.85E+01	216.7	2.96E+18	3.85E+00	1.19E+00	2.78E-01	2.49E-02	1.55E+00
18.0	7.56E+01	216.7	2.53E+18	3.83E+00	1.59E+00	2.67E-01	1.97E-02	1.52E+00
19.0	6.46E+01	216.7	2.16E+18	3.85E+00	2.03E+00	2.53E-01	1.55E-02	1.48E+00
20.0	5.52E+01	216.7	1.84E+18	3.90E+00	2.58E+00	2.37E-01	1.33E-02	1.42E+00
21.0	4.72E+01	217.6	1.57E+18	3.98E+00	3.03E+00	2.19E-01	1.23E-02	1.36E+00
22.0	4.04E+01	218.6	1.34E+18	4.07E+00	3.65E+00	2.05E-01	1.23E-02	1.27E+00
23.0	3.46E+01	219.6	1.14E+18	4.20E+00	4.17E+00	1.97E-01	1.31E-02	1.19E+00
24.0	2.97E+01	220.6	9.76E+17	4.30E+00	4.63E+00	1.88E-01	1.40E-02	1.12E+00
25.0	2.54E+01	221.6	8.33E+17	4.43E+00	5.12E+00	1.76E-01	1.50E-02	1.06E+00
27.5	1.74E+01	224.0	5.64E+17	4.58E+00	5.80E+00	1.59E-01	1.60E-02	9.87E-01
30.0	1.19E+01	226.5	3.83E+17	4.73E+00	6.55E+00	1.42E-01	1.71E-02	9.14E-01
32.5	8.01E+00	230.0	2.52E+17	4.83E+00	7.37E+00	1.17E-01	1.85E-02	8.30E-01
35.0	5.74E+00	236.5	1.76E+17	4.90E+00	7.84E+00	9.28E-02	2.01E-02	7.46E-01
37.5	4.15E+00	242.9	1.23E+17	4.95E+00	7.80E+00	6.69E-02	2.22E-02	6.62E-01
40.0	2.87E+00	250.4	8.31E+16	5.03E+00	7.30E+00	4.51E-02	2.50E-02	5.64E-01

Appendix B: MODTRAN Aerosol Models

8.5.1 Composition

The following details are taken from [185] and are applicable to the aerosol attenuation models used in MODTRAN4 [63].

In the boundary layer (0-2 km) the shape of the aerosol size distribution and composition for marine and rural haze models is assumed to be invariant with altitude. Therefore only the total particle number is being varied with altitude, this is only a good approximation when dealing with clear and stable atmospheres with visibility of ≤ 23 km, i.e. those used in this thesis.

Rural Aerosols

The rural model is intended to represent the aerosol conditions one finds in continental areas which are not directly influenced by urban and/or industrial sources. This continental rural aerosol background is partly the product of reactions between various gases in the atmosphere, and partly due to dust particles picked up from the surface. The particle concentration is largely dependant on the history of the airmass, carrying the aerosol particles.

In 1963, Junge suggested that the most measured aerosol size distributions over the range of radius from 0.1 to 10 μ m could be described by an inverse power law [106]. However the data itself shows a bimodal distribution, with one broad peak between 0.1 and 1.0 μ m and the second (and larger peak) between 5 and 100 μ m. In order to represent this feature as well as to be approximately consistent with all the experimental data, the size distribution used for the rural model is the sum of two log-normal distributions, given by:

$$\frac{dN(r)}{dr} = \sum_{i=1}^2 \left(\frac{N_i}{\ln(10)r\sigma_i\sqrt{2\pi}} \right) \exp - \left(\frac{(\log r - \log r_i)^2}{2\sigma_i^2} \right) \quad (\text{B-1})$$

Where $N(r)$ is the cumulative number density, and r is the particle radius. The other parameters are given in table B-1 for comparison with those due to the maritime model.

Maritime Model

The aerosol compositions and distributions over the oceans are significantly different from continental aerosol types. The maritime aerosol component is due to the salt particles which are caused by the evaporation of seaspray droplets. This atmosphere is also applicable to coastal sites, such as the HEGRA site on La Palma. The maritime model is therefore composed of two parts: the sea spray produced component, and a continental component which is assumed to be identical to the rural haze model, with the exception that most of the very large particles were eliminated, since they are eventually lost due to fallout as the air mass move across the ocean. The properties of the seaspray produced component especially in the lower 100m or so above the water depend strongly on relative humidity and also windspeed. The number of seaspray produced aerosols increases with windspeed.

Troposphere

In the troposphere above the boundary layer, the distribution and nature of the atmospheric aerosols becomes less sensitive to geography and the meso or synoptic scale meteorological variations. However some variations can be seen, for instance the count rate of the HEGRA system has been seen to be effected by changes in the amount of dust blown from the Sahara [17]. It is also possible to study the movement of these large aerosol migrations using the Total Ozone Mapping Spectrometer (TOMS) satellite [192].

So far however, only a simple single model (basically a scaled version of the rural haze model, minus the larger particles) exists within MODTRAN for the troposphere. Though it has been suggested that the aerosol concentrations are greater in the spring-summer period [25], therefore 2 versions of the models exist with the spring-summer having slightly higher aerosol concentration.

Stratospheric Aerosol Models

Measurements taken indicate a rather uniform aerosol concentration in the region from 10 to 30km (the lower part of which typically contains the shower maximum). This background may be increased by a factor of 100 after a volcanic eruption, and the effects on the stratospheric aerosol composition may last for months afterwards. We ignore this effect and use only the normal background model. The size distributions of aerosols in the stratosphere has a modified form to that used in the lower parts of the atmosphere.

It is given by:

$$\frac{dN}{dr} = n(r) = Ar^\alpha \exp(-Br^\nu) \quad (\text{B-2})$$

Overall Models

The overall parameters of aerosol size used (as applicable to Chapter 7) are shown below in table B-1.

Aerosol Model Type	N_1^*	r_1	σ_1	N_2^*	r_2	σ_2
Rural	0.9999975	0.005 μm	0.475	2.5×10^{-6}	0.5 μm	0.475
Maritime(1)	1	0.005 μm	0.475			
Maritime(2)	1	0.3 μm	0.4			
	A	α	ν	B		
Stratospheric	324	1	1	18		

Table B-1: Table showing size distribution parameters for different aerosol models used in MODTRAN calculations of Chapter 7. Normalised to 1 particle cm^{-3} . * indicates that for this condition $N_1 + N_2 = 1$.

The most important factor on absolute aerosol number levels for any particular model is the relative humidity used. In each case the value used is based around the water content and temperature derived from the atmospheric profiles outlined in appendix A.

8.5.2 Light Attenuation Calculation

Once the size distribution and the refractive index (as derived from appendix A) of the aerosol models are specified, the optical properties such as the scattering and absorption coefficients can be calculated from Mie theory (for Cherenkov astronomy the scattering typically removes the light from the field of view and can therefore be thought of as an attenuating process as well). For the Mie calculations the aerosols are assumed to be symmetrical, however this is only true for the liquid aerosols, dust for instance will obviously be irregularly shaped. In this treatment, one considers the electromagnetic interaction between the sphere and the plane light wave (as expressed in vector spherical harmonics), the scattering and attenuation amplitude functions may then be calculated. This is described in detail in [93], and code used for this calculation in MODTRAN is detailed in [109].

Appendix C: Cameras Images

This appendix contains some simulated sample camera images from the first stand alone H.E.S.S. telescope camera for gamma-ray and cosmic ray events. The red tubes indicate those which do not form part of the image. They have a Poissonian distribution of NSB noise with mean 300 digital counts. This mean value has been subtracted from each tube, so their values fluctuate around zero. The green coloured tubes are those which possess a signal greater than 4.25σ of the NSB. The blue coloured tubes possess a signal greater than 2.25σ of the NSB. The blue tubes must also be neighbouring a green tube. Two figures are included for each event; the face on camera view, and a side view to show the magnitude of the event in digital counts. The specifics of the featured events are given in table C-1.

Figure No.	Primary	Primary Energy (TeV)	Core Location (m)
1 & 2	Gamma-Ray	1.43	77.1
3 & 4	Gamma-Ray	0.12	107.7
5 & 6	Gamma-Ray	0.08	110.0
7 & 8	Proton	5.2	67.6
9 & 10	Proton	0.6	107.0
11 & 12	Proton	0.225	105.0

Table C-1: Table of images contained within appendix C, giving primary, primary energy and core location.

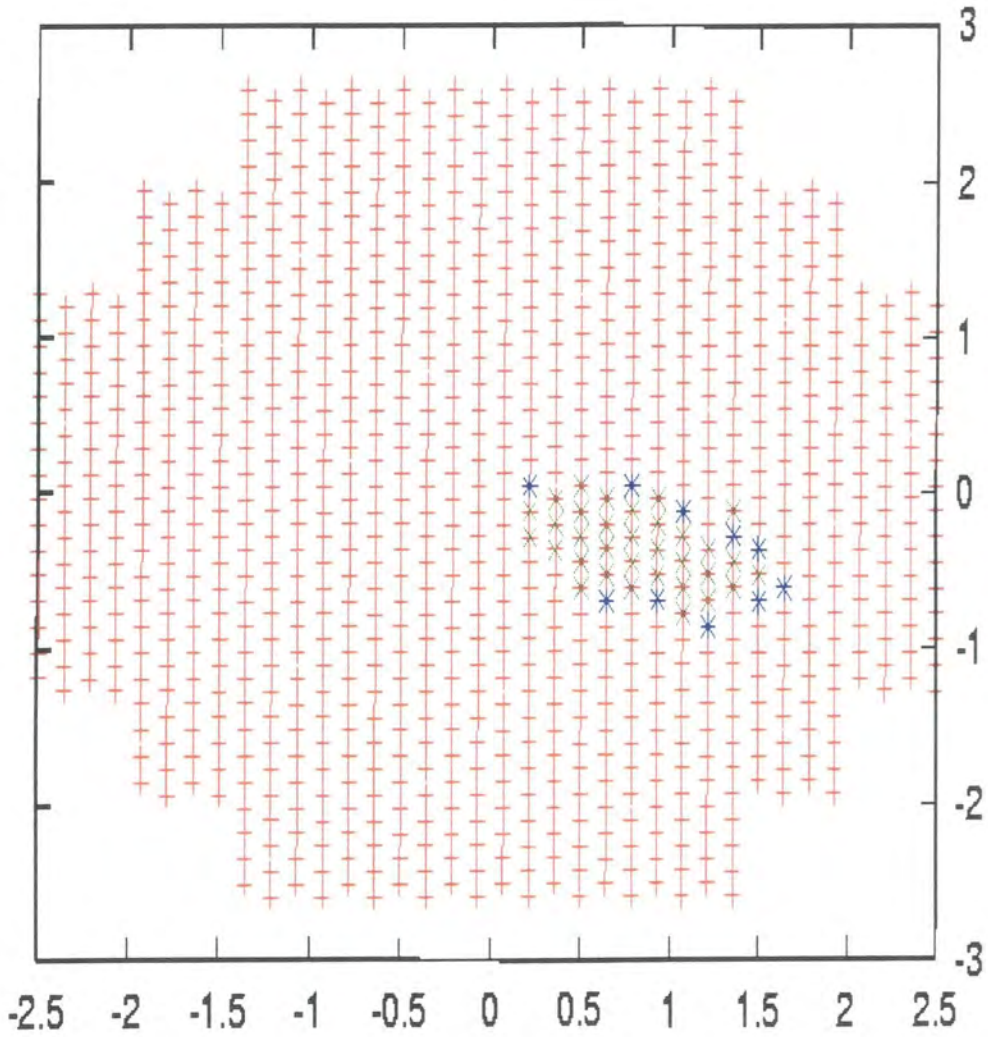


Figure C-1: View of simulated first H.E.S.S. camera, and its response to a 1.43 TeV gamma-ray landing 77.1m away. The X (horizontal) and Y (vertical) axis are in degrees.

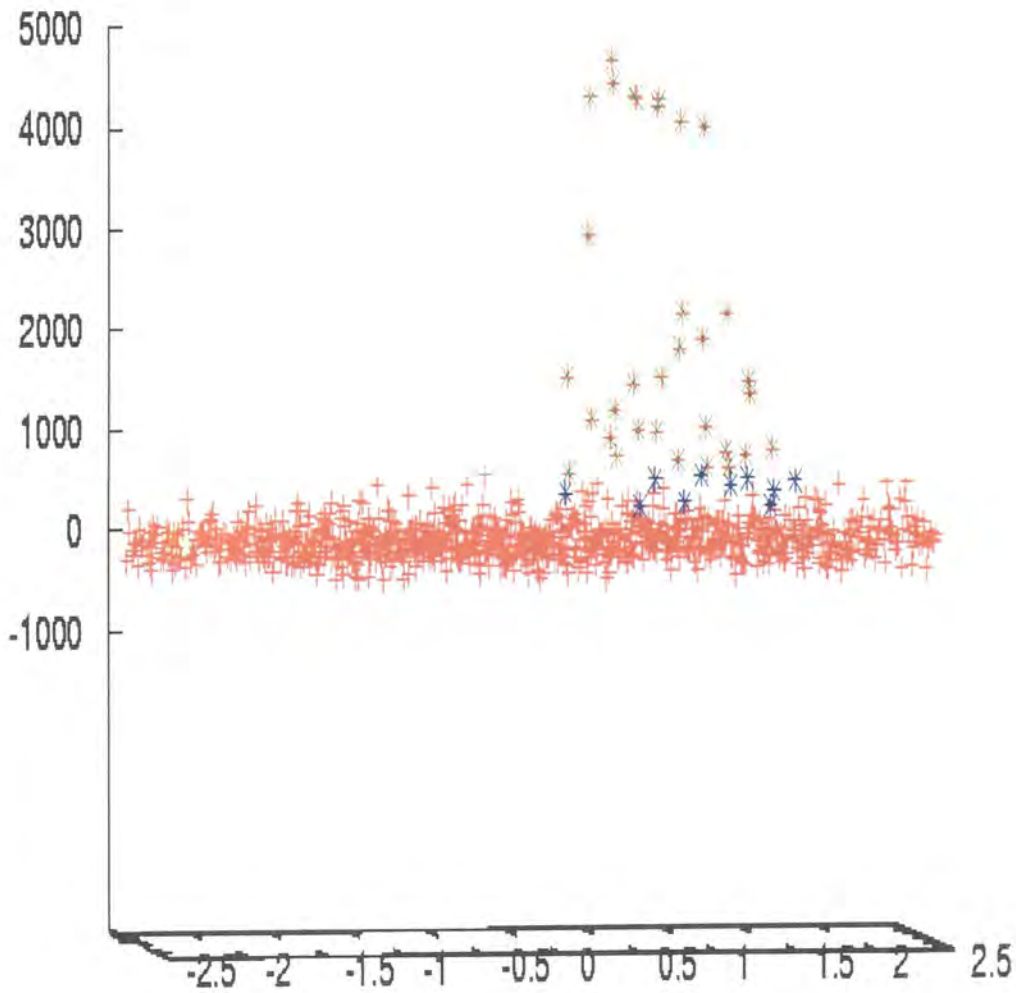


Figure C-2: Edge on perspective from figure C-1. Z axis (vertical) is in digital counts.

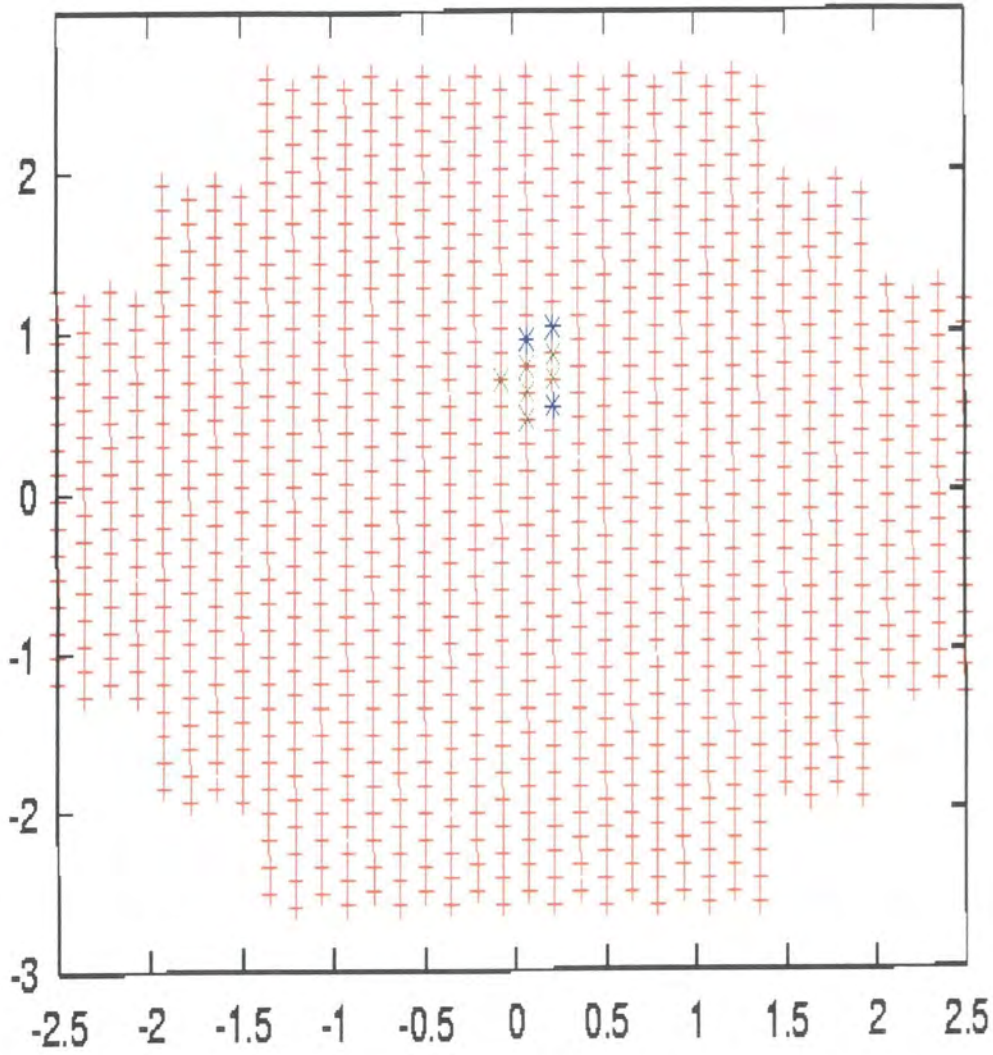


Figure C-3: View of simulated first H.E.S.S. camera, and its response to a 0.12 TeV gamma-ray landing 107.7m away. The X (horizontal) and Y (vertical) axis are in degrees.

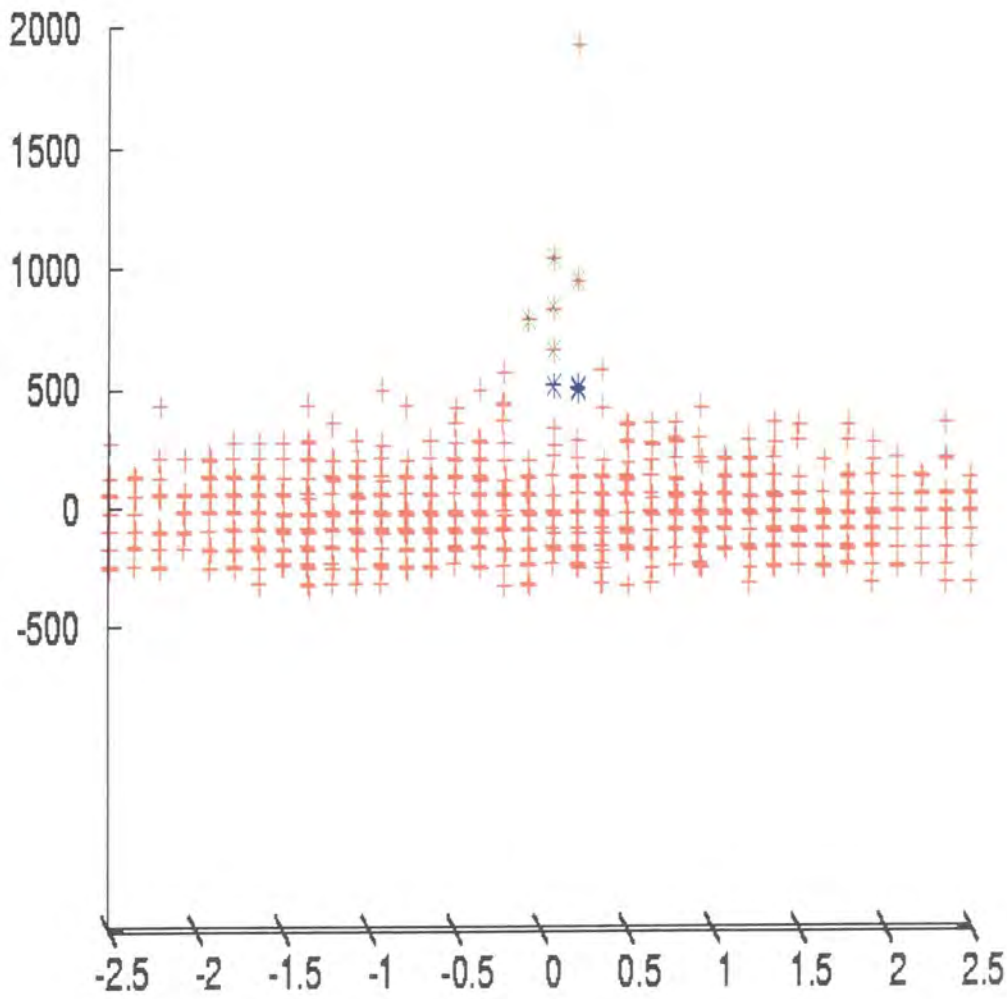


Figure C-4: Edge on perspective from figure C-3. Z (vertical) axis is in digital counts.

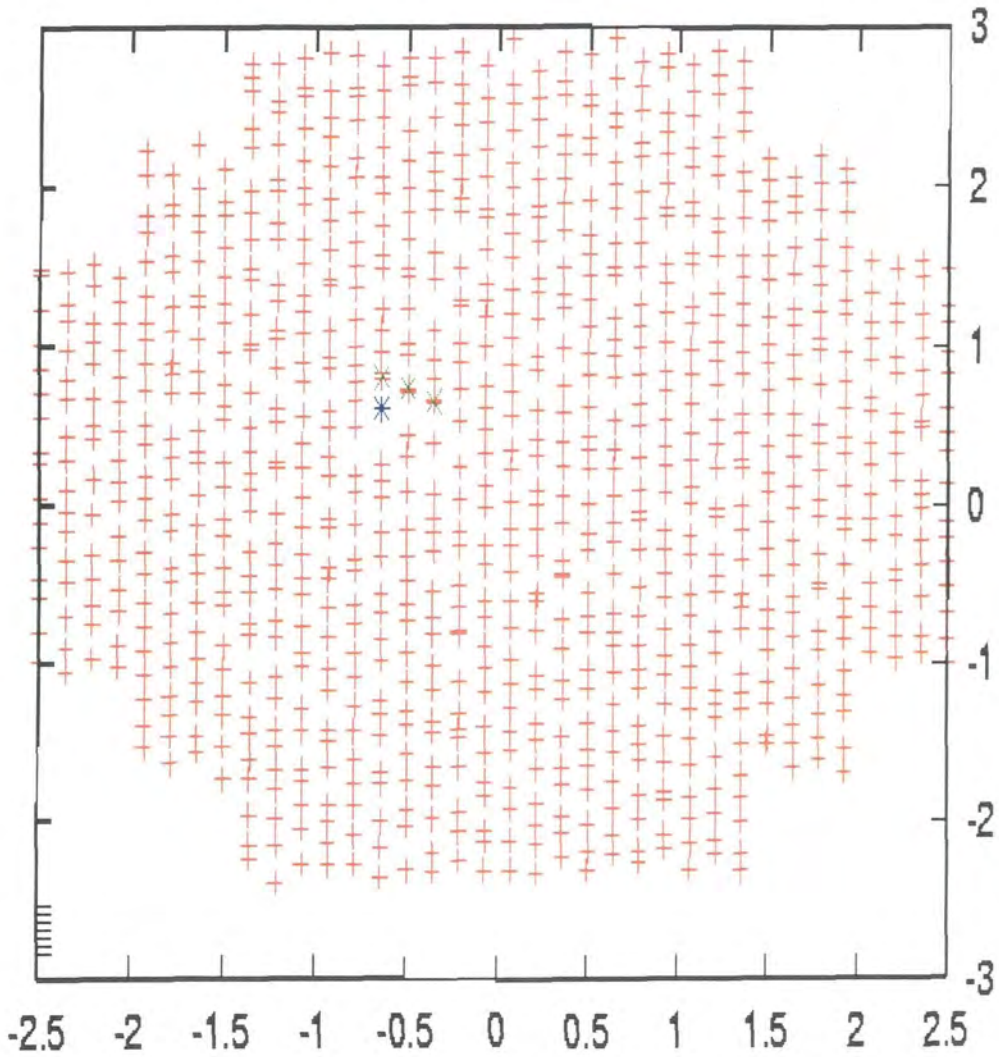


Figure C-5: View of simulated first H.E.S.S. camera, and its response to a 0.08 TeV gamma-ray landing 110.0m away. The X (horizontal) and Y (vertical) axis are in degrees.

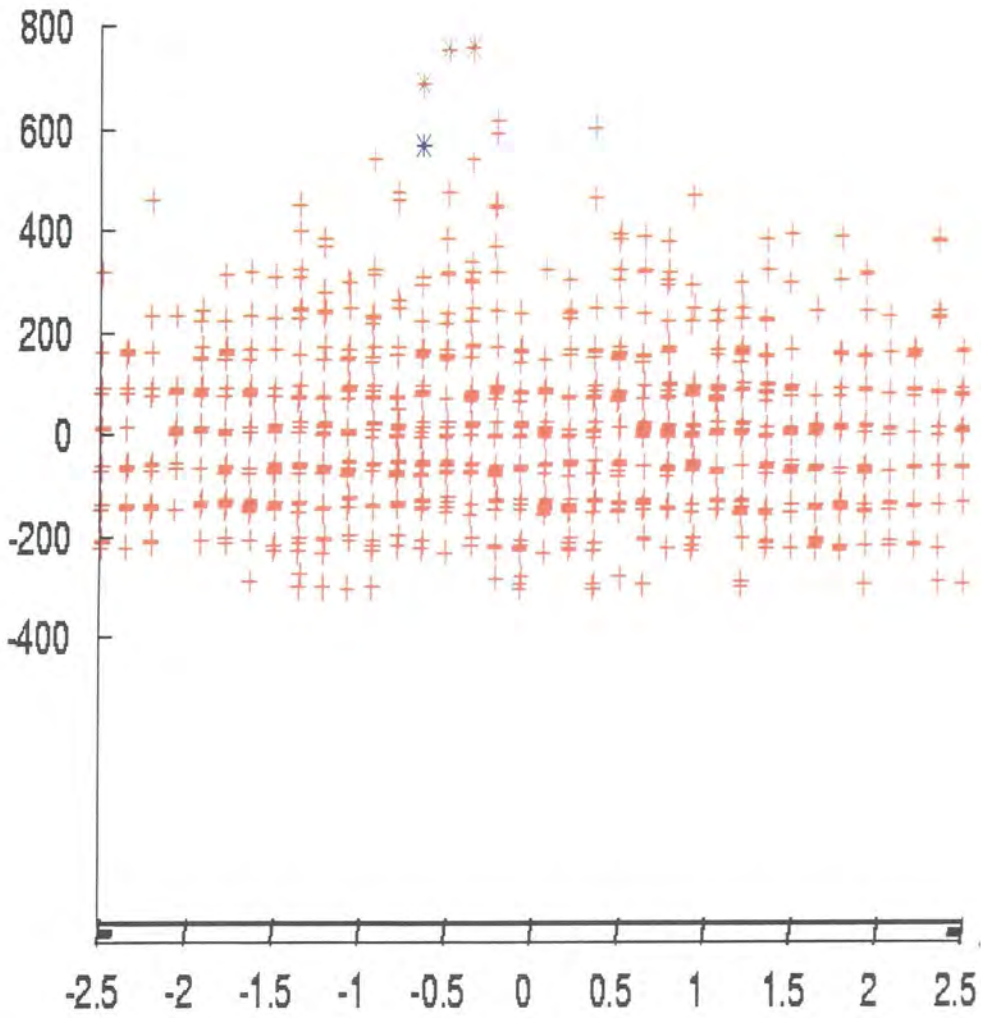


Figure C-6: Edge on perspective from figure C-5. Z (vertical) axis is in digital counts.

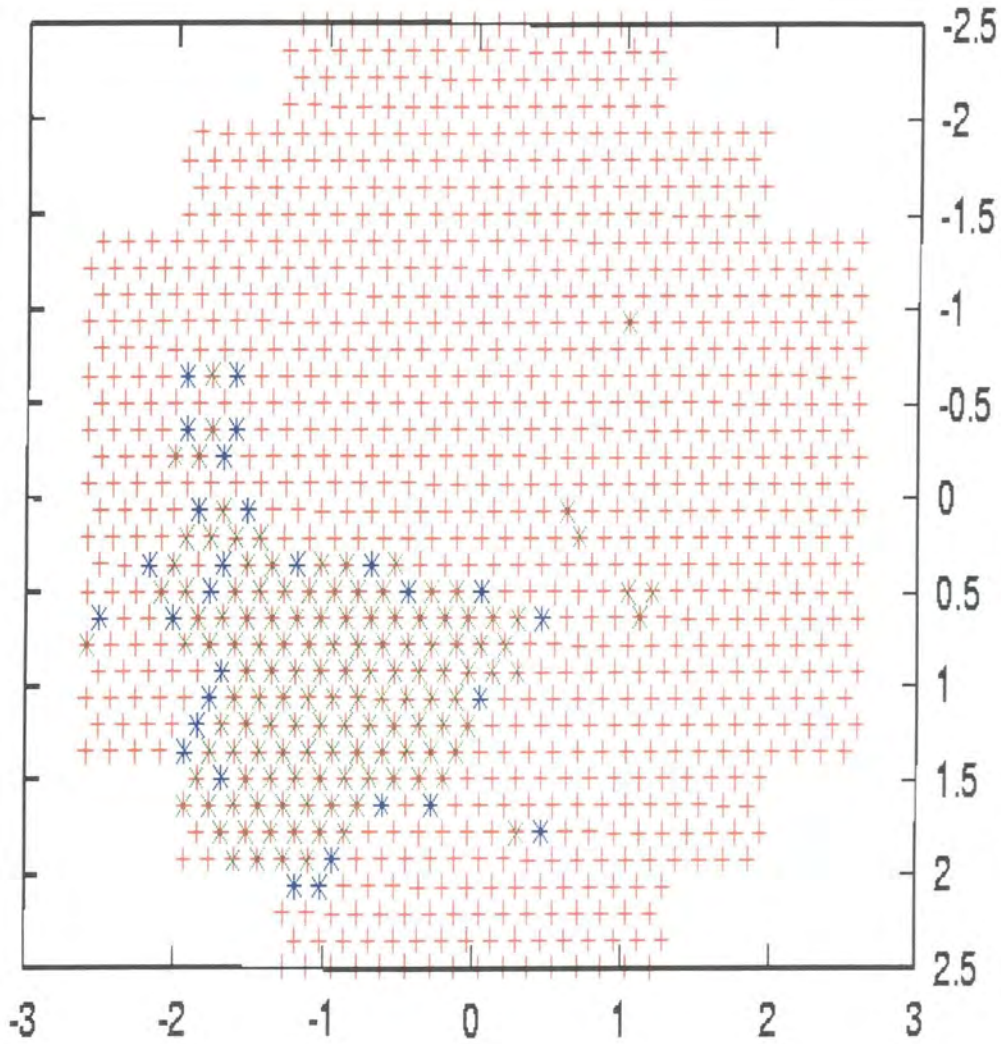


Figure C-7: View of simulated first H.E.S.S. camera, and its response to a 5.2 TeV cosmic ray landing 67.6m away. The X (horizontal) and Y (vertical) axis are in degrees

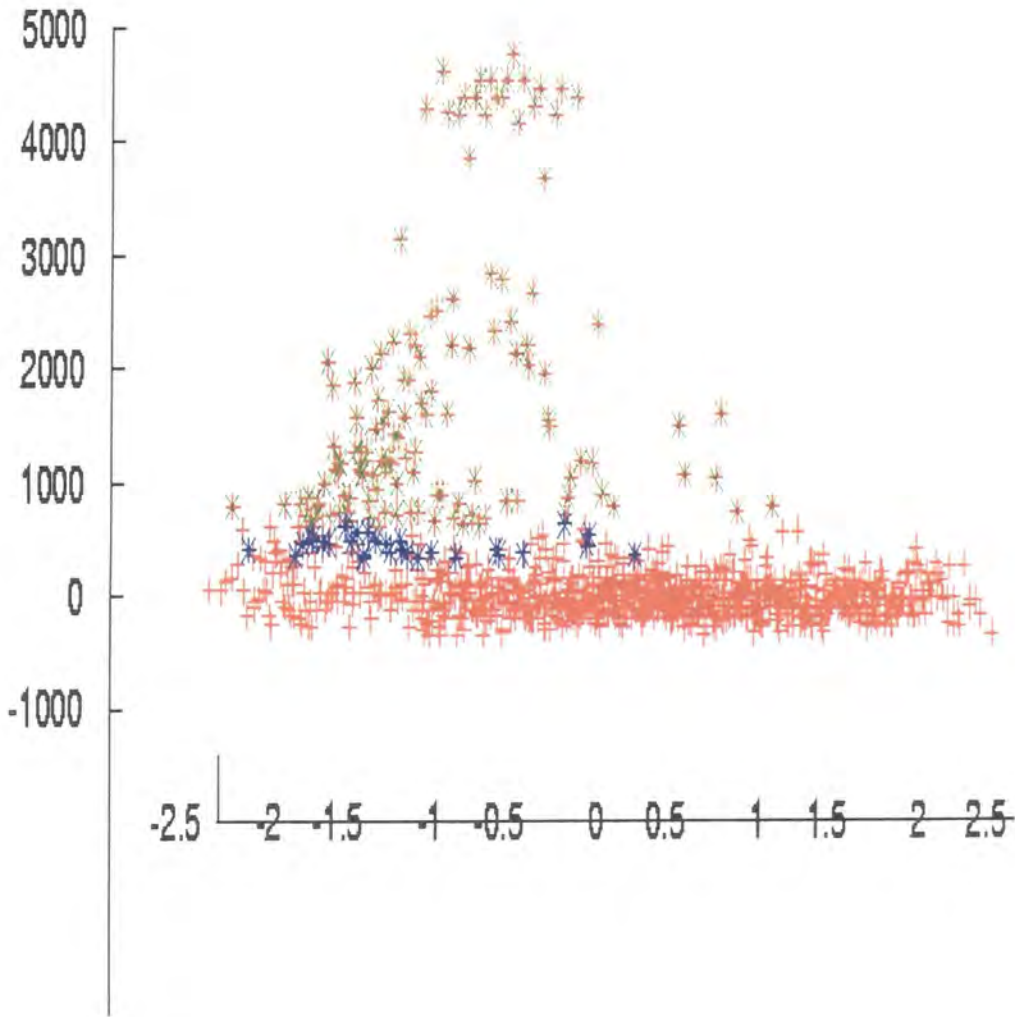


Figure C-8: Edge on perspective from figure C-7. Z (vertical) axis is in digital counts

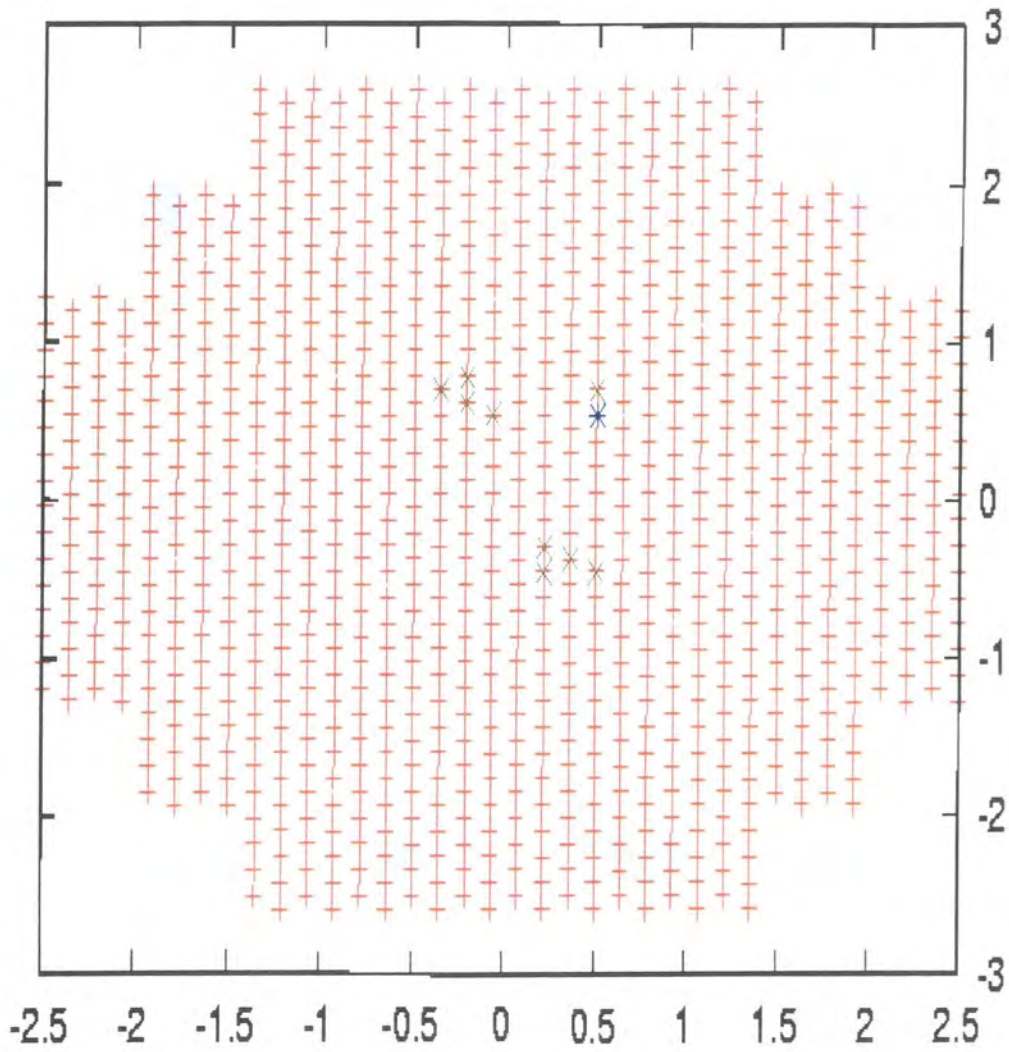


Figure C-9: View of simulated first H.E.S.S. camera, and its response to a 0.6 TeV cosmic ray landing 107.0m away. The X (horizontal) and Y (vertical) axis are in degrees

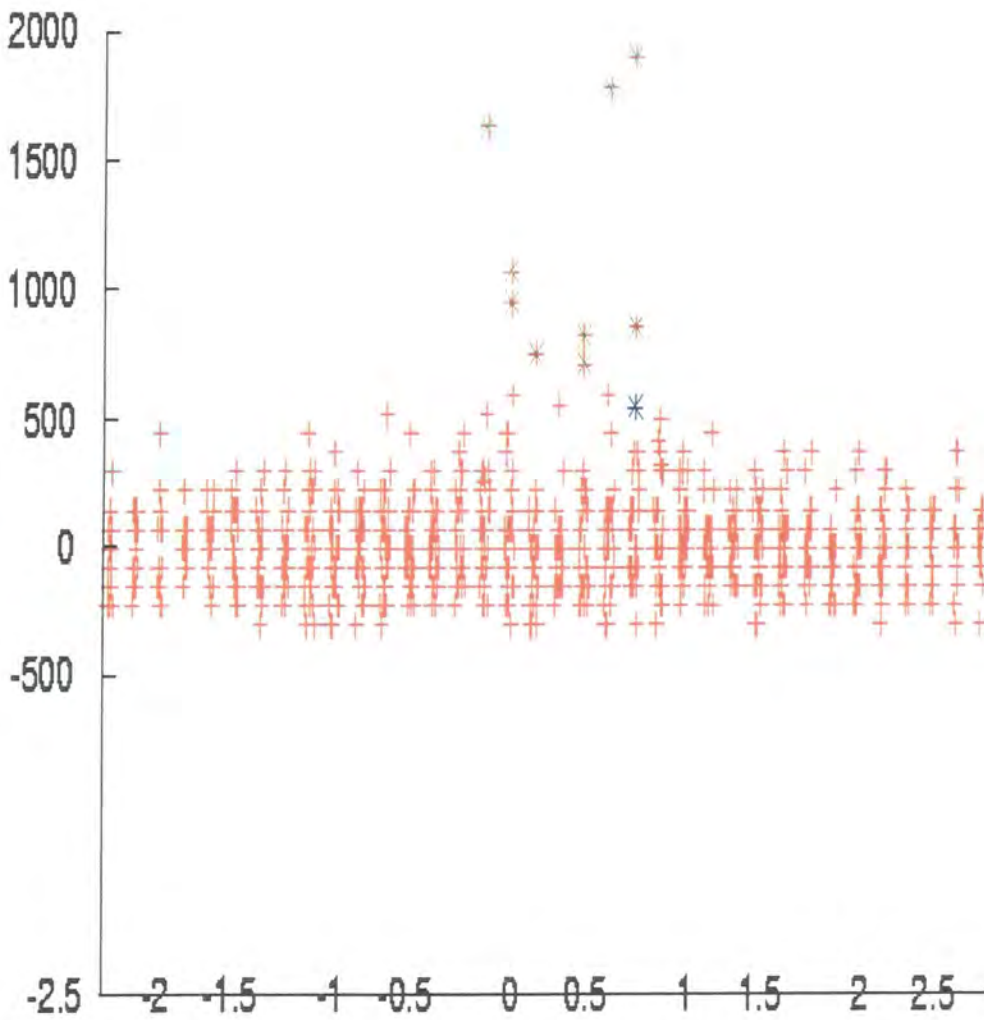


Figure C-10: Edge on perspective from figure C-9. Z (vertical) axis is in digital counts

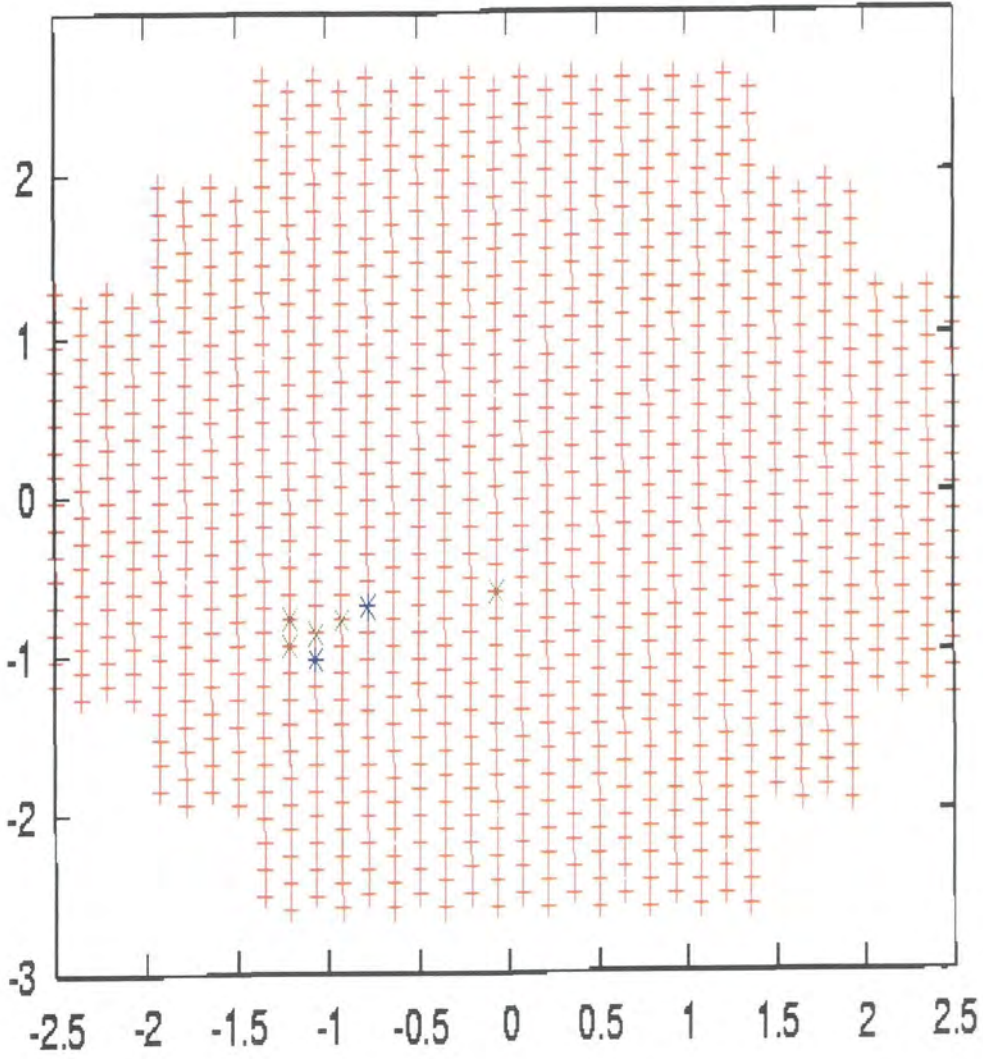


Figure C-11: View of simulated first H.E.S.S. camera, and its response to a 0.225 TeV cosmic ray landing 105.0m away. The X (horizontal) and Y (vertical) axis are in degrees

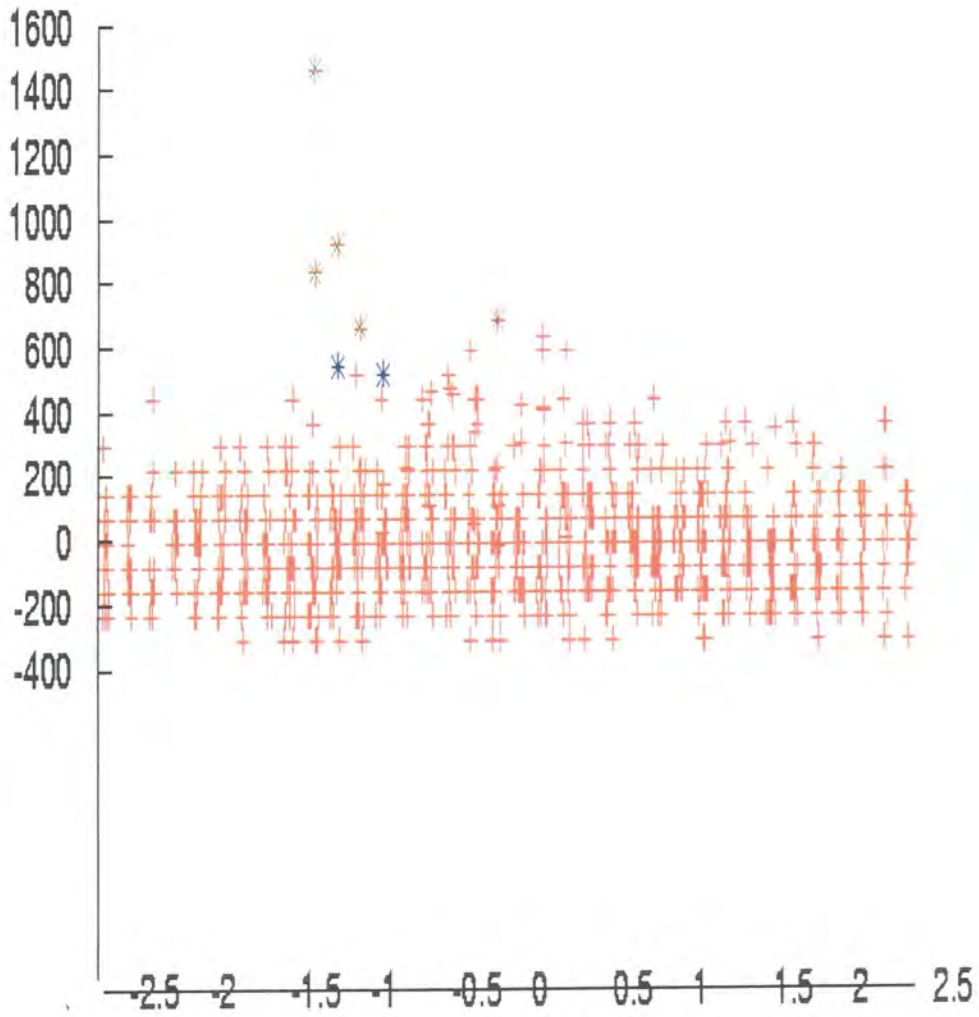


Figure C-12: Edge on perspective from figure C-11. Z (vertical) axis is in digital counts

Appendix D: Differences In Hillas Parameter Distributions due to Atmosphere

This appendix presents the Hillas parameter distributions for the stand-alone H.E.S.S. telescope produced with MOCCA and CameraHESS for spectra of cosmic rays and gamma-rays given atmospheres with ground layers set at 0 metres a.s.l. and 1800 m a.s.l. The histograms given are listed in table D-1. It should be noted that each histogram gives the results for a particular parameter and primary type (gamma-ray/cosmic ray) for both atmospheres, and that the results for the more attenuating atmosphere (with ground level at 1800 m) have been scaled such that the areas under both plots are identical. Errors given are at the 1σ level for each bin. All data has been cut on distance (0.3–2.0 degrees), SIZE (≥ 3000 d.c.) and number of tubes in image (≥ 4). For length, width and α (the most discriminating parameters), a cut on energy is also included; (< 0.1 TeV for gamma-rays and < 0.3 TeV for cosmic rays), to further investigate the effects of atmosphere at lower energies (see figures: D-3, D-4, D-7, D-8, D-11, D-12).

Figure No.	Primary	Parameter	Energy Cut (TeV)
D-1	Gamma-Ray	Length	—
D-2	Cosmic Ray	Length	—
D-3	Gamma-Ray	Length	< 0.1
D-4	Cosmic Ray	Length	< 0.3
D-5	Gamma-Ray	Width	—
D-6	Cosmic Ray	Width	—
D-7	Gamma-Ray	Width	< 0.1
D-8	Cosmic Ray	Width	< 0.3
D-9	Gamma-Ray	Alpha	—
D-10	Cosmic Ray	Alpha	—
D-11	Gamma-Ray	Alpha	< 0.1
D-12	Cosmic Ray	Alpha	< 0.3
D-13	Gamma-Ray	Concentration	—
D-14	Cosmic Ray	Concentration	—
D-15	Gamma-Ray	SIZE	—
D-16	Cosmic Ray	SIZE	—
D-17	Gamma-Ray	No. Image Tubes	—
D-18	Cosmic Ray	No. Image Tubes	—
D-19	Gamma-Ray	Distance	—
D-20	Cosmic Ray	Distance	—

Table D-1: Table of Hillas parameter distributions given in appendix D.

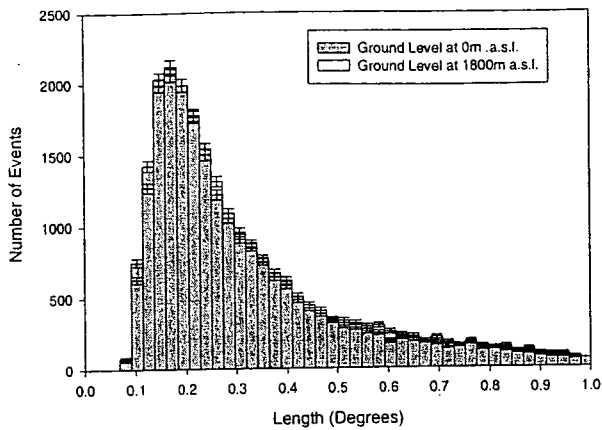


Figure D-1: Plot shows histogram of the simulated response of the stand-alone H.E.S.S. telescope to a spectrum of gamma-rays produced with MOCCA in terms of the length parameter for cut datasets as detailed. The two different plots are for atmospheric attenuation with a ground level set at sea level and at the telescope altitude.

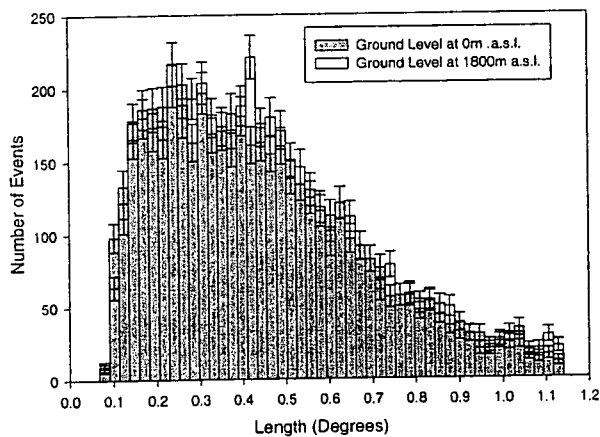


Figure D-2: Plot shows histogram of the simulated response of the stand-alone H.E.S.S. telescope to a spectrum of cosmic rays produced with MOCCA in terms of the length parameter for cut datasets as detailed. The two different plots are for atmospheric attenuation with a ground level set at sea level and at the telescope altitude.

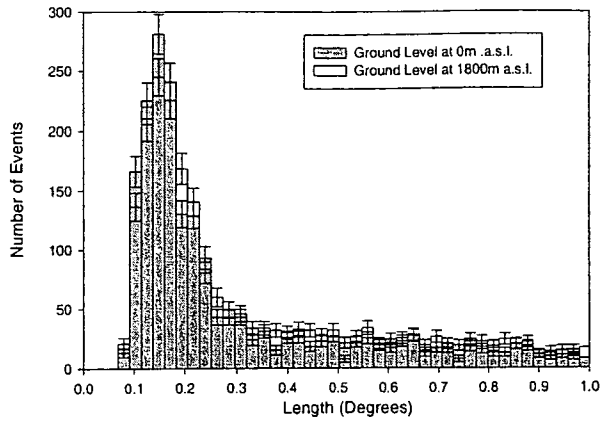


Figure D-3: Plot shows histogram of the simulated response of the stand-alone H.E.S.S. telescope to a spectrum of gamma-rays (with energies less than or equal to 0.1 TeV), produced with MOCCA, in terms of the length parameter for cut datasets as detailed. The two different plots are for atmospheric attenuation with a ground level set at sea level and at the telescope altitude.

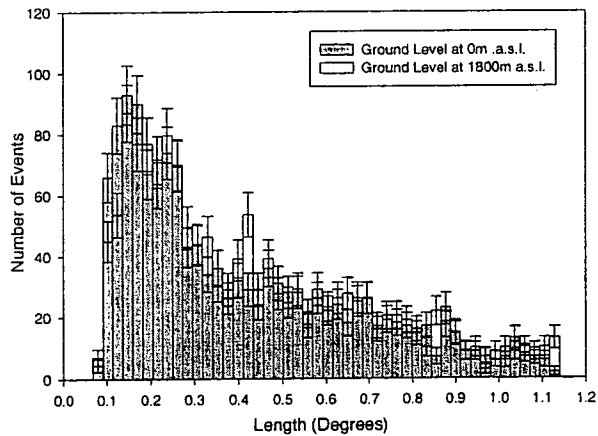


Figure D-4: Plot shows histogram of the simulated response of the stand-alone H.E.S.S. telescope to a spectrum of cosmic rays (with energies less than or equal to 0.3 TeV), produced with MOCCA in terms of the length parameter for cut datasets as detailed. The two different plots are for atmospheric attenuation with a ground level set at sea level and at the telescope altitude.

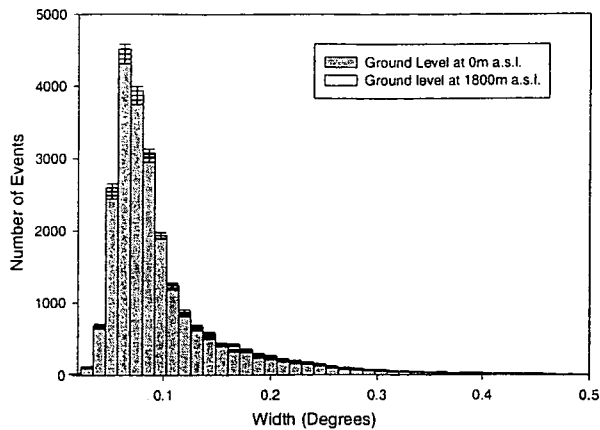


Figure D-5: Plot shows histogram of the simulated response of the stand-alone H.E.S.S. telescope to a spectrum of gamma-rays produced with MOCCA in terms of the width parameter for cut datasets as detailed. The two different plots are for atmospheric attenuation with a ground level set at sea level and at the telescope altitude.

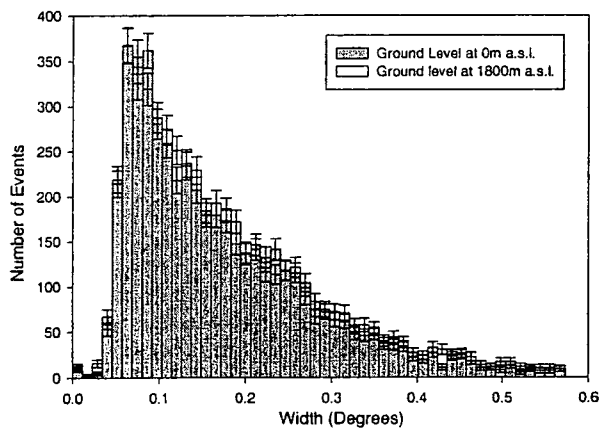


Figure D-6: Plot shows histogram of the simulated response of the stand-alone H.E.S.S. telescope to a spectrum of cosmic rays produced with MOCCA in terms of the width parameter for cut datasets as detailed. The two different plots are for atmospheric attenuation with a ground level set at sea level and at the telescope altitude.

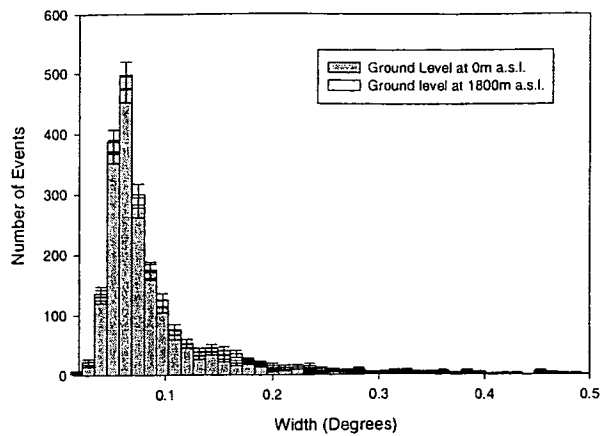


Figure D-7: Plot shows histogram of the simulated response of the stand-alone H.E.S.S. telescope to a spectrum of gamma-rays (with energies less than or equal to 0.1 TeV), produced with MOCCA, in terms of the width parameter for cut datasets as detailed. The two different plots are for atmospheric attenuation with a ground level set at sea level and at the telescope altitude.

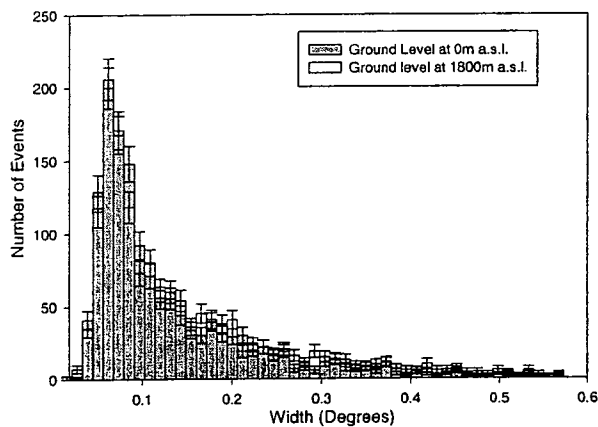


Figure D-8: Plot shows histogram of the simulated response of the stand-alone H.E.S.S. telescope to a spectrum of cosmic rays (with energies less than or equal to 0.3 TeV), produced with MOCCA in terms of the width parameter for cut datasets as detailed. The two different plots are for atmospheric attenuation with a ground level set at sea level and at the telescope altitude.

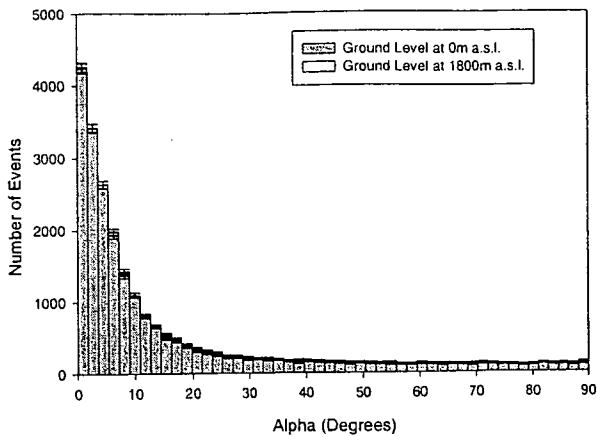


Figure D-9: Plot shows histogram of the simulated response of the stand-alone H.E.S.S. telescope to a spectrum of gamma-rays produced with MOCCA in terms of the alpha parameter for cut datasets as detailed. The two different plots are for atmospheric attenuation with a ground level set at sea level and at the telescope altitude.

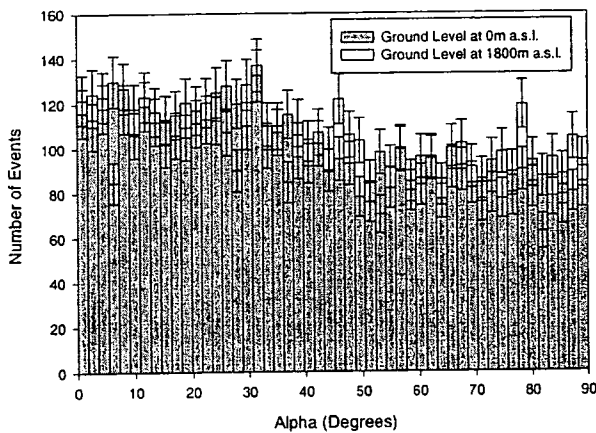


Figure D-10: Plot shows histogram of the simulated response of the stand-alone H.E.S.S. telescope to a spectrum of cosmic rays produced with MOCCA in terms of the alpha parameter for cut datasets as detailed. The two different plots are for atmospheric attenuation with a ground level set at sea level and at the telescope altitude.

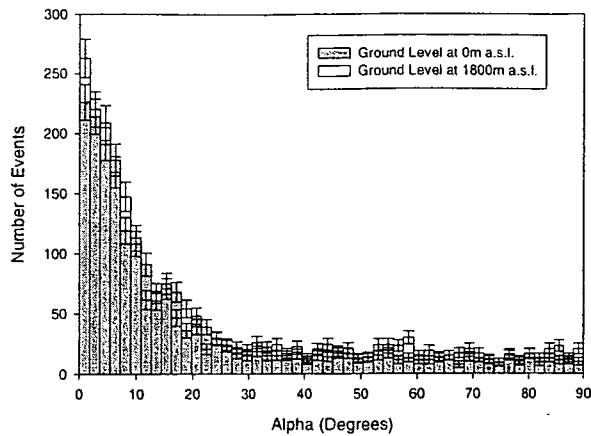


Figure D-11: Plot shows histogram of the simulated response of the stand-alone H.E.S.S. telescope to a spectrum of gamma-rays (with energies less than or equal to 0.1 TeV), produced with MOCCA, in terms of the alpha parameter for cut datasets as detailed. The two different plots are for atmospheric attenuation with a ground level set at sea level and at the telescope altitude.

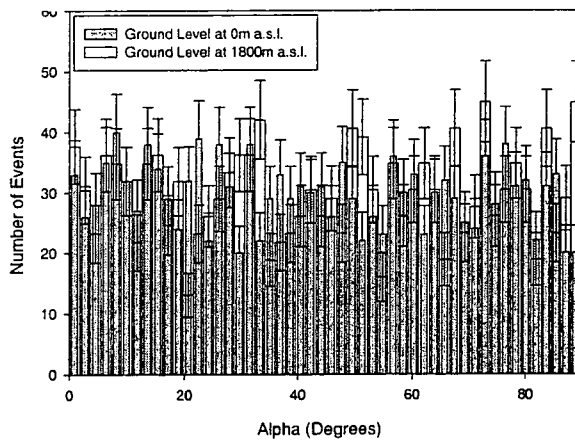


Figure D-12: Plot shows histogram of the simulated response of the stand-alone H.E.S.S. telescope to a spectrum of cosmic rays (with energies less than or equal to 0.3 TeV), produced with MOCCA in terms of the alpha parameter for cut datasets as detailed. The two different plots are for atmospheric attenuation with a ground level set at sea level and at the telescope altitude.

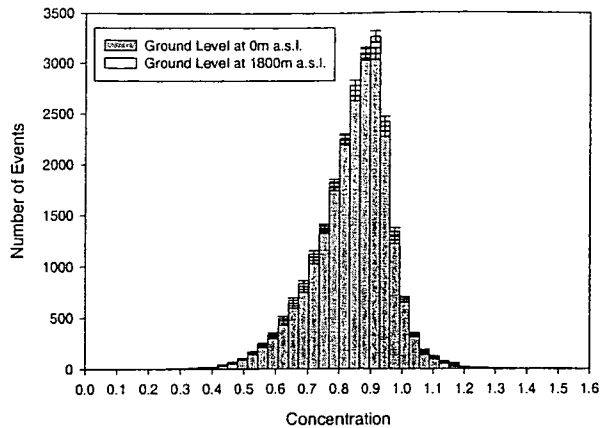


Figure D-13: Plot shows histogram of the simulated response of the stand-alone H.E.S.S. telescope to a spectrum of gamma-rays produced with MOCCA in terms of the concentration parameter for cut datasets as detailed. The two different plots are for atmospheric attenuation with a ground level set at sea level and at the telescope altitude.

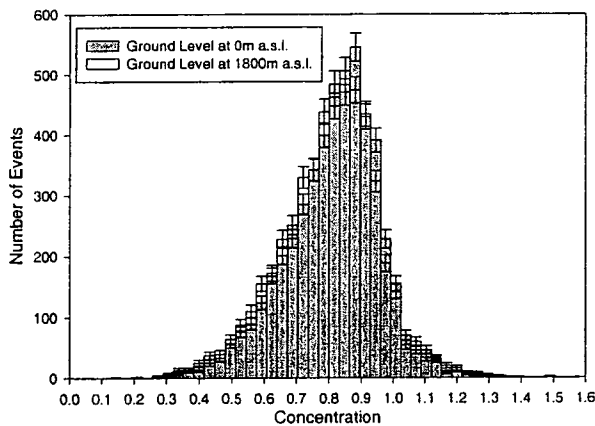


Figure D-14: Plot shows histogram of the simulated response of the stand-alone H.E.S.S. telescope to a spectrum of cosmic rays produced with MOCCA in terms of the concentration parameter for cut datasets as detailed. The two different plots are for atmospheric attenuation with a ground level set at sea level and at the telescope altitude.

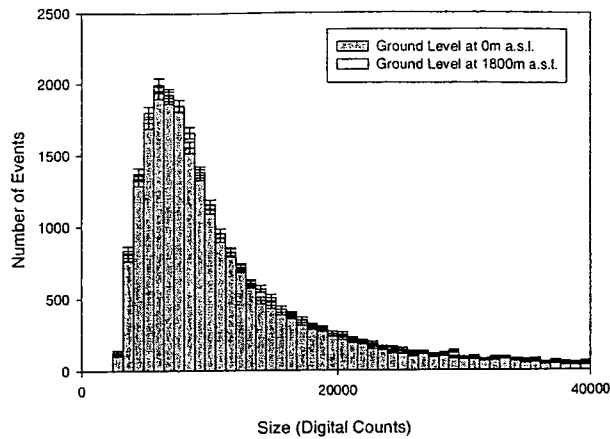


Figure D-15: Plot shows histogram of the simulated response of the stand-alone H.E.S.S. telescope to a spectrum of gamma-rays produced with MOCCA in terms of the SIZE parameter for cut datasets as detailed. The two different plots are for atmospheric attenuation with a ground level set at sea level and at the telescope altitude.

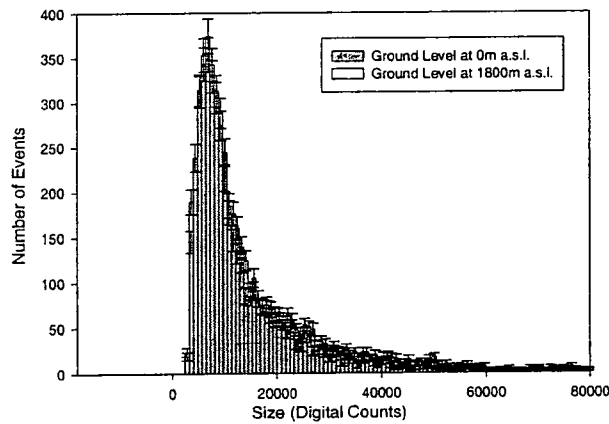


Figure D-16: Plot shows histogram of the simulated response of the stand-alone H.E.S.S. telescope to a spectrum of cosmic rays produced with MOCCA in terms of the SIZE parameter for cut datasets as detailed. The two different plots are for atmospheric attenuation with a ground level set at sea level and at the telescope altitude.

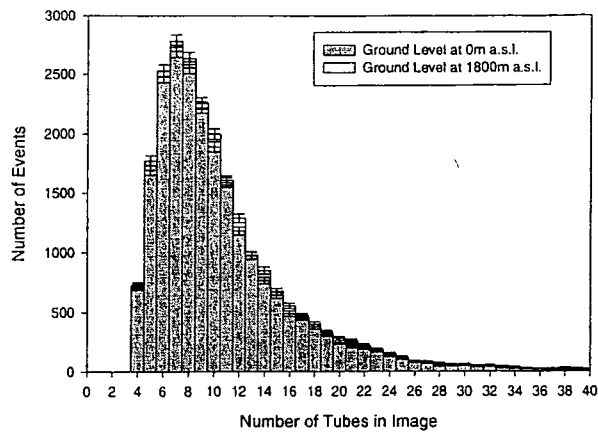


Figure D-17: Plot shows histogram of the simulated response of the stand-alone H.E.S.S. telescope to a spectrum of gamma-rays produced with MOCCA in terms of the number of tubes in image for cut datasets as detailed. The two different plots are for atmospheric attenuation with a ground level set at sea level and at the telescope altitude.

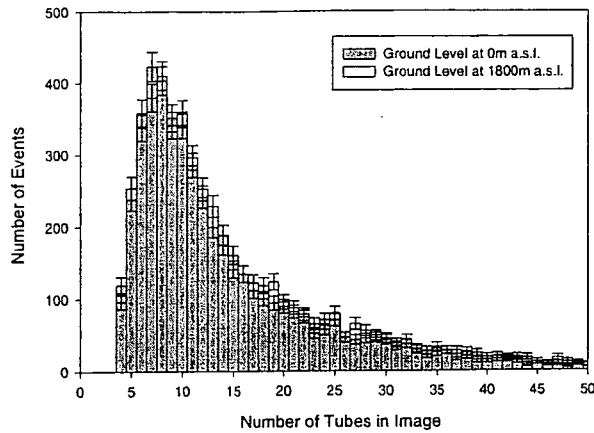


Figure D-18: Plot shows histogram of the simulated response of the stand-alone H.E.S.S. telescope to a spectrum of cosmic rays produced with MOCCA in terms of the number of tubes in image for cut datasets as detailed. The two different plots are for atmospheric attenuation with a ground level set at sea level and at the telescope altitude.

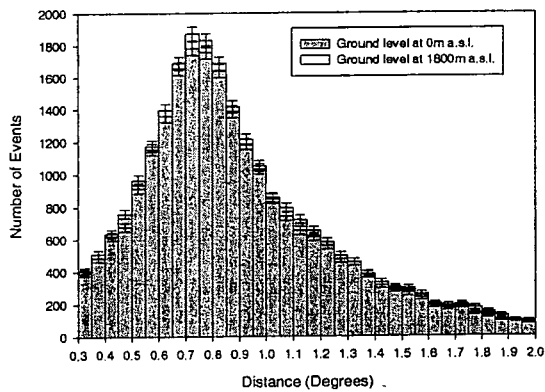


Figure D-19: Plot shows histogram of the simulated response of the stand-alone H.E.S.S. telescope to a spectrum of gamma-rays produced with MOCCA in terms of the distance parameter for cut datasets as detailed. The two different plots are for atmospheric attenuation with a ground level set at sea level and at the telescope altitude.

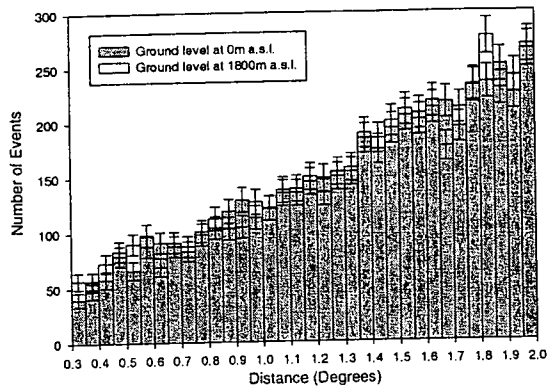


Figure D-20: Plot shows histogram of the simulated response of the stand-alone H.E.S.S. telescope to a spectrum of cosmic rays produced with MOCCA in terms of the distance parameter for cut datasets as detailed. The two different plots are for atmospheric attenuation with a ground level set at sea level and at the telescope altitude.

Bibliography

- [1] Acharya, B.S. et al., (1992), *A. & A.*, **258**, 412
- [2] Aharonian, F.A. et al., (2001), *Astropart. Phys.*, **15**, 335
- [3] Aharonian, F.A. et al., (2001), *A. & A.*, **370**, 112
- [4] Aharonian, F.A. et al., (2002), *astro-ph/0202072*
- [5] Aharonian, F.A., & Atoyan, A.M., (1991), *Ap. J.*, **381**, 220
- [6] Aharonian, F.A., & Atoyan, A.M., (1998), *New Astron. Rev.*, **42**, 579
- [7] Allan, (1971), *Prog. Elem. Part. and Cosmic Ray Physics*, **10**, 170
- [8] Amelino-Camelia, G. et al., (1998), *Nature*, **393**, 765
- [9] Armstrong, P. et al., (1999), *Exp. Astron.*, **9**, 51
- [10] Atkins, R. et al., (2000), *Ap. J.*, **522**, L119
- [11] Atoyan, A.M. & Aharonian, F.A., (1999), *M.N.R.A.S.*, **302**, 253
- [12] Atoyan, A.M. et al., (2002), *A. & A.*, **383**, 864
- [13] Aye, K.-M. et al., (2001), *Proc. 27th Int. Cosmic Ray Conf., Hamburg*, **7**, 2597
- [14] Aye, K.-M. et al., (2001), *Proc. 27th Int. Cosmic Ray Conf., Hamburg*, **7**, 2842
- [15] Bade, N., Fink, H.H. & Ekers, R.D., (1965), *Australian J Phys.*, **18**, 627
- [16] Barrau, A. et al., (1999), *Nucl. Inst. Meth. A.*, **416**, 278

-
- [17] Bernlöhr, K., (2000), *Astropart. Phys.*, **12**, 255
- [18] Bernlöhr, K., (2002), "Shadowing in a H.E.S.S. telescope due to masts and other elements", H.E.S.S. Internal Note
- [19] Bernlöhr, K., (2002), Private Communication
- [20] Bhat, P.N. et al., (1980), *A. & A.*, **81**, L3
- [21] Bhat, C.L., et al., (1993), *Bulletin of the Astronomical Society of India*, **21**, 519
- [22] Biller S.D., et al., (1999), *Phys. Rev. Lett.*, **83**, 2108
- [23] Blackett, P.M.S., (1948), *Phys. Soc. London, Gaiassot. Comm. Rep.*, 34
- [24] Blandford, R.D. & Rees, M.J., (1978), *Proc. Conf. on BL-Lac Objects, Pittsburgh*, 328- & 347-
- [25] Blifford, I.H. & Ringer, L.D., (1969), *J. Atmos. Sci*, **26**, 716
- [26] Bloom, S.D. & Marscher, A.P., (1996), *Ap. J.*, **461**, 657
- [27] Bondi, H. & Hoyle, F., (1944), *M.N.R.A.S.*, **104**, 273
- [28] Bowden, C.C.G. et al., (1992), *Astropart. Phys.*, **1**, 47
- [29] Browning, R. & Turver, K.E., (1977), *Nuovo Cimento*, **38A**, 223
- [30] Bussino, S. & Mari, S.M., (2000), *Astropart. Phys.*, **15**, 65
- [31] Carraminana, A., (1989), *Ap. J.*, **346**, 967
- [32] Catanese, M. et al., (1996), *Ap. J.*, **501**, 616
- [33] Catanese, M.A. et al., (1997), *Ap. J.*, **487**, L143
- [34] Cawley, M.F. et al., (1990), *Ex. As.*, **vol. 1, 3**, 173
- [35] Chadwick, P.M. et al., (1985), *Proc. 19th Int. Cosmic Ray Conf., La Jolla*, **1**, 155
- [36] Chadwick, P.M. et al., (1990). *J. Phys. G*, **16**, 1773

- [37] Chadwick, P.M. et al., (1999), Proc. 26th Int. Cosmic Ray Conf., Salt Lake City, **5**, 231
- [38] Chadwick, P.M. et al., (1999), Ap. J., **513**, 161
- [39] Chadwick P.M. et al., (2000), J. Phys. G., **26**, L5
- [40] Cheng, K.S. et al., (1986), Ap. J., **300**, 500- and 522-
- [41] Cheng, K.S. & Ruderman, M., (1991), Ap. J., **373**, 187
- [42] Cherenkov, P.A., (1937), Phys. Rev., **52**, 378
- [43] Chiappetti, L. et al., (1999), Ap. J., **521**, 552
- [44] Cocconi, G., (1959), Proc. 7th Int. Cosmic Ray Conf., Moscow, **2**, 309
- [45] CORSIKA Website, <http://www-ik3.fzk.de/heck/corsika/>
- [46] Courvoisier, T. J. et al., (1995), Ap. J., **438**, 108
- [47] Dahl, O.I. & Lynch, G.R., (1991), Nucl. Inst. Meth. B., **58**, 6
- [48] Daum, A et al., (1997), Astropart. Phys., **8**, 1
- [49] Daugherty, J & Harding, A, (1983), Ap. J., **273**, 761
- [50] Davidson, K. & Ostriker, J.P., (1973), Ap. J., **179**, 585
- [51] Diehl, R., (1988), Space Science Reviews, **49**, no. 1- 2, 85
- [52] Dowthwaite, J.C. et al., (1984), Ap. J., **286**, L35
- [53] Enomoto, R. et al., (2001), Proc. 27th Int. Cosmic Ray Conf., Hamburg, **6**, 2477
- [54] Enomoto, R. et al., (2002), Astropart. Phys., **16**, 235
- [55] Erber, T., (1966), Rev. Modern. Phys., **38**, 626
- [56] Fegan, D.J. et al., (1994), Proc. Towards a Major Cherenkov Detector III, Kifune, T. (ed.), 149

- [57] Fermi, E., (1949), *Phys. Rev.*, **75**, 1169
- [58] Fichtel, C.E. et al., (1994), *Ap. J. S.*, **94**, 551
- [59] Fishman, G.J., et al., (1985), *Proc. 19th Int. Cosmic Ray Conf., La Jolla*, **3**, 343
- [60] Fortin, P, (2002), *Meeting 200 of the American Astronomical Society*, 21.01
- [61] Fossati, G. et al., (1998), *M.N.R.A.S.*, **299**, 433
- [62] Frank, I.M. and Tamm, I.G., (1937), *Dokl. Fys. Nauk. SSSR.*, **14**, 109
- [63] F.X. Kneizys et al., (1996), "The MODTRAN 2/03 Report and LOWTRAN 7 Model", Phillips Laboratory (Hanscom AFB, MA 01731, USA)
- [64] Gaisser, T.K., (1990), "Cosmic Rays & Particle Physics", Cambridge University Press
- [65] Gaisser, T.K, Protheroe, R.J. et al., (1998), *Ap. J.*, **492**, 219
- [66] Galbraith, W., and Jelley, J.V., (1953), *Nature*, **171**, 349
- [67] Gawiser, E. & Silk, J.,(1998), *Science*, **280**, 1405
- [68] Gehrels, N., and Michelson, P., (1999), *Astropart. Phys.*, **11**, 277G
- [69] Goeckel, (1910), *Phys. Zeits.*, **11**, 280
- [70] Gould, R.J. and Schreder, G.P., (1965), *Phys. Rev. Lett.*, **15**, 511
- [71] Gould, R.J., & Schreder, G.P., (1966), *Phys. Rev. Lett.*, **16**, 252
- [72] Gribov, L. et al., (1983), *Phys. Rep.*, **100**, 1
- [73] Grindlay, J.E., (1971), *Nuovo Cimento*, **2B**, 119
- [74] Guy, J., (2002), "More on the photoelectron pulse shape", H.E.S.S. Internal Note
- [75] Hartman, R. C., et al., (1992), *Compton Observatory Science Workshop*, Schrader C.R., et al., (eds.), Berg-en-Dal, 166

- [76] Hartman, R.C., et al., (1999), *Ap. J. S.*, **123**, 79H
- [77] Hauser, M.G. et al., (1998), *Ap. J.*, **508**, 25
- [78] Heaviside, O., (1890), *Electrical Paper*, **2**, 494
- [79] Heck., D. et al., (1998), FZKA report-6019, ed. FZK (Karlsruhe)
- [80] Hess, V.F., (1911), *Phys. Zeits.*, **12**, 998
- [81] van den Heuvel, E.P.J., (1983), "Accretion Driven Stellar X Ray Sources", (Lewin, W.H.G & van den Heuvel, E.P.J, Eds.), Cambridge University Press
- [82] Hewish, A. et al., (1968), *Nature*, **217**, 709
- [83] Hill, D.A. and Porter, N.A., (1961), *Nature*, **191**, 690
- [84] Hillas, A.M., (1979), *Proc. 16th Int. Cosmic Ray Conf., Kyoto*, **6**, 13
- [85] Hillas, A.M., (1981), *Proc. 17th Int. Cosmic Ray Conf., Paris*, **8**, 193
- [86] Hillas, A.M., (1982), *J. Phys. G.*, **8**, 1461
- [87] Hillas, A.M., (1985), *Proc. 19th Int. Cosmic Ray Conf., La Jolla*, **3**, 445
- [88] Hillas, A.M. et al., (1989), *Ap. J.*, **503**, 744
- [89] Hillas, A.M., (1996), *Space Science Reviews*, **75**, 17
- [90] Hillas, A.M. et al., (1998), *Ap. J.*, **503**, 744
- [91] Hofmann, W. et al., (1999), *Proc. GeV-TeV Gamma-Ray Astrophysics Workshop (Snowbird)*, AIP **515**, 500
- [92] Horan, D. et al., (2001), *Proc. 26th Int. Cosmic Ray Conf., Hamburg*, **7**, 2622
- [93] van de Hulst, H.C., (1957), "Light Scattering by Small Particles"
- [94] Hurley, K., (1994), *Nature*, **372**, 652
- [95] de Jager, O.C., (2001), *Bulletin of the Astronomical Society of India*, **30**, 85

- [96] de Jager, O.C. & Mastichiadis, A, (1997), *Ap. J.*, **482**, 874
- [97] de Jager, O.C. & Stecker, F.W.,(1998), *A. & A.*, **334**, L85-87
- [98] de Jager, O.C. & Stecker, F.W., (2001), *astroph/107103*
- [99] de Jager, O.C. & Stecker, F.W., (2002), *Ap. J.*, **566**, 738
- [100] Jelley, J.V., (1958), "Cherenkov Radiation and Its Application", London Peragamon Press
- [101] Jelley, J.V. and Galbraith, W., (1955), *J. Atmos. Phys.*, **6**, 304
- [102] Jelley, J.V., (1966), *Phys. Rev. Lett*, **16**, 479
- [103] Johnson, W.N, et al., (1993), *Ap. J. S.*, **86**, 693
- [104] Jones, T.W. et al., (1998), *P.A.S.P.*, **110**, 125
- [105] Jordan, M. et al., (2001), *Proc. 26th Int. Cosmic Ray Conf., Hamburg*, **7**, 2691
- [106] Junge, C.E., (1963), "Air Chemistry and Radioactivity", Academic Press, pp382
- [107] Kalekin, O.R. et al., (1995), *Astron. Letters.*, **21**, 163
- [108] Kanbach, G., et al., (1988), *Space Science Reviews*, **49**, no. 1-2, 69
- [109] Kattawar, C.W., & Plass, G.N., (1967), *Appl. Opt.*, **6**, 1377
- [110] Keplikov, N.P., (1954), *Zh. Eksperim. Teor. Fiz.*, **26**, 19
- [111] Kifune, T. et al., (1995), *Ap. J.*, **438**, L91
- [112] Kirk, J.G., & Dendy, R.O., (2001), *J. Phys. G.*, **27**, 1589
- [113] van der Klis, M., (1988), *Scientific American*, **Nov**, 50
- [114] Knapp, J. et al., (2002), *astroph/206414*
- [115] Kohnle, A. et al., (1996), *Astropart. Phys.*, **5**, 119

- [116] Konopelko, A. & Plyasheshnikov, A., (2000), *Nucl. Inst. Meth. A*, **450**, 419
- [117] Konopelko, A., (2002), "Monte Carlo Study of different strategies of triggering a single stand-alone H.E.S.S. telescope", H.E.S.S. Internal Note
- [118] Konopelko, A., (2002), Private Communication
- [119] Koul, R. et al., (2001), *Proc. 27th Int. Cosmic Ray Conf., Hamburg*, **7**, 2875
- [120] Koyama, K. et al., (1995), *Nature*, **378**, 255
- [121] Lamb, R.C. & Macomb, D.J., (1997), *Ap. J.*, **488**, 872
- [122] Le Gallou, R., (2001), *Proc. 27th Int. Cosmic Ray Conf., Hamburg*, **7**, 2609
- [123] LIDAR Website, <http://www.soest.hawaii.edu/lidar/opss0061.htm>
- [124] Longair, M.S., (1997), "High Energy Astrophysics", Vol. 1 & 2, Cambridge University Press
- [125] Lorenz, E. et al., (2001), *Proc. 27th Int. Cosmic Ray. Conf., Hamburg*, **7**, 2789
- [126] Lorenz, E., (2001), *J. Phys. G*, **27**, 1675
- [127] Lyne, A.G and Graham-Smith, F., (1990), "Pulsar Astronomy", Cambridge University Press
- [128] McKenny, J., in production, "Studies of Southern Hemisphere AGN", Ph.D. Thesis
- [129] Macminn, D & Primack, J.R., (1996), *Space Science Reviews*, **75**, 413
- [130] Madau, P, & Pozzetti, L., (2001), *M.N.R.A.S.*, **312**, L9
- [131] Malkan, M.A. & Stecker, F.W., (1998), *Ap. J.*, **496**, 13
- [132] Mallet, L., (1926), *C. R. Acad. Sci. (Paris)*, **183**, 274
- [133] Mannheim, K., (1993), *A. & A.*, **269**, 67
- [134] Mannheim, K. & Biermann, P.L., (1992), *A. & A.*, **253**, L21

- [135] Maraschi, L. et al., (1999), *Ap. J.*, **526**, L81-L84
- [136] Masterson, C., (2002), Private Communication
- [137] Matsumoto, T., (2000), Institute of Space and Astronomical Science, Kanagawa, Japan, Report No. 14
- [138] Matthews, J.A. et al., (2001), *Proc. 27th Int. Cosmic Ray Conf.*, Hamburg, **2**, 745
- [139] Meintjes, P.J. et al., (1992), *Ap. J.*, **401**, 325
- [140] Miller R.S., et al., (2000), *Bulletin of the American Astronomical Society*, **31**, 719
- [141] Mohanty, G. et al., (1998), *Astropart. Phys.*, **9**, 15
- [142] Molière, G.Z., (1948), *Z. Naturforsch 3a*, 78
- [143] Muraishi, H. et al., (1999), *Proc. 25th Int. Cosmic Ray Conf.*, Utah, **3**, 500
- [144] Murzin, V.S., (1988), "Introduction to Cosmic Ray Physics", Moscow State University
- [145] NASA Cosmic Ray Composition Website,
http://imagine.gsfc.nasa.gov/docs/science/known/cosmic_rays.html
- [146] Navarro, J.F., Frenk, C.S., White, S.D.M., (1996), *Ap. J.*, **462**, 563
- [147] Nelson, W.R., Hirayama, H. & Rogers, D.W.O., (1985), Report 265, Stanford Linear Accelerator Center
- [148] Nesphor, Y.I. et al., (1998), *Ap. Lett.*, **24**, 139
- [149] Nesphor, Y.I. et al., (2001), *Astronomy Reports*, **v45, i4**, 249
- [150] Nikolsky, S.I. et al., (1993), *Bulletin of the Astronomical Society of India*, **21**, 511
- [151] Nithiyama, N. et al., (1999), *Proc. 25th Int. Cosmic Ray Conf.*, Utah, **3**, 370
- [152] Ogelman, H., et al., (1976), *Proc. Gamma-Ray Symposium*, Goddard, 118

- [153] Ong, R.A., (1998), Phys. Rep., **305**, 93
- [154] Page, D.N. & Hawking, S.W., (1976), Ap. J., **206**, 1
- [155] Perlman, E.S. et al., (1998), A. J., **115**, 1253
- [156] Pesce, J.E. et al., (1997), Ap. J., **486**, 770
- [157] Petry, D. et al., (2002), astro-ph/0207506
- [158] Petry, D. and Kranichm, D., (1997), Proc. Towards a Major Cherenkov Detector V, de Jager, O.C (ed.), 368
- [159] Pian, E. et al., (1997), Ap. J., **486**, 784
- [160] Plaga, R., (1998), XVIII Physics in Collision Conference (Frascati), 369
- [161] Primack, J.R., et al., (1997), Astropart. Phys., **8**, 101
- [162] Primack, J.R., (1998), Science, **280**, 1398
- [163] Pringle, J.E & Rees, M.J., (1972), A. & A., **21**, 1
- [164] Puelhofer, G. et al., (1999), Proc. 25th Int. Cosmic Ray Conf., Utah, **3**, 492
- [165] Punch, M. et al., (1991), Proc. 22nd Int. Cosmic Ray Conf., Dublin, **1**, 464
- [166] Punch, M. et al., (1992), Nature, **358**, 477
- [167] Quinn, J. et al., (1996), Ap. J., **456**, L83
- [168] RADIOSONDE Website, <http://raob.fsl.noaa.gov>
- [169] Ramana-Murthy, P.V. and Wolfendale, A.W., (1986), "Gamma-Ray Astronomy", Cambridge Univerisity Press
- [170] Rand, R.J. & Lyne A.G., (1994), M.N.R.A.S., **268**, 497
- [171] Ranft, J. & Routti, J., (1972), Particle Accelerators, **4**, 101

- [172] Rappaport, S.A & Joss, P.C., (1983), "Accretion Driven Stellar X Ray Sources", (Lewin, W.H.G & van den Heuvel, E.P.J, Eds.), Cambridge University Press
- [173] Reynolds, (1993), *Ap. J.*, **404**, 206
- [174] Rieke, G.H., (1969), S.A.O., Special Reports No.:301
- [175] Robson, I., (1996), "Active Galactic Nuclei", Wilson-Praxis Publishers
- [176] Rossi, B., (1952), "High Energy Particles", Prentice Hall, Englewood Cliffs, New Jersey
- [177] Rossi, B. & Greisen, (1941), "Cosmic Ray Physics", Addison- Wesley Publishing Company
- [178] Rowell, G. et al., (2001), *Proc. 26th Int. Cosmic Ray Conf., Hamburg*, **6**, 2497
- [179] Rutherford E. et al., (1903), *Phys. Rev.*, **16**, 183
- [180] Schlenker, S., (2002), "Simulations of the night sky background trigger rate for the H.E.S.S. camera", H.E.S.S. Internal Note
- [181] Scott, W.T., (1963), *Rev. Modern Phys.*, **35**, 231
- [182] Shabelski Yu, M., (1987), *Nucl. Phys.*, **45**, 223
- [183] Shaw, S.E., (1999), Ph. D. Thesis
- [184] Shettle, E. & Fenn, R., (1975), "Models of the Atmospheric Aerosols and their Optical Properties", Electromagnetic Wave Propagation Panel Symposium, Lyngby, Denmark, AGARD-CP-183
- [185] Shettle, E. & Fenn, R., (1979), "Models of the Aerosols of the Lower Atmosphere and the Effects of Humidity Variations on Their Optical Properties, Air Force Geophysics Laboratory", AFGL-TR-79-0214
- [186] Sikora, M. et al., (1994), *Ap. J.*, **421**, 153

- [187] Stecker, F.W. et al., (1996), *Ap. J.*, **473**, L75
- [188] Stepanian, A.A. et al., (1983), *Izvestia, CAO J*, **66**, 234
- [189] Sturrock, P.A., (1971), *Ap. J.*, **164**, 529
- [190] Tanimori, T. et al., (1998), *Ap. J.*, **497**, L25
- [191] Toller, G.N., (1990), "The Galactic and Extragalactic Background Radiation", (Ed. Bowyer, S. and Leinert, C.), Kluwer Academic Publishers, Dordrecht, 21
- [192] TOMS Website, <http://jwocky.gsfc.nasa.gov/>
- [193] Turver, K.E. & Weekes, T.C., (1978), *Nuovo Cimento*, **45B**, 99
- [194] Turver K.E. et al., (1997), *Toward a Major Atmospheric Cherenkov Detector V*, de Jager, O.C. (ed.), 389
- [195] Ueda, Y. et al., (2002), *astro-ph/0202154*
- [196] Urry, C.M. and Padovani, P., (1995), *P.A.S.P.*, **107**, 803
- [197] Vestrand, W. T. et al., (1995), *Ap. J.*, **454**, L93
- [198] Vestrand, W.T. et al., (1999), *Astropart. Phys.*, **11**, 197
- [199] Wdowczyk, J. and Wolfendale, A., (1972), *J. Phys. A.*, **5**, 1419
- [200] Weekes, T.C. et al., (1988), *Phys. Reports*, **160**, 1
- [201] Weekes, T.C. et al., (1989), *Ap. J.*, **342**, 379
- [202] Weekes, T.C. et al., (1997), *Proc. Towards a Major Cherenkov Detector V*, de Jager, O.C (ed.), 202
- [203] Weekes, T.C. et al., (2002), *Astropart. Phys.*, **17**, 221
- [204] Wiebel-Sooth, B. et al., (1995), *Proc. 25th Int. Cosmic Ray Conf., Rome*, **2**, 656
- [205] Wolter, A., (1999), Private Communication

-
- [206] Yoshikoshi, T. et al., (1997), Ap. J., **487**, L65
- [207] Zatsepin, V.I. &, Chudakov, A.E, (1962a), Sov. Phys., JETP, **15**, 1126
- [208] Zatsepin, V.I. &, Chudakov, A.E, (1962b), Sov. Phys., JETP, **24**, 1622
- [209] Zombeck, M.V., (1990), "Handbook of Space Astronomy and Astrophysics", 2nd ed., Cambridge University Press

